Nanostructure Science and Technology
Series Editor: David J. Lockwood

Balasubramanian Viswanathan
Vaidyanathan (Ravi) Subramanian
Jae Sung Lee *Editors*

Materials and Processes for Solar Fuel Production

Springer

Nanostructure Science and Technology

Series Editor:
David J. Lockwood, FRSC
National Research Council of Canada
Ottawa, Ontario, Canada

More information about this series at
http://www.springer.com/series/6331

Balasubramanian Viswanathan •
Vaidyanathan (Ravi) Subramanian • Jae Sung Lee
Editors

Materials and Processes for Solar Fuel Production

Springer

Editors
Balasubramanian Viswanathan
National Centre for Catalysis Research
Indian Institute of Technology Madras
Chennai, India

Vaidyanathan (Ravi) Subramanian
Department of Chemical and Materials Engineering
University of Nevada
Reno, NV, USA

Jae Sung Lee
Pohang University of Science & Tech.
Pohang
Korea, Republic of (South Korea)

ISSN 1571-5744 ISSN 2197-7976 (electronic)
ISBN 978-1-4939-1627-6 ISBN 978-1-4939-1628-3 (eBook)
DOI 10.1007/978-1-4939-1628-3
Springer New York Heidelberg Dordrecht London

Library of Congress Control Number: 2014949916

Printed on acid-free paper

Springer is part of Springer Science+Business Media (www.springer.com)

Preface

The increase in the demand for energy by a growing world is stretching already maximized conventional resources to dangerously thin levels. Addressing this issue along with the need of a clean and sustainable approach to meet climatic challenges can be safely considered as the primary challenges for present and upcoming generations. Tapping the solar power—a well-established and historically proven approach—is still quite relevant as a solution to the aforementioned problems. This is because the global consumption (on the TW scale) can be met easily if one can tap into the sun's energy falling on the earth's surface over a small fraction of time alone. The challenge however lies in the limitations in harvesting this energy. While photovoltaics is a common, well-accepted, and commercially viable approach to solar energy utilization, the option of using solar power to produce hydrocarbon or hydrogen fuels is also equally fascinating. Admittedly, the technology is still in its infancy and will require an incubation period of a few decades to attain maturity. There are several approaches that can be pursued to make solar fuel generation a reality.

Utilization of solar energy and its conversion to value-added products such as electricity and fuels require seamless integration along several fronts. Material development, modeling-driven experiments, smart systems that integrate environmental remediation with simultaneous clean energy conversion, and strategies to mitigate greenhouse gas effects CO_2 fixation will all be critical to harnessing solar energy. The editors would like to point out that each of these areas is an independent topic that can be written about in considerable detail. This book strives to increase awareness about the breadth of solar energy application and the importance of solar fuels as an emerging area. The current level of knowledge and adaptation are at an elementary stage due to various factors including the critical mass of research activity in this important area. While many of the efforts in this direction may be frustrating, they must be pursued with vigor and innovation so that in the near future society can enjoy pollution-free energy conversion technologies. The chapters in this volume advance towards this goal.

The contributors to this book are experts in areas ranging from basic science and theory to application. This makes the set of papers compiled in the book an interesting and complementary read in the area of solar fuels. The editors are pleased to offer this compilation from an international group of authors with several decades of cumulative experience in areas allied to solar energy. The editors would like to thank the contributors for their thoughtful manuscripts and the publishers for proposing a book in such an emerging and important topic of energy research. We sincerely hope that this compilation gives perspective on the varied approaches to solar energy utilization with emphasis on solar fuels.

Chennai, India — B. Viswanathan
Reno, United States of America — V. Subramanian
Pohang, Republic of Korea — J. S. Lee

Acknowledgment

This book has contributions in the area of photovoltaics, solar hydrogen, and modeling of materials for solar fuels. The presenting authors are from Asia, Europe, and the United States, and have made significant contributions in the area of solar fuels.

Contents

Strategic Design of Heterojunction CdS Photocatalysts for Solar Hydrogen 1
Jum Suk Jang and Hyunwoong Park

Encapsulation for Improving the Efficiencies of Solar Cells 23
Sindhu Seethamraju, Praveen C Ramamurthy, and Giridhar Madras

Solar Photocatalytic Hydrogen Production: Current Status and Future Challenges 41
Jenny Schneider, Tarek A. Kandiel, and Detlef W. Bahnemann

Electrochemical and Optical Characterization of Materials Band Structure 75
Suman Parajuli and Mario A. Alpuche-Aviles

New Cu(I)-Based *p*-Type Semiconducting Metal Oxides for Solar-to-Fuel Conversion: Investigation and Challenges 97
Upendra A. Joshi

Theoretical Modeling of Oxide-Photocatalysts for PEC Water Splitting 113
Muhammad N. Huda

Photo-Fuel-Cells: An Alternative Route for Solar Energy Conversion . . . 135
Maria Antoniadou and Panagiotis Lianos

Simultaneous Photodegradation and Hydrogen Production with TiO_2/Pt/CdS Using UV–Visible Light in the Presence of a Sacrificial Agent and a Pollutant 153
Aaron Peterson, Winn Wilson, Bratindranath Mukherjee and Vaidyanathan (Ravi) Subramanian

Stability of the Nanoporous Bismuth Oxide Photoanodes for Solar Water Splitting 173
Kalyan Chitrada and K.S. Raja

Passivating the Surface of TiO_2 Photoelectrodes with Nb_2O_5 and Al_2O_3 for High-Efficiency Dye-Sensitized Solar Cells 201
Zhaoyue Liu and Lin Li

Reduction of Carbon Dioxide: Photo-Catalytic Route to Solar Fuels . . . 211
B. Viswanathan

Index 235

About the Editors

Jae Sung Lee is a professor of Energy and Chemical Engineering at Ulsan National Institute of Science and Technology (UNIST) in Ulsan, Korea. Combined with his former tenure at Pohang University of Science and Technology (POSTECH), he has 30 years of experience in teaching and research in catalysis and energy technologies. He obtained his Ph.D. in Chemical Engineering from Stanford University, M.Sc. from KAIST, and B.S. from Seoul National University. He worked for Catalytica as a research fellow (1984–1986), and was a visiting professor to Yale University (1993–1994). His current research projects include photocatalytic water splitting for solar fuels, electrocatalysis for low temperature fuel cells, and catalysis for energy and environment. He has published more than 300 scientific papers and 90 patents in the field, and his work has been cited ~12,000 times (h-Index ~56) as of May 2014. He is a full member of Korean Academy of Engineers, and a recipient of Green Energy Awards and Yeosan Catalytic Science Awards. He is on editorial boards of *Journal of Catalysis*, *Journal of Applied Catalysis A*, *Journal of Molecular Catalysis A*, and *Catalysis Letters*.

Vaidyanathan Subramanian is Associate Professor of Chemical Engineering and an Adjunct Professor of Chemistry at the University of Nevada, Reno. He is also the Solar Energy thrust area coordinator in the Renewable Energy Center at the University. Prof. Subramanian's research focus is on nanostructured materials for solar energy utilization and fuel cells. His primary interest is in the development of materials for photovoltaics, fuel cells, clean fuel production, and environmental remediation. In his 14 years of research he has developed inorganic materials including semiconductor–semiconductor and semiconductor–metal nanocomposites for applications related to solar energy utilization and fuel cells. He has received several awards as a student (AIChE Poster Award, Catalysis Club Award, and Best Thesis Award) and as a faculty member (Japanese Society for Promotion of Science Fellowship—JSPS). Prof. Subramanian has received research grants and contracts from federal agencies such as the National Science Foundation, the Department of Defense (DARPA), the Department of Energy, as well as from industrial partners.

Balasubramanian Viswanathan is a faculty member in the Department of Chemistry, Indian Institute of Technology, Chennai (Madras) and since 2006 he has headed the National Centre for Catalysis Research in the same institute. He is a renowned scientist and a distinguished teacher. His research contributions are extensive in the fields of Heterogeneous Catalysis, Materials Science, Theoretical Chemistry, and Energy. He has published over 500 peer-reviewed journal articles and authored more than 25 books and some of these publications including titles like Chemical and Electrochemical Energy Systems and Fuel Cells have won several awards and a number of fellowships at both national and international levels.

Strategic Design of Heterojunction CdS Photocatalysts for Solar Hydrogen

Jum Suk Jang and Hyunwoong Park

1 Solar Hydrogen

In 2004, more than 57 million metric ton of H_2 was produced, and the production rate has been increasing by approximately 10 % per year [1–4]. Currently, a significant portion of H_2 produced comes from natural gas through steam methane reformation. A quick estimation indicates that this process stoichiometrically produces ca. 5.5 kg CO_2 per kg H_2 [5–7]. This implies that we are consuming "dirty" hydrogen even if we use this hydrogen to drive fuel-cell vehicles with zero emission. Although there are several other potential renewable energy sources such as biomass (5–7 TW), underground heat (~10 TW), ocean/tide/current (2 TW), and wind (2–4 TW), yet sunlight (which is the most abundant energy source on earth, with 36,000 TW on land) overwhelms the sum of energies provided by all these renewable sources [8]. That is why solar hydrogen research is being performed worldwide, although the efficiency of the state-of-the-art technology is still low [1–3, 5–7, 9–39]. If a 10 %-efficiency solar hydrogen plant is built on 25 km^2 land, approximately 570 t of H_2 could be produced every day [40]. If 10,000 solar plants are built, 2.1 billion ton of H_2 can be harvested per year. This amount corresponds to one-third of the global energy projected to be required in 2050 (~30 TW). However, for sustainable hydrogen production, approximately ten times more water (5,100 t/day) is required and the solar plant (or hydrogen-evolving materials) should continuously operate with 10 % efficiency.

J.S. Jang
Division of Biotechnology and Advanced Institute of Environmental and Bioscience, College of Environmental and Bioresource Sciences, Chonbuk National University, Iksan 570-752, South Korea

H. Park (✉)
School of Energy Engineering, Kyungpook National University, Daegu 702-701, South Korea
e-mail: hwp@knu.ac.kr

B. Viswanathan et al. (eds.), *Materials and Processes for Solar Fuel Production*, Nanostructure Science and Technology 174, DOI 10.1007/978-1-4939-1628-3_1

2 Photocatalytic Hydrogen Production

2.1 Operation Mechanism

Photocatalytic processes are initiated by the absorption of photons by semiconductors that create photoelectrons in the conduction band (CB) and holes in the valence band (VB) (Fig. 1) [37, 41]. The electrons and holes reduce and oxidize water, respectively, producing a 2:1 mixture of H_2 and O_2, according to the following reactions [40, 42]:

$$\text{Water oxidation}: \quad H_2O + 2h^+ \rightarrow 2H^+ + 1/2O_2 \tag{1}$$

$$\text{Water reduction}: \quad 2H^+ + 2e^- \rightarrow H_2 \tag{2}$$

$$\text{Overall reaction}: \quad H_2O \rightarrow H_2 + 1/2O_2 \tag{3}$$

The overall reaction is a four-electron-transfer reaction (per O_2 molecule) and is usually promoted by metals or metal oxides (called auxiliary catalysts or cocatalysts) deposited on the semiconductor surfaces [36, 43]. These cocatalysts are known to collect charge carriers and provide catalytic reaction sites for water splitting [37]. Because the reaction involves the standard Gibbs free energy change (ΔG°) of 237 kJ/mol (equivalent to 1.23 eV), semiconductors should possess a bandgap (E_g) energy value greater than 1.23 eV to drive the water splitting reaction. In addition, the E_g value should be less than ca. 3.0 eV ($E_g = hc/\lambda = 1{,}240/\lambda$) to absorb visible light. The band position of the photocatalyst is also important. For a facile charge transfer, the CB should be located at a more negative potential than the reduction potential of water, while the VB should be located at a more positive position than the oxidation potential of water [9, 14]. Other factors such as charge separation, mobility, and lifetime of the photogenerated electrons and holes also affect the photocatalytic properties. These properties are strongly influenced by the bulk and surface properties of the material (e.g., crystallinity and surface area,

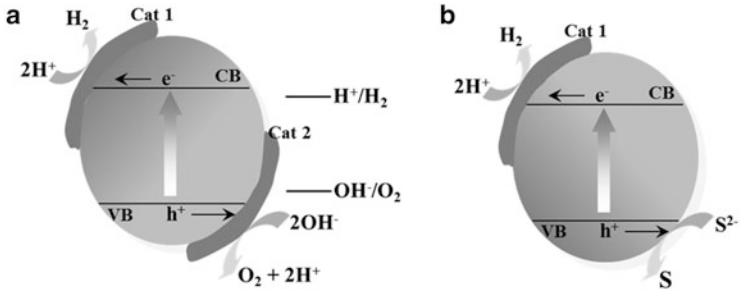

Fig. 1 Schematic illustration for the principles of photocatalytic (**a**) water splitting and (**b**) hydrogen sulfide decomposition. The *bottom* of the conduction band should be more negative than the reduction potentials of water and the sulfides, whereas the *top* of the valence band should be more positive than the water oxidation potential [43]

respectively) [26]. Cocatalysts such as Pt [44–47], Rh [48, 49], NiO [50], RuO_2 [51–53], IrO_2 [54], and Rh/Cr_2O_3 [42] are often loaded on the surface for introducing active sites for H_2 evolution. Therefore, suitable bulk/surface properties and structures are necessary for effective photocatalysis.

2.2 H_2 Production from Hydrogen Sulfides

Hydrogen sulfide (H_2S) has been considered as an alternative source for solar hydrogen production because of the following reasons: (1) H_2S is an intermediate in several thermochemical cycles from which hydrogen must be recovered; (2) Sour gas and steam from geothermal sources often contain a high percentage of H_2S; (3) H_2S is formed as a by-product from hydrogen reduction and acid leaching of sulfide ores, as well as from the hydrodesulfurization of petroleum; (4) H_2S must be converted into an environmentally harmless form. Currently, over ten million ton of H_2S is produced yearly, and the production is expected to increase in the near future. Practically, the photocatalytic splitting of H_2S is a more favorable reaction compared to water splitting [55]. The cleavage of H_2S by two photons requires 39.4 kcal/mol (reactions 4–6), which is only 4 % of the energy required for water splitting (237 kJ/mol).

$$H_2S \rightarrow HS^-_{(aq)} + H^+_{(aq)} \tag{4}$$

$$2\,h^+ + 2HS^- \rightarrow S_2^{2-} + 2H^+ \tag{5}$$

$$2e^- + 2H^+ \rightarrow H_2 \tag{6}$$

In alkaline solutions, the decomposition pathway of H_2S changes (reactions 7–10).

$$H_2S + OH^- \rightarrow HS^- + H_2O \tag{7}$$

$$HS^- + OH^- \rightarrow S + H_2O + 2e^- \tag{8}$$

$$S + HS^- + H_2O \rightarrow {S_2}^{2-} + H_2O \tag{9}$$

$$2H_2O + 2e^- \rightarrow H_2 + 2OH^- \tag{10}$$

If molecular hydrogen could be recovered from H_2S instead of simply burning it to H_2O (Claus process), approximately 7.7×10^9 m^3 y^{-1} of H_2 could be produced.

2.3 CdS Semiconductors

A variety of semiconductors are available, but most are unsuitable for hydrogen evolution under visible light because of the wide E_gs (>3 eV) and the unsuitable CB levels located negative of the hydrogen evolution potential (0 V_{NHE}) [1, 3, 4, 41].

Although oxide semiconductors such as TiO_2 ($E_g = 3 \sim 3.2$ eV), ZnO ($E_g = 3.2$ eV), and SnO_2 ($E_g = 3.8$ eV) are quite stable in water, they cannot be used because of the wide E_gs. WO_3 ($E_g = 2.6$ eV), $BiVO_4$ ($E_g = 2.5$ eV), and α-Fe_2O_3 ($E_g = 2.2$ eV) operate under visible light but are unable to produce H_2 because of the unsuitable CB levels.

CdS may be one of the most appropriate semiconductors because of its narrow E_g (~2.5 eV, corresponding to $\lambda <$ ca. 500 nm) and suitable CB (-0.75 V_{NHE}) and VB (+1.75 V_{NHE}) levels. Although photocorrosion limits its widespread applicability, CdS is useful as a model semiconductor for solar hydrogen production particularly from H_2S [56–62]. To improve the photocatalytic activity of CdS, charge separation and charge injection should be simultaneously considered. The simplest and most effective method to enhance charge separation is to couple with noncorrosive, wide bandgap oxide semiconductors. For cascaded transfers of photogenerated charge carriers from CdS, the semiconductors of interest must have proper band positions. A variety of semiconductors can be employed for coupling, including oxides [63–71] (e.g., TiO_2 [57, 72–80], ZnO [81–83], and WO_3 [84]) and chalcogenides (e.g., CdSe [85] and ZnS [86]).

Among all the possible combinations, CdS/TiO_2 should be the most representative because the VB and CB of CdS are ideally placed with respect to those of TiO_2 for charge separation and CdS can absorb a substantial portion of visible light ($\lambda \leq 500$ nm). TiO_2 plays a dual role in the hybrid [61, 62]: It supports CdS and prevents the aggregation of CdS particles, and enhances the charge separation by forming a potential gradient at the interface of CdS and TiO_2. Owing to the latter effect, the photogenerated CdS CB electrons are rapidly transported to the CB of TiO_2, while the TiO_2 VB hole has a counterflow toward the VB of CdS. Under optimal conditions, the coupling reduces the average emission life time of CdS by a factor of 4 because of the trapping of the CB electron by TiO_2 [76]. CdS/TiO_2 has also been applied to the environmental remediation of methane [87], methyl orange [88], indole [89], acid orange II [90], and 1,2,3,4-tetrachlorobenzene [91], among others. As the TiO_2 particle size decreases to a level of quantum size and its bandgap widens, the TiO_2 CB edge moves upward and becomes more negative than the CdS CB edge. This hinders the electron transport from CdS to TiO_2 [92, 93].

Improving the charge-injection efficiency also remains a challenge. The most widely employed method is to load metal particles at the CdS surface and create a Schottky barrier [94–97]. Upon irradiation, Fermi level equilibration takes place between CdS and the loaded metals through charge transfer and distribution [95, 97]. The charges trapped at the metal particles then effectively catalyze various redox reactions of interest. The direct charge transfer from CdS to water requires high overpotentials, but such overpotentials are significantly reduced at the metal/solution interface. Therefore, the metals are also called auxiliary catalysts or cocatalysts. Transition metals and their oxides, including Pt, Rh, NiO, RuO_2, IrO_2, and Rh/Cr_2O_3, have been employed as cocatalysts. Pt-group metals are popular and effective, but are very expensive and in limited supply; therefore, demand for earth-abundant and cost-effective alternatives is increasing.

3 Heterojunction CdS/TiO_2 Photocatalysts

This section briefly reviews the effects of hybrid configurations and cocatalysts in terms of photocatalytic hydrogen production, particularly based on our recent results. First of all, the morphology effects will be discussed in detail. Then, the effects of hydrogen-evolving catalysts (e.g., non-Pt and Pt-group metals) on charge injection will also be described. Pt nanoparticles are often deposited on CdS or CdS/TiO_2. However, the Pt effects are very diverse and often contradictory. The inconsistency is most likely related to the chemical interaction at the CdS/Pt interface. Instead of expensive Pt-group metals, tungsten carbide (WC) and inexpensive carbon-based materials can be used. These cocatalysts are very attractive because of their unique physicochemical properties such as thermal conductivity, electrical resistivity, and *sp* valence hybrid configuration [60, 85, 98, 99].

3.1 Nano-TiO_2/Bulk-CdS Versus Nano-CdS/Bulk-TiO_2

Jang et al. have developed a heterojunction of highly crystalline, bulky CdS (bulk-CdS) and TiO_2 nanoparticles (nano-TiO_2) to maximize the interfacial contact and surface area (Fig. 2) [70]. CdS was prepared via a typical precipitation method and calcined at 1,073 K under a flow of helium. As-prepared CdS was stirred in 2-propanol and tetra-titanium iso-propoxide (TTIP) at a molar ratio of Cd: Ti = 1:4. Through this simple precipitation and sol–gel process, a well-developed hexagonal-phase CdS and anatase TiO_2 heterojunction was successfully obtained. Transmission electron microscopic (TEM) analysis showed that CdS particles of ca. 1–2 μm were decorated with TiO_2 nanoparticles of ca. 10–20 nm (Figs. 2b and 3a).

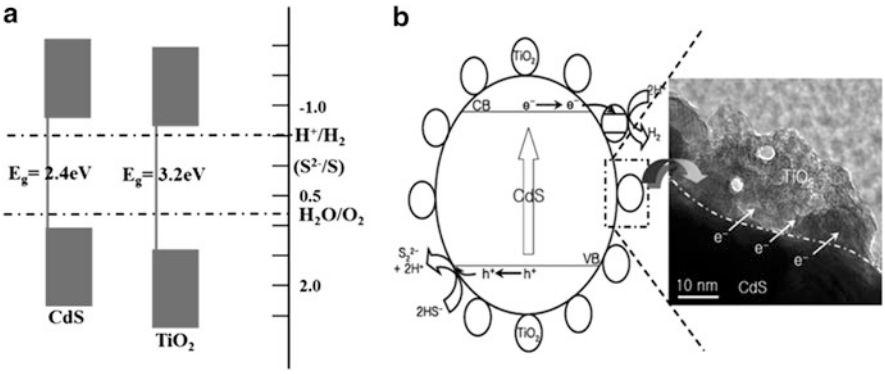

Fig. 2 (**a**) Bandgap positions of CdS and TiO_2 photocatalysts. (**b**) A new configuration consisting of highly crystalline bulky CdS decorated with nanosized TiO_2 particles. The possible role of TiO_2 nanoparticles is to provide sites for collecting the photoelectrons generated from CdS, enabling an efficient electron–hole separation as depicted [70]

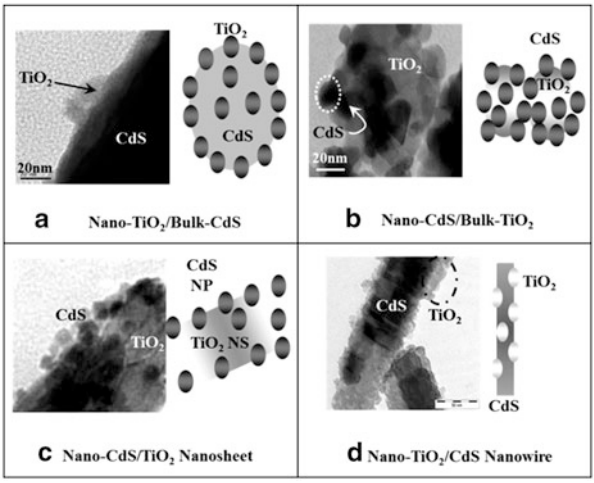

Fig. 3 TEM images and schematic models of CdS/TiO_2 heterojunction photocatalysts with different configurations: (**a**) nano-TiO_2/bulk-CdS, (**b**) nano-CdS/bulk-TiO_2, (**c**) nano-CdS/TiO_2-nanosheets, and (**d**) nano-TiO_2/CdS-nanowires

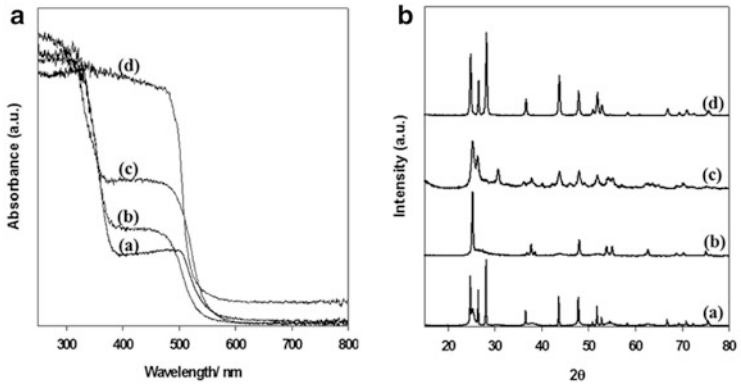

Fig. 4 (**a**) Diffuse reflection spectra and (**b**) X-ray diffraction patterns (XRD) of (**a**) nano-TiO_2/bulk-CdS, (**b**) nano-CdS/bulk-TiO_2, (**c**) nano-CdS/TiO_2-nanosheets, and (**d**) nano-TiO_2/CdS-nanowires

According to the diffuse reflectance spectra, bulk-CdS showed a sharp edge at 570 nm, while that of nano-TiO_2 was observed at 390 nm [70]. The spectra of CdS and TiO_2 in heterojunction appeared as one spectrum, although CdS in heterojunction showed a blue-shift of the main absorbance edge to 550 nm (Fig. 4a). The shift in the bandgap of CdS in heterojunction by an electronic semiconductor–support interaction was also reported by Kisch et al. [100, 101].

This nano-TiO_2/bulk-CdS heterojunction showed an unexpectedly high rate of hydrogen production from aqueous sulfide and sulfite under visible light ($\lambda > 420$ nm) (Fig. 5). The high hydrogen production could be exploited for the practical process of simultaneous hydrogen production and H_2S removal (e.g., the

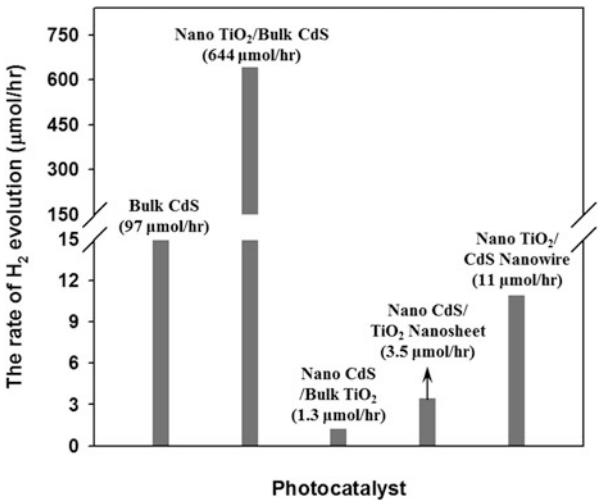

Fig. 5 Rate of hydrogen production of nano-TiO_2/bulk-CdS, nano-CdS/bulk-TiO_2, nano-CdS/TiO_2-nanosheets, and nano-TiO_2/CdS-nanowires. Catalyst: CdS/TiO_2 heterojunction (0.1 g; loaded with 1 wt% Pt), light source: Hg-arc lamp (500 W) equipped with UV cut-off filter ($\lambda > 420$ nm)

treatment of Claus plant tail-gas stream or vents of hydrodesulfurization plants) [102–105]. In the H_2S scrubbers used in such industries, alkaline water is commonly employed for effective H_2S scrubbing by an acid–base reaction. Soluble alkali metal sulfides are common sacrificial reagents for hydrogen production with metal sulfide photocatalysts and are also employed to improve the activity and stability of the sulfide photocatalysts.

A heterojunction of nanosized CdS and bulky TiO_2 (nano-CdS/bulk-TiO_2) also was synthesized by a precipitation and sol–gel process and was grown by the hydrothermal treatment (Fig. 3b) [67]. This model has an advantage in that CdS nanoparticles absorb visible light and can be dispersed well on the surface of bulky TiO_2 particles. This heterojunction exhibited optical properties similar to nano-TiO_2/bulk-CdS and displayed the pure cubic phases of CdS and well-developed TiO_2 anatase phases (Fig. 4a, b). However, the photocatalytic activity for H_2 evolution was only 0.3 % compared to that of nano-TiO_2/bulk-CdS (Fig. 5). This indicated that, despite the similar composition, the fabrication method of the composite showed a considerable effect [67].

3.2 Nano-CdS/TiO_2-Nanosheets

CdS nanoparticles and TiO_2 nanosheets (NS) were coupled via a simple one-step procedure [106]. In this configuration, TiO_2 worked as an effective medium for the separation and transport of photogenerated electrons and holes generated on CdS (Fig. 3c). TiO_2 synthesized by the hydrothermal treatment was composed of anatase-phase nanorods (NR) with a diameter of ca. 30–40 nm and a length of 80–100 nm (surface area: 63 $m^2\ g^{-1}$), while CdS had a cubic structure of ca. 20 nm

(surface area: 61 m^2 g^{-1}). However, upon coupling with CdS, the morphology of TiO_2 was changed to nanosheets with a width of 70–80 nm, a thickness of 10–20 nm, and a length of 200 nm. The surface area of the heterojunction was approximately 100 m^2 g^{-1}. This heterojunction exhibited an optical response similar to TiO_2 NR and CdS in the ranges $\lambda < 360$ and $\lambda > 500$ nm, respectively (Fig. 4). This suggested that the optical properties of the heterojunction are a combination of the individual properties of CdS and TiO_2. The rate of H_2 evolution was approximately 3.5 μmol h^{-1} in visible light-irradiated nano-CdS/TiO_2-NS suspensions. This value was ca. 2.7-fold higher than that in nano-CdS/bulk-TiO_2, indicating the superiority of TiO_2 NS.

3.3 Nano-TiO_2/CdS-Nanowires

Finally, TiO_2 nanoparticles were coupled to CdS nanowires (NW), and the surface properties and photocatalytic activities of the heterojunction of nano-TiO_2/CdS-NW was examined (Fig. 3d) [57]. Quasi-one-dimensional CdS NW were synthesized via a solvothermal route in ethylenediamine, a structure-forming agent, at 160 °C for 48 h. When the molar ratio of TiO_2 NP to CdS NW was increased, the (101) plane of the anatase TiO_2 in the XRD pattern became clearer (Fig. 4). The CdS NW showed a well-developed hexagonal phase in the single form and in the heterojunction, and its crystallinity was similar to that of the single CdS NW. The length and diameter were approximately 3 μm and 50 nm, respectively. The surface area of the heterojunction increased linearly with increasing amounts of TiO_2. However, the optimal molar ratio of Ti and Cd in terms of H_2 evolution was 0.25. Notably, the molar ratio of TiO_2 NP to CdS NW had no correlation with the surface area of the composite in terms of H_2 evolution [57]. This suggests that an optimum coverage of TiO_2 NP decorating CdS NW is needed for effective and fast charge separation. However, excess coverage can hinder the contact of the solution and the CdS surface responsible for hole scavenging.

A comparison of the four heterojunctions reveals that key factors for superior H_2 evolution include rapid charge separation and transfer and optimized heterojunctions (Fig. 2). Simultaneously, it is important to synthesize and effectively couple highly crystalline, hexagonal-phase CdS to TiO_2 because heterojunctions with less-crystallized CdS (nano-CdS/bulk-TiO_2, nano-CdS/TiO_2-NS, and nano-TiO_2/CdS-NW) are far less active (Fig. 5). Although nano-TiO_2/CdS-NW did not exhibit enhanced photocatalytic activities, this configuration was slightly more active than the CdS NW. To further improve the activity, high quality individual components (e.g., crystallinity and surface property) and elaborate contact between the two compounds are necessary.

4 Effects of Cocatalysts on Heterojunction Photocatalysis

As discussed previously, the photocatalytic efficiency of CdS is substantially influenced by coupled materials [67, 106–108], as well as by various factors such as the degree of crystallinity [109], surface area [108], surface etching [105, 110, 111], pH and related properties (e.g., flat band potential and surface charge) [112–116], electron donors, solvent (e.g., alcohols, sulfide, and sulfite) [59, 105, 108, 115, 117], and cocatalysts (e.g., Pt and Ni) [59, 108, 110, 111, 114, 117–122]. Specifically, the coupling of cocatalysts to semiconductors is required to reduce the overvoltage for hydrogen and oxygen evolution. The cocatalyst also suppresses the recombination of photogenerated charges by the efficient removal of photoelectrons from the charge-generation sites and also provides catalytic sites for the reduction of H^+. Charge recombination is the main cause of efficiency loss because some of the absorbed photoenergy is wasted as fluorescence or heat. Transition metals and their oxides such as Pt, Rh, NiO, RuO_2, IrO_2, and Rh/Cr_2O_3 have been often employed as cocatalysts.

4.1 Pt Nanoparticles

Metallic Pt(0) particles are among the most effective cocatalysts. There are several ways to load Pt on CdS, including physical mixing with Pt particles (Pt black or Pt sol) and photodeposition. These methods are facile, simple, and highly reproducible. Nevertheless, the effects of Pt on photocatalysis are very diverse and often contradictory. For example, platinized CdS (Pt-CdS) obtained by photodeposition showed an enhanced hydrogen production rate of 300 mL h^{-1} at 1.5 wt% Pt-loading [108]. Interestingly, another group reported that the enhancement of hydrogen production by platinization was almost negligible [121]. Photoplatinization presumably facilitates better contact at the Pt/CdS interface than physical mixing; however, the former is reportedly much less effective than the latter, particularly in the decomposition of organic acids [123]. Such a result may be obtained because of the complicated surface chemistry of CdS that typically interferes with the photochemical reduction of Pt ions (Pt^{4+}). According to Li et al. [114], the photochemical process with aqueous Pt ions is rather complex (reactions 11–14):

$$CdS + H_2O \rightarrow Cd(OH)^+ + SH^- \tag{11}$$

$$PtCl_6^{2-}(ad) + 2e^- \rightarrow PtCl_4^{2-}(ad) + 2Cl^- \tag{12}$$

$$PtCl_4^{2-}(ad) + SH^- \rightarrow PtS(s) + H^+ + 4Cl^- \tag{13}$$

$$PtCl_4^{2-}(ad) + 2OH^-(ad) \rightarrow Pt(OH)_2(s) + 4Cl^- \tag{14}$$

They argued that PtS is deposited on the CdS surface under acidic conditions (reaction 13) and $Pt(OH)_2$ is deposited under basic conditions (reaction 14).

The formation of these Pt species is not desired because of their low catalytic abilities than Pt. Conversion of PtS or $Pt(OH)_2$ to metallic Pt (Pt^0) requires subsequent heat treatment (>400 °C).

An alternative but indirect method for the electrical connection of CdS to Pt particles is to couple CdS to pre-platinized metal oxides such as Pt–TiO_2. Notably, the coupling of Pt to TiO_2 (instead of CdS) is effective and reproducible and is not susceptible to the deactivation or detachment of Pt [124]. In this ternary configuration of CdS/Pt–TiO_2, the role of TiO_2 is important. It supports CdS, prevents the aggregation of CdS, and enhances charge separation. Because of the robust contact, the rate of photoinduced electron transfer at CdS increases tenfold in the presence of TiO_2 [92, 125, 126]. However, the coupling of Pt to pre-coupled CdS/TiO_2 was not efficient [108]. Alternatively, CdS can be physically mixed with platinized TiO_2 (CdS + Pt–TiO_2); however, the resulting activity varies. The hydrogen production rate was enhanced as compared to plain CdS [120], though occasionally the efficiency was lowered by eight times [121]. Recently, some groups reported comparative studies on the hybridization of CdS, TiO_2, and Pt in terms of hydrogen production under visible light ($\lambda > 420$ nm) [61, 127]. According to their results, changing the order of hybridization in the preparation step significantly altered the hydrogen production efficiency. For example, CdS/Pt–TiO_2 produced hydrogen at the millimolar level ((6–9) $\times 10^3$ mol h^{-1} g^{-1}) and was far more efficient than any other CdS/TiO_2 hybrid photocatalysts reported. The detailed mechanism is illustrated in Fig. 6.

In the ternary hybrids, the preparation of CdS is also highly critical. For fabricating CdS/Pt–TiO_2, an aqueous sulfide (S^{2-}) solution was usually dropped onto an aqueous suspension of Pt–TiO_2 with cadmium ions (Cd^{2+}) at a 1:1 ratio of Cd and S. When the cadmium solution was dropped onto the Pt–TiO_2 suspension with sulfide ions, the photocatalytic H_2 evolution was enhanced by a factor of 4–10 [62]. Such phenomena were also found with other cocatalysts (Pt, Pd, Au, RuO_x) [62]. According to an energy-dispersive X-ray spectroscopic analysis, the chemical precipitation of the former provided a cadmium-rich CdS (Cd_RS with S/Cd values of 0.98 at free CdS and 0.52 at ternary), whereas the latter provided a sulfur-rich CdS (CdS_R with S/Cd values of 1.05 at free CdS and 1.31 at ternary). The high activity of CdS_R was, however, very sensitive to the photocatalytic running conditions, namely the type and concentration of electron donor (Na_2S and/or Na_2SO_3), which largely altered the hydrogen production ratio of CdS_R to Cd_RS. Detailed surface analyses indicated that the physicochemical properties of CdS_R are very different from those of Cd_RS, including a larger and red-shifted onset light absorption and altered photoluminescence, and hexagonal crystallinity (versus cubic-Cd_RS) (Fig. 6e, f).

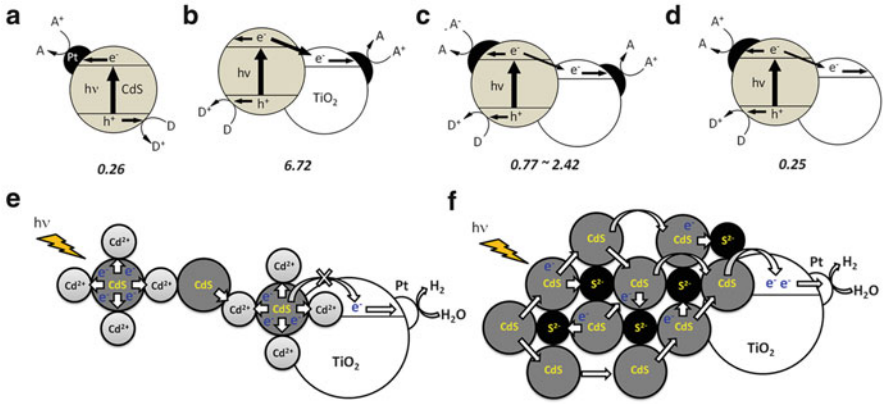

Fig. 6 Schematic illustration of photogenerated electron transfers in CdS and TiO_2 hybrids under visible light. (**a**) Pt/CdS, (**b**) CdS/(Pt–TiO_2), (**c**) Pt/(CdS/TiO_2), (**d**) sgTiO_2/(Pt/CdS), (**e**) Cd_RS/(Pt–TiO_2), and (**f**) CdS_R/(Pt–TiO_2). sg and R refer to sol–gel and rich, respectively. Numbers indicate the amount of H_2 ($\times 10^{-3}$ mol h^{-1} g^{-1}). Modified from the original figures [61, 62]

4.2 Tungsten Carbide (WC)

Transition-metal carbides, including WC, have received attention as novel catalytic materials because of their unique physicochemical properties [128–131]. Nevertheless, their application as cocatalysts in photocatalysis has received less attention [132–137]. For example, Oosawa compared the photocatalytic hydrogen production in UV-irradiated suspensions of TiO_2 powders loaded with metal borides, nitrides, phosphides, and carbides [138]. Among them, WC showed the highest activity. However, its activity was only 20 % of that of Pt. The low activity was attributed to the difficulty in coupling large WC particles onto small TiO_2 particles. Until then, the capability of WC as a cocatalyst was not fully manifested because of the inadequate properties of the WC samples derived from high-temperature ceramic processes (e.g., particle size, surface property, and surface contact between cocatalyst and photocatalyst).

Recently, Jang et al. fabricated a WC/CdS heterojunction by precipitation, followed by a hydrothermal treatment that allowed an intimate contact between the two phases (Fig. 7a) [139]. The bare CdS was prepared by precipitation, followed by hydrothermal treatment (150 °C for 24 h). The bare CdS exhibited a well-developed hexagonal phase with high crystallinity, whereas the crystallinity of the composite CdS was lower. This indicated that WC could inhibit the growth of CdS particles. XRD analysis revealed that WC had a simple hexagonal phase with lattice parameters $a = 2.906$ Å and $c = 2.83$ Å (JCPDS card no. 12070-12-1), a crystal size of ca. 5 nm, and a BET surface area of 76 m^2 g^{-1} [139]. The morphology of WC comprised irregular spherical particles (ca. 50 nm), whereas CdS particles were agglomerates of nanosized particles (ca. 30–40 nm) with no

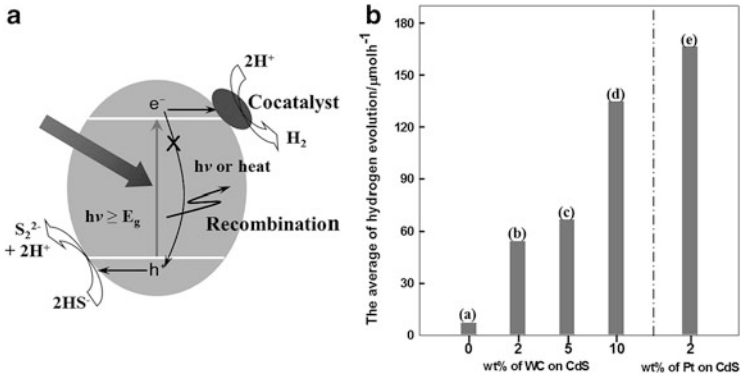

Fig. 7 (**a**) New configuration of CdS and WC nanoparticles. An important role of WC is to provide active sites for collecting the photoelectrons generated from CdS, enabling an efficient electron–hole separation as depicted. (**b**) The average rate of H_2 evolution over the CdS photocatalysts combined with different amounts of WC. Catalyst: CdS photocatalyst (0.1 g of loaded cocatalysts), light source: Hg-arc lamp (500 W) equipped with UV cut-off filter ($\lambda > 420$ nm) [139]

distinctive morphological features. These CdS and WC particles were not discernible in the composite.

Under visible light, CdS with 2 wt%-WC exhibited an approximately 7.5-fold larger amount of hydrogen production than bare CdS (Fig. 7b). The photocatalytic activity of CdS loaded with 10 wt% WC increased by a factor of 23. As the amount of WC on CdS increased, the photocatalytic activity also increased. This result indicated that WC acted as a cocatalyst with a similar efficiency as that of Pt in hydrogen production. In the time-profiled hydrogen production, CdS coupled with 10 wt% WC showed a stable rate of hydrogen production without any sign of deactivation. Comparison of the 2 wt% Pt-loaded CdS sample prepared by the photochemical method and CdS loaded with 10 wt% WC indicated that the former showed only a marginally higher rate of hydrogen production compared to the latter. Considering the low cost and availability of WC, its comparable catalytic activity to Pt is remarkable and suggests a strong potential as a cocatalyst in photocatalytic hydrogen production under visible light.

4.3 Carbon-Based Materials

Recently, carbon-based materials have been extensively studied as catalysts in photocatalysis [60, 85, 98, 99, 140–144]. These materials exhibit very attractive physicochemical properties, including thermal conductivity, electrical resistivity, BET surface area, and *sp* valence hybrid configurations [145]. Traditionally, activated carbon has been coupled to photocatalysts for increasing the surface area of the host photocatalyst (Fig. 8) [146]. However, as carbon synthesis and chemistry

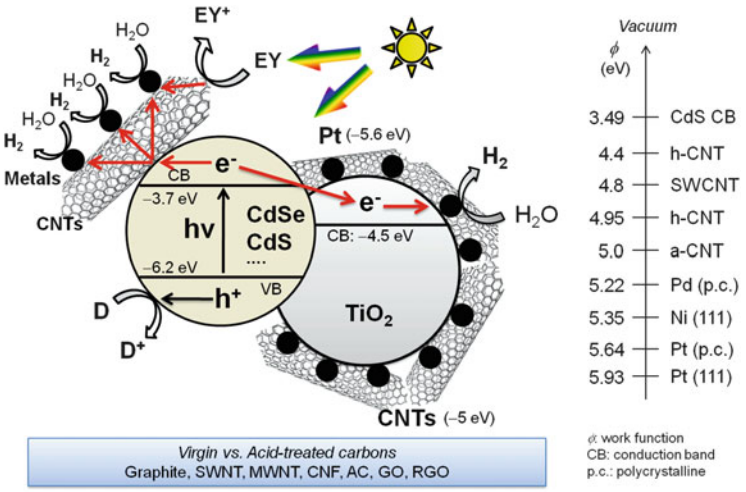

Fig. 8 Carbon-catalyzed solar hydrogen production. For example, visible light-absorbing materials (CdS, CdSe, or Eosin Y) can be coupled with metal (Pt, Pd, Ni)-decorated CNTs and/or TiO_2 with various virgin and surface-treated carbon materials

advances, a variety of carbon-based materials, including graphite (GP) [147–149], carbon fibers (CF) [150, 151], single- and multiwalled carbon nanotubes (CNTs; SWNT [143, 152–154] and MWNT [60, 85, 98, 99, 144], respectively), graphene oxides (GO) [155, 156], graphene (GR) [157–161], and g-C_3N_4 [162], are being actively tested as catalysts.

Among them, CNTs are of high interest because of their unique configuration, thermal stability, and high electric conductivity. In the presence of sulfide and sulfite mixtures, CNTs/CdS, obtained via hydrolysis, exhibited a H_2-production rate that is more than 40 times greater than the rate obtained using bare CdS under visible light [60]. Interestingly, the enhanced activity was greatly influenced by the surface treatment of the CNTs (heat vs. acid treatment). Although both the treatments increased the H_2 production, the heat-treatment method was more effective primarily because of the increase in the graphitic carbon content as compared to disordered carbon (i.e., I_G/I_D), as well as the suitable work function. However, when hybridized with CdS and Pt, acid-treated CNTs exhibited the largest amount of hydrogen production (acid treated > heat treated > crude), even though all the CNTs had similar functional groups to bind metal catalyst on their surfaces [60]. The enhanced hydrogen production in the binary and ternary hybrids could be partially ascribed to the suitably positioned work functions among the hybrid components and thus the vectorial charge transfer through the work function energy gradient.

In addition to CNTs, other carbon-based materials were also shown to serve as cocatalysts. For example, acid-treated graphite and carbon fibers exhibited higher catalytic performances for H_2 evolution over carbon/CdS particles than MWNTs under visible light [85]. On the other hand, MWNTs were by far the most effective

catalyst for H_2 evolution over carbon/TiO_2 particles under UV irradiation [99]. This raises an important question: Which physiochemical properties are the primary factors in improving photocatalytic H_2 production? To address this issue, various physicochemical properties (such as morphology, surface area, degree of graphite, electrical conductivity, and sulfide/sulfite adsorption) were investigated in an attempt to correlate their effect on H_2 production. Although CdSe was used instead of CdS, the results were interesting. The plots of H_2 production with respect to physicochemical properties showed that decreases in the surface area and I_D/I_G (ratio of disordered carbon and graphitic carbon) increased the H_2 production [85]. More importantly, the amount of H_2 produced exhibited a correlation with the logarithmic electrical conductivities of the carbon-based materials. This revealed that the electrical conductivities of the carbon-based materials were paramount to the catalysis. This property of MWNTs is promising, particularly in reducing the use of Pt in photocatalytic H_2 production. Khan et al. demonstrated that although the catalytic performance of MWNTs is only one-third of that of Pt, the amount of Pt could be reduced by approximately 90 % by MWNTs-loading in visible light-irradiated CdS/TiO_2 suspensions [98]. A similar synergistic effect of MWNTs/Pt was found in eosin Y-sensitized H_2 production under visible light [144].

5 Concluding Remarks

This chapter discussed the strategic design of heterojunction CdS photocatalysts for an efficient production of solar hydrogen. There are a number of reports on the fabrication of bare and composite CdS particles and their applications to energy and environmental technologies. Although diverse and often contradictory results have been obtained, the conclusions for high-performance CdS photocatalysis can be summarized as follows. First, highly crystalline CdS should be utilized as a light absorber. Hexagonal-phase CdS is generally better than cubic-phase CdS. The former is obtained at a high temperature, and hence, its surface area is usually small compared to that of the cubic phase. Quantum-sized CdS has a considerably large surface area but a widened bandgap, thus limiting the availability of visible light. Second, the photogenerated charge carriers must be efficiently separated for a high quantum yield. The diffusion lengths, mobilities, and lifetimes of majority and minority carriers are different and the charge recombination at a single CdS particle is inevitable. Coupling with wide-bandgap semiconductors such as TiO_2 may be appropriate for inhibiting the charge recombination. In the hybrids, the match of the energy levels between two semiconductors needs to be carefully considered for cascaded charge transfers. Simultaneously, defect-free interfaces should be created because defects often work as recombination centers. Finally, hydrogen-evolving catalysts can be loaded to reduce the activation energy barrier and drive an effective charge-injection process. A variety of traditional yet highly active catalysts are available. The challenge is to find low-cost and synthetically facile alternatives.

Tungsten carbides and carbon-based materials are emerging candidates because of their abundance and stability over a wide range of pH values.

Acknowledgments This research was financially supported by the Basic Science Research Programs (Nos. 2012R1A2A2A01004517 and 2011-0021148), Framework of International Cooperation Program (No. 2013K2A1A2052901), and Korea Center for Artificial Photosynthesis (KCAP) (No. 2009-0093880) through the National Research Foundation (NRF), Korea.

References

1. C.A. Grimes, O.K. Varghese, S. Ranjan, *Light, Water, Hydrogen: The Solar Generation of Hydrogen by Water Photoelectrolysis* (Springer, New York, 2008).
2. K. Rajeshwar, R. McConnell, S. Licht, *Solar Hydrogen Generation: Toward a Renewable Energy Future* (Springer, New York, 2008).
3. L. Vayssieres, *On Solar Hydrogen & Nanotechnology* (Wiley, Singapore, 2009).
4. R. van de Krol, M. Gratzel, *Photoelectrochemical Solar Hydrogen* (Springer, New York, 2012).
5. H. Park, C.D. Vecitis, W. Choi, O. Weres, M.R. Hoffmann, Solar-powered production of molecular hydrogen from water, J. Phys. Chem. C **112**, 885-889 (2008).
6. H. Park, C.D. Vecitis, M.R. Hoffmann, Solar-powered electrochemical oxidation of organic compounds coupled with the cathodic production of molecular hydrogen, J. Phys. Chem. A **112**, 7616-7626 (2008).
7. H. Park, C.D. Vecitis, M.R. Hoffmann, Electrochemical water splitting coupled with organic compound oxidation: The role of active chlorine species, J. Phys. Chem. C **113**, 7935-7945 (2009).
8. N.S. Lewis, D.G. Nocera, Powering the planet: Chemical challenges in solar energy utilization, Proc. Natl. Acad. Sci. U.S.A. **103**, 15729-15735 (2006).
9. A. Kudo, Development of photocatalyst materials for water splitting with the aim at photon energy conversion, J. Ceram. Soc. Jpn. **109**, S81-S88 (2001).
10. V.M. Aroutiounian, V.M. Arakelyan, G.E. Shahnazaryan, Metal oxide photoelectrodes for hydrogen generation using solar radiation-driven water splitting, Sol. Energy **78**, 581-592 (2005).
11. Y.H. Yang, Q.Y. Chen, Z.L. Yin, J. Li, Progress in research of photocatalytic water splitting, Prog. Chem. **17**, 631-642 (2005).
12. M. Ni, M.K.H. Leung, D.Y.C. Leung, K. Sumathy, A review and recent developments in photocatalytic water-splitting using TiO_2 for hydrogen production, Renew. Sust. Energ. Rev. **11**, 401-425 (2007).
13. M.D. Hernandez-Alonso, F. Fresno, S. Suarez, J.M. Coronado, Development of alternative photocatalysts to TiO_2: Challenges and opportunities, Energy Environ. Sci. **2**, 1231-1257 (2009).
14. A. Kudo, Y. Miseki, Heterogeneous photocatalyst materials for water splitting, Chem. Soc. Rev. **38**, 253-278 (2009).
15. R.M.N. Yerga, M.C.A. Galvan, F. del Valle, J.A.V. de la Mano, J.L.G. Fierro, Water splitting on semiconductor catalysts under visible-light irradiation, ChemSusChem **2**, 471-485 (2009).
16. W.J. Youngblood, S.H.A. Lee, K. Maeda, T.E. Mallouk, Visible light water splitting using dye-sensitized oxide semiconductors, Accounts Chem. Res. **42**, 1966-1973 (2009).
17. J.F. Zhu, M. Zach, Nanostructured materials for photocatalytic hydrogen production, Curr. Opin. Colloid Interface Sci. **14**, 260-269 (2009).
18. R. Abe, Recent progress on photocatalytic and photoelectrochemical water splitting under visible light irradiation, J. Photochem. Photobiol. C **11**, 179-209 (2010).

19. X.B. Chen, S.H. Shen, L.J. Guo, S.S. Mao, Semiconductor-based photocatalytic hydrogen generation, Chem. Rev. **110**, 6503-6570 (2010).
20. P.F. Ji, M. Takeuchi, T.M. Cuong, J.L. Zhang, M. Matsuoka, M. Anpo, Recent advances in visible light-responsive titanium oxide-based photocatalysts, Res. Chem. Intermed. **36**, 327-347 (2010).
21. D.Y.C. Leung, X.L. Fu, C.F. Wang, M. Ni, M.K.H. Leung, X.X. Wang, X.Z. Fu, Hydrogen production over titania-based photocatalysts, ChemSusChem **3**, 681-694 (2010).
22. Y. Li, J.Z. Zhang, Hydrogen generation from photoelectrochemical water splitting based on nanomaterials, Laser Photon. Rev. **4**, 517-528 (2010).
23. R.M. Navarro, M.C. Alvarez-Galvan, J.A.V. de la Mano, S.M. Al-Zahrani, J.L.G. Fierro, A framework for visible-light water splitting, Energy Environ. Sci. **3**, 1865-1882 (2010).
24. M. Cargnello, A. Gasparotto, V. Gombac, T. Montini, D. Barreca, P. Fornasiero, Photocatalytic H_2 and added-value by-products. The role of metal oxide systems in their synthesis from oxygenates, Eur. J. Inorg. Chem. 4309-4323 (2011).
25. M.A. Henderson, A surface science perspective on TiO_2 photocatalysis, Surf. Sci. Rep. **66**, 185-297 (2011).
26. K. Maeda, Photocatalytic water splitting using semiconductor particles: History and recent developments, J. Photochem. Photobiol. C **12**, 237-268 (2011).
27. M. Pelaez, N.T. Nolan, S.C. Pillai, M.K. Seery, P. Falaras, A.G. Kontos, P.S.M. Dunlop, J.W.J. Hamilton, J.A. Byrne, K. O'Shea, M.H. Entezari, D.D. Dionysiou, A review on the visible light active titanium dioxide photocatalysts for environmental applications, Appl. Catal. B **125**, 331-349 (2012).
28. J. Xing, W.Q. Fang, H.J. Zhao, H.G. Yang, Inorganic photocatalysts for overall water splitting, Chem. Asian J. **7**, 642-657 (2012).
29. N. Zhang, Y.H. Zhang, Y.J. Xu, Recent progress on graphene-based photocatalysts: Current status and future perspectives, Nanoscale **4**, 5792-5813 (2012).
30. Z.S. Li, W.J. Luo, M.L. Zhang, J.Y. Feng, Z.G. Zou, Photoelectrochemical cells for solar hydrogen production: current state of promising photoelectrodes, methods to improve their properties, and outlook, Energy Environ. Sci. **6**, 347-370 (2013).
31. K. Maeda, Z-scheme water splitting using two different semiconductor photocatalysts, ACS Catal. **3**, 1486-1503 (2013).
32. Y. Moriya, T. Takata, K. Domen, Recent progress in the development of (oxy)nitride photocatalysts for water splitting under visible-light irradiation, Coord. Chem. Rev. **257**, 1957-1969 (2013).
33. V. Preethi, S. Kanmni, Photocatalytic hydrogen production, Mater. Sci. Semicond. Process **16**, 561-575 (2013).
34. S. Rawalekar, T. Mokari, Rational design of hybrid nanostructures for advanced photocatalysis, Adv. Energy Mater. **3**, 12-27 (2013).
35. Y.J. Wang, Q.S. Wang, X.Y. Zhan, F.M. Wang, M. Safdar, J. He, Visible light driven type II heterostructures and their enhanced photocatalysis properties: A review, Nanoscale **5**, 8326-8339 (2013).
36. J.H. Yang, D.G. Wang, H.X. Han, C. Li, Roles of cocatalysts in photocatalysis and photoelectrocatalysis, Accounts Chem. Res. **46**, 1900-1909 (2013).
37. N. Serpone, E. Pelizzetti, *Photocatalysis: Fundamentals and Applications* (Wiley, New York, 1989).
38. H. Park, A. Bak, Y.Y. Ahn, J. Choi, M.R. Hoffmann, Photoelectrochemical performance of multi-layered BiO_x-TiO_2/Ti electrodes for degradation of phenol and production of molecular hydrogen in water, J. Hazard. Mater. **211-212**, 47-54 (2012).
39. H. Park, A. Bak, T.H. Jeon, S. Kim, W. Choi, Photo-chargeable and dischargeable TiO_2 and WO_3 heterojunction electrodes, Appl. Catal. B **115-116**, 74-80 (2012).
40. K. Maeda, K. Domen, Photocatalytic water splitting: recent progress and future challenges, J. Phys. Chem. Lett. **1**, 2655-2661 (2010).

41. H. Park, Y. Park, W. Kim, W. Choi, Surface modification of TiO_2 photocatalyst for environmental applications, J. Photochem. Photobiol. C **15**, 1-20 (2013).
42. K. Maeda, K. Teramura, D.L. Lu, T. Takata, N. Saito, Y. Inoue, K. Domen, Photocatalyst releasing hydrogen from water - Enhancing catalytic performance holds promise for hydrogen production by water splitting in sunlight, Nature **440**, 295-295 (2006).
43. J.S. Jang, H.G. Kim, J.S. Lee, Heterojunction semiconductors: A strategy to develop efficient photocatalytic materials for visible light water splitting, Catal. Today **185**, 270-277 (2012).
44. S. Sato, J.M. White, Photocatalytic water decomposition and water-gas shift reactions over NaOH-coated, platinized TiO_2, J. Catal. **69**, 128-139 (1981).
45. K. Sayama, H. Arakawa, Effect of Na_2CO_3 addition on photocatalytic decomposition of liquid water over various semiconductor catalysis, J. Photochem. Photobiol. A **77**, 243-247 (1994).
46. S. Tabata, N. Nishida, Y. Masaki, K. Tabata, Stoichiometric photocatalytic decomposition of pure water in Pt/TiO_2 aqueous suspension system, Catal. Lett. **34**, 245-249 (1995).
47. J.P. Lehn, J.P. Sauvage, R. Ziessel, Photochemical water splitting. Continuous generation of hydrogen and oxygen on irradiation of aqueous suspensions of metal loaded strontium titanate, Nouv. J. Chim. **4**, 623-627 (1980).
48. A. Kudo, Development of photocatalyst materials for water splitting, Int. J. Hydrogen Energy **31**, 197-202 (2006).
49. K. Yamaguchi, S. Sato, Photolysis of water over metallized powdered titanium dioxide, J. Chem. Soc. Faraday Trans. **81**, 1237-1246 (1985).
50. K. Domen, N. Saito, S. Soma, M. Onishi, K. Tamura, Photocatalytic decomposition of water vapour on an $NiO\text{-}SrTiO_3$ catalyst, Chem. Commun. **12**, 543-544 (1980).
51. T. Kawai, T. Sakata, Photocatalytic decomposition of gaseous water over TiO_2 and TiO_2-RuO_2 surfaces, Chem. Phys. Lett. **72**, 87-89 (1980).
52. S. Sato, N. Saito, H. Nishiyama, Y. Inoue, Photocatalytic activity for water decomposition of indates with octahedrally coordinated d^{10} configuration. I. Influences of preparation conditions on activity, J. Phys. Chem. B **107**, 7965-7969 (2003).
53. K. Teramura, K. Maeda, T. Saito, T. Takata, N. Saito, Y. Inoue, K. Domen, Characterization of ruthenium oxide nanocluster as a cocatalyst with $(Ga_{1-x}Zn_x)(N_{1-x}O_x)$ for photocatalytic overall water splitting, J. Phys. Chem. B **109**, 21915-21921 (2005).
54. A. Iwase, H. Kato, A. Kudo, A novel photodeposition method in the presence of nitrate ions for loading of an iridium oxide cocatalyst for water splitting, Chem. Lett. **34**, 946-947 (2005).
55. S.A. Naman, S.M. Ahwi, K.A. Emara, Hydrogen production from the splitting of H_2S by visible light irradiation of vanadium sulfides dispersion loaded with RuO_2, Int. J. Hydrogen Energy **11**, 33-38 (1986).
56. J. Choi, S.Y. Ryu, W. Balcerski, T.K. Lee, M.R. Hoffmann, Photocatalytic production of hydrogen on $Ni/NiO/KNbO_3/CdS$ nanocomposites using visible light, J. Mater. Chem. **18**, 2371-2378 (2008).
57. J.S. Jang, H.G. Kim, U.A. Joshi, J.W. Jang, J.S. Lee, Fabrication of CdS nanowires decorated with TiO_2 nanoparticles for photocatalytic hydrogen production under visible light irradiation, Int. J. Hydrogen Energy **33**, 5975-5980 (2008).
58. S.Y. Ryu, W. Balcerski, T.K. Lee, M.R. Hoffmann, Photocatalytic production of hydrogen from water with visible light using hybrid catalysts of CdS attached to microporous and mesoporous silicas, J. Phys. Chem. C **111**, 18195-18203 (2007).
59. S.Y. Ryu, J. Choi, W. Balcerski, T.K. Lee, M.R. Hoffmann, Photocatalytic production of H_2 on nanocomposite catalysts, Ind. Eng. Chem. Res. **46**, 7476-7488 (2007).
60. Y.K. Kim, H. Park, Light-harvesting multi-walled carbon nanotubes and CdS hybrids: application to photocatalytic hydrogen production from water, Energy Environ. Sci. **4**, 685-694 (2011)
61. H. Park, W. Choi, M.R. Hoffmann, Effects of the preparation method of the ternary $CdS/TiO_2/Pt$ hybrid photocatalysts on visible light-induced hydrogen production, J. Mater. Chem. **18**, 2379-2385 (2008).

62. H. Park, Y.K. Kim, W. Choi, Reversing CdS preparation order and its effects on photocatalytic hydrogen production of CdS/Pt-TiO_2 hybrids under visible light, J. Phys. Chem. C **115**, 6141-6148 (2011).
63. P. Brown, P.V. Kamat, Electrophoretic deposition of CdSe – C60 composite films and capture of photogenerated electrons with nC60 cluster shell, J. Am. Chem. Soc. **130**, 8890-8891 (2008).
64. M. Ranjbar, S.M. Mahdavi, A.I. Zad, Pulsed laser deposition of W–V–O composite films: Preparation, characterization and gasochromic studies, Sol. Energy Mater. Sol. Cells **92**, 878-883 (2008).
65. D.G. Wang, Z.G. Zou, J. Ye, Photocatalytic water splitting with the Cr-doped $Ba_2In_2O_5$/In_2O_3 composite oxide semiconductors, Chem. Mater. **17**, 3255-3261 (2005).
66. H.G. Kim, P.H. Borse, W. Choi, J.S. Lee, Photocatalytic nanodiodes for visible-light photocatalysis, Angew. Chem. Int. Edit. **44**, 4585-4589 (2005).
67. J.S. Jang, W. Li, S.H. Oh, J.S. Lee, Fabrication of CdS/TiO_2 nano-bulk composite photocatalysts for hydrogen production from aqueous H_2S solution under visible light, Chem. Phys. Lett. **425**, 278-282 (2006).
68. T. Kida, G. Guan, N. Yamada, T. Ma, K. Kimura, A. Yoshida, Hydrogen production from sewage sludge solubilized in hot-compressed water using photocatalyst under light irradiation, Int. J. Hydrogen Energy **29**, 269-274 (2004).
69. K.S. Leshkies, R. Duvakar, J. Basu, E.E. Pommer, J.E. Boercker, C.B. Carter, U.R. Kortshagen, D.J. Norris, E.S. Aydil, Photosensitization of ZnO nanowires with CdSe quantum dots for photovoltaic devices, Nano Lett. **7**, 1793-1798 (2005).
70. J.S. Jang, H.G. Kim, P.H. Borse, J.S. Lee, Simultaneous hydrogen production and decomposition of H_2S dissolved in alkaline water over CdS-TiO_2 composite photocatalysts under visible light irradiation, Int. J. Hydrogen Energy **32**, 4786-4791 (2007).
71. H.G. Kim, E.D. Jeong, P.H. Borse, S. Jeon, K. Yong, J.S. Lee, Photocatalytic ohmic layered nanocomposite for efficient utilization of visible light photons, Appl. Phys. Lett. **89**, 64101-64103 (2006).
72. D.R. Baker, P.V. Kamat, Photosensitization of TiO_2 nanostructures with CdS quantum dots: Particulate versus tubular support architectures, Adv. Funct. Mater. **19**, 805-811 (2009).
73. S. Banerjee, S.K. Mohapatra, P.P. Das, M. Misra, Synthesis of coupled semiconductor by filling 1D TiO_2 nanotubes with CdS, Chem. Mater. **20**, 6784-6791 (2008).
74. Y.J. Chi, H.G. Fu, L.H. Qi, K.Y. Shi, H.B. Zhang, H.T. Yu, Preparation and photoelectric performance of ITO/TiO_2/CdS composite thin films, J. Photochem. Photobiol. A. **195**, 357-363 (2008).
75. J.C. Kim, J. Choi, Y.B. Lee, J.H. Hong, J.I. Lee, J.W. Yang, W.I. Lee, N.H. Hur, Enhanced photocatalytic activity in composites of TiO_2 nanotubes and CdS nanoparticles, Chem. Commun. 5024-5026 (2006).
76. A. Kumar, A.K. Jain, Photophysics and photochemistry of colloidal CdS-TiO_2 coupled semiconductors - Photocatalytic oxidation of indole, J. Mol. Catal. A **165**, 265-273 (2001).
77. C.J. Lin, Y.H. Yu, Y.H. Liou, Free-standing TiO_2 nanotube array films sensitized with CdS as highly active solar light-driven photocatalysts, Appl. Catal. B **93**, 119-125 (2009).
78. J.C. Lee, T.G. Kim, W. Lee, S.H. Han, Y.M. Sung, Growth of CdS nanorod-coated TiO_2 nanowires on conductive glass for photovoltaic applications, Cryst. Growth Des. **9**, 4519-4523 (2009).
79. W.W. So, K.J. Kim, S.J. Moon, Photo-production of hydrogen over the CdS-TiO_2 nanocomposite particulate films treated with $TiCl_4$, Int. J. Hydrogen Energy **29**, 229-234 (2004).
80. S. Kim, H. Park, Sunlight-harnessing and storing heterojunction TiO_2/Al_2O_3/WO_3 electrodes for nighttime applications, RSC Adv. **3**, 17551-17558 (2013).
81. G.M. Wang, X.Y. Yang, F. Qian, J.Z. Zhang, Y. Li, Double-sided CdS and CdSe quantum dot co-sensitized ZnO nanowire arrays for photoelectrochemical hydrogen generation, Nano Letters **10**, 1088-1092 (2010).

82. S.T. Martin, H. Herrmann, W.Y. Choi, M.R. Hoffmann, Time-resolved microwave conductivity. 1. TiO_2 photoreactivity and size quantization, J. Chem. Soc. Farad. Trans. **90**, 3315-3322 (1994).
83. H.M. Zhu, B.F. Yang, J. Xu, Z.P. Fu, M.W. Wen, T. Guo, S.Q. Fu, J. Zuo, S.Y. Zhang, Construction of Z-scheme type CdS-Au-TiO_2 hollow nanorod arrays with enhanced photocatalytic activity, Appl. Catal. B **90**, 463-469 (2009).
84. H. Kim, J. Kim, W. Kim, W. Choi, Enhanced photocatalytic and photoelectrochemical activity in the ternary hybrid of CdS/TiO_2/WO_3 through the cascadal electron transfer, J. Phys. Chem. C **115**, 9797-9805 (2011).
85. Y.K. Kim, H. Park, How and to what extent do carbon materials catalyze solar hydrogen production from water? Appl. Catal. B **125**, 530-537 (2012).
86. S.V. Tambwekar, D. Venugopal, M. Subrahmanyam, H_2 production of (CdS-ZnS)-TiO_2 supported photocatalytic system, Int. J. Hydrogen Energy **24**, 957-963 (1999).
87. D.X. Shi, Y.Q. Feng, S.H. Zhong, Photocatalytic conversion of CH_4 and CO_2 to oxygenated compounds over Cu/CdS-TiO_2/SiO_2 catalyst, Catal. Today **98**, 505-509 (2004).
88. C.Y. Wang, H.M. Shang, T. Ying, T.S. Yuan, G.W. Zhang, Properties and morphology of CdS compounded TiO_2 visible-light photocatalytic nanofilms coated on glass surface, Sep. Purif. Technol. **32**, 357-362 (2003).
89. A. Kumar, A.K. Jain, Photophysics and photocatalytic properties of Ag^+-activated sandwich Q-CdS-TiO_2, J. Photochem. Photobiol. A **156**, 207-218 (2003).
90. Y. Bessekhouad, N. Chaoui, M. Trzpit, N. Ghazzal, D. Robert, J.V. Weber, UV-vis versus visible degradation of Acid Orange II in a coupled CdS/TiO_2 semiconductors suspension, J. Photochem. Photobiol. A **183**, 218-224 (2006).
91. H.B. Yin, Y. Wada, T. Kitamura, T. Sakata, H. Mori, S. Yanagida, Enhanced photocatalytic dechlorination of 1,2,3,4-tetrachlorobenzene using nanosized CdS/TiO_2 hybrid photocatalyst under visible light irradiation, Chem. Lett. 334-335 (2001).
92. P.A. Sant, P.V. Kamat, Interparticle electron transfer between size-quantized CdS and TiO_2 semiconductor nanoclusters, Phys. Chem. Chem. Phys. **4**, 198-203 (2002).
93. H. Matsumoto, T. Matsunaga, T. Sakata, H. Mori, H. Yoneyama, Size dependent fluorescence quenching of CdS nanocrystals caused by TiO_2 colloids as a potential-variable quencher, Langmuir **11**, 4283-4287 (1995).
94. N. Chandrasekharan, P.V. Kamat, Improving the photoelectrochemical performance of nanostructured TiO_2 films by adsorption of gold nanoparticles, J. Phys. Chem. B **104**, 10851-10857 (2000).
95. M. Jacob, H. Levanon, P.V. Kamat, Charge distribution between UV-irradiated TiO_2 and gold, Nano Lett. **3**, 353-358 (2003).
96. V. Subramanian, E.E. Wolf, P.V. Kamat, Catalysis with TiO_2/gold nanocomposites, J. Am. Chem. Soc. **126**, 4943-4950 (2004).
97. K. Vinodgopal, I. Bedja, P.V. Kamat, Nanostructured semiconductor films for photocatalysis. Photoelectrochemical behavior of SnO_2/TiO_2 composite systems and its role in photocatalytic degradation of a textile azo dye, Chem. Mater. **8**, 2180-2187 (1996).
98. G. Khan, S.K. Choi, S. Kim, S.K. Lim, J.S. Jang, H. Park, Carbon nanotubes as an auxiliary catalyst in heterojunction photocatalysis for solar hydrogen, Appl. Catal. B **142-143**, 647-653 (2013).
99. G. Khan, Y.K. Kim, S.K. Choi, D.S. Han, A. Abdel-Wahab, H. Park, Evaluating the catalytic effects of carbon materials on the photocatalytic reduction and oxidation reactions of TiO_2, Bull. Kor. Chem. Soc. **34**, 1137-1144 (2013).
100. H. Kisch, H. Weiss, Tuning photoelectrochemical and photocatalytic properties through electronic semiconductor-support interaction, Adv. Funct. Mater. **12**, 483-488 (2002).
101. H. Weib, A. Fernandez, H. Kisch, Electronic semiconductor–support interaction. A novel effect in semiconductor photocatalysis, Angew. Chem. Int. Edit. **40**, 3825-3827 (2001).

102. M. Barbeni, E. Pelizzetti, E. Borgarello, N. Serpone, M. Gratzel, L. Balducci, M. Visca, Hydrogen from hydrogen-sulfide cleavage - Improved efficiencies via modification of semiconductor particles, Int. J. Hydrogen Energy **10**, 249-253 (1985).
103. C.A. Linkous, N.Z. Muradov, S.N. Ramser, Consideration of reactor design for solar hydrogen production from hydrogen sulfide using semiconductor particulates, Int. J. Hydrogen Energy **20**, 701-709 (1995).
104. L.R. Grzyll, J.J. Thomas, R.G. Barile, Photoelectrochemical conversion of hydrogen sulfide to hydrogen using artificial light and solar radiation. Int. J. Hydrogen Energy **14**, 647-651 (1989).
105. N. Buhler, K. Meier, J.F. Reber, Photochemical hydrogen production with CdS suspensions, J. Phys. Chem. **88**, 3261-3268 (1984).
106. J.S. Jang, S.H. Choi, H. Park, W. Choi, J.S. Lee, A composite photocatalyst of CdS nanoparticles deposited on TiO_2 nanosheets, J. Nanosci. Nanotechnol. **6**, 3642-3646 (2006).
107. M.K. Arora, N. Sahu, S.N. Upadhyay, A.S.K. Sinha, Activity of cadmium sulfide photocatalysts for hydrogen production from water: Role of support, Ind. Eng. Chem. Res. **38**, 2659-2665 (1999).
108. J.F. Reber, M. Rusek, Photochemical hydrogen production with platinized suspensions of cadmium sulfide and cadmium zinc sulfide modified by silver sulfide, J. Phys. Chem. **90**, 824-834 (1986).
109. M. Matsumura, S. Furukawa, Y. Saho, H. Tsubomura, Cadmium sulfide photocatalyzed hydrogen production from aqueous solutions of sulfite: Effect of crystal structure and preparation method of the catalyst, J. Phys. Chem. **89**, 1327-1329 (1985).
110. Z.S. Jin, Z.S. Chen, Q.L. Li, C.J. Xi, X.H. Zheng, On the conditions and mechanism of PtO_2 formation in the photoinduced conversion of H_2PtCl_6, J. Photochem. Photobiol. A **81**, 177-182 (1994).
111. Z.S. Jin, Q.L. Li, L.B. Feng, Z.S. Chen, X.H. Zheng, C.J. Xi, Investigation of the functions of CdS surface composite layer and Pt on treated Pt/CdS for photocatalytic dehydrogenation of aqueous alcohol solutions, J. Mol. Catal. **50**, 315-332 (1989).
112. M.C. Guindo, L. Zurita, J.D.G. Duran, A.V. Delgado, Electrokinetic behavior of spherical colloidal particles of cadmium sulfide, Mater. Chem. Phys. **44**, 51-58 (1996).
113. T. Inoue, T. Watanabe, A. Fujishima, K. Honda, Investigation of CdS photoanode reaction in the electrolyte solution containing sulfide ion, Bull. Chem. Soc. Jpn. **52**, 1243-1250 (1979).
114. Q.L. Li, Z.S. Chen, X.H. Zheng, Z.S. Jin, Study of photoreduction of hexachloroplatinate on cadmium sulfide, J. Phys. Chem. **96**, 5959-5962 (1992).
115. M. Matsumura, M. Hiramoto, T. Iehara, H. Tsubomura, Photocatalytic and photoelectrochemical reactions of aqueous solutions of formic acid, formaldehyde, and methanol on platinized cadmium sulfide powder and at a cadmium sulfide electrode, J. Phys. Chem. **88**, 248-250 (1984).
116. T. Watanabe, Fujishim.A, K.I. Honda, Potential variation at semiconductor-electrolyte interface through a chance in pH of solution, Chem. Lett. 897-900 (1974).
117. Z.S. Jin, Q.L. Li, X.H. Zheng, C.J. Xi, C.P. Wang, H.Q. Zhang, L.B. Feng, H.Q. Wang, Z.S. Chen, Z.C. Jiang, Surface properties of Pt/CdS and mechanism of photocatalytic dehydrogenation of aqueous alcohol, J. Photochem. Photobiol. A **71**, 85-96 (1993).
118. L. Borrell, S. Cerveramarch, J. Gimenez, R. Simarro, J.M. Andujar, A comparative study of CdS-based semiconductor photocatalysts for solar hydrogen production from sulphide + sulphite substrates, Sol. Energy Mater. Sol. Cells 25, 25-39 (1992).
119. A. Mills, G. Williams, Photosensitized oxidation of water by CdS-based suspensions, J. Chem. Soc. Farad. Trans. **85**, 503-519 (1989).
120. J. Sabate, S. Cerveramarch, R. Simarro, J. Gimenez, A comparative study of semiconductor photocatalysts for hydrogen production by visible light using different sacrificial substrates in aqueous media, Int. J. Hydrogen Energy **15**, 115-124 (1990).

121. N. Serpone, E. Borgarello, M. Gratzel, Visible light induced generation of hydrogen from H_2S in mixed semiconductor dispersions; Improved efficiency through inter-particle electron transfer, J. Chem. Soc. Chem. Commun. 342-344 (1984).
122. A. Sobczynski, A.J. Bard, A. Campion, M.A. Fox, T. Mallouk, S.E. Webber, J.M. White, Photoassisted hydrogen generation - Pt and CdS supported on separate particles, J. Phys. Chem. **91**, 3316-3320 (1987).
123. H. Harada, T. Sakata, T. Ueda, Effect of semiconductor on photocatalytic decomposition of lactic acid, J. Am. Chem. Soc. **107**, 1773-1774 (1985).
124. H. Tada, T. Mitsui, T. Kiyonaga, T. Akita, K. Tanaka, All-solid-state Z-scheme in CdS-Au-TiO_2, Nature Mater. **5**, 782-786 (2006).
125. L. Spanhel, H. Weller, A. Henglein, Photochemistry of semiconductor colloids. 22. Electron injection from illuminated CdS into attached TiO_2 and ZnO particles, J. Am. Chem. Soc. **109**, 6632-6635 (1987).
126. L. Wu, J.C. Yu, X.Z. Fu, Characterization and photocatalytic mechanism of nanosized CdS coupled TiO_2 nanocrystals under visible light irradiation, J. Mol. Catal. A **244**, 25-32 (2006).
127. J.S. Jang, S.H. Choi, H.G. Kim, J.S. Lee, Location and state of Pt in platinized CdS/TiO_2, J. Phys. Chem. C **112**, 17200-17205 (2008).
128. J.S. Lee, S. Locatelli, S.T. Oyama, M. Boudart, Molybdenum carbide catalysts 3. Turnover rates for the hydrogenolysis of n-butane, J. Catal. **125**, 157-170 (1990).
129. J.S. Lee, S.T. Oyama, M. Boudart, Molybdenum carbide catalysts: I. Synthesis of unsupported powders, J. Catal. **106**, 125-133 (1987).
130. R.B. Levy, M. Boudart, Platinum-like behavior of tungsten carbide in surface catalysis, Science **181**, 547-549 (1973).
131. J.S. Lee, M. Boudart, In situ carburization of metallic molybdenum during catalytic reactions of carbon-containing gases, Catal. Lett. **20**, 97-106 (1993).
132. C.J. Barnett, G.T. Burstein, A.R.J. Kucernak, K.R. Williams, Electrocatalytic activity of some carburised nickel, tungsten and molybdenum compounds, Electrochim. Acta **42**, 2381-2388 (1997).
133. S. Bodoardo, M. Maja, N. Penazzi, F.E.G. Henn, Oxidation of hydrogen on WC at low temperature, Electrochim. Acta **42**, 2603-2609 (1997).
134. M.B. Zeller, J.G. Chen, Surface science and electrochemical studies of WC and W_2C PVD films as potential electrocatalysts, Catal. Today **99**, 299-307 (2005).
135. D.R. McIntyre, G.T. Burstein, A. Vossen, Effect of carbon monoxide on the electrooxidation of hydrogen by tungsten carbide, J. Power Sources **107**, 67-73 (2002).
136. R. Ganesan, J.S. Lee, Tungsten carbide microspheres as a noble-metal-economic electrocatalyst for methanol oxidation, Angew. Chem. Int. Edit. **44**, 6557-6560 (2005).
137. R. Ganesan, D.J. Ham, J.S. Lee, Platinized mesoporous tungsten carbide for electrochemical methanol oxidation, Electrochem. Commun. **9**, 2576-2579 (2007).
138. Y. Oosawa, Photocatalytic hydrogen evolution from an aqueous methanol solution over ceramics-electrocatalyst/TiO_2, Chem. Lett. **12**, 577-580 (1983).
139. J.S. Jang, D.J. Ham, N. Lakshminarasimhan, W. Choi, J.S. Lee, Role of platinum-like tungsten carbide as cocatalyst of CdS photocatalyst, Appl. Catal. A **346**, 149-154 (2008).
140. L. Jia, D.-H. Wang, Y.-X. Huang, A.-W. Xu, H.-Q. Yu, Highly durable N-doped graphene/CdS nanocomposites with enhanced photocatalytic hydrogen evolution from water under visible light irradiation, J. Phys. Chem. C **115**, 11466-11473 (2011).
141. Q. Li, B. Guo, J. Yu, J. Ran, B. Zhang, H. Yan, J.R. Gong, Highly efficient visible-light-driven photocatalytic hydrogen production of CdS-cluster-decorated graphene nanosheets, J. Am. Chem. Soc. **2011**, 10878-10884 (2011).
142. Y.H. Ng, I.V. Lightcap, K. Goodwin, M. Matsumura, P.V. Kamat, To what extent do graphene scaffolds improve the photovoltaic and photocatalytic response of TiO_2 nanostructured films? J. Phys. Chem. Lett. **1**, 2222-2227 (2010).

143. I. Robel, B.A. Bunker, P.V. Kamat, Single-walled carbon nanotube-CdS nanocomposites as light-harvesting assemblies: Photoinduced charge-transfer interactions, Adv. Mater. **17**, 2458-2463 (2005).
144. H.W. Jeong, H. Park, Carbon-catalyzed dye sensitization for solar hydrogen production, Catal. Today **230**, 15-19 (2014).
145. P. Serp, J.L. Figueiredo, *Carbon Materials for Catalysis* (Wiley, New Jersey, 2009).
146. T. Torimoto, Y. Okawa, N. Takeda, H. Yoneyama, Effect of activated carbon content in TiO_2-loaded activated carbon on photodegradation behaviors of dichloromethane, J. Photochem. Photobiol. A **103**, 153-157 (1997).
147. A. Modestov, V. Glezer, I. Marjasin, O. Lev, Photocatalytic degradation of chlorinated phenoxyacetic acids by a new buoyant titania-exfoliated graphite composite photocatalyst, J. Phys. Chem. B **101**, 4623-4629 (1997).
148. T.-F. Yeh, J.-M. Syu, C. Cheng, T.-H. Chagn, H. Teng, Graphite oxide as a photocatalyst for hydrogen production from water, Adv. Func. Mater. **20**, 2255-2262 (2010).
149. L.-W. Zhang, H.-B. Fu, Y.-F. Zhu, Efficient TiO_2 photocatalysts from surface hybridization of TiO_2 particles with graphite-like carbon, Adv. Func. Mater. **18**, 2180-2189 (2008).
150. S. Kim, S.K. Lim, Preparation of TiO_2-embedded carbon nanofibers, Appl. Catal. B **84**, 16-20 (2008).
151. R. Yuan, J. Zheng, R. Guan, Y. Zhao, Surface characteristics and photocatalytic activity of TiO_2 loaded on activated carbon fibers, Colloid Surface A **254**, 131-136 (2005).
152. A. Kongkanand, R.M. Dominguez, P.V. Kamat, Single wall carbon nanotube scaffolds for photoelectrochemical solar cells. Capture and transport of photogenerated electrons, Nano Lett. **7**, 676-680 (2007).
153. L. Sheeney-Haj-Khia, B. Basnar, I. Willner, Efficient generation of photocurrents by using CdS/carbon nanotube assemblies on electrodes, Angew. Chem. Int. Edit. **44**, 78-83 (2005).
154. K. Woan, G. Pyrgiotakis, W. Sigmund, Photocatalytic carbon-nanotube-TiO_2 composites, Adv. Mater. **21**, 2233-2239 (2009).
155. O. Akhavan, M. Abdolahad, A. Esfandiar, M. Mohatashamifar, Photodegradation of graphene oxide sheets by TiO_2 nanoparticles after a photocatalytic reduction, J. Phys. Chem. C **114**, 12955-12959 (2010).
156. Y. Park, S.-H. Kang, W. Choi, Exfoliated and reorganized graphite oxide on titania nanoparticles as an auxiliary co-catalyst for photocatalytic solar conversion, Phys. Chem. Chem. Phys. **13**, 9425-9431 (2011).
157. N.J. Bell, H.N. Yun, A.J. Du, H. Coster, S.C. Smith, R. Amal, Understanding the enhancement in photoelectrochemical properties of photocatalytically prepared TiO_2-reduced graphene oxide composite, J. Phys. Chem. C **115**, 6004-6009 (2011).
158. W. Fan, Q. Lai, Q. Zhang, Y. Wang, Nanocomposites of TiO_2 and reduced graphene oxide as efficient photocatalysts for hydrogen evolution, J. Phys. Chem. C **115**, 10694-10701 (2011).
159. I.V. Lightcap, T.H. Kosel, P.V. Kamat, Anchoring semiconductor and metal nanoparticles on a two-dimensional catalyst mat. Storing and shuttling electrons with reduced graphene oxide, Nano Lett. **10**, 577-583 (2010).
160. H. Zhang, X.J. Lv, Y.M. Li, Y. Wang, J.H. Li, P25-graphene composite as a high performance photocatalyst, ACS Nano **4**, 380-386 (2010).
161. Y.H. Zhang, Z.R. Tang, X.Z. Fu, Y.J. Xu, TiO_2-graphene nanocomposites for gas-phase photocatalytic degradation of volatile aromatic pollutant: Is TiO_2-graphene truly different from other TiO_2-carbon composite materials? ACS Nano **4**, 7303-7314 (2010).
162. K. Kondo, N. Murakami, C. Ye, T. Tsubota, T. Ohno, Development of highly efficient sulfur-doped TiO_2 photocatalysts hybridized with graphitic carbon nitride, Appl. Catal. B **142-143**, 362-367 (2013).

Encapsulation for Improving the Efficiencies of Solar Cells

Sindhu Seethamraju, Praveen C Ramamurthy, and Giridhar Madras

1 Introduction

The urgency to increase the energy production in order to meet the present and future energy demands has led to explore various renewable energy resources [1]. Solar energy can be harvested and used by three basic mechanisms: solar to thermal/voltaic/chemical energy for various applications [2]. Even though solar energy has seemed to be the plausible solution in terms of sustainability, portability, and availability, it is not commercially viable in short term as compared to conventional fuels. This is due to inorganic semiconductor processing technologies and material supply limitations. With the introduction of thin film and organic photovoltaics, the feasibility of coating/printing solar devices conformally onto various flexible substrate surfaces has increased the hope of fabricating economically compliant solar devices [3–5]. The potential impact of the emerging polymer-based solar technologies could be on the niche of energy market due to their ability to work in diffuse light and promising large-scale scalability. For example, fabricating lighter, wearable, flexible devices with roll processability suitable for large areas and portable applications is possible [6, 7]. The expectations on the commercialization of organic-based solar devices can be realized only if some of the challenges involving efficiency and lifetimes of these devices are met. Photovoltaic power conversion efficiency of about ~12 % has been achieved in organic solar cells whereas it is about ~44 % in inorganic semiconductor devices [8]. Even though the parity in efficiencies is higher, other factors such as lower economy,

S. Seethamraju • G. Madras (✉)
Center for Nanoscience and Engineering, Indian Institute of Science, Bangalore 560012, India
e-mail: giridhar@chemeng.iisc.ernet.in

P.C. Ramamurthy
Center for Nanoscience and Engineering, Indian Institute of Science, Bangalore 560012, India

Department of Materials Engineering, Indian Institute of Science, Bangalore 560012, India

B. Viswanathan et al. (eds.), *Materials and Processes for Solar Fuel Production*,
Nanostructure Science and Technology 174, DOI 10.1007/978-1-4939-1628-3_2

aesthetic aspects, and suitability for domestic applications indicate organic solar devices as a better option over inorganic photovoltaics [4, 9]. Photoelectrochemical water splitting is another developing research field for production of solar-based fuels for industrial and domestic applications. Various semiconducting materials with suitable bandgaps matching with photocatalysts for water splitting reaction can be used to generate feedstock fuels for use in various industries and transportation [10].

2 Need for Encapsulation

Silicon-based solar cells are themselves brittle, apart from the glass encapsulation. The water vapor transmission rate (WVTR) to be possessed by the encapsulant for these solar modules is about 0.1–1 g/m^2/day. Hence, polymers like ethylene vinyl acetate, poly (vinyl butyral), ionomers, polyolefins, and thermoplastic polyurethanes are commonly used as encapsulant and back sheets in standard commercial photovoltaic modules. The effective functioning of these materials is essential for corrosion-free solar module. The chemicals released due to degradation of the polymer corrode the metallic components in the module [11]. Hence, various filler materials like antioxidants, UV absorbers, permeation delaying components, and stabilizers are added to increase the performance of the encapsulant. Mono- and polycrystalline silicon-based solar cell have thickness of about 100–400 μm of which only the upper region comprising up to 15 μm can capture visible light by absorption. Hence, thin film-based solar devices provide a better solution as they are much thinner and flexible with the ability to absorb the light throughout the thickness (<5 μm). These materials include amorphous Si, cadmium telluride (CdTe), and copper indium gallium selenide (CIGS). However, the process complexity and continuous production strategies are further required to be explored for their commercialization. Even these thin film materials require a flexible, weathering, and UV-resistant encapsulant with WVTR of the range $<10^{-3}$ g/m^2/day which is about three orders lower than the standard food packaging requirement [12].

The basic device architecture of an organic photovoltaic (OPV) device is given in Fig. 1. The incident light is absorbed by the photoactive layer, generating excitons, which dissociate at the donor–acceptor interface of the OPV device. In order to separate these excitons, a strong electric field is required for the conversion into final photovoltaic energy. As the exciton binding energies are higher in organic semiconductors than that in the inorganic materials, it helps in designing much thinner devices. The dissociated charges are transported to the electrodes where they are collected.

The device architecture, interfacial contacts at the electrodes, interfacial nanomorphology of the active layers, bandgaps of the materials used, and contaminant-free processing determine the organic device performance. Hence, organic chemistry and device physics helps choosing and engineering the suitable

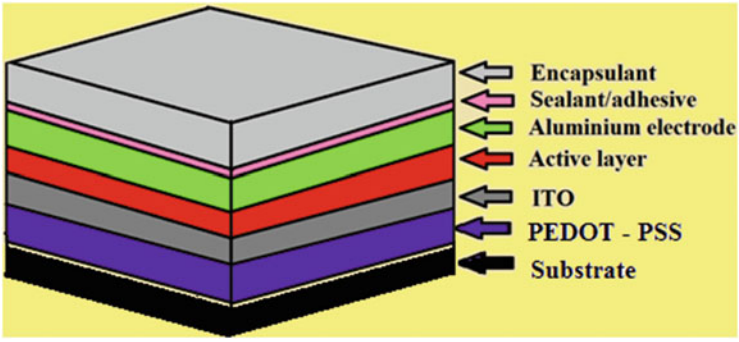

Fig. 1 Basic schematic for cross-sectional view of encapsulated organic solar device

active component materials for fabricating the organic solar device dynamically [13, 14]. However, the lifetime of the device is dependent on the effective working of the active materials in the fabricated device. Most of the active materials used in OPV devices are not stable under ultraviolet (UV) radiation and in humid environmental conditions. The major reasons include degradation of the active components, oxidation of electrodes, and delamination of the layers in the fabricated OPV device upon exposure to moisture, oxygen, or ultraviolet radiation. As the degradation in device performance is caused by external elements, the optimal solution would be to protect the device from interfering with such environments which can be achieved by encapsulating the OPV device with a high barrier material.

The encapsulant material must be capable of reducing the ingress of moisture, oxygen as well as remain resistant to UV radiation. The encapsulant ideally should be impermeable to moisture and oxygen or exhibit at least permeability with the acceptable transmission rates through the material being $<10^{-6}$ g/m^2/day and $<10^{-5}$ cc/m^2/day/atm, respectively [15]. The conventional encapsulant material that satisfies the prescribed transmission rates is glass [16]. However, it is brittle, heavy, and not suitable for large area and large-scale processing, leading to detrimental effect on the main features and advantages of organic solar devices. Thus, it is unsuitable for being used as an encapsulant. Hence, an easily processable, monolithic, flexible, high vapor and gas barrier material, which can conform into various surfaces and shapes, is required as an OPV encapsulant. This led to exploration of various organic, inorganic, and hybrid layers for their use as encapsulants. Along with the development of the material for encapsulation, suitable techniques to determine the ultra low transmission rates of water vapor and oxygen through the encapsulants are required for characterization.

3 Lifetimes and Performance of OPV Devices

The lifetime and performance is the key to the commercialization of the organic solar cells. Degradation of performance is one of the major limitations in OPVs. The problem lies in the appropriate understanding about the mechanisms of degradation that occur in OPV devices. Various degradation causes have been probed so far relating to degradation.

The active materials like P3HT and PEDOT-PSS oxidize in the presence of light and oxygen [17]. Moreover, the rate of oxidation increases in the presence of H_2O [18] as well as with an increase in temperature [19–21]. UV light-induced degradation of conjugated polymers has also been observed [22, 23]. The mobility and conductivity of fullerene/pentacene-based molecules decrease drastically because of their oxidation. Even the ingress of moisture decreases mobility of the charge carriers [24]. Organic materials and metal electrode materials such as aluminum are susceptible to reactions with oxygen and water, further leading to delamination of individual layers. The diffusion of oxygen through the electrode materials results in indium diffusion to the active layer through the ITO electrode [25].

In bulk heterojunction OPVs, interpenetrating donor–acceptor blends are used. The donor–acceptor interfacial stability changes with time due to either processing conditions or thermodynamic equilibrium [26]. The blend morphology also is affected with oxidation of blend components or the impurities. Sometimes, physical changes occur in active layer, changing the morphology due to thermodynamic instabilities [27].

Degradation of PEDOT: PSS layer is one of the major reasons in the failure of OPVs. The interfacial contact between the PEDOT:PSS and the electrode delaminates due to oxidation and absorption of water vapor [28–31]. Most of the residual oxygen and moisture during processing result in primary damage [25]. Mechanical stresses develop due to the bending/handling of solar modules. Hotspots were also evident in some cases resulting in electrical stresses. These stresses result in variation in the performance of the flexible devices [32–34].

As all the above discussed factors affecting the lifetime performance of the device are interlinked, it is difficult to clearly determine the actual degradation mechanism. In order to choose an appropriate encapsulant for the organic photovoltaic device, it is required to understand the cause for degradation and its mechanism. Internal factors affecting the performance of these devices include interfacial stability, active layer, and morphology which could be overcome by appropriate design and engineering of the device. The external factors are related to the ingress of moisture, oxygen, and UV radiation. The detrimental effects due to external factors can be subdued if the OPV device is encapsulated by an ultra-high barrier material. The barrier coating/composite/layered film used for device encapsulation must be able to restrict the diffusion of permeating molecules through the barrier material which initiate/increase the intrinsic/extrinsic degradation and filter UV light.

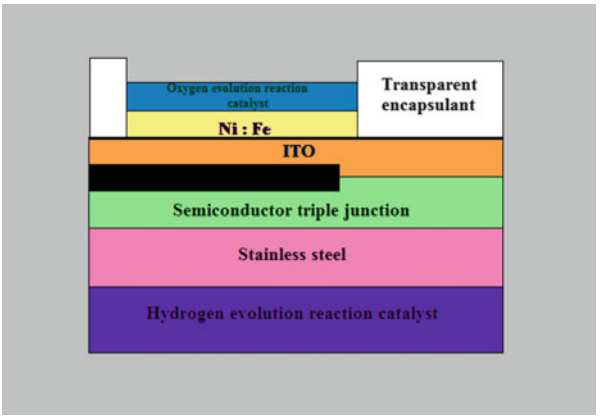

Fig. 2 Basic schematic of encapsulated photo electrode for water splitting reaction

The semiconductor photoelectrodes (schematic given in Fig. 2), photosensitive dyes (synthetic pigments and complexes), and other nano materials used for photocatalytic water splitting are prone to degradation either due to UV radiation or environmental deterrents. Hence, a suitable non-corrosive (on exposure to electrolyte), nonconducting, highly transparent barrier material is required for encapsulation of the device [35, 36].

4 Encapsulation of Solar Devices

The major applications of solar devices involve conformal coatings, battery charging, and solar lighting for domestic applications, automobile applications, as well as wireless instrumentation applications and wearable power devices on clothing, unmanned aerial vehicles for defense applications. Therefore, the barrier material should possess some of the crucial properties which help the effective functioning of these devices to be used in the previously discussed specific applications:

1. *Flexibility*: Encapsulant material must be flexible enough, along with the device substrate without the formation of cracks
2. *Hermetic*: It must be possible to seal the device completely isolating from external environment, protecting from external deterrents of degradation like O_2, H_2O, chlorofluorocarbons, and UV light
3. *Ultra low gas permeability*: The encapsulant should provide sufficient barrier to penetrating gases like oxygen and moisture
4. *Stability*: The encapsulant must be dimensionally, chemically (non-corrosive), thermally, and electrically stable
5. *Ease of processing*: Processing compatibility with the final product for integration is a major requirement in terms of energy and economy minimization

Hence, in order to satisfy these specific requirements various organic and inorganic materials are being investigated for their use as encapsulants. As the present conventional methods cannot measure below 10^{-4} g/m^2/day for WVTR, suitable techniques for determining ultra low permeabilities have to be explored.

5 Characterization of Barrier Properties of Encapsulants

Available techniques to determine WVTR through the barrier films are discussed in this section:

1. Gravimetric-based technique
2. Capacitance/resistance/coulometric moisture sensor-based measurement
3. Tritium-based radioactive technique
4. Optical/electrical calcium degradation test
5. Spectroscopy-based techniques

1. *Gravimetric-based technique*: ASTM E96/E96M–12 technique includes two basic methods, the desiccant method and the water method. The sample to be tested is placed in between two cells with different humid conditions in both the cases. The variation is in the service conditions on the high humidity (wetted) and the low humidity sides of the specimen. In the desiccant method, the sample is sealed on the top of the test cell with a dry desiccant and the setup is placed in a controlled humid environment. Anhydrous calcium chloride is used as the desiccant. Periodically, the weight of the desiccant is determined to measure the WVTR through the sealed test cell. In the water method, the test cell contains distilled water instead of the desiccant and the periodic weights determine the WVTR through the specimen from the water to the controlled atmosphere [37, 38].

In ASTM E398–03 dynamic relative humidity method, the sample is mounted between two chambers with variation in humidity. After conditioning and isolation of the chamber, the rate at which the transmission of moisture increases is measured within the relatively lower relative humidity chamber over a predetermined range of interest. This rate is further compared to the WVTR of a calibration sample, which is calibrated gravimetrically initially to determine the WVTR of the barrier sample [39]. In another method, the dried sample film is placed in a controlled humid environment and then transferred to the test cell which is equipped with a halogen lamp. The heating of the sample releases moisture and the amount is measured gravimetrically [40]. However, these techniques based on gravimetry cannot be used for reliably for determining WVTRs below 1 g/m^2/day.

2. *Capacitance/resistance/coulometric moisture sensor-based measurement*: In this technique, the sample is placed in between two chambers of a test cell with different, controlled humid environments. The water vapor is transmitted through the sample due to the relative difference in pressure or concentration of humidity on either side of the sample film. Thus, the WVTR from higher humid condition to lower humid condition is sensed by using a capacitive/resistive/coulometric-based

humidity measurement sensor. Even when the initial sensitivity of the sensors is good, the saturation of these sensors due to oxide layer formation cannot fulfil long time accurate measurements [41–43]. In commercialized techniques like MOCON, Permatran, and Aquatran techniques, coulometric sensors are used where the change in concentration of the analyte is used for sensing. Theoretical limits of measurement are very low but practical values of about ~10^{-3} g/m^2/day have only been achieved till date.

3. *Tritium-based radioactive technique*: In this technique, H_2O doped with Tritium is used on one side of the test material. The transmitted HTO is monitored with time to determine the WVTR. Two methods are used for quantification of HTO. The permeated HTO is swept with a carrier gas to an ionization chamber. In the other case, HTO is collected by a hygroscopic salt and then analyzed for the tritium concentration by scintillation. Though these radioactive-based techniques can be used for WVTRs in the range of ~10^{-6} g/m^2/day, they are not economical, environmental friendly and it is not possible to differentiate the signals due to permeated elemental tritium and HTO [44].

4. *Optical/electrical calcium degradation test*: In the calcium degradation test to determine the WVTR, calcium is deposited onto a clean, highly impermeable substrate like glass. Stable metal electrodes like aluminum, silver, or gold are deposited to provide electrical contact for measuring the resistance of calcium, as shown in the schematic. Then the calcium on the substrate is sealed with the sample barrier films to be tested using a sealant/glue over the edges. The sealed calcium-based moisture sensing device is placed in an environmental chamber with controllable temperature and humidity. The water vapor permeates through the barrier film and reacts with calcium deposited on the substrate. This results in the change of optical transmittance, as determined from optical microscopy and an increase of resistance (R) which can be measured as a function of time (t) using a programmable digital multimeter. When calcium reacts with moisture, the thickness of calcium deposited decreases with time, when uniform surface oxidation of the calcium thin film is assumed. Hence the measured transmittance/resistance of calcium film varies with time as it gets oxidized and this change in optical/electrical property is correlated to the change in thickness, which further gives the value of WVTR [45, 46].

In optical calcium degradation test, optical images are saved periodically using an optical microscope from which oxidized areas are estimated. Quantification based on visual analysis cannot be as exact as in the electrical calcium test (Fig. 3).

In electrical calcium degradation test, the change in thickness results in change of resistance which gives the amount of calcium reacted [47]. The resistivity of calcium (ρ) is independent of calcium film thickness only above 100 nm [48]. Hence, the change in resistance, over the calcium thickness variation from an initial thickness of h to 100 nm is used for calculation. As one molecule of calcium can react with two molecules of H_2O forming $Ca(OH)_2$, the water vapor permeated through the barrier film over calcium is determined using Eq. (2) where molecular weight of water is M_{H_2O} (18) and that of calcium is M_{Ca} (40). If the

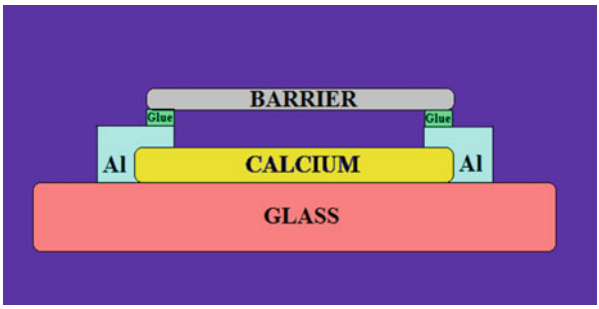

Fig. 3 Schematic for calcium degradation test

density of calcium is ∂ for a film thickness of h, with deposition area being l × b, the WVTR through the sealed barrier film is given by:

$$\mathrm{WVTR} = -2\frac{M_{\mathrm{H_2O}}}{M_{\mathrm{Ca}}}\partial\rho\left(\frac{1}{b}\right)\frac{\mathrm{d}(1/R)}{\mathrm{d}t} \tag{1}$$

WVTR in the range ~10^{-5} g/m^2/day can be determined using this method. However, the assumption of uniform oxidation of calcium, permeability through the glue used for sealing and constant resistivity of calcium, which changes with film thickness, limit the long-term testing of the material for barrier property.

5. *Spectroscopy-based techniques*: In infrared sensor-based technique, ASTM F1249–06, the dry side is separated from the wet side of the test chamber both of which are under controlled conditions of temperature and humidity by the sample barrier material to be tested. The water vapor passing through the sample film from wet to dry side of the diffusion cell is carried to a pressure-modulated infrared sensor. The fraction of infrared energy absorbed by the water vapor is measured by the sensor and an electrical signal is produced, whose amplitude is proportional to water vapor concentration. This amplitude is then compared to the signal produced by the initial measurement of a calibration film of known WVTR, from which the value of transmission rate is determined for the sample film [49]. WVTR values up to 10^{-3} g/m^2/day have been determined using this method.

In mass spectroscopic-based measurement technique, the sample to be tested is mounted onto a diffusion cell where both sides of the film are evacuated. One side of the sample is exposed to a constant flow of water vapor at constant pressure. The water vapor permeated through the film is swept by inert flow gas to a gas chromatogram for water vapor quantification [50, 51]. Even though the lower limit of detection for WVTR is ~10^{-6} g/m^2/day, the system is complex (with leak-free chambers) and is not economical.

Oxygen transmission rate: There are three major techniques by which oxygen permeated through the barrier film material can be determined:

1. Coulometric-based technique
2. Calcium degradation test
3. ASTM 3985

1. *Coulometric-based technique*: OTR is primarily determined by using a coulometric sensor similar to the procedure discussed previously for determining WVTR. This method can be used by following two procedures; one is a manometric method where pressure difference is maintained and the other is a volumetric method where concentration difference is maintained with no difference in total pressures on either side of the film [52].

2. *Calcium degradation test*: The setup for calcium degradation test is the same as used for WVTR determination. Instead of placing the sealed calcium device in a humid environment, it is placed in oxygen environment with controllable humid conditions. The change in resistance gives the amount of calcium reacted with oxygen which finally gives OTR through the sealed test film [46].

$$\mathrm{WVTR} = -0.5\frac{M_{\mathrm{O}_2}}{M_{\mathrm{Ca}}}\partial\rho\left(\frac{1}{b}\right)\frac{\mathrm{d}(1/R)}{\mathrm{d}t} \tag{2}$$

3. *ASTM 3985*: This method is for determining oxygen vapor barrier measurement of flexible materials, which is under validation by ASTM. It is very similar to the ASTM 1249 method and apparatus as previously discussed except that it has a micro fuel cell with oxygen sensor instead of humidity sensor [53].

5.1 Materials for Encapsulation

In order to design the encapsulant requirement for organic-based devices, basic differences between the permeation mechanisms through organic and inorganic materials must be discussed. The inorganic thin film materials offer high barrier towards permeant penetration. The presence of defect sites and the pin holes in the homogeneous thin film provide the pathway for the penetrant. But in the case of organic materials like polymers, permeation of gases/vapors follows standard mechanism of solution-diffusion. The permeant first gets adsorbed onto the surface and then dissolve in the polymer matrix. The available free volume between the molecular chains, provide the pathway for diffusion of the dissolved permeant. Then the permeant is desorbed on the other end of the polymer.

Therefore, defect-free inorganic thin films materials are brittle, and are not crack resistant even though they offer high barrier towards moisture permeation. Organic polymer encapsulants are suitable in terms of flexibility, processability, and conformability. But the permeation rates of gases through polymers are quite higher. Hence, a combination of both organic and inorganic materials has been the choice to meet the requirement of flexibility as well as high gas barrier in multilayered architecture as it provides redundancy and tortuosity. Various approaches for organic solar device encapsulation by single layered/curing/composite/multilayered films, etc. have been used by various research groups.

Hence, alternate coatings of inorganic and organic materials have been chosen as an apt solution for retaining the barrier property of inorganic material as well as the flexibility and crack resistance of organic material. The inorganic oxides were coated onto polymeric substrates by either physical or chemical vapor deposition techniques in layer-by-layer method to achieve ultra low permeabilities. In this technique, the base film surface quality is critical for inorganic oxide deposition to achieve defect-free thin film and much higher barrier.

1-(3-methoxycarbonyl) propyl-1-phenyl[6,6]C61 (PCBM)-based solar cells were encapsulated using a flexible and transparent poly(ethylene naphthalate) (PEN)-based ultra-high barrier material which is fabricated by plasma enhanced chemical vapor deposition (PECVD). Five inorganic and organic bilayers, SiO_x and PECVD-deposited organosilicon, were grown sequentially on the PEN film, which resulted in about 500 nm thick layer. This encapsulation raised the shelf lifetime by 50 % of the initial efficiency of solar cells from tens of hours to beyond 3,000 h [54]. Barrier material based on alternate coatings of polyacrylate/Al_2O_3 was used for organic device encapsulation. It followed a multistep process where organic monomer is flash evaporated, cured by incident UV radiation and then coating of inorganic material on organic layer by reactive sputtering. A WVTR of 2×10^{-6} g/m^2/day at 20 °C and 50 % RH was achieved from calcium degradation test of the barrier material [55, 56]. Similarly in another work, barrier material was fabricated by atomic layer deposition (ALD) of Al_2O_3 onto a PEN substrate, which showed a WVTR of 1.7×10^{-5} g/m^2/day at 38 °C and 85 % relative humidity (RH) [57]. SiO_x/Al_2O_3/parylene layers were used for device encapsulation where WVTR was found to be ~10^{-5} g/m^2/day [58]. Series of organic and inorganic layers were used in Barix™, Vitex technology, assuming the offset of defects due to the presence of organic layer over inorganic oxides [59]. Hermenau and group used different encapsulations for small molecule organic solar cells and observed that a loss of 50 % of initial efficiency is observed when 0.01 g/m^2 water entered the device either through the encapsulant or the electrode. PET with 245 nm sputtered ZTO had shown the better performance next to the glass-encapsulated device [60].

Diamond like amorphous carbon was used by high energy sputter deposition along with silicon and oxygen over polymer substrates with multilayered architecture for encapsulating organic devices [61]. Polymer multilayered stacks were used along with nitride, oxide, and oxy-nitride layers over a PET substrate for achieving WVTR < 0.005 g/m^2/day [62]. Deposition of inorganic oxides like SiO_2, AlO_x by techniques like ALD, thermal co-evaporation, sputtering, PECVD techniques can be used for OPV encapsulation, as discussed above. Defects caused by particles and surface imperfections were found to have major detrimental effect on the barrier properties in such multilayered coatings [63]. A model was proposed for defect-mediated permeation in oxide-coated gas barrier films. This model accounts for diffusion through the amorphous inorganic oxide lattice, nano-defects within the lattice, and macro-defects. Even though no defects could be detected from microscopic measurements, the permeation data through the barrier films indicate the presence of defects. It was estimated that macro-defects (>1 nm), nano-defects (0.3–0.4 nm), and the lattice interstices (<0.3 nm) exist in such coatings and all of

them contribute to the total permeation [64]. However, due to the presence of pinholes and defects in these inorganic layers, they could not suffice the need for ultra low permeable material. Moreover, the deposition techniques are quite expensive and lack scalability. Hence, alternate materials with simplified, economic processing methodology are still a major requirement.

Polymer nanocomposites and blends are used as conventional encapsulants in food and pharmaceutical industries. But they are not sufficient for being used for organic solar device encapsulation. Generally various inorganic micro- and nano fillers are used in the polymer to increase the permeation pathway. As the permeation through polymers follows the solution-diffusion mechanism, the choice of the matrix polymer and the filler material determines the solubility of H_2O in the composite and the geometry of the filler determines the diffusion pathway. Moreover, the filler and polymer can be chosen in such a way that would decrease the free volume available for permeant penetration through the composite if they interact favorably. Nano platelet-structured morphologies of the fillers with parallel orientation to the film in the composite would provide more tortuous pathway for the permeant to penetrate. Generally composites are prepared by solution casting, blending, or in situ polymerization techniques, which are more energy intensive as compared to physical and chemical vapor deposition, sputtering-based encapsulation techniques. Further, various composite films can be used in multilayered architecture to achieve further reduction in permeability.

The optimization of sodium-montmorillonite clay (MMT–Na) content in poly (vinyl alcohol) (PVA) nanocomposite to obtain the properties required for organic solar cell encapsulation was discussed. These nanocomposites were fabricated by following an environmentally friendly processing of aqueous solution by casting technique. The nanocomposite layer was used for encapsulating organic solar cells and the increased device stability was observed [65]. Saran-based boron nitride nanotube composites were reported as barrier material for OPV devices [66].

Functionalized acrylic UV curable hard coat materials with silane functionalized silica particles were discussed for solar cell encapsulation with a WVTR of 10^{-1} g/m^2/day [67]. The use of polyurethane as encapsulant for polymer solar cells has been explored in eight different countries in different weather conditions. Reduction in degradation of the performance of solar device was observed. The average efficiencies with at least 40 % of the initial values were observed up to 4½ months of outdoor exposure [68].

Polymer nanocomposites were fabricated using SiO_2, Al_2O_3, and ZnO as filler materials in different polymer matrices for their use as OPV encapsulants. Nano SiO_2 and Al_2O_3 were functionalized by coupling with different siloxane functional groups to increase the compatibility with the polymer [69–71]. PVA/ZnO-based composite was optimized for barrier property from calcium degradation test and organic device encapsulation results. Encapsulation with this optimized composite material improved the device lifetime by four times compared to the lifetime of non-encapsulated organic device [72].

The presence of interactions between the filler and the polymer results in better compatibility and decreases the free volume availability in polymer composites.

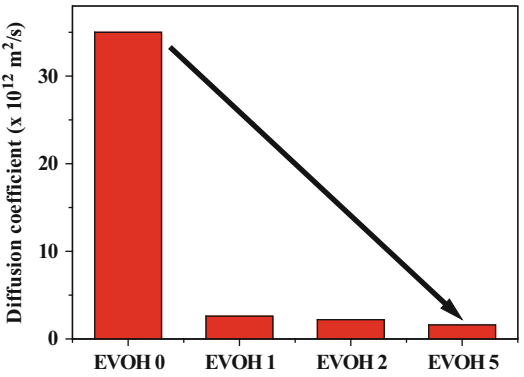

Fig. 4 Decreasing trend of coefficient of diffusivities for water vapor through the neat polymer (EVOH 0) and composite (EVOH 1, 2, 5 compositions represent 1, 2, and 5 wt% of MMT in EVOH, respectively) films

Filler materials like clays with platelet geometry offer longer diffusion pathway to the permeant through the polymer than compared to one dimensional fillers. Clays are arranged as stacked sheets and hence the gallery spacing between the layers determine the diffusion pathway. When they are intercalated or exfoliated, the gallery spacing between the sheets increase and thus provide a more tortuous pathway to the penetrant through the polymer composite. Therefore, gallery spacing is higher in organically functionalized clays.

Poly (ethylene-co-vinyl alcohol) (EVOH)-based nanocomposite barrier films with dispersed montmorillonite clay surface modified with octadecylamine (15–35 wt%) and aminopropyltriethoxysilane (0.5–5 wt%) (MMT) were fabricated by solution casting technique. Due to the hydrogen bond and van der Waals interactions in the EVOH/MMT composite, helped forming a strongly interacting composite decreasing the available free volume for permeation and increasing the permeation barrier. The coefficient of diffusion for water vapor as determined from calcium degradation test decreased by more than one order for the composite material than that of the neat polymer (Fig. 4). These EVOH/MMT composite films exhibited WVTR in the order of 10^{-3} g/m^2/day. Moreover, the composite-encapsulated P3HT-based Schottky devices exhibited lifetimes that were ten times higher than the neat polymer-encapsulated devices [73].

Blending of two different polymers can be devised effectively to attain high barrier material. Two copolymers, namely poly (ethylene-co-methacrylic acid) (PEMA) and EVOH were melt blended with PEMA as the base component. Both the copolymers used for blending are capable of forming hydrogen bonds with permeating H_2O molecules. This helps in providing a strongly interacting environment for water molecules. The blend of ionomer and copolymer is compatible, because of the electrostatic interactions as well as hydrogen bonding, resulting in an interacting complex blend. These interactions decreased the free volume available for permeation (Fig. 5). Moreover, the theoretical molecular dynamics simulations have shown that the intersegmental motion of the polymer chains decreased in case of the blend system compared to that observed in the neat system. Hence, these blend films showed much lower permeability values (Fig. 6) towards moisture with WVTR of 10^{-4} g/m^2/day than the neat polymer films. The diffusivity of H_2O

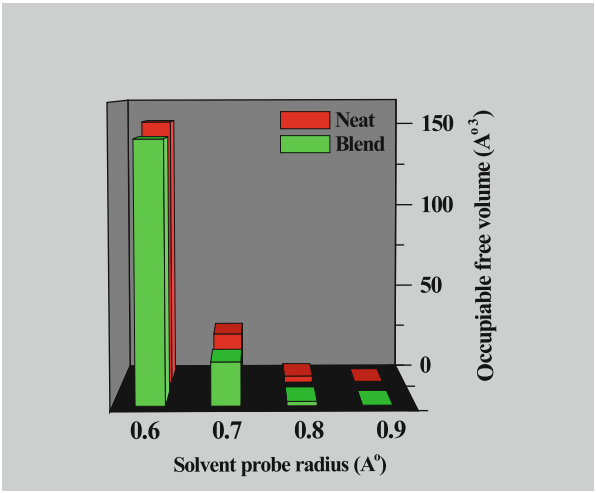

Fig. 5 Occupiable free volume of a unit cell of 340 Å^3 for the neat PEMA and the blend system (10 wt % of EVOH in PEMA) with different solvent probe radii as determined from molecular dynamics simulations

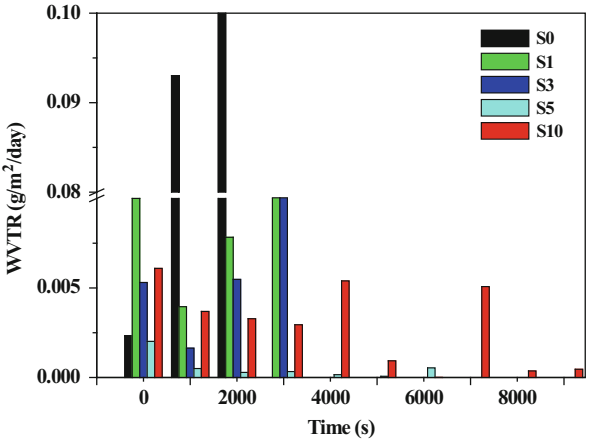

Fig. 6 WVTR for the neat PEMA (S0) and blend films (S1, 3, 5, 10 represent 1, 3, 5, and 10 wt% of EVOH in PEMA, respectively) calculated from calcium degradation test

decreased in the case of blend composition as determined from molecular dynamics simulations. The lifetimes of the encapsulated P3HT (also used in solar cells)-based Schottky organic devices increased by more than 20 times compared to the bare device [74].

Though, polymer-based composites and blends could not satisfy the barrier property as a single layer, the barrier property could further be improved when used as multilayered films. Moreover these organic-based encapsulants fabricated by simple processing techniques by casting, blending, etc. offer better economic solution as well as scalability for roll processing as compared to inorganic atomic layer, chemical vapor deposition techniques. Theoretical understanding and practical characterization of the interactions between the filler and the matrix in the

composite at the atomistic level would provide a better solution to design the barrier material satisfying all the requirements of an encapsulant for organic devices.

Sputter-deposited TiO_2 has been used as the transparent encapsulant for photoelectrode in solar-based water splitting application. Due to the change in potentials of the TiO_2 surfaces, oxygen evolution and other active corrosion reactions were observed. Hence, it was replaced with Master Bond polymer system EP39-2, a transparent epoxy polymer, which was designed specifically for electronics packaging application. It was found that it has good stability in KOH and was compatible with traditional printing techniques [75]. It can be conformally coated onto the planar photoelectrode structure, as required for water splitting applications. Therefore, polymeric encapsulants must be suitable for photoelectrode encapsulation application over inorganic materials.

6 Conclusions

The effective working of the solar photovoltaic device requires an effective encapsulant layer for protecting it from detrimental factors. The efficient functioning of the photoelectrodes used in solar-based water splitting technologies requires a non-corrosive, stable encapsulant. Of the various materials that have been explored so far, while some exhibit sufficient barrier to WVTR, they are difficult to process and are not economical. Therefore, various materials that are potential encapsulants are discussed. The characterization of the barrier property for WVTR and OTR is another issue for designing encapsulant materials with ultra-high barrier. Various techniques that are available for determining WVTR and OTR are discussed.

Acknowledgements This work is supported in part under the US-India Partnership to Advance Clean Energy-Research (PACE-R) for the Solar Energy Research Institute for India and the United States (SERIIUS), funded jointly by the US Department of Energy (Office of Science, Office of Basic Energy Sciences, and Energy Efficiency and Renewable Energy, Solar Energy Technology Program, under Subcontract DE-AC36-08GO28308 to the National Renewable Energy Laboratory, Golden, Colorado) and the Government of India, through the Department of Science and Technology under Subcontract IUSSTF/JCERDC-SERIIUS/2012 dated 22nd Nov. 2012.

References

1. International Energy Outlook 2013, US Energy Information and Administration. Retrieved from http://www.eia.gov/forecasts/ieo/pdf/0484(2013).pdf
2. Hammarström, L., & Hammes-Schiffer, S. (2009). Artificial Photosynthesis and Solar Fuels. *Accounts of Chemical Research, 42*(12), 1859-1860. doi: 10.1021/ar900267k
3. Brabec, C. J., Hauch, J. A., Schilinsky, P., & Waldauf, C. (2005). Production Aspects of Organic Photovoltaics and Their Impact on the Commercialization of Devices. *MRS Bulletin, 30*(01), 50-52.

4. K. Zweibel, (2005). The terawatt challenge for thin film PV. *NREL*, National Renewable Energy Laboratory.
5. Kaltenbrunner, M., White, M. S., Głowacki, E. D., Sekitani, T., Someya, T., Sariciftci, N. S., & Bauer, S. (2012). Ultrathin and lightweight organic solar cells with high flexibility. *Nat Commun, 3*, 770.
6. Editorial article, (2013). Plastic Fantastic. Nature, *499*, 379. http://www.nature.com/news/plastic-fantastic-1.13429
7. Pagliaro, M., Ciriminna, R., & Palmisano, G. (2008). Flexible Solar Cells. *ChemSusChem, 1* (11), 880-891. doi: 10.1002/cssc.200800127
8. Heo, J. H., Im, S. H., Noh, J. H., Mandal, T. N., Lim, C. S., Chang, J. A., Seok, S. I. (2013). Efficient inorganic–organic hybrid heterojunction solar cells containing perovskite compound and polymeric hole conductors. *Nat Photon, 7*(6), 486–491. doi: 10.1038/nphoton.2013.80
9. Azzopardi, B., Emmott, C. J. M., Urbina, A., Krebs, F. C., Mutale, J., & Nelson, J. (2011). Economic assessment of solar electricity production from organic-based photovoltaic modules in a domestic environment. *Energy & Environmental Science, 4*(10), 3741–3753. doi: 10.1039/C1EE01766G
10. Tryk, D. A., Fujishima, A., & Honda, K. (2000). Recent topics in photoelectrochemistry: achievements and future prospects. *Electrochimica Acta, 45*(15–16), 2363-2376. http://dx.doi.org/10.1016/S0013-4686(00)00337-6
11. Peike, C., Hulsmann, P., Matthias, B., Philipp, S., Karl-Anders, W. & Michael, K. (2012). Impact of Permeation Properties and Backsheet-Encapsulant Interactions on the Reliability of PV Modules. *ISRN Renewable Energy, 2012*, 5. doi: 10.5402/2012/459731
12. Chopra, K. L., Das, S. R. (1983). In *Thin Film Solar Cells: Degradation and Encapsulation of Solar Cells* (pp. 549-559).
13. Brabec, C. J., Gowrisanker, S., Halls, J. J. M., Laird, D., Jia, S., & Williams, S. P. (2010). Polymer–Fullerene Bulk-Heterojunction Solar Cells. *Advanced Materials, 22*(34), 3839-3856. doi: 10.1002/adma.200903697
14. Dang, M. T., Hirsch, L., & Wantz, G. (2011). P3HT:PCBM, Best Seller in Polymer Photovoltaic Research. *Advanced Materials, 23*(31), 3597-3602. doi: 10.1002/adma.201100792
15. Dennler, G., Lungenschmied, C., Neugebauer, H., Sariciftci, N. S., & Labouret, A. (2005). Flexible, conjugated polymer-fullerene-based bulk-heterojunction solar cells: Basics, encapsulation, and integration. *Journal of Materials Research, 20*(12), 3224-3233. doi: 10.1557/jmr.2005.0399
16. Krebs, F. C. (2006). Encapsulation of polymer photovoltaic prototypes. *Solar Energy Materials and Solar Cells, 90*(20), 3633-3643. http://dx.doi.org/10.1016/j.solmat.2006.06.055
17. Manceau, M., Rivaton, A., Gardette, J.-L., Guillerez, S., & Lemaître, N. (2009). The mechanism of photo- and thermooxidation of poly(3-hexylthiophene) (P3HT) reconsidered. *Polymer Degradation and Stability, 94*(6), 898-907. http://dx.doi.org/10.1016/j.polymdegradstab.2009.03.005
18. Hintz, H., Egelhaaf, H. J., Lüer, L., Hauch, J., Peisert, H., & Chassé, T. (2010). Photodegradation of P3HT—A Systematic Study of Environmental Factors. *Chemistry of Materials, 23*(2), 145-154. doi: 10.1021/cm102373k
19. Shaheen, S. E., Brabec, C. J., Sariciftci, N. S., Padinger, F., Fromherz, T., & Hummelen, J. C. (2001). 2.5% efficient organic plastic solar cells. *Applied Physics Letters, 78*(6), 841-843.
20. Schilinsky, P., Waldauf, C., & Brabec, C. J. (2002). Recombination and loss analysis in polythiophene based bulk heterojunction photodetectors. *Applied Physics Letters, 81*(20), 3885-3887.
21. Li, G., Shrotriya, V., Huang, J., Yao, Y., Moriarty, T., Emery, K., & Yang, Y. (2005). High-efficiency solution processable polymer photovoltaic cells by self-organization of polymer blends. *Nat Mater, 4*(11), 864-868.
22. Reese, M. O., Nardes, A. M., Rupert, B. L., Larsen, R. E., Olson, D. C., Lloyd, M. T., . . . Kopidakis, N. (2010). Photoinduced Degradation of Polymer and Polymer–Fullerene Active

Layers: Experiment and Theory. *Advanced Functional Materials, 20*(20), 3476-3483. doi: 10.1002/adfm.201001079
23. Tromholt, T., Manceau, M., Helgesen, M., Carlé, J. E., & Krebs, F. C. (2011). Degradation of semiconducting polymers by concentrated sunlight. *Solar Energy Materials and Solar Cells, 95*(5), 1308-1314. http://dx.doi.org/10.1016/j.solmat.2010.09.022
24. Reese, M. O., Morfa, A. J., White, M. S., Kopidakis, N., Shaheen, S. E., Rumbles, G., & Ginley, D. S. (2008). Pathways for the degradation of organic photovoltaic P3HT:PCBM based devices. *Solar Energy Materials and Solar Cells, 92*(7), 746-752. http://dx.doi.org/10.1016/j.solmat.2008.01.020
25. Norrman, K., Larsen, N. B., & Krebs, F. C. (2006). Lifetimes of organic photovoltaics: Combining chemical and physical characterisation techniques to study degradation mechanisms. *Solar Energy Materials and Solar Cells, 90*(17), 2793-2814. http://dx.doi.org/10.1016/j.solmat.2006.04.009
26. Norrman, K., Gevorgyan, S. A., & Krebs, F. C. (2008). Water-Induced Degradation of Polymer Solar Cells Studied by H218O Labeling. *ACS Applied Materials & Interfaces, 1*(1), 102-112. doi: 10.1021/am800039w
27. Yang, X., & Loos, J. (2007). Toward High-Performance Polymer Solar Cells: The Importance of Morphology Control. *Macromolecules, 40*(5), 1353-1362. doi: 10.1021/ma0618732
28. Kawano, K., Pacios, R., Poplavskyy, D., Nelson, J., Bradley, D. D. C., & Durrant, J. R. (2006). Degradation of organic solar cells due to air exposure. *Solar Energy Materials and Solar Cells, 90*(20), 3520-3530. http://dx.doi.org/10.1016/j.solmat.2006.06.041
29. Sharma, A., Watkins, S. E., Lewis, D. A., & Andersson, G. (2011). Effect of indium and tin contamination on the efficiency and electronic properties of organic bulk hetero-junction solar cells. *Solar Energy Materials and Solar Cells, 95*(12), 3251-3255. http://dx.doi.org/10.1016/j.solmat.2011.07.012
30. Hauch, J. A., Schilinsky, P., Choulis, S. A., Rajoelson, S., & Brabec, C. J. (2008). The impact of water vapor transmission rate on the lifetime of flexible polymer solar cells. *Applied Physics Letters, 93*(10), 103306-103303.
31. de Jong, M. P., van Ijzendoorn, L. J., & de Voigt, M. J. A. (2000). Stability of the interface between indium-tin-oxide and poly(3,4-ethylenedioxythiophene)/poly(styrenesulfonate) in polymer light-emitting diodes. *Applied Physics Letters, 77*(14), 2255-2257.
32. Grossiord, N., Kroon, J. M., Andriessen, R., & Blom, P. W. M. (2012). Degradation mechanisms in organic photovoltaic devices. *Organic Electronics, 13*(3), 432-456. http://dx.doi.org/10.1016/j.orgel.2011.11.027
33. Reese, M. O., White, M. S., Rumbles, G., Ginley, D. S., & Shaheen, S. E. (2008). Optimal negative electrodes for poly(3-hexylthiophene): [6,6]-phenyl C61-butyric acid methyl ester bulk heterojunction photovoltaic devices. *Applied Physics Letters, 92*(5), 053307-053303.
34. Lloyd, M. T., Olson, D. C., Lu, P., Fang, E., Moore, D. L., White, M. S., . . . Hsu, J. W. P. (2009). Impact of contact evolution on the shelf life of organic solar cells. *Journal of Materials Chemistry, 19*(41), 7638–7642. doi: 10.1039/B910213B
35. Miller, E. L., Rocheleau, R. E., & Deng, X. M. (2003). Design considerations for a hybrid amorphous silicon/photoelectrochemical multijunction cell for hydrogen production. *International Journal of Hydrogen Energy, 28*(6), 615-623. http://dx.doi.org/10.1016/S0360-3199(02)00144-1
36. E.L. Miller, R.E. Rocheleau, Photoelectrochemical hydrogen production, In: Proceedings of the 2000 U.S. Department of Energy Hydrogen Program Annual Review Meeting, San Ramon, California, U.S. Department of Energy, 2000.
37. Standard Test Methods for Water Vapor Transmission of Materials, ASTM E96/E96M–12, Annual Book of ASTM Standards, Vol. 04.06, The American Society for Testing and Materials.
38. N.D. Bornstein, L. Pike, A Gravimetric Calibration Procedure for Modern Controls IRD-2 Infrared Water Vapor Diffusometer and Its Correlation with Results from Test Methods E-96, ASTM STP 548, 1973, 20.

39. Standard Test Method for Water Vapor Transmission Rate of Sheet Materials Using Dynamic Relative Humidity Measurement, ASTM E398–03, Vol. 15.09, The American Society for Testing and Materials.
40. L. Paul, Measuring Instrument for Gravimetric Moisture Determination. US 7591169 B2, 2009.
41. AQUATRAN® Model: High Sensitivity Coulometric Water Vapor Transmission Rate Test System. Retrieved from http://www.mocon.com/pdf/brochures/Aquatran.pdf
42. C. Charton, N. S., M. Fahland, A. Hollander, A. Wedel, K. Noller. (2006). Development of high barrier films on flexible polymer substrates. *Thin Solid Films, 502*, 5. doi: 10.1016/j.tsf.2005.07.253
43. Taylor, S. R. (1989). Assessing the Moisture Barrier Properties of Polymeric Coatings Using Electrical and Electrochemical Methods. *IEEE Transactions on Electrical Insulation, 24*(5).
44. O'Brien, K. C., Koros, W. J., Barbari, T. A., & Sanders, E. S. (1986). A new technique for the measurement of multicomponent gas transport through polymeric films. *Journal of Membrane Science, 29*(3), 229-238. http://dx.doi.org/10.1016/S0376-7388(00)81262-4
45. Kempe, M. D., Reese, M. O., & Dameron, A. A. (2013). Evaluation of the sensitivity limits of water vapor transmission rate measurements using electrical calcium test. *Review of Scientific Instruments, 84*(2), 025109-025110.
46. Choi, J. H., Kim, Y. M., Park, Y. W., Huh, J. W., Ju, B. K., Kim, I. S., & Hwang, H. N. (2007). Evaluation of gas permeation barrier properties using electrical measurements of calcium degradation. *Review of Scientific Instruments, 78*(6), 064701-064705.
47. Kumar, R. S., Auch, M., Ou, E., Ewald, G., & Jin, C. S. (2002). Low moisture permeation measurement through polymer substrates for organic light emitting devices. *Thin Solid Films, 417*(1–2), 120-126. http://dx.doi.org/10.1016/S0040-6090(02)00584-9
48. Renucci, P., Gaudart, L., Petrakian, J. P., & Roux, D. (1982). Grain-boundary effect in calcium thin films. *Physical Review B, 26*(10), 5416-5425.
49. Test Method for Water Vapor Transmission Rate Through Plastic Film and Sheeting Using a Modulated Infrared Sensor, ASTM F1249-06,2011, The American Society for Testing and Materials.
50. Arrelaine A. Dameron, Matthew O. Reese, Michael Kempe, Thomas J. Moricone, Understanding moisture ingress and packaging requirements for photovoltaic modules, 2009.
51. Retrieved from http://www.vgs-plastic-electronics.com/pdfs/VG_Scienta_Vacutran_Brochure.pdf
52. The Standard for Oxygen Transmission Rate Testing of Flat Films & Finished Packages. Retrieved from http://www.mocon.com/pdf/brochures/oxtran/OX221%20Brochure%20Pages.pdf
53. D-3985 Test Method for Oxygen Transmission Rate Through Plastic Film and Sheeting Using a Coulometric Sensor, Annual Book of ASTM Standards, Vol. 15.09, The American Society for Testing and Materials.
54. Dennler, G., Lungenschmied, C., Neugebauer, H., Sariciftci, N. S., Latrèche, M., Czeremuszkin, G., & Wertheimer, M. R. (2006). A new encapsulation solution for flexible organic solar cells. *Thin Solid Films, 511–512*(0), 349-353. http://dx.doi.org/10.1016/j.tsf.2005.12.091
55. Affinito, J. D., Gross, M. E., Mounier, P. A., Shi, M. K., & Graff, G. L. (1999). *Ultrahigh rate, wide area, plasma polymerized films from high molecular weight/low vapor pressure liquid or solid monomer precursors*, Baltimore, Maryland (USA).
56. Dameron, A. A., Davidson, S. D., Burton, B. B., Carcia, P. F., McLean, R. S., & George, S. M. (2008). Gas Diffusion Barriers on Polymers Using Multilayers Fabricated by Al2O3 and Rapid SiO2 Atomic Layer Deposition. *The Journal of Physical Chemistry C, 112*(12), 4573-4580. doi: 10.1021/jp076866+
57. G. Nisato, M. Kuilder, P. Bouten, L. Moro, O. Philips, and N. Rutherford, *Society for Information Display, 2003 International Symposium*, Digest of Technical Papers, 2003, Vol. XXXIV, p. 88.

58. Carcia, P. F., McLean, R. S., Reilly, M. H., Groner, M. D., & George, S. M. (2006). Ca test of Al_2O_3 gas diffusion barriers grown by atomic layer deposition on polymers. *Applied Physics Letters, 89*(3), 031915-031913.
59. Robert, J. V. Barix, Multilayers: a Water and Oxygen Barrier for Flexible Organic Electronics. Retrieved from http://www.mitstanfordberkeleynano.org/events_past/0504%20-%20Organic%20Electronics/5%20-%20Nanoforum050422a.pdf
60. Hermenau, M., Scholz, S., Leo, K., & Riede, M. (2011). Total charge amount as indicator for the degradation of small molecule organic solar cells. *Solar Energy Materials and Solar Cells, 95*(5), 1278-1283. http://dx.doi.org/10.1016/j.solmat.2010.09.031
61. Fred B. McCormick, Moses M. David, Mark A.Roehrig, Manoj Nirmal, US patent, US 2008/0006819 A1, 3M Innovative Properties Company, USA.
62. Gordon Lee Graff, Mark Edward Gross, Ming Kun Shi, Michael Gene Hall, Peter MAclyn Martin, Eric Sidney Mast, US patent, US 6,413,645 B1, 2002.
63. Hermenau, M., Schubert, S., Klumbies, H., Fahlteich, J., Müller-Meskamp, L., Leo, K., & Riede, M. (2012). The effect of barrier performance on the lifetime of small-molecule organic solar cells. *Solar Energy Materials and Solar Cells, 97*(0), 102-108. http://dx.doi.org/10.1016/j.solmat.2011.09.026
64. Langowski, H. C., Moosheimer, U., Peukert, W., Hanika, M. (2003) Inorganic Layers on Polymeric Films—Influence of Defects and Morphology on Barrier Properties, *Chemical Engineering and Technology 26* (5) 605-614.
65. Gaume, J., Taviot-Gueho, C., Cros, S., Rivaton, A., Thérias, S., & Gardette, J.-L. (2012). Optimization of PVA clay nanocomposite for ultra-barrier multilayer encapsulation of organic solar cells. *Solar Energy Materials and Solar Cells, 99*(0), 240-249. http://dx.doi.org/10.1016/j.solmat.2011.12.005
66. Ravichandran, J., Manoj, A. G., Liu, J., Manna, I., Carroll, D. L. (2008). A novel polymer nanotube composite for photovoltaic packaging applications. *Nanotechnology, 19*(8) 5712. doi: 10.1088/0957-4484/19/8/085712
67. Philip Capps, Paul Adriani, James R Sheats US 2012/0090661 A1, Apr. 19, 2012.
68. Søndergaard, R. R., Makris, T., Lianos, P., Manor, A., Katz, E. A., Gong, W., Krebs, F. C. (2012). The use of polyurethane as encapsulating method for polymer solar cells—An inter laboratory study on outdoor stability in 8 countries. *Solar Energy Materials and Solar Cells, 99*(0), 292-300. http://dx.doi.org/10.1016/j.solmat.2011.12.013
69. Gupta, S., Ramamurthy, P. C., & Madras, G. (2011). Synthesis and characterization of flexible epoxy nanocomposites reinforced with amine functionalized alumina nanoparticles: a potential encapsulant for organic devices. *Polymer Chemistry, 2*(1), 221-228. doi: 10.1039/C0PY00270D
70. Gupta, S., Ramamurthy, P. C., & Madras, G. (2011). Covalent Grafting of Polydimethylsiloxane over Surface-Modified Alumina Nanoparticles. *Industrial & Engineering Chemistry Research, 50*(11), 6585-6593. doi: 10.1021/ie200283w
71. Gupta, S., Seethamraju, S., Ramamurthy, P. C., & Madras, G. (2013). Polyvinylbutyral Based Hybrid Organic/Inorganic Films as a Moisture Barrier Material. *Industrial & Engineering Chemistry Research, 52*(12), 4383-4394. doi: 10.1021/ie3022412
72. Gupta, S., Sindhu, S., Varman, K. A., Ramamurthy, P. C., & Madras, G. (2012). Hybrid nanocomposite films of polyvinyl alcohol and ZnO as interactive gas barrier layers for electronics device passivation. *RSC Advances, 2*(30), 11536-11543. doi: 10.1039/C2RA21714G
73. Seethamraju, S., Ramamurthy, P. C., & Madras, G. (2013). Flexible poly(vinyl alcohol-co-ethylene)/modified MMT moisture barrier composite for encapsulating organic devices. *RSC Advances, 3*(31), 12831-12838. doi: 10.1039/C3RA41557K
74. Seethamraju, S., Ramamurthy, P. C., & Madras, G. (2013). Ionomer Based Blend as Water Vapor Barrier Material for Organic Device Encapsulation. *ACS Applied Materials & Interfaces, 5*(10), 4409-4416. doi: 10.1021/am4007808
75. Eric Miller and Richard Rocheleau, Proceedings of the 2001 DOE Hydrogen Program Review, NREL/CP-570-30535.

Solar Photocatalytic Hydrogen Production: Current Status and Future Challenges

Jenny Schneider, Tarek A. Kandiel, and Detlef W. Bahnemann

Due to the increase of the worldwide demand for energy along with the global warming and the increasing level of atmospheric CO_2, solar hydrogen has been proposed as an optimal fuel as it can be produced from water using solar energy which emerges as the most promising energy source in terms of abundance and sustainability. So far, the main commercial process for producing molecular hydrogen is steam reforming of hydrocarbons which is, however, connected with a CO_2 emission disadvantage. Carbon-free hydrogen production can be achieved by water splitting employing an electrolyzer powered by photovoltaics, but a potentially more cost-effective route is to perform direct photocatalytic water splitting using semiconductor photocatalysts. Herein, the authors present the principles of this process, the maximum solar-to-hydrogen conversion efficiency, the most active photocatalysts reported so far and the challenges for the development of the optimum photocatalyst for the efficient release of hydrogen from water. Since the efficiency of the overall photocatalytic water splitting is still very low and the photocatalytic reforming of biomass compounds can be considered as an intermediate step between the current fossil fuel consumption and the dream for an efficient direct photocatalytic water splitting utilizing solar energy, the photocatalytic hydrogen production employing different so-called sacrificial reagents, i.e., electron donors, is also presented and discussed herein. Commonly, the system employing TiO_2 as the photocatalyst and methanol as the sacrificial reagent is investigated, thus, details concerning the possibility of enhancing the photocatalytic activity of this system as well as the current knowledge of the underlying mechanism are presented at the end of this chapter.

J. Schneider • D.W. Bahnemann
Photocatalysis and Nanotechnology Research Unit, Institute of Technical Chemistry, Leibniz University of Hannover, Callinstrasse 3, 30167 Hannover, Germany

T.A. Kandiel (✉)
Chemistry Department, Faculty of Science, Sohag University, Sohag 82524, Egypt
e-mail: kandiel@science.sohag.edu.eg

B. Viswanathan et al. (eds.), *Materials and Processes for Solar Fuel Production*, Nanostructure Science and Technology 174, DOI 10.1007/978-1-4939-1628-3_3

1 Introduction

Hydrogen is the most common element on earth, but it does not occur to a significant extent in its molecular form. It is mostly present bound to other atoms such as in water, in biomass, and in hydrocarbons. As far as technical processes are concerned, hydrogen gas is currently produced from a variety of primary sources, such as natural gas, naphtha, heavy oil, methanol, biomass, wastes, coal, solar energy, wind energy, hydropower, and nuclear energy [1]. It can be considered as a clean energy fuel since the chemical energy stored in the H–H bond is released when it reacts with molecular oxygen, e.g., in a fuel cell or upon incineration, forming water as the only reaction product. Accordingly, a future energy infrastructure based on H_2 is regarded as an ideal long-term solution to energy-related environmental problems. There is no doubt that molecular hydrogen has the potential to provide a clean and affordable energy supply that can minimize our dependence on oil and therefore reduce environmental pollution. It is generally understood that over the next 10–20 years all renewable energy-based processes for H_2 production (solar photochemical and photobiological water decomposition, electrolysis of water employing electricity generated by photovoltaic cells or wind turbines, etc.) are unlikely to generate significant reductions in hydrogen gas costs. Currently, the industrial production of hydrogen gas from fossil fuel amounts to 48 million tons globally each year [2]. Almost half of this amount of hydrogen is used for the synthesis of ammonia, while refineries use the second largest volume of hydrogen gas for chemical processes such as the removal of sulfur from gasoline and the conversion of heavy hydrocarbons into gasoline and diesel fuel. Food producers add a small percentage of hydrogen gas to some edible oils through a catalytic hydrogenation process. The demand for H_2 is expected to grow over the next 10 years, for both, these traditional uses and for alternative applications, e.g., for fuel cells. At least in the near future, this “thirst” for molecular hydrogen will have to be quenched primarily through the use of fossil fuels.

The industrially most widely used and most economical process for the production of hydrogen gas is steam methane reforming (SMR) [2]. Although SMR is a complex process involving many different catalytic steps, it will continue to be the technology of choice for the mass production of H_2, as long as natural gas (or CH_4) and hydrocarbon fuels remain at a low or even moderate price. Nonetheless, the use of fossil fuels will eventually have to be abandoned to ensure that the hydrogen economy will work in the future. One approach to reach this goal is to alternatively apply steam-reforming methods to renewable materials derived from crops. Not only would such biomass conversion schemes be able to turn waste into a valuable product, but, according to the current philosophy of many researchers there would be another benefit: any carbon dioxide released in these processes could be converted into the required biomass by planting new crops. Such a biomass strategy of hydrogen gas generation could be a useful intermediate step between the current fossil fuel method and the dream of efficient direct water splitting employing solar energy [2]. Moreover, in view of the high energy demand and the complexity

associated with all reforming processes, it is also of interest to explore photocatalysis as an alternative technology for the H_2 production from biomass-derived compounds, e.g., methanol, ethanol, or glycerol [3].

2 Photocatalytic H_2 Production from Water

2.1 Principle of Photocatalytic Water Splitting

Since the discovery of the photoelectrochemical (PEC) water splitting employing TiO_2 rutile single crystals electrode by Fujishima and Honda in 1972 [4], numerous studies, related to this finding, have been performed. As a result, excellent reviews summarizing the knowledge concerning the photocatalysis principle and its applications for water and air purification, organic synthesis, and hydrogen production have been published [5–7]. In the 1990s and also later, the photocatalysis research was focused mainly on environmental remediation applications leading to the development of various photocatalytically active materials now being available commercially. Recently, initiated by environmental problems and the interest to substitute nuclear as well as fossil energy utilization by that of regenerative energies, extensive research is being performed to produce solar hydrogen as an alternative fuel and thus many review articles have appeared summarizing the progress in this field [1, 8–13]. In fact, the overall water splitting for the production of molecular hydrogen using particulate photocatalysts has been examined since 1980 [14]. From the viewpoint of large-scale hydrogen gas production, particulate photocatalyst systems are sometimes considered to be advantageous over more complex multilayer or tandem structure devices and have been proposed to serve a wider range of potential applications. However, a suitable and economical method for the separation of the simultaneously produced H_2 and O_2 still remains to be developed. Therefore, traditional PEC devices employing semiconductor electrodes separated from the respective counter electrodes are an important option as this gas separation step is not required [4]. Thermodynamically, the overall water splitting is an uphill reaction with a large positive change in Gibbs free energy ($\Delta G^\circ = 237$ kJ mol^{-1}) [15]. Figure 1a presents a schematic illustration of the basic principle of the overall water splitting employing a heterogeneous photocatalyst. Upon irradiation with an energy equivalent to or greater than the bandgap energy of the semiconductor photocatalyst, electrons are excited from the valence into the conduction band, leaving holes behind in the valence band. These photogenerated electrons and holes are capable of initiating reduction and oxidation reactions, respectively. To achieve overall water splitting, the bottom of the conduction band must be located at a potential that is more negative than the reduction potential of H^+ to H_2 (0 V vs. NHE at pH 0), while the top of the valence band must be positioned more positively than the oxidation potential of H_2O to O_2 (1.23 V vs. NHE at pH 0). Therefore, the minimum photon energy thermodynamically

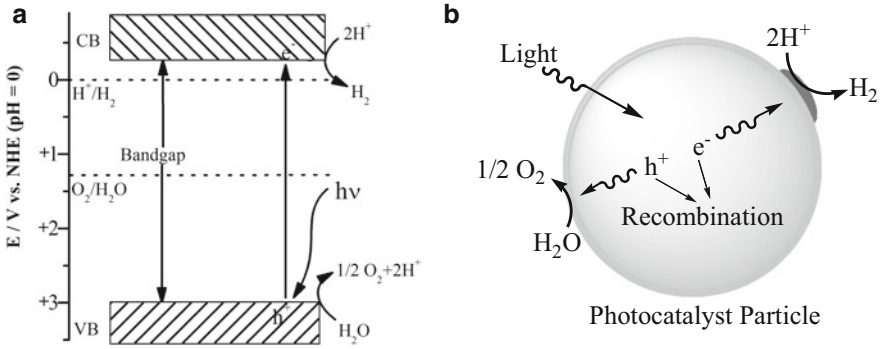

Fig. 1 Basic principles of the overall water splitting reactions employing a heterogeneous photocatalyst, e.g., TiO_2

required to drive the reaction is 1.23 eV, corresponding to a wavelength of ca. 1,000 nm, i.e., in the near-infrared region. Accordingly, it appears to be possible to utilize the entire visible spectral range for this process. However, there are activation barriers associated with both charge-transfer processes, necessitating photon energies exceeding 1.23 eV to drive the overall water splitting reaction at reasonable reaction rates. Thus, the minimum bandgap energy of a semiconductor that can be utilized for the water splitting process can be determined by the energy required to split water (1.23 eV) plus the thermodynamic losses (0.3–0.4 eV [16]) and the overpotentials that are required to generate O_2 and H_2 at various points in the system to ensure sufficiently fast reaction kinetics (0.4–0.6 eV) [17, 18]. Hence, the minimal bandgap energy required to achieve water splitting has been calculated to be at least 1.9 eV corresponding to a wavelength of ca. 650 nm. In addition, the backward reaction, that is, water formation from H_2 and O_2, must be strictly inhibited, and the photocatalysts themselves must be stable during the reaction. The main steps of the overall photocatalytic water splitting on a semiconductor photocatalyst are summarized in Fig. 1b. The photocatalyst absorbs photons the energy of which is greater than the semiconductor's bandgap energy thus generating electron/hole pairs in its bulk. Subsequently, the charge carriers can separate and migrate to the surface provided that their undesired recombination can be avoided.

Subsequently, surface adsorbed H_2O molecules are reduced and oxidized, respectively, by the photogenerated electrons and holes to produce H_2 and O_2, respectively. The first two steps in this reaction sequence, i.e., the e^-/h^+ generation and the charge carrier diffusion to the surface, are strongly dependent on the structural and electronic properties of the photocatalyst. In general, high crystallinity should have a positive effect on the activity since the density of defects, which act as recombination centers for photogenerated carriers, decreases with increasing crystallinity. The third step, on the other hand, usually requires the promotion by suitable co-catalysts. These co-catalysts are typically noble metals (e.g., Pt, Rh) or

metal oxides (e.g., NiO, RuO_2) and are often loaded onto the photocatalyst surface from the respective dispersions of nanoparticles. It is thus important to design both, the bulk and the surface properties of the light absorbing, semiconducting material carefully so as to obtain high photocatalytic activity for the overall water splitting reaction [15].

2.2 Solar-to-Hydrogen Conversion Efficiency

Unfortunately, the ideal photocatalyst for solar hydrogen production has not been discovered yet. In the following section the maximum theoretical solar-to-hydrogen (STH) conversion efficiency will be calculated. Figure 2 shows the distribution of the solar irradiance (in units of J s^{-1} m^{-2} nm^{-1}) at a global Air Mass of 1.5 (AM 1.5) as reported by the National Renewable Energy Laboratory (NREL) [19]. Utilizing this data, the number of photons at different wavelengths (J_λ) can readily be calculated according to Eq. (1), where E_λ is the solar irradiance at a single wavelength (J s^{-1} m^{-2} nm^{-1}), λ is the wavelength (nm), h is the Planck constant (6.626×10^{-34} J s), and c is the velocity of light (2.998×10^{17} nm s^{-1}). The number of absorbed photons J_g for solar wavelengths $\lambda \leq \lambda_g$ can be obtained according to Eq. (2), where $\alpha(\lambda)d\lambda$ is the fraction of incident radiation absorbed in the wavelength band $d\lambda$. Accordingly, the STH conversion efficiency can be obtained employing Eq. (3) [18] assuming that every absorbed photon is 100 % effective in generating hydrogen, i.e., the quantum efficiency is $\varphi = 1$, the required chemical potential for water splitting is $\mu = 1.97 \times 10^{-19}$ J $photon^{-1}$, and the total solar irradiance is $S = 1$ sun (1,000 J s^{-1} m^{-2}). The calculated values are presented in Fig. 2.

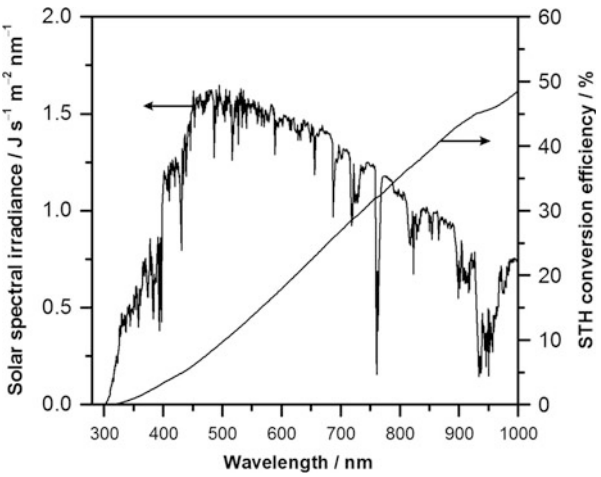

Fig. 2 Solar spectral irradiance at a global air mass of 1.5 as a function of the wavelength and the maximum theoretical solar-to-hydrogen (STH) conversion efficiency

$$J_\lambda = \frac{E_\lambda \lambda}{hc} \quad [\text{photons s}^{-1}\text{m}^{-2}\text{nm}^{-1}] \tag{1}$$

$$J_g = \int_0^{\lambda g} J\lambda\, \alpha(\lambda)\, d\lambda \quad [\text{photons s}^{-1}\text{m}^{-2}] \tag{2}$$

$$\text{STH conversion efficiency} = \frac{J_g\, \mu\, \varphi}{S} \times 100[\%] \tag{3}$$

By analyzing the solar irradiance, the maximum theoretical STH conversion efficiency is calculated to be 48 %, following an integration from the UV (280 nm) to the maximal usable wavelength of 1,000 nm (1.23 eV). This result is readily explained by the fact that molecular hydrogen is the sole useful product, i.e., only the H_2-equivalent energy can be utilized and any excess energy of a photon exceeding 1.23 eV will be dissipated (mainly as heat) [20]. It is obvious from Fig. 2 that the energy loss becomes more apparent as the wavelength decreases. For example, the maximum conversion efficiency that is achievable in the UV region (<400 nm) is 3.3 %. To realize significant solar energy conversion (namely, exceeding a 5 % STH efficiency), visible light has hence to be utilized. This fact clearly justifies the fact that the development of visible light-responsive photocatalysts is essential to reach high STH conversion efficiencies.

According to recent estimations, one-third of the human society energy needs in 2050 can be obtained from solar energy employing approximately 10,000 "solar plants" as shown in Fig. 3 (with an area of 5 km × 5 km per plant) with a solar energy conversion efficiency of 10 % [13]. According to the data presented in Fig. 2, a 10 % STH conversion efficiency is corresponding to a bandgap energy ca. 2.5 eV (ca. 500 nm), however, it should be mentioned here that the data presented in Fig. 2 have been calculated assuming that all absorbed photons contribute effectively to the hydrogen production (i.e., $\varphi = 1$). In reality, the achievement of such an ideal value of the quantum efficiency will be very difficult,

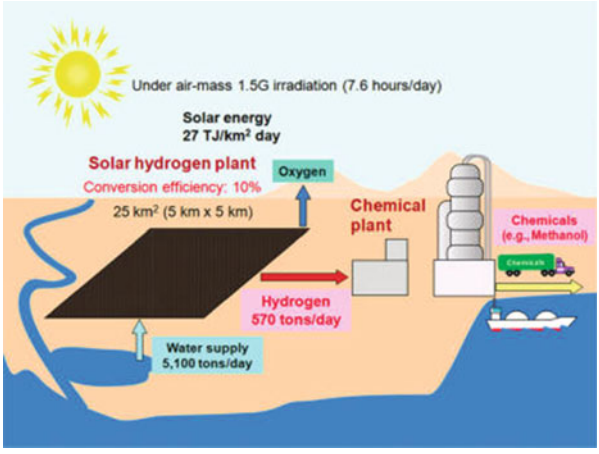

Fig. 3 Possible scheme for the large-scale H_2 production employing solar water splitting. Reprinted with permission from Ref. [13]. Copyright (2010) American Chemical Society

e.g., due to the fast recombination of the photogenerated charge carriers. Thus, photocatalysts with smaller bandgaps are urgently required to achieve the desired 10 % STH conversion efficiency that can, for example, be realized employing a photocatalyst with a bandgap energy of 2.0 eV and a quantum efficiency $\varphi = 0.5$, i.e., only 50 % of the solar photons must be utilized for the hydrogen production.

Regarding the overall system approach, a unique reactor for the PEC hydrogen production has been proposed recently [21] when James et al. reported a technoeconomic analysis of conceptual solarchemical H_2 production systems. According to this report, shallow horizontal "pools" or "beds" consisting of flexible clear plastic thin-film baggies, containing a reactant solution and a photocatalyst, are potential candidates for inexpensive water splitting reactors. Similar system analyses, including suitable water splitting reactors, H_2 and O_2 gas separators, solarchemical plants, and associated facilities, are expected to be of utmost importance for the future practical realization of solar energy-to-fuel conversion concepts.

2.3 Photocatalysts for Water Splitting

The most commonly used photocatalyst for the photocatalytic (PC) and the PEC water splitting is titanium dioxide (TiO_2). Employing a TiO_2 rutile single crystal electrode as photoanode Fujishima and Honda were able to split water in a PEC cell [4]. However, an external bias was required due to the unfavorable position of the conduction band edge of rutile ($E_{CB} = +0.04$ V vs. NHE) being almost the same as the standard electrode potential of hydrogen evolution (H^+/H_2; 0 V vs. NHE) [22, 23]. For anatase and brookite TiO_2, E_{CB} is positioned more favorable, i.e., these materials should be able to achieve H_2O splitting even without external bias [24]. However, also anatase TiO_2 cannot split water without modifications such as the loading with co-catalysts. For example, Sato and White [14] observed the stoichiometric evolution of H_2 and O_2 on anatase TiO_2 powder that has been impregnated by a Pt co-catalyst via the photodecomposition of hexachloroplatinate in an aqueous acetic acid solution. In this study, ^{18}O-labeling experiments also confirmed the O_2 production from water. Without Pt, no H_2 was formed. However, as a drawback, the Pt islands on the surface of TiO_2 were found to also catalyze the reverse of the water splitting reaction, i.e., the formation of water through the reaction of molecular hydrogen with molecular oxygen, thus limiting the yields in particular at high H_2 partial pressure. Mills and Porter discovered that O_2 production could be less than stoichiometric or, in some cases, be even entirely absent [25]. This was attributed to the fact that photoexcited TiO_2 tends to strongly adsorb oxygen as O_2^- or as O_2^{2-}. Following initial reports on the beneficial effect of a NaOH coating on the photocatalytic efficiency [26]. Arakawa's group reported in 1992 that the O_2 evolution activity of TiO_2 could be enhanced significantly by the addition of 0.1–2.2 M Na_2CO_3 to the aqueous catalyst dispersion [27]. Although

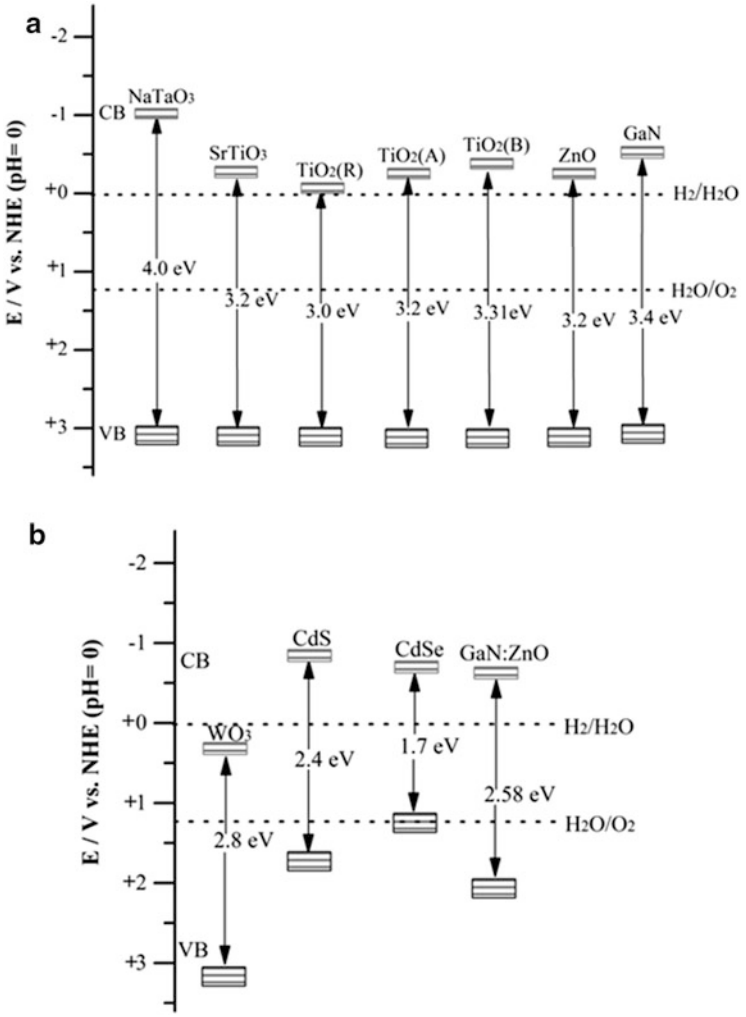

Fig. 4 Schematic illustration of the energy levels of (**a**) UV and (**b**) visible light-active semiconductor photocatalysts. Data extracted from Refs. [9, 15, 22]

there were several studies evincing the simultaneous production of H_2 and O_2 in particulate systems, the reproducibility of some of these experiments was found to be poor or the overall STH efficiency was rather low [28, 29]. The bandgap energies of TiO_2 modifications as well as the energy levels of some other wide bandgap semiconductor photocatalysts are given in Fig. 4a. $NaTaO_3$, $SrTiO_3$, and TiO_2 possess suitable band positions for water splitting. These materials are active for water splitting when they are suitably modified with co-catalysts [8], but unfortunately, they exhibit very low solar conversion efficiencies due to their large bandgap energies. For example, the theoretical STH conversion efficiency can be

calculated to be 4.0 % for TiO_2 with a bandgap energy 3.0 eV (rutile phase) assuming that all solar photons below 415 nm are effectively absorbed and participate in the molecular hydrogen production.

Figure 4b shows the bandgap energies and energy levels for some semiconductor photocatalysts with potential application under visible light illumination. Although CdS and CdSe seem to have suitable band positions and a bandgap with visible light response, they are not active for water splitting into H_2 and O_2 since S^{2-} and Se^{2-} are more susceptible to oxidation than OH^-, causing the CdS or CdSe photocatalyst itself to be oxidized and thus to be anodically degraded [30–32]. For instance, S^{2-} in CdS rather than H_2O is oxidized by the photogenerated holes accompanied with the anodic dissolution of the semiconductor and the formation of Cd^{2+} according to the following equations [9]:

$$\mathrm{CdS} \xrightarrow{h\nu} e^-_{\mathrm{CB}} + h^+_{\mathrm{VB}} \tag{4}$$

$$\mathrm{CdS} + 2h^+_{\mathrm{VB}} \longrightarrow \mathrm{Cd}^{2+} + \mathrm{S} \tag{5}$$

In the presence of molecular oxygen, the overall process will be:

$$\mathrm{CdS} + 2\mathrm{O}_2 \longrightarrow \mathrm{Cd}^{2+} + \mathrm{SO}_4^{2-} \tag{6}$$

Reactions (5) and (6) are called photocorrosion and present a fundamental problem for the applicability of metal sulfide photocatalysts for cyclic water splitting. Even for a metal oxide such as ZnO, photocorrosion has also been observed under bandgap excitation in the absence of noble metal co-catalysts [9].

$$\mathrm{ZnO} \xrightarrow{h\nu} e^-_{\mathrm{CB}} + h^+_{\mathrm{VB}} \tag{7}$$

$$\mathrm{ZnO} + 2h^+_{\mathrm{VB}} \longrightarrow \mathrm{Zn}^{2+} + \frac{1}{2}\,\mathrm{O}_2 \tag{8}$$

WO_3 functions as a stable photocatalyst for O_2 evolution under visible light illumination in the presence of appropriate electron acceptors such as silver ions, but unfortunately, it cannot reduce water to H_2 due to the fact that the bottom of its conduction band is located at a more positive potential than that of the water reduction. As a result, WO_3 does not have the ability to reduce H^+ to H_2. Until very recently, reproducible photocatalytic systems for the visible light driven overall water splitting had not been realized, although there are several reports claiming the decomposition of water under visible light illumination [33–37]. The difficulty in developing a suitable photocatalyst can be attributed to the lack of known materials meeting all three requirements, i.e., (1) band edge potentials suitable for overall water splitting, (2) bandgap energy smaller than 3 eV, and (3) stability against photocorrosion during the photocatalytic reaction. For the development of visible light active photocatalysts, it is very important to be able to control the band structure. In metal oxide photocatalysts, the bottom of the conduction bands consists mainly of empty transition-metal d orbitals located at

potentials between 0 V and −1 V (vs. NHE) at pH 0 (cf. Fig. 4a). On the other hand, the top of the valence bands consists of O2p atomic orbitals located at very positive potentials (around +3 V vs. NHE, see Fig. 4a) [15, 38]. Consequently, these metal oxides exhibit large bandgap energies thus limiting their visible light harvesting abilities. Through the introduction (doping) of other elements, e.g., nitrogen and sulfur, which have atomic orbitals (N2p and S3p, respectively) with a potential energy exceeding that of O2p new valence bands will be formed resulting in a decrease of the bandgap energy without affecting the conduction band level. This approach has been shown to result in the formation of visible light-driven photocatalysts with band edge potentials that are potentially suitable for the overall water splitting [15]. Domen and coworkers were able to use this strategy for the development of several (oxy)nitrides and oxysulfides that could be used as photocatalysts for water reduction and/or oxidation under visible light illumination [39–48]. Most of these materials are composed of transition-metal cations such as Ti^{4+}, Nb^{5+}, or Ta^{5+} with d^0 electronic configuration [49–54]. However, considering the electronic band structure, d^{10}-based semiconducting materials should be advantageous over the d^0 configurations because the bottom of their conduction bands is composed of hybridized s and p orbitals with large dispersion. Thus, the mobility of photogenerated electrons in the conduction band of the d^{10} materials is higher than that of the d^0 semiconductors and consequently, the former exhibit higher photocatalytic activities for water splitting [55–58]. For instance, a highly active (oxy)nitride photocatalyst with d^{10} electronic configuration, namely, the GaN:ZnO solid solution $(Ga_{1-x}Zn_x)$-$(N_{1-x}O_x)$, has been successfully prepared by nitridation of a mixture of Ga_2O_3 and ZnO under NH_3 flow [39, 40]. Even though the bandgap energies of GaN and ZnO are larger than 3 eV (see Fig. 4a), the resulting solid solution exhibits a narrower bandgap (see Fig. 4b). This bandgap narrowing has been attributed to the p-d repulsion (i.e., N2p-Zn3d repulsion) shifting the valence band maximum upwards without affecting the conduction band minimum [59]. The as-prepared (oxy)nitride $(Ga_{1-x}Zn_x)$-$(N_{1-x}O_x)$, exhibits little photocatalytic activity for water decomposition even under UV irradiation. However, its loading with co-catalysts such as RuO_2 nanoparticles remarkably enhances the H_2 and O_2 evolution evincing the importance of the presence of a co-catalyst. The photocatalytic activity of this material under visible light irradiation ($\lambda > 420$ nm) could be further enhanced either by loading with Rh/Cr_2O_3 core/shell structures [60, 61] or with Rh/Cr_2O_3 core/shell structures together with Mn_3O_4 nanoparticles as H_2 and O_2 evolution promoters, respectively [56]. Considerable attention has also been paid to the development of visible light-active photocatalysts employing ternary metal oxides to overcome the intrinsic limitations of binary metal oxides such as high resistance and unfavorable indirect bandgap transitions. Therefore, various new visible light-active ternary metal oxides have been extensively investigated, such as $InTaO_4$, Bi_2WO_6, $BiVO_4$, and $InVO_4$ [62]. They exhibit great potential for the utilization of solar energy. However, their low photocatalytic efficiencies still limit their applications considerably.

A metal-free photocatalyst made of only carbon and nitrogen was also investigated for the evolution of hydrogen from water [63]. Such carbonitrides can readily be prepared by the thermal polycondensation of common organic monomers

resulting in the synthesis of graphitic carbon nitrides (g-C_3N_4) with various architectures. Their graphitic planes are usually constructed from tri-s-triazine units connected by planar amino groups. Different thermal condensation processes enable the fine adjustment of their electronic and optical properties, as indicated by the ultraviolet–visible absorption spectrum for carbon nitrides prepared at different condensation temperatures. The absorption edge can thus be moved towards longer wavelengths, indicating a decreasing bandgap with increasing condensation temperatures. The bandgap energy of condensed graphitic carbon nitride is estimated to be 2.7 eV, showing an intrinsic semiconductor-like absorption in the blue region of the visible spectrum. This bandgap is sufficiently large to overcome the endothermic character of the water splitting reaction.

3 Photocatalytic H_2 Production Employing Sacrificial Reagents

One of the most important limitations for the application of photocatalysis for water decomposition is that the process employing pure water is rather inefficient. This is related to the fact that the simultaneous reduction and oxidation of water is a complex multistep reaction involving four electrons. Using sacrificial molecules as electron donors can remarkably improve the H_2 production [64], as holes are scavenged by these molecules and charge carrier recombination can be greatly reduced. Furthermore, as O_2 is not produced, the back reaction to produce water is suppressed, increasing the H_2 yield and avoiding a subsequent gas separation stage. However, it should be noted here that the yield of the H_2 formation can also be reduced by the competing reduction reactions with the products formed upon the oxidation of the sacrificial reagents. Table 1 summarizes commonly employed photocatalysts and sacrificial reagents for photocatalytic hydrogen production. These sacrificial reagents can be divided into organic and inorganic electron donors.

3.1 Organic Sacrificial Reagents

Organic compounds such as alcohols, organic acids, and hydrocarbons can act as efficient hole scavengers (i.e., as electron donors) for the photocatalytic H_2 generation [82]. In particular, methanol is frequently used as sacrificial reagent. For practical applications, the utilization of methanol will only be environmentally sensible provided that it is derived from biomass or from toxic residues that must be disposed of. Adding methanol as electron donor to react irreversibly with the photo-generated VB holes can enhance the photocatalytic electron/hole separation efficiency resulting in higher quantum efficiencies. Since electron donors are consumed in the photocatalytic reaction, their continuous addition is required to sustain H_2 production. Kawai et al. [83] proposed the following overall methanol

Table 1 Different sacrificial photocatalytic hydrogen production systems

Photocatalyst	Sacrificial reagent	Light source	Rate of H_2 evolution ($\mu mol\ h^{-1}\ g^{-1}$)	Reference
TiO_2	2-Propanol (aq)	450 W Hg	30	[65]
Pt/TiO_2	5 M methanol (aq)	450-W Xe (>420 nm)	127	[28]
Pt/TiO_2	12 M methanol (aq)	100-W Hg	834	[66]
Pd/TiO_2			306	
Au/TiO_2			300	
Pt/TiO_2	5 M methanol (aq)	450 W Xe (300–700 nm)	816	[67]
Pd/TiO_2			774	
Au/TiO_2			402	
Pt/TiO_2	1 M TEOA (aq)	150 W Halogen	3,333	[68]
Co/TiO_2			1,160	
Ni/TiO_2			983	
$Pt/MoO_3/TiO_2$	5 M methanol (aq)	75 W Xe	169	[69]
NiO/TiO_2	0.01 M KCN	100 W Hg	1,500	[70]
Pt/CdS	0.24 M Na_2S/0.35 M Na_2SO_3 (aq)	4,500 W Xe (>300 nm)	12,262	[71]
Pt/CdS	0.1 M Na_2S/Na_2SO_3 (aq)	300 W Xe (>420 nm)	13,800	[72]
Pt/CdS	1 M $(NH_4)_2SO_3$ (aq)	Xe (>420 nm)	13,282	[73]
Pt/CdS	0.25 M Na_2S/0.35 M Na_2SO_3 (aq)	300 W Xe (>420 nm)	27,333	[74]
MoS_2/CdS	Lactic acid	300 W Xe (>420 nm)	5,400	[75]
CdSe	0.1 M Na_2S/Na_2SO_3 (aq)	LED (440 nm)	240	[76]
MoS_2/CdSe			890	
Pt/CdSe	0.25 M Na_2S/0.35 M Na_2SO_3 (aq)	Xe (>420 nm)	36,250	[77]
CdSe (QDs)	0.1 M Na_2SO_3 (aq)	300 W Xe (>320 nm)	9,062	[78]
RuO_2/CdS	H_2S, 0.1 M Na_2S/Na_2SO_3	1,500 W Halogen	878	[79]
CdS	0.3 M H_2S (DEA)	300 W Xe (>420 nm)	7,200	[80]
Pd/CdS			25,600	
Pt/CdS			26,800	
PdS/CdS			24,800	
Pt-Pd/CdS			42,800	
Pt-PdS/CdS			58,400	
Pt-Pt/CdS			47,600	
Rh/CdS			17,600	
Rh_2S_3/CdS			24,000	
Ru/CdS			17,200	
Ru_2S_3/CdS			22,800	
$Pt/CdS/TiO_2$	H_2S, 1 M NaOH	500 W Hg (>420 nm)	9,800	[81]

decomposition reaction mechanism resulting in a lower energy that can be stored as compared with the cyclic splitting of water [84]:

$$CH_3OH\ (l) \xrightarrow{h\nu,\ TiO_2} HCHO\ (g) + H_2(g) \quad \Delta G^\circ = 64.1\ kJ\ mol^{-1} \tag{9}$$

$$HCHO\ (g) + H_2O\ (l) \xrightarrow{h\nu,\ TiO_2} HCOOH\ (l) + H_2\ (g)\ \Delta G^\circ = 47.8\ kJ\ mol^{-1} \tag{10}$$

$$HCOOH\ (l) \xrightarrow{h\nu,\ TiO_2} CO_2\ (g) + H_2\ (g) \quad \Delta G^\circ = -95.8\ kJ\ mol^{-1} \tag{11}$$

with the overall reaction being

$$CH_3OH\ (l) + H_2O\ (l) \xrightarrow{h\nu,\ TiO_2} CO_2\ (g) + 3H_2(g) \quad \Delta G^\circ = 16.1\ kJ\ mol^{-1} \tag{12}$$

The first two reactions (Eqs. (9) and (10)) have a positive Gibbs free energy, thus both reactions are thermodynamically unfavorable at room temperature. The photon energy will be used to raise the chemical potential of the reactants thus driving the reactions to the product side. The third reaction (Eq. 11) has a large negative Gibbs energy, thus it intrinsically provides a barrier for the undesired reverse consumption of the generated H_2 gas.

Two possible mechanisms have been proposed for photocatalytic oxidation of methanol: (1) the direct oxidation by photogenerated holes and (2) the indirect oxidation via interfacially formed $^\bullet OH$ radicals that are products of the trapping of valence band holes by surface −OH groups or adsorbed water molecules [85–88]. It is still a challenge to distinguish between the two mechanisms in practice due to the lack of suitable probe techniques. Wang et al. [89] have reported recently that the methanol photooxidation pathway, direct or indirect, depends on the molecular species adsorbed at the TiO_2 surface. These authors studied the competitive adsorption process between water and methanol on TiO_2 through the in situ use of sum frequency generation, a nonlinear spectroscopic technique. Accordingly, they concluded that the indirect oxidation by $^\bullet OH$ radicals is the mechanism when water is the dominant surface species with the critical molar ratio between water and methanol for the $^\bullet OH$ radical mechanism to become the dominant process being ≈300. Such a high ratio apparently applies to the photooxidation of methanol by TiO_2 in aqueous systems. If the water content is lower than this critical value, the direct oxidation of methanol by photogenerated holes will be the predominant process at the TiO_2 surface.

Hydroxyl radicals, $^\bullet OH$, are known to react with methanol mainly through the abstraction of a hydrogen atom from a C–H bond. Sun and Bolton [90] have used the reaction of methanol to determine the quantum yield for the photochemical generation of $^\bullet OH$ radicals in TiO_2 suspensions. The $^\bullet OH$ radical generation rate is determined through the R–H atom abstraction from methanol by these $^\bullet OH$ radicals (Eq. 13), followed by monitoring the formation rate of the first principal stable product, i.e., formaldehyde (Eq. 14).

$$CH_3OH + {}^\bullet OH \longrightarrow {}^\bullet CH_2OH + H_2O \tag{13}$$

$$^{\bullet}CH_2OH + O_2 \longrightarrow HCHO + HO_2^{\bullet} \quad (14)$$

In the presence of oxygen, formaldehyde is formed as the dominant stable product in a quantitative reaction (Eq. 14), whereas, in the absence of oxygen, formaldehyde is formed through the electron injection into the conduction band of TiO_2, a process called "current doubling" [22, 91]. In the presence of a co-catalyst such as Pt these electrons will be utilized to form H_2 while otherwise they will be trapped at Ti^{IV} yielding Ti^{III}. The Ti^{III} formation results in a blue coloration of the respective TiO_2 suspensions and eventually in the termination of the formaldehyde formation. HCHO can be further oxidized in an analogous manner producing HCOOH and finally CO_2 [92, 93]. Asmus et al. [94] showed that the efficiency of the reaction of $^{\bullet}OH$ radicals with methanol by R–H abstraction is 93 %. The remaining 7 % are accounted for by methoxy radicals formed through the H-abstraction reaction from the hydroxyl group (Eq. 15).

$$CH_3OH + {}^{\bullet}OH \longrightarrow CH_3O^{\bullet} + H_2O \quad (15)$$

The concentration of HCHO formed photocatalytically, divided by a factor of 0.93, is thus used to calculate the corresponding $^{\bullet}OH$ radical concentration. Sun and Bolton [90] have used the same factor as that found in the homogeneous system (0.93) to calculate the $^{\bullet}OH$ radical concentration in case of the heterogeneous TiO_2 system.

Other alcohols such as ethanol or 2-propanol can also act as efficient hole scavengers for the photocatalytic H_2 evolution. Using transient absorption spectroscopy following laser excitation, Tamaki et al. found for the oxidation efficiency of alcohols by trapped holes the order methanol > ethanol > 2-propanol, while water was hardly oxidized by the holes photogenerated in TiO_2 [95]. However, Domen et al. investigated the photocatalytic H_2 evolution on different photocatalysts in the presence of 2-propanol as sacrificial reagent [65]. Since they did not observe H_2 evolution in pure 2-propanol or pure water solutions, but in 2-propanol/water mixtures, they regarded the photocatalytic H_2 evolution on NiO-$SrTiO_3$, TiO_2(anatase), and CdS as a coupling reaction of the photodecomposition of H_2O and the photooxidation of 2-propanol as follows:

$$2H_2O \longrightarrow H_{aq}^{+} + 2OH_{aq}^{-} \quad (16)$$

$$2H_{aq}^{+} + 2e^{-} \longrightarrow H_{2\,(g)} \quad (17)$$

$$(CH_3)_2CHOH + 2OH_{aq}^{-} + 2h^{+} \longrightarrow (CH_3)_2CO + 2H_2O \quad (18)$$

with the overall reaction being

$$(CH_3)_2CHOH \longrightarrow H_{2(g)} + (CH_3)_2CO \quad (19)$$

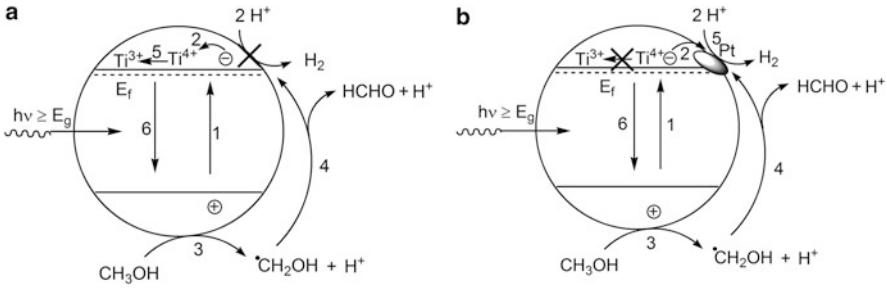

Fig. 5 Processes involved in the photocatalytic H_2 evolution from aqueous methanol solution on (**a**) bare TiO_2 and (**b**) on Pt-loaded TiO_2. (1) photogeneration of charge carriers, e^- and h^+; (2) trapping of e^- by Ti^{4+} (**a**) or by Pt islands (**b**); (3) first oxidation step of CH_3OH; (4) formation of HCHO through e^- injection into the conduction band of TiO_2 (current-doubling); (5) formation of Ti^{3+} (**a**) or reduction of H^+ (**b**); (6) recombination channel. *Note*: For simplicity, the formation of $^{\bullet}CH_2OH$ radicals by trapped holes ($\equiv Ti^{IV}OH^{\bullet+}$) or by $^{\bullet}OH$ radicals is represented by the hole oxidation step

In the absence of any co-catalysts ZnO, WO_3, $SrTiO_3$, and CdSe were found to be inactive for this reaction, while the bare TiO_2 showed very low photocatalytic activity due to the higher overpotential for hydrogen production (0.05 V) [96] and to the fast recombination of molecular hydrogen and oxygen forming water. However, other authors have reported that bare TiO_2 is not able to catalyze the H_2 evolution even in the presence of methanol. In the presence of an electron donor, such as methanol, and in the absence of O_2, the excess holes will be consumed and the photogenerated electrons will be trapped near the surface forming trivalent titanium (Ti^{3+}) instead of reducing H^+ (see Fig. 5a). This phenomenon has been observed by Bahnemann et al. [97] in laser-flash photolysis experiments employing suspensions of colloidal TiO_2. Moreover, the formation of highly colored Ti^{3+} centers can even be used technically in a process called photochromism.

If TiO_2 is loaded with Pt^0, a Schottky barrier will be formed at the Pt^0/TiO_2 interface [7]. Since the work function of TiO_2 (4.2 eV) is smaller than that of Pt (5.65 eV), the electrons in the conduction band of TiO_2 migrate to Pt until the thermodynamic equilibrium is reached [98, 99]. Upon illumination of Pt^0/TiO_2 particles with the UV light, this thermodynamic equilibrium will be perturbed. This causes a continuous flow of the photogenerated electrons to Pt^0, while the photogenerated holes migrate to the TiO_2 surface. The transfer of the electrons from TiO_2 to Pt^0 could be detected by means of electron spin resonance (ESR) [100]. The ESR signal intensity of photoformed active Ti^{3+} sites on bare TiO_2 has been found to increase linearly with the irradiation time, while Pt^0-loaded catalysts showed almost no change in the signal intensity. The results from diffuse reflectance spectroscopy experiments indicate that the observed electron migration process from photoexcited TiO_2 to Pt^0 leads to enhanced electron/hole separation and thus to enhanced formation of H_2 gas (see Fig. 5b) [28, 88, 101, 102].

The H_2 production reaction on Pt/TiO_2 starts with the transfer of excess electrons from Pt to adsorbed H^+_{ads} and H_2O_{ads} to form adsorbed $H_{ads}^{\bullet}$ atoms via the Volmer reaction [103]:

$$H^+_{ads} + e^- \left(Pt^0\right) \longrightarrow H^{\bullet}_{ads} \left(Pt^0\right) \tag{20}$$

$$H_2O_{ads} + e^- \left(Pt^0\right) \longrightarrow H^{\bullet}_{ads} \left(Pt^0\right) + OH^- \tag{21}$$

The subsequent production of molecular H_2 can proceed via two reaction paths, namely, via the Heyrovsky (22) and the Tafel (23) reactions, respectively [104, 105]:

$$H^{\bullet}_{ads} \left(Pt^0\right) + e^- \left(Pt^0\right) + H^+_{ads} \left(Pt^0\right) \longrightarrow H_{2(g)} \tag{22}$$

$$H^{\bullet}_{ads} \left(Pt^0\right) + H^{\bullet}_{ads} \left(Pt^0\right) \longrightarrow H_{2(g)} \tag{23}$$

Rabani et al. concluded from the observed pseudo-first-order kinetics and the dependency of the first-order rate of $[H^+]$ reduction on the $[Pt^0]$ concentration that the rate determining step of the catalytic reduction is the transfer of the excess electron from Pt^0 to H^+ and H_2O, respectively [106].

An improvement of the photocatalytic activity for molecular H_2 production was also observed by loading TiO_2 with other noble metals such as Au, Pd, Ru, or Rh. In most cases, however, Pt/TiO_2 shows the highest photocatalytic activity [66, 107–109]. This has been explained by the lowest overpotential for H_2 formation and a larger work function of Pt resulting in more effective electron-acceptor properties. In contradiction to these reports, Rabani et al. found for the photocatalytic H_2 production in the presence of 2-propanol the order $Au^0/TiO_2 > Pt^0/TiO_2 \geq Pd^0/TiO_2$. In contrast to TiO_2 coated with Pt^0 and Pd^0 Au^0/TiO_2 apparently promotes the H_2 abstraction from 2-propanol by $H_{ads}^{\bullet}$. Subsequently, the thus generated 2-propanol radical injects an electron into Au^0/TiO_2 leading to an increased photocatalytic efficiency through a free radical chain reaction [110]:

$$H^{\bullet}_{ads} \left(Au^0\right) + CH_3CHOHCH_3 \longrightarrow Au^0 + H_{2(g)} + CH_3{}^{\bullet}COHCH_3 \tag{24}$$

The loading of TiO_2 with Au provides another essential advantage over Pt, since Pt^0/TiO_2 can only be excited by UV light, while Au^0/TiO_2 has been reported to be excitable also in the visible light region. For example, Fang et al. observed three times higher H_2 evolution rates for Au^0/TiO_2 as compared with Pt^0/TiO_2 upon excitation at $\lambda > 400$ nm. They attribute the visible light-induced H_2 evolution to the Surface Plasmon Resonance of Au [111]. In response to photon absorption resonant surface plasmons are formed localizing electromagnetic energy close to their surface. The interaction of this localized electric field with the semiconductor induces the formation of charge carriers near the surface of the semiconductor; hence, these charge carriers can reach these surface sites more readily. This enhances the electron/hole separation thus increasing the H_2 evolution yield [112].

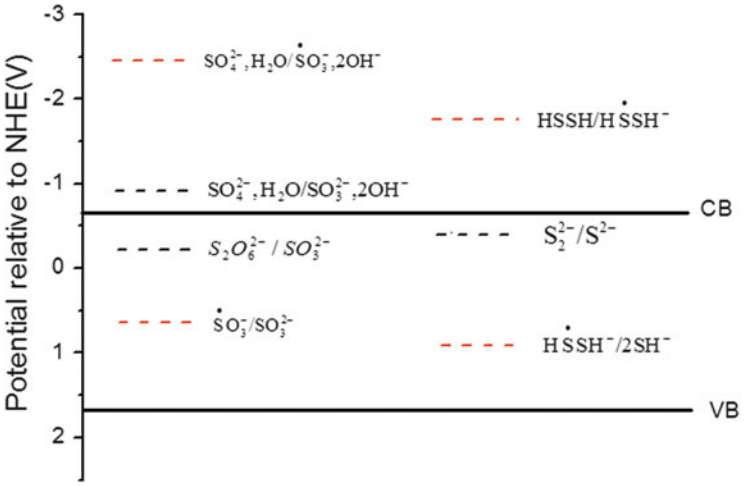

Fig. 6 Schematic diagram of the energy levels between the semiconductor CdS and various reducing agents (the reduction potentials of one-electron couples are taken from [120])

3.2 Inorganic Sacrificial Reagents

Sulfide, S^{2-}, and sulfite, SO_3^{2-}, can act as inorganic sacrificial reagents for the photocatalytic H_2 generation since they are very efficient hole acceptors enabling the effective separation of the charge carriers [73, 74, 113–117]. Large amounts of sulfide and sulfite are released from fossil energy resources such as crude oil, coal, and natural gas. These sulfur compounds can be converted by photocatalytic oxidation into environmentally less harmful products.

CdS has been mostly used as photocatalyst for H_2 production in the presence of S^{2-} and/or SO_3^{2-}. The energy level of the valence band of CdS is positive enough (+1.7 V) to promote the oxidation of these sulfur compounds (cf. Fig. 6) [118]. The oxidation of S^{2-} and SO_3^{2-} can either occur by a two-electron transfer process or even through a one-electron oxidation which is thermodynamically less favorable (e.g., through the intermediate formation of $^{\bullet}SO_3^-$ (see Fig. 6)). SO_3^{2-} can be oxidized to both, SO_4^{2-} and $S_2O_6^{2-}$. Although the formation of $S_2O_6^{2-}$ is thermodynamically less favorable than the conversion of SO_3^{2-} to SO_4^{2-}, Bühler et al. observed a significant concentration of $S_2O_6^{2-}$ in the reaction media [71]. This was explained by a higher concentration of SO_3^{2-} ions near the CdS surface as compared with the concentration of OH^- ions, which are required for the formation of SO_4^{2-}.

It has been argued that using S^{2-} and/or SO_3^{2-} as sacrificial reagents instead of alcohols is advantageous, since the redox potentials of these compounds are more positive than the oxidation potential of CdS (0.37 V vs. NHE, pH = 7). Hence, the undesired photocorrosion reaction (Eq. 5) of the semiconductor can be reduced, but

not prevented entirely [71, 119]. Another advantage of the use of S^{2-} (as compared with an alcohol) for the photocatalytic H_2 generation employing CdS is that due to the presence of sulfide in the surrounding solution dissolved Cd^{2+} can react with S^{2-} to rebuild CdS. In an aqueous methanol solution, however, this repair mechanism is not feasible.

Whenever the photocatalytic generation of H_2 was carried out in an aqueous sulfite rather than in a sulfide solution a decrease of the efficiency was reported [71]. During this reaction, hydroxyl ions will be formed increasing the pH of the reaction mixture. Since the flatband potential of CdS hardly depends on the pH, the H_2 production will thermodynamically be hindered in the strong alkaline solutions [121]. Inoue et al. demonstrated a cathodic shift of the flatband potential of CdS in the presence of sulfide due to the strong interaction between sulfide and the CdS surface [122]. Thus, the photocatalytic H_2 evolution on CdS becomes feasible in a strongly alkaline solution. However, the photocatalytic efficiency of the H_2 production was found to decrease in solutions just containing sulfide ions. This was attributed to the formation of disulfide ions, S_2^{2-}, which exhibit a less negative reduction potential than the protons and are able to act as an optical filter reducing the light absorption of CdS [71]. The addition of reducing agents such as SO_3^{2-} prevents the formation of disulfide ions. Because of these facts, using a S^{2-}/SO_3^{2-} mixture leads to an improvement of the quantum yield for H_2 production from water. For example, Yan et al. obtained the highest quantum yield of 93 % for H_2 production for a Pt-PdS/CdS photocatalyst in the presence of a S^{2-}/SO_3^{2-} mixture under visible light irradiation [123]. The reaction mechanism suggested for the photocatalytic H_2 evolution in the presence of S^{2-}/SO_3^{2-} mixtures is described by the equations (25)–(30):

$$2H_2O + 2e^- \longrightarrow H_2 + 2OH^- \tag{25}$$

$$SO_3^{2-} + 2OH^- + 2h^+ \longrightarrow SO_4^{2-} + H_2O \tag{26}$$

$$2SO_3^{2-} + 2h^+ \longrightarrow S_2O_6^{2-} \tag{27}$$

$$2S^{2-} + 2h^+ \longrightarrow S_2^{2-} \tag{28}$$

$$SO_3^{2-} + S^{2-} + 2h^+ \longrightarrow S_2O_3^{2-} \tag{29}$$

$$S_2^{2-} + SO_3^{2-} \longrightarrow S_2O_3^{2-} + S^{2-} \tag{30}$$

In contrast to metal sulfides, metal selenides and CdSe in particular, do not catalyze the H_2 evolution from water even in the presence of sacrificial reagents [124]. This is attributed to a large overpotential for the proton reduction on the CdSe surface. However, it was demonstrated that for quantum size-confined CdSe photocatalysts the proton reduction is possible, because the effect of the overpotential is compensated by the increased bandgap as a consequence of the quantum confinement effect [78, 125–127]. Such a correlation between the particle size and the photocatalytic activity of the semiconductor has already been predicted by the Gerischer theory [128]. According to this theory, the widening of the semiconductor bandgap with

decreasing particle size leads to a higher electron transfer rate between the semiconductor and the reduction couple in the solution, since the reduction potential of the electrons becomes more negative and the oxidation potential of the holes more positive leading to an increase in the thermodynamic driving force for both processes.

3.3 H_2S Splitting

Apart from water, the hydrogen sulfide (H_2S) splitting should be regarded as an alternative source of H_2. H_2S is a toxic and corrosive compound formed as a by-product during the hydrodesulfurization of petroleum, paper production, and wastewater treatment. Therefore, to convert H_2S into less harmful products is a relevant challenge. Currently, the main industrial removal processes of H_2S are the wet absorption by Na_2CO_3 or complex ferric compounds and the Claus process, whereby H_2S is decomposed into water and elemental sulfur. The photocatalytic destruction of H_2S using TiO_2 has also been reported to be efficient with the formation of SO_4^{2-} and SO_2 as the reaction products [129–131]. However, the molecular hydrogen potentially stored in H_2S is not reclaimed by any of these processes. Thus, the recovery of H_2 from H_2S could satisfy both, the energetic and the environmental requirements.

The photocatalytic H_2S cleavage is reported to proceed in water or alkaline solution [79, 81, 132, 133]. The most used photocatalyst for this reaction is CdS (either by itself or as a mixture with other semiconductors). The conversation of H_2S to S and H_2 is thermodynamically unfavorable ($\Delta G^\circ = 33$ kJ/mol); however, it is preferred as compared with the H_2O splitting (requiring 237 kJ/mol). Mechanistically, the H_2S cleavage starts with the H_2S dissociation to HS^- [132]:

$$H_2S + OH^- \longrightarrow HS^- + H_2O \tag{31}$$

Szynkarczuk et al. found that the HS^- oxidation proceeds in two steps, starting with the formation of polysulfides and followed by the oxidation to sulfur [134, 135].

$$nHS^- + 2(n-1)h^+ \longrightarrow S_n^{2-} + nH^+ \quad E^0 = 0.003 - 0.298\ (\text{V vs. NHE}) \quad \text{for } n = 2-5 \tag{32}$$

$$S_n^{2-} + 2h^+ \longrightarrow nS^0 \quad E^0 = (-0.33) - (-0.34)\ (\text{V vs. NHE}) \text{ for } n = 4,\ 5 \tag{33}$$

From a thermodynamic point of view the oxidation of HS^- directly to S is the more favorable process and should therefore also be considered here:

$$HS_{aq}^- + 2h^+ \longrightarrow S^0 + H^+ \quad E^0 = -0.065\ (\text{V vs. NHE}) \tag{34}$$

In contrast to the photocatalytic H_2O splitting the H_2S decomposition can be executed in the absence of any sacrificial reagent, since the dissociation products

of H_2S such as HS^- and S^{2-} can act as efficient hole scavengers. As discussed above, reducing agents such as SO_3^{2-} and $H_2PO_2^-$ must often be added to the reaction media to maintain the photocatalytic activity. Consequentially, under these conditions the observed reaction products are various sulfur oxylates instead of sulfur. Ma et al. demonstrated that H_2S can be stoichiometrically converted to H_2 and S under visible light illumination with a quantum efficiency of 30 % in the absence of any sacrificial reagents when ethanolamine is used as the solvent [80]. Ethanolamine was found to be the more suitable reaction media for H_2S splitting in comparison to aqueous Na_2S/NaOH solutions, because it supports the proton transfer thus preventing the reduction of polysulfides to disulfide, which otherwise competes with the H_2 formation according to:

$$2e^- + S_2^{2-} \longrightarrow 2S^{2-} \quad E^0 = -0.483 \text{ vs. NHE} \tag{35}$$

3.4 The Role of Sacrificial Electron Acceptors

While the choice of sacrificial electron donors for studies concerning the photocatalytic formation of molecular H_2 appears to be rather large, the sacrificial photocatalytic oxidation of water is only reported for a rather limited variety of electron acceptors. By far the vast majority of research groups working on this topic employs silver cations, Ag^+, as electron acceptors with the involved reactions being proposed as follows [53, 136, 137]:

$$4h^+ + 2H_2O \xrightarrow{h\nu} O_2 + 4H_{aq}^+ \tag{36}$$

$$4e^- + 4Ag^+ \xrightarrow{h\nu} 4Ag^0 \tag{37}$$

$$nAg^0 \xrightarrow{h\nu} Ag_n^0 \tag{38}$$

Hence, the photocatalytic formation of molecular oxygen is accompanied by the deposition of metallic silver nano-contacts (Ag_n^0) on the semiconductor's surface. Obviously, this will lead to irreversible optical changes of the systems studied here due to the formation of the plasmonic absorption band of the silver nanoparticles in the visible spectral region. Moreover, noble metal nanoparticles are known for their catalytic activity resulting most likely in changes in the chemical and/or photochemical properties of these systems.

It is interesting to note that these rather drastic changes are hardly ever discussed in the respective literature nor is any experimental work conducted to ensure that the photocatalytic properties of the systems studied remain unchanged upon the formation of the silver particles. Even though no exact count exists here, it seems fair to say that Ag^+ is employed in at least 95 % of the published papers dealing with the sacrificial photocatalytic water oxidation. In some cases, it could be shown that molecular oxygen is also formed when ferric ions are employed as sacrificial electron acceptors [138]:

$$4h^+ + 2H_2O \xrightarrow{h\nu} O_2 + 4H^+_{aq} \tag{39}$$

$$4e^- + 4Fe^{3+} \xrightarrow{h\nu} 4Fe^{2+} \tag{40}$$

However, no O_2 is formed once electron acceptors such as carbon tetrachloride, CCl_4, or tetranitromethane, $C(NO_2)_4$, are used even though their irreversible one-electron reduction is readily observed [139–141]:

$$e^- + CCl_4 \xrightarrow{h\nu} {}^{\bullet}CCl_3 + Cl^-_{aq} \tag{41}$$

$$e^- + C(NO_2)_4 \xrightarrow{h\nu} C(NO_2)^-_3 + NO_2 \tag{42}$$

Also, O_2 is not formed when more complex nitroaromatic compounds are employed as electron acceptors [142]. Even though all of these studies have been conducted in aqueous solutions, i.e., in the presence of 55 M H_2O, the photogenerated holes are exclusively reacting with the organic moiety being present in micro- and millimolar amounts at the most. It should be noted here that both, the CCl_4 and the $C(NO_2)_4$ system initially do not contain any oxidizable organic species. The latter are only formed upon the reductive process.

The above discussion suggests that the role of suitable sacrificial electron acceptors such as Ag^+ and Fe^{3+} is highly underestimated. In particular, their possible involvement in the actual water oxidation mechanism has so far not been discussed at all. However, due to the rather high one-electron oxidation potential of the holes photogenerated in most semiconductors that have been found to exhibit high activities for the photocatalytic water oxidation, e.g., metal oxides, both, Ag^+ and Fe^{3+} can be readily oxidized:

$$h^+ + Ag^+ \longrightarrow Ag^{2+} \tag{43}$$

$$h^+ + Fe^{3+} \longrightarrow Fe^{4+} \tag{44}$$

It is well-known that Ag^{2+} tends to form peroxides in aqueous solution:

$$2Ag^{2+} + 2H_2O \longrightarrow Ag_2O_2 + 4H^+_{aq} \tag{45}$$

The subsequent photocatalytic oxidation of these peroxides is then proposed to result in the observed O_2 formation:

$$2h^+ + Ag_2O_2 \longrightarrow 2Ag^+ + O_2 \tag{46}$$

Similar reactions can be envisaged for Fe^{4+} which is known to be able to oxidize water resulting in the formation of hydroxyl radicals:

$$Fe^{4+} + H_2O \longrightarrow Fe^{3+} + H^+_{aq} + {}^{\bullet}OH \quad (47)$$

Alternatively, further oxidation of Fe^{4+}, via:

$$h^+ + Fe^{4+} \longrightarrow Fe^{5+} \quad (48)$$

appears to be possible followed by reactions such as:

$$2Fe^{5+} + 2H_2O \longrightarrow [Fe_2O_2]^{6+} + 4H^+_{aq} \quad (49)$$

$$[Fe_2O_2]^{6+} \longrightarrow 2Fe^{3+} + O_2 \quad (50)$$

Based upon these possible reactions, it is most certainly highly indicated to study the role of metal cations such as Ag^+ and Fe^{3+} in the photocatalytic water oxidation in detail. The catalytic role proposed here for Ag^+ and Fe^{3+} could be part of a much more general mechanism and open up new design features for photocatalytic and PEC energy-to-fuel conversion systems.

4 Photocatalytic Hydrogen Production on TiO_2

4.1 Enhancement of the Activity

The inhibition of the charge carrier's recombination rate is the bottleneck for enhancing photocatalytic processes even in the presence of electron donors, i.e., of "sacrificial reagents." Commonly, for photocatalytic hydrogen production Pt nanoparticles are used as sink for the photogenerated electrons, thus reducing the recombination rate and catalyzing the molecular hydrogen evolution. Interestingly, the simultaneous separation of photogenerated holes and electrons can be effectively achieved through the modification of the photocatalyst, e.g., TiO_2 P25, by Pt–polypyrrole nanocomposites [143]. The pyrrole monomers are found to undergo oxidative polymerization in the presence of Pt(IV) under mild aqueous conditions at ambient temperature leading to the formation of Pt–polypyrrole nanocomposites [144]. If this reaction occurs in suspensions of a photocatalyst, very thin films from these Pt–polypyrrole nanocomposites are deposited on the photocatalyst surface. The resulting modified photocatalysts exhibit photocatalytic H_2 production activities from aqueous methanol solution that are three times higher than those observed for photocatalysts only loaded with Pt nanoparticles prepared by a photochemical deposition method. This enhanced photocatalytic activity is explained considering both, the properties of Pt nanoparticles and of polypyrrole. As mentioned earlier, upon photon absorption by the photocatalyst, an electron/hole pair is generated. Pt islands present on the TiO_2 surface have the ability to trap the photogenerated electrons, while the polypyrrole is assumed to collect and to channel the

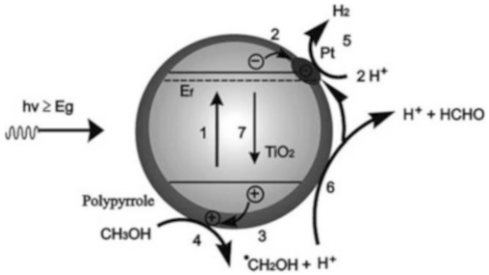

Fig. 7 Scheme representing the enhancement of the charge carrier separation and the photocatalytic activity of TiO_2 modified with Pt–polypyrrole nanocomposites. Reproduced from Ref. [143] with permission from the European Society for Photobiology, the European Photochemistry Association, and the Royal Society of Chemistry

photogenerated holes to the polymer/solution interface [145, 146]. Combining the properties of the Pt nanoparticles and of the polypyrrole, a synergistic effect between Pt nanoparticles and polypyrrole will promote the charge carrier separation more effectively than the modification of TiO_2 with Pt or polypyrrole alone. Figure 7 summarizes the proposed mechanism and the pathways as follows: (1) photogeneration of charge carriers, e^- and h^+; (2) trapping of e^- by Pt islands; (3) photogenerated holes channeling by polypyrrole to the polymer/solution interface; (4) first oxidation step of CH_3OH; (5) reduction of H^+; (6) formation of HCHO through e^- injection into the conduction band of TiO_2 (current-doubling); (7) recombination channel. Note, these steps are not mentioned in ordered manner; in fact the photocatalytic process is rather complex including the competition between all different processes.

TiO_2 exists mainly in three crystal phases: anatase, rutile, and brookite and it is commonly employed as a photocatalyst for hydrogen production from aqueous methanol solutions [147, 148]. Based upon the majority of the current scientific reports, it seems that anatase is the most active phase for the photocatalytic hydrogen production while rutile hardly photocatalyzes the hydrogen formation due to the fact that its conduction band potential almost coincides with the potential required for the hydrogen evolution [149]. Thus, in comparison with the anatase phase, the driving force for the H^+ reduction on rutile is very small or even absent (see Fig. 4a). In general, any negative shift of the conduction band potential is expected to raise the photocatalytic hydrogen production rate. In fact, this has been observed for brookite [24]. An examination of the flatband potential and the quasi Fermi level of both, the anatase and the brookite TiO_2 phase employing impedance spectroscopy and photovoltage measurements, respectively, indicates that the potential of the conduction band electrons in the brookite phase is positioned more cathodically by approximately 140 mV than that of anatase (assuming that the flatband potential and the quasi-Fermi level are a direct measure of the lower edge of the conduction band) [24]. This cathodic shift of the flatband potential is, therefore, expected to favor reduction reactions initiated by the conduction band

electrons such as the photocatalytic hydrogen production. Consequently, brookite exhibits enhanced photocatalytic activity as compared with anatase for the sacrificial photocatalytic hydrogen production.

4.2 Mechanistic Investigations

Methanol is frequently used as an electron donor in the so-called sacrificial systems for the photocatalytic H_2 production; however, only few mechanistic studies of this system have been published [85, 86]. Some reports describe the photocatalytic H_2 production from aqueous methanol solutions as water splitting [150–154], while other reports describe the process as dehydrogenation of methanol to formaldehyde or reforming of methanol to carbon dioxide [88, 155]. A recent report even states that the water splitting reaction can be assisted by using low methanol concentrations with molecular oxygen being formed simultaneously. Moreover, the amount of evolved hydrogen gas was reported to exceed the amount expected from the complete reforming of methanol [154]. Apparently, water photooxidation seems to compete with the methanol photooxidation. During long-term investigations of the photocatalytically evolved gases from a 0.03 M aqueous methanol suspension of platinized TiO_2-P25 photocatalysts, it was observed that only H_2 and CO_2 are formed [156]. No traces of CO, O_2, or CH_4 were detected employing a very sensitive quadrupole mass spectrometer (QMS). The ratio of evolved H_2 to CO_2 was calculated to be ca. 3 to 1. Moreover, the amount of H_2 formed was found to be equal to the amount expected from the complete reforming of methanol, evincing that methanol is acting as a sacrificial reagent and that the amount of H_2 evolved does not exceed the amount expected from the complete consumption of methanol. These results exclude the possibility of water splitting on Pt-loaded TiO_2-P25 even in the presence of low concentrations of methanol.

The origin of the evolved hydrogen gas has moreover been identified by carrying out a series of photocatalytic hydrogen production tests employing the following (deuterated) water and (deuterated) methanol mixtures: (a) CH_3OH/H_2O, (b) CD_3OD/D_2O, (c) CD_3OD/H_2O, and (d) CH_3OH/D_2O. Carrying out a detailed analysis of the evolved gases, i.e., H_2, HD, and D_2, revealed that in cases (a) and (b) only H_2 and D_2 are detected. In case (c), when a CD_3OD/H_2O mixture was employed, the evolved gas was mainly H_2 evincing that the evolved H_2 is formed by the reduction of H^+ mainly originating from H_2O. If H_2 would originate from methanol, a notable amount of HD, at least, should be detected supposing that methanol will be photooxidized by hydrogen abstraction and release of D^+ and/or H^+ [90]. Note that a rapid H^+/D^+ exchange is highly expected. If the released D^+ and H^+ would be directly reduced at the surface of the Pt-co-catalyst, a notable amount of HD gas should be evolved as schematically shown in Fig. 8a. Since the evolved gas was found to be mainly H_2, it is more likely that the photooxidation and the photoreduction take place at separate sites. Most probably, the photogenerated holes are reacting with methanol while, at the same time, the photogenerated

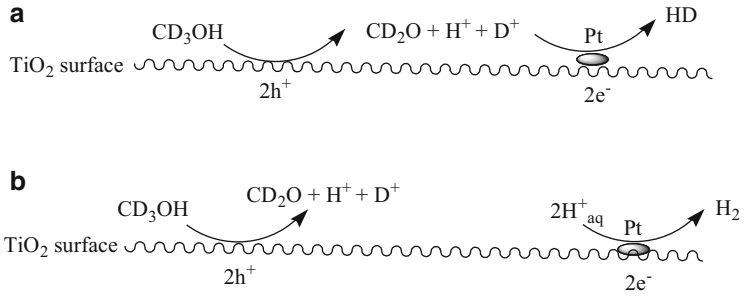

Fig. 8 Proposed mechanism of the photocatalytic H_2 formation from aqueous methanol solutions. Reproduced from Ref. [156]

electrons reduce adsorbed H^+ originating from H_2O as illustrated schematically in Fig. 8b. Consequently, however, even though methanol is acting as a sacrificial reagent, the evolved molecular hydrogen originates from water. It is important to mention here that even though the H_2 is most likely originating from water, this does not mean that indeed a water splitting reaction is being observed! The evolution of only H_2 in case (c), however, where fully deuterated CD_3OD has been employed, can be explained by statistical considerations. The ratio of H to D is calculated for this experiment to be 925 to 1. Hence, the probability of H^+ reduction by conduction band electrons is much higher than the reduction of D^+ formed via the oxidation of CD_3OH by valance band holes taking into consideration the H/D exchange. In case (d) where a CH_3OH/D_2O mixture was employed, the evolved gas is mainly D_2 with a notable amount of H_2 and HD. The detection of H_2 and HD in this case can be explained by the fact that the reduction of H^+ is easier than that of D^+, i.e., it occurs at a more positive potential, thus, the reduction of the former by conduction band electrons competes with the reduction of the later [157]. However, by statistical considerations the amount of H^+ is much smaller than that of D^+ and, thus, D_2 is detected as the main gas component. This confirms that the hydrogen gas photocatalytically evolved from aqueous methanol solutions indeed originates from water.

5 Summary and Outlook

The discovery of appropriate photocatalysts for water splitting process holds the key for successful solar hydrogen production. Until today, the development of a photocatalyst fulfilling all requirements, i.e., (a) good (visible) light absorption; (b) high chemical stability in the dark and under illumination; (c) band edge positions that straddle the water reduction and oxidation potentials; (d) efficient charge transport; (e) low overpotentials for reduction/oxidation of water; and

(f) low cost, has not been discovered. The development of such materials is still very challenging indeed. However, even though many metal oxides, nitrides, oxynitrides, and oxysulfides have been investigated as potential photocatalysts, they are either found to be unstable or to exhibit rather low solar to hydrogen conversion efficiencies. Thus, there is a strong need for basic research in solar photocatalytic water splitting and for more researchers to get involved in the discovery and optimization of these materials. Currently, different organic and inorganic sacrificial reagents are employed in studies concerning solar hydrogen production. This is related to the fact that the simultaneous reduction and oxidation of water is a complex multistep reaction involving four electrons. Using sacrificial molecules as electron donors can improve the H_2 production remarkably, since holes are scavenged by these molecules thus reducing the charge carrier recombination to a great extend. Furthermore, as O_2 is not produced, the back reaction to produce water is suppressed, increasing the H_2 yield and avoiding a subsequent gas separation stage. However, particular care should be taken when selecting suitable sacrificial reagents as their involvement into the overall photocatalytic process is usually highly underestimated! Employing sacrificial reagents, in particular biomass-derived compounds, for hydrogen gas generation could be a useful intermediate step between the current fossil fuel method and the dream of efficient direct water splitting utilizing solar energy. However, suitable construction concepts for solar hydrogen reactors, solar hydrogen chemical plants, as well as technoeconomic analysis of the overall photocatalytic hydrogen production are still needed for realizing the practical application of these concepts in the future.

Acknowledgments Financial support from the BMBF (Bundesministerium für Bildung und Forschung) within the project HyCats (Grant No. 01RC1012C) and from the Gottfried Wilhelm Leibniz University of Hanover within the WiF II project No. 60420974 is gratefully acknowledged. The authors thank Dr. R. Dillert for the stimulating discussions.

References

1. Navarro, R. M.; Sanchez-Sanchez, M. C.; Alvarez-Galvan, M. C.; del Valle, F.; Fierro, J. L. G., Hydrogen production from renewable sources: biomass and photocatalytic opportunities. *Energy Environ. Sci.* **2009,** *2* (1), 35-54.
2. Navarro, R. M.; Pena, M. A.; Fierro, J. L. G., Hydrogen production reactions from carbon feedstocks: Fossils fuels and biomass. *Chem. Rev.* **2007,** *107* (10), 3952-3991.
3. Hamelinck, C. N.; Faaij, A. P. C., Future prospects for production of methanol and hydrogen from biomass. *J. Power Sources* **2002,** *111* (1), 1-22.
4. Fujishima, A.; Honda, K., Electrochemical photolysis of water at a semiconductor electrode. *Nature* **1972,** *238*, 37-38.
5. Mills, A.; Davies, R. H.; Worsley, D., Water-purification by semiconductor photocatalysis. *Chem. Soc. Rev.* **1993,** *22* (6), 417-425.
6. Hoffmann, M. R.; Martin, S. T.; Choi, W. Y.; Bahnemann, D. W., Environmental applications of semiconductor photocatalysis. *Chem. Rev.* **1995,** *95* (1), 69-96.
7. Linsebigler, A. L.; Lu, G. Q.; Yates, J. T., Photocatalysis on TiO_2 surfaces—principles, mechanisms, and selected results. *Chem. Rev.* **1995,** *95* (3), 735-758.

8. Osterloh, F. E., Inorganic materials as catalysts for photochemical splitting of water. *Chem. Mater.* **2008,** *20* (1), 35-54.
9. Kudo, A.; Miseki, Y., Heterogeneous photocatalyst materials for water splitting. *Chem. Soc. Rev.* **2009,** *38* (1), 253-278.
10. van de Krol, R.; Liang, Y.; Schoonman, J., Solar hydrogen production with nanostructured metal oxides. *J. Mater. Chem.* **2008,** *18* (20), 2311-2320.
11. Shimura, K.; Yoshida, H., Heterogeneous photocatalytic hydrogen production from water and biomass derivatives. *Energy Environ. Sci.* **2011,** *4* (7), 2467-2481.
12. Sivula, K.; Le Formal, F.; Gratzel, M., Solar water splitting: Progress using hematite (α-Fe_2O_3) photoelectrodes. *Chemsuschem* **2011,** *4* (4), 432-449.
13. Maeda, K.; Domen, K., Photocatalytic Water splitting: Recent progress and future challenges. *J. Phys. Chem. Lett.* **2010,** *1* (18), 2655-2661.
14. Sato, S.; White, J. M., Photo-decomposition of water over P-TiO_2 catalysts. *Chem. Phys. Lett.* **1980,** *72* (1), 83-86.
15. Maeda, K.; Domen, K., New non-oxide photocatalysts designed for overall water splitting under visible light. *J. Phys. Chem. C* **2007,** *111* (22), 7851-7861.
16. Weber, M. F.; Dignam, M. J., Splitting water with semiconducting photoelectrodes: Efficiency considerations. *Int. J. Hydrogen Energy* **1986,** *11* (4), 225-232.
17. Murphy, A. B.; Barnes, P. R. F.; Randeniya, L. K.; Plumb, I. C.; Grey, I. E.; Horne, M. D.; Glasscock, J. A., Efficiency of solar water splitting using semiconductor electrodes. *Int. J. Hydrogen Energy* **2006,** *31* (14), 1999-2017.
18. Bolton, J. R.; Strickler, S. J.; Connolly, J. S., Limiting and realizable efficiencies of solar photolysis of water. *Nature* **1985,** *316* (6028), 495-500.
19. National Renewable Energy Laboratory (NREL) website: http://rredc.nrel.gov/solar/spectra/
20. Takanabe, K.; Domen, K., Preparation of Inorganic Photocatalytic materials for overall water splitting. *ChemCatChem* **2012,** *4* (10), 1485-1497.
21. James, B. D.; Baum, G. N.; Perez, J.; Baum, K. N. *Technoeconomic Analysis of Photoelectrochemical (PEC) Hydrogen Production*; Final Report; U.S. Department of Energy: December 2009.
22. Memming, R., Photoinduced charge-transfer processes at semiconductor electrodes and particles. In *Electron Transfer I*, 1994; Vol. 169, pp. 105-181.
23. Prieto-Mahaney, O. O.; Murakami, N.; Abe, R.; Ohtani, B., Correlation between photocatalytic activities and structural and physical properties of titanium(IV) oxide Powders. *Chem. Lett.* **2009,** *38* (3), 238-239.
24. Kandiel, T. A.; Feldhoff, A.; Robben, L.; Dillert, R.; Bahnemann, D. W., Tailored titanium dioxide nanomaterials: Anatase nanoparticles and brookite nanorods as highly active photocatalysts. *Chem. Mater.* **2010,** *22* (6), 2050-2060.
25. Mills, A.; Porter, G., Photosensitized dissociation of water using dispersed suspensions of n-type semiconductors. *J. Chem. Soc.-Faraday Trans. I* **1982,** *78*, 3659-3669.
26. Yamaguti, K.; Sato, S., Photolysis of Water over Metallized Powdered Titanium-Dioxide. *J. Chem. Soc.-Faraday Transactions I* **1985,** *81*, 1237-1246.
27. Sayama, K.; Arakawa, H., Significant effect of carbonate addition on stoichiometric photodecomposition of liquid water into hydrogen and oxygen from platinum titanium(IV) oxide suspension. *J. Chem. Soc.-Chem. Commun.* **1992**, (2), 150-152.
28. Kiwi, J.; Gratzel, M., Optimization of conditions for photochemical water cleavage—aqueous Pt/TiO_2 (anatase) dispersions under ultraviolet-light. *J. Phys. Chem.* **1984,** *88* (7), 1302-1307.
29. Abe, T.; Suzuki, E.; Nagoshi, K.; Miyashita, K.; Kaneko, M., Electron source in photoinduced hydrogen production on Pt-supported TiO_2 particles. *J. Phys. Chem. B* **1999,** *103* (7), 1119-1123.
30. Meissner, D.; Memming, R.; Kastening, B.; Bahnemann, D., Fundamental problems of water splitting at cadmium-sulfide. *Chem. Phys. Lett.* **1986,** *127* (5), 419-423.
31. Williams, R., Becquerel photovoltaic effect in binary compounds. *J. Chem. Phys.* **1960,** *32* (5), 1505-1514.

32. Ellis, A. B.; Kaiser, S. W.; Bolts, J. M.; Wrighton, M. S., Study of n-type semiconducting cadmium chalcogenide-based photoelectrochemical cells employing polychalcogenide electrolytes. *J. Am. Chem. Soc.* **1977,** *99* (9), 2839-2848.
33. Abe, R.; Sayama, K.; Sugihara, H., Development of new photocatalytic water splitting into H_2 and O_2 using two different semiconductor photocatalysts and a shuttle redox mediator IO3 (-)/I. *J. Phys. Chem. B* **2005,** *109* (33), 16052-16061.
34. Kudo, A.; Omori, K.; Kato, H., A novel aqueous process for preparation of crystal form-controlled and highly crystalline $BiVO_4$ powder from layered vanadates at room temperature and its photocatalytic and photophysical properties. *J. Am. Chem. Soc.* **1999,** *121* (49), 11459-11467.
35. Kato, H.; Kobayashi, H.; Kudo, A., Role of Ag^+ in the band structures and photocatalytic properties of $AgMO_3$ (M: Ta and Nb) with the perovskite structure. *J. Phys. Chem. B* **2002,** *106* (48), 12441-12447.
36. Kato, H.; Kudo, A., Visible-light-response and photocatalytic activities of TiO_2 and $SrTiO_3$ photocatalysts codoped with antimony and chromium. *J. Phys. Chem. B* **2002,** *106* (19), 5029-5034.
37. Kim, H. G.; Borse, P. H.; Choi, W.; Lee, J. S., Photocatalytic nanodiodes for visible-light photocatalysis. *Ange. Chem. Inter. Ed.* **2005,** *44* (29), 4585-4589.
38. Scaife, D. E., Oxide semiconductors in photoelectrochemical conversion of solar energy. *Sol. Energy* **1980,** *25* (1), 41-54.
39. Maeda, K.; Takata, T.; Hara, M.; Saito, N.; Inoue, Y.; Kobayashi, H.; Domen, K., GaN : ZnO solid solution as a photocatalyst for visible-light-driven overall water splitting. *J. Am. Chem. Soc.* **2005,** *127* (23), 8286-8287.
40. Maeda, K.; Teramura, K.; Takata, T.; Hara, M.; Saito, N.; Toda, K.; Inoue, Y.; Kobayashi, H.; Domen, K., Overall water splitting on $(Ga_{1-x}Zn_x)(N_{1-x}O_x)$ solid solution photocatalyst: Relationship between physical properties and photocatalytic activity. *J. Phys. Chem. B* **2005,** *109* (43), 20504-20510.
41. Teramura, K.; Maeda, K.; Saito, T.; Takata, T.; Saito, N.; Inoue, Y.; Domen, K., Characterization of ruthenium oxide nanocluster as a cocatalyst with $(Ga_{1-x}Zn_x)(N_{1-x}O_x)$ for photocatalytic overall water splitting. *J. Phys. Chem. B* **2005,** *109* (46), 21915-21921.
42. Hirai, T.; Maeda, K.; Yoshida, M.; Kubota, J.; Ikeda, S.; Matsumura, M.; Domen, K., Origin of visible light absorption in GaN-Rich $(Ga_{1-x}Zn_x)(N_{1-x}O_x)$ photocatalysts. *J. Phys. Chem. C* **2007,** *111* (51), 18853-18855.
43. Sun, X.; Maeda, K.; Le Faucheur, M.; Teramura, K.; Domen, K., Preparation of (Ga1-xZnx) $(N_{1-x}O_x)$ solid-solution from $ZnGa_2O_4$ and ZnO as a photo-catalyst for overall water splitting under visible light. *Appl. Catal. A-Gen.* **2007,** *327* (1), 114-121.
44. Maeda, K.; Teramura, K.; Domen, K., Effect of post-calcination on photocatalytic activity of $(Ga_{1-x}Zn_x)(N_{1-x}O_x)$ solid solution for overall water splitting under visible light. *J. Catal.* **2008,** *254* (2), 198-204.
45. Daling Lu, T. T., Nobuo Saito,; Yasunobu Inoue, K. D., Photocatalyst releasing hydrogen from water. *Nature* **2006,** *440* (16), 295.
46. Abe, R.; Higashi, M.; Domen, K., Facile fabrication of an efficient oxynitride TaON photoanode for overall water splitting into H_2 and O_2 under visible light irradiation. *J. Am. Chem. Soc.* **2010,** *132* (34), 11828-11829.
47. Maeda, K.; Domen, K., Solid solution of GaN and ZnO as a stable photocatalyst for overall water splitting under visible light. *Chem. Mater.* **2010,** *22* (3), 612-623.
48. Maeda, K.; Higashi, M.; Siritanaratkul, B.; Abe, R.; Domen, K., $SrNbO_2N$ as a Water-Splitting Photoanode with a Wide Visible-Light Absorption Band. *J. Am. Chem. Soc.* **2011,** *133* (32), 12334-12337.
49. Kasahara, A.; Nukumizu, K.; Hitoki, G.; Takata, T.; Kondo, J. N.; Hara, M.; Kobayashi, H.; Domen, K., Photoreactions on $LaTiO_2N$ under visible light irradiation. *J. Phys. Chem. A* **2002,** *106* (29), 6750-6753.

50. Hitoki, G.; Takata, T.; Kondo, J. N.; Hara, M.; Kobayashi, H.; Domen, K., An oxynitride, TaON, as an efficient water oxidation photocatalyst under visible light irradiation ($\lambda \leq 500$ nm). *Chem. Commun.* **2002,** (16), 1698-1699.
51. Hara, M.; Chiba, E.; Ishikawa, A.; Takata, T.; Kondo, J. N.; Domen, K., Ta_3N_5 and TaON thin films on Ta foil: Surface composition and stability. *J. Phys. Chem. B* **2003,** *107* (48), 13441-13445.
52. Hara, M.; Nunoshige, J.; Takata, T.; Kondo, J. N.; Domen, K., Unusual enhancement of H_2 evolution by Ru on TaON photocatalyst under visible light irradiation. *Chem. Commun.* **2003,** (24), 3000-3001.
53. Ishikawa, A.; Takata, T.; Kondo, J. N.; Hara, M.; Kobayashi, H.; Domen, K., Oxysulfide $Sm_2Ti_2S_2O_5$ as a stable photocatalyst for water oxidation and reduction under visible light irradiation ($\lambda \leq 650$ nm). *J. Am. Chem. Soc.* **2002,** *124* (45), 13547-13553.
54. Abe, R.; Takata, T.; Sugihara, H.; Domen, K., Photocatalytic overall water splitting under visible light by TaON and WO_3 with an IO_3^-/I^- shuttle redox mediator. *Chem. Commun.* **2005,** (30), 3829-3831.
55. Sato, J.; Kobayashi, H.; Ikarashi, K.; Saito, N.; Nishiyama, H.; Inoue, Y., Photocatalytic activity for water decomposition of RuO_2-dispersed Zn_2GeO_4 with d^{10} configuration. *J. Phys. Chem. B* **2004,** *108* (14), 4369-4375.
56. Sato, J.; Saito, N.; Nishiyama, H.; Inoue, Y., Photocatalytic activity for water decomposition of indates with octahedrally coordinated d^{10} configuration. I. Influences of preparation conditions on activity. *J. Phys. Chem. B* **2003,** *107* (31), 7965-7969.
57. Sato, J.; Saito, N.; Nishiyama, H.; Inoue, Y., New photocatalyst group for water decomposition of RuO_2-loaded p-block metal (In, Sn, and Sb) oxides with d^{10} configuration. *J. Phys. Chem. B* **2001,** *105* (26), 6061-6063.
58. Ikarashi, K.; Sato, J.; Kobayashi, H.; Saito, N.; Nishiyama, H.; Inoue, Y., Photocatalysis for water decomposition by RuO_2-dispersed $ZnGa_2O_4$ with d^{10} configuration. *J. Phys. Chem. B* **2002,** *106* (35), 9048-9053.
59. Wei, S. H.; Zunger, A., Role of metal d-states in II–VI semiconductors. *Phys. Review B* **1988,** *37* (15), 8958-8981.
60. Maeda, K.; Teramura, K.; Lu, D. L.; Saito, N.; Inoue, Y.; Domen, K., Noble-metal/Cr_2O_3 core/shell nanoparticles as a cocatalyst for photocatalytic overall water splitting. *Angew. Chem.-Int. Edit.* **2006,** *45* (46), 7806-7809.
61. Maeda, K.; Lu, D.; Teramura, K.; Domen, K., Direct deposition of nanoparticulate rhodium-chromium mixed-oxides on a semiconductor powder by band-gap irradiation. *J. Mater. Chem.* **2008,** *18* (30), 3539-3542.
62. Zhang, L. W.; Baumanis, C.; Robben, L.; Kandiel, T.; Bahnemann, D., Bi_2WO_6 Inverse opals: Facile fabrication and efficient visible-light-driven photocatalytic and photoelectrochemical water-splitting activity. *Small* **2011,** *7* (19), 2714-2720.
63. Wang, X.; Maeda, K.; Thomas, A.; Takanabe, K.; Xin, G.; Carlsson, J. M.; Domen, K.; Antonietti, M., A metal-free polymeric photocatalyst for hydrogen production from water under visible light. *Nat. Mater.* **2009,** *8* (1), 76-80.
64. Kawai, T.; Sakata, T., Conversion of carbohydrate into hydrogen fuel by a photocatalytic process. *Nature* **1980,** *286* (5772), 474-476.
65. Domen, K.; Naito, S.; Onishi, T.; Tamaru, K., Photocatalytic hydrogen-production from a mixture of water and 2-propanol on some semiconductors. *Chem. Lett.* **1982,** (4), 555-558.
66. Kanno, H.; Yamamoto, Y.; Harada, H., TiO_2-based photocatalysts prepared from titanium isopropoxide and aqueous-electrolyte solutions. *Chem. Phys. Lett.* **1985,** *121* (3), 245-248.
67. Cihlar, J.; Bartonickova, E., Low-temperature sol-gel synthesis of anatase nanoparticles modified by Au, Pd and Pt and activity of TiO_2/Au, Pd, Pt photocatalysts in water splitting. *J. Sol-Gel Sci. Technol. 65* (3), 430-442.
68. Tran, P. D.; Xi, L. F.; Batabyal, S. K.; Wong, L. H.; Barber, J.; Loo, J. S. C., Enhancing the photocatalytic efficiency of TiO_2 nanopowders for H_2 production by using non-noble transition metal co-catalysts. *Phys. Chem. Chem. Phys. 14* (33), 11596-11599.

69. Ma, B. J.; Kim, J. S.; Choi, C. H.; Woo, S. I., Enhanced hydrogen generation from methanol aqueous solutions over $Pt/MoO_3/TiO_2$ under ultraviolet light. *Inter. J. Hydrogen Energy 38* (9), 3582-3587.
70. Lee, S. G.; Lee, S.; Lee, H. I., Photocatalytic production of hydrogen from aqueous solution containing CN^- as a hole scavenger. *Appl. Catal. a-Gen.* **2001,** *207* (1-2), 173-181.
71. Buhler, N.; Meier, K.; Reber, J. F., Photochemical hydrogen-production with cadmium-sulfide suspensions. *J. Phys. Chem.* **1984,** *88* (15), 3261-3268.
72. Wang, Y. B.; Wang, Y. S.; Xu, R., Photochemical deposition of Pt on CdS for H_2 evolution from water: Markedly enhanced activity by controlling Pt reduction environment. *J. Phys. Chem. C 117* (2), 783-790.
73. Yao, W. F.; Song, X. L.; Huang, C. P.; Xu, Q. J.; Wu, Q., Enhancing solar hydrogen production via modified photochemical treatment of Pt/CdS photocatalyst. *Catal. Today 199*, 42-47.
74. Bao, N. Z.; Shen, L. M.; Takata, T.; Domen, K., Self-templated synthesis of nanoporous CdS nanostructures for highly efficient photocatalytic hydrogen production under visible. *Chem. Mater.* **2008,** *20* (1), 110-117.
75. Zong, X.; Yan, H. J.; Wu, G. P.; Ma, G. J.; Wen, F. Y.; Wang, L.; Li, C., Enhancement of photocatalytic H_2 evolution on CdS by loading MOS_2 as cocatalyst under visible light irradiation. *J. Am. Chem. Soc.* **2008,** *130* (23), 7176-7177.
76. Frame, F. A.; Osterloh, F. E., CdSe-MoS_2: A Quantum size-confined photocatalyst for hydrogen evolution from water under visible light. *J. Phys. Chem. C 114* (23), 10628-10633.
77. Bang, J. U.; Lee, S. J.; Jang, J. S.; Choi, W.; Song, H., Geometric Effect of Single or Double Metal-Tipped CdSe Nanorods on Photocatalytic H_2 Generation. *J. Phys. Chem. Lett. 3* (24), 3781-3785.
78. Holmes, M. A.; Townsend, T. K.; Osterloh, F. E., Quantum confinement controlled photocatalytic water splitting by suspended CdSe nanocrystals. *Chem. Commun.* **2012,** *48* (3), 371-373.
79. Grzyll, L. R.; Thomas, J. J.; Barile, R. G., Photoelectrochemical conversion of hydrogen-sulfide to hydrogen using artificial-light and solar-radiation. *Inter. J. Hydrogen Energy* **1989,** *14* (9), 647-651.
80. Ma, G. J.; Yan, H. J.; Shi, J. Y.; Zong, X.; Lei, Z. B.; Li, C., Direct splitting of H_2S into H_2 and S on CdS-based photocatalyst under visible light irradiation. *J. Catal.* **2008,** *260* (1), 134-140.
81. Jang, J. S.; Kim, H. G.; Borse, P. H.; Lee, J. S., Simultaneous hydrogen production and decomposition of H2S dissolved in alkaline water over CdS-TiO_2 composite photocatalysts under visible light irradiation. *Inter. J. Hydrogen Energy* **2007,** *32* (18), 4786-4791.
82. Chen, X. B.; Shen, S. H.; Guo, L. J.; Mao, S. S., Semiconductor-based photocatalytic hydrogen generation. *Chem. Rev.* **2010,** *110* (11), 6503-6570.
83. Kawai, T.; Sakata, T., Photocatalytic hydrogen-production from liquid methanol and water. *J. Chem. Soc.-Chem. Commun.* **1980,** (15), 694-695.
84. Lin, W. C.; Yang, W. D.; Huang, I. L.; Wu, T. S.; Chung, Z. J., Hydrogen production from methanol/water photocatalytic decomposition using $Pt/TiO_{2-x}N_x$ catalyst. *Energy & Fuels* **2009,** *23*, 2192-2196.
85. Chen, J.; Ollis, D. F.; Rulkens, W. H.; Bruning, H., Photocatalyzed oxidation of alcohols and organochlorides in the presence of native TiO_2 and metallized TiO_2 suspensions. Part (I): Photocatalytic activity and pH influence. *Water Research* **1999,** *33* (3), 661-668.
86. Chen, J.; Ollis, D. F.; Rulkens, W. H.; Bruning, H., Photocatalyzed oxidation of alcohols and organochlorides in the presence of native TiO_2 and metallized TiO_2 suspensions. Part (II): Photocatalytic mechanisms. *Water Res.* **1999,** *33* (3), 669-676.
87. Wang, C. Y.; Rabani, J.; Bahnemann, D. W.; Dohrmann, J. K., Photonic efficiency and quantum yield of formaldehyde formation from methanol in the presence of various TiO_2 photocatalysts. *J. Photochem. Photobiol. A-Chem.* **2002,** *148* (1-3), 169-176.
88. Wang, C. Y.; Pagel, R.; Bahnemann, D. W.; Dohrmann, J. K., Quantum yield of formaldehyde formation in the presence of colloidal TiO_2-based photocatalysts: Effect of intermittent

illumination, platinization, and deoxygenation. *J. Phys. Chem. B* **2004,** *108* (37), 14082-14092.
89. Wang, C. Y.; Groenzin, H.; Shultz, M. J., Direct observation of competitive adsorption between methanol and water on TiO_2: An in situ sum-frequency generation study. *J. Am. Chem. Soc.* **2004,** *126* (26), 8094-8095.
90. Sun, L. Z.; Bolton, J. R., Determination of the quantum yield for the photochemical generation of hydroxyl radicals in TiO_2 suspensions. *J. Phys. Chem.* **1996,** *100* (10), 4127-4134.
91. Hykaway, N.; Sears, W. M.; Morisaki, H.; Morrison, S. R., Current-doubling reactions on titanium-dioxide photoanodes. *J. Phys. Chem.* **1986,** *90* (25), 6663-6667.
92. Nogami, G.; Kennedy, J. H., Investigation of current doubling mechanism of organic-compounds by the rotating-ring disk electrode technique. *J. Electrochem. Soc.* **1989,** *136* (9), 2583-2588.
93. Villarreal, T. L.; Gomez, R.; Neumann-Spallart, M.; Alonso-Vante, N.; Salvador, P., Semi-conductor photooxidation of pollutants dissolved in water: A kinetic model for distinguishing between direct and indirect interfacial hole transfer. I. Photoelectrochemical experiments with polycrystalline anatase electrodes under current doubling and absence of recombination. *J. Phys. Chem. B* **2004,** *108* (39), 15172-15181.
94. Asmus, K. D.; Mockel, H.; Henglein, A., Pulse radiolytic study of Site of OH radical attack on aliphatic alcohols in aqueous-solution. *J. Phys. Chem.* **1973,** *77* (10), 1218-1221.
95. Tamaki, Y.; Furube, A.; Murai, M.; Hara, K.; Katoh, R.; Tachiya, M., Direct observation of reactive trapped holes in TiO_2 undergoing photocatalytic oxidation of adsorbed alcohols: Evaluation of the reaction rates and yields. *J. Am. Chem. Soc.* **2006,** *128* (2), 416-417.
96. Weber, M. F.; Dignam, M. J., Efficiency of splitting water with semiconducting photoelectrodes. *J. Electrochem. Soc.* **1984,** *131* (6), 1258-1265.
97. Bahnemann, D.; Henglein, A.; Lilie, J.; Spanhel, L., Flash-photolysis observation of the absorption-spectra of trapped positive holes and electrons in colloidal TiO_2. *J. Phys. Chem.* **1984,** *88* (4), 709-711.
98. Imanishi, A.; Tsuji, E.; Nakato, Y., Dependence of the work function of TiO_2 (Rutile) on crystal faces, studied by a scanning auger microprobe. *J. Phys. Chem. C* **2007,** *111* (5), 2128-2132.
99. Eastman, D. E., Photoelectric work functions of transition, rare-earth, and noble metals. *Phys. Rev. B* **1970,** *2* (1), 1-&.
100. Anpo, M.; Takeuchi, M., The design and development of highly reactive titanium oxide photocatalysts operating under visible light irradiation. *J. Catal.* **2003,** *216* (1-2), 505-516.
101. Furube, A.; Asahi, T.; Masuhara, H.; Yamashita, H.; Anpo, M., Direct observation of a picosecond charge separation process in photoexcited platinum-loaded TiO_2 particles by femtosecond diffuse reflectance spectroscopy. *Chem. Phys. Lett.*. **2001,** *336* (5-6), 424-430.
102. Bahnemann, D.; Henglein, A.; Spanhel, L., Detection of the intermediates of colloidal TiO_2-catalyzed photoreactions. *Faraday Discussions* **1984,** *78*, 151-163.
103. Erdey-Gruz, T.; Volmer, M., Zur theorie der wasserstoffüberspannung. *Z. Phys. Chem.* **1930,** *150*, 203-213.
104. Heyrovsky, J., Eine Theorie der Überspannung. *Rec. Trav. Chim. Pays-Bas* **1925,** *44*, 499-513.
105. Tafel, J., Über die Polarisation bei kathodischer Wasserstoffentwicklung. *Z. Phys. Chem.* **1905,** *50*, 641-712.
106. Kasarevic-Popovic, Z.; Behar, D.; Rabani, J., Role of excess electrons in TiO_2 nanoparticles coated with Pt in reduction reactions studied in radiolysis of aqueous solutions. *J. Phys. Chem. B* **2004,** *108* (52), 20291-20295.
107. Mizukoshi, Y.; Makise, Y.; Shuto, T.; Hu, J. W.; Tominaga, A.; Shironita, S.; Tanabe, S., Immobilization of noble metal nanoparticles on the surface of TiO_2 by the sonochemical method: Photocatalytic production of hydrogen from an aqueous solution of ethanol. *Ultrason. Sonochem.* **2007,** *14* (3), 387-392.

108. Bamwenda, G. R.; Tsubota, S.; Nakamura, T.; Haruta, M., Photoassisted hydrogen-production from a water-ethanol solution—a Comparison of activities of Au-TiO_2 and Pt-TiO_2. *J. Photochem. Photobiol. A-Chem.* **1995,** *89* (2), 177-189.
109. Jang, J. S.; Ji, S. M.; Bae, S. W.; Son, H. C.; Lee, J. S., Optimization of CdS/TiO_2 nano-bulk composite photocatalysts for hydrogen production from Na_2S/Na_2SO_3 aqueous electrolyte solution under visible light ($\lambda \geq 420$ nm). *J. Photochem. Photobiol. A-Chem.* **2007,** *188* (1), 112-119.
110. Behar, D.; Rabani, J., Kinetics of hydrogen production upon reduction of aqueous TiO_2 nanoparticles catalyzed by Pd^0, Pt^0, or Au^0 coatings and an unusual hydrogen abstraction; Steady state and pulse radiolysis study. *J. Phys. Chem. B* **2006,** *110* (17), 8750-8755.
111. Fang, J.; Cao, S. W.; Wang, Z.; Shahjamali, M. M.; Loo, S. C. J.; Barber, J.; Xue, C., Mesoporous plasmonic Au-TiO_2 nanocomposites for efficient visible-light-driven photocatalytic water reduction. *Inter. J. Hydrogen Energy 37* (23), 17853-17861.
112. Ingram, D. B.; Linic, S., Water splitting on composite plasmonic-metal/semiconductor photoelectrodes: Evidence for selective plasmon-induced formation of charge carriers near the semiconductor surface. *J. Am. Chem. Soc. 133* (14), 5202-5205.
113. Saadi, S.; Bouguelia, A.; Derbal, A.; Trari, M., Hydrogen photoproduction over new catalyst $CuLaO_2$. *J. Photochem. Photobiol. A-Chem.* **2007,** *187* (1), 97-104.
114. Peng, T. Y.; Li, K.; Zeng, P.; Zhang, Q. G.; Zhang, X. G., Enhanced photocatalytic hydrogen production over graphene oxide-cadmium sulfide nanocomposite under visible light irradiation. *J. Phys. Chem. C 116* (43), 22720-22726.
115. Boudjemaa, A.; Bouarab, R.; Saadi, S.; Bouguelia, A.; Trari, M., Photoelectrochemical H_2-generation over Spinel $FeCr_2O_4$ in X^{2-} solutions ($X^{2-} = S^{2-}$ and SO_3^{2-}). *Appl. Energy* **2009,** *86* (7-8), 1080-1086.
116. Zhang, J.; Yu, J. G.; Jaroniec, M.; Gong, J. R., Noble metal-free reduced graphene oxide-$Zn_xCd_{1-x}S$ nanocomposite with enhanced solar photocatalytic H_2 production performance. *Nano Lett. 12* (9), 4584-4589.
117. Tsuji, I.; Kato, H.; Kobayashi, H.; Kudo, A., Photocatalytic H_2 evolution reaction from aqueous solutions over band structure-controlled $(AgIn)_xZn_{2(1-x)}S_2$ solid solution photocatalysts with visible-light response and their surface nanostructures. *J. Am. Chem. Soc.* **2004,** *126* (41), 13406-13413.
118. Chen, S. Y.; Wang, L. W., Thermodynamic oxidation and reduction potentials of photocatalytic semiconductors in aqueous solution. *Chem. Mater.* **2012,** *24* (18), 3659-3666.
119. Minoura, H.; Tsuiki, M., Anodic reactions of several reducing agents on illuminated cadmium-sulfide electrode. *Electrochim. Acta* **1978,** *23* (12), 1377-1382.
120. Wardman, P., Reduction potentials of one-electron couples involving free-radicals in aqueous-solution. *J. Phys. Chem. Ref. Data* **1989,** *18* (4), 1637-1755.
121. Watanabe, T.; Fujishim.A; Honda, K. I., Potential variation at semiconductor-electrolyte interface through a change in ph of solution. *Chem. Lett.* **1974,** (8), 897-900.
122. Inoue, T.; Watanabe, T.; Fujishima, A.; Honda, K., investigation of CdS photoanode reaction in the electrolyte solution containing sulfide ion. *Bull. Chem. Soc. Jpn* **1979,** *52* (5), 1243-1250.
123. Yan, H. J.; Yang, J. H.; Ma, G. J.; Wu, G. P.; Zong, X.; Lei, Z. B.; Shi, J. Y.; Li, C., Visible-light-driven hydrogen production with extremely high quantum efficiency on Pt-PdS/CdS photocatalyst. *J. Catal.* **2009,** *266* (2), 165-168.
124. Kambe, S.; Fujii, M.; Kawai, T.; Kawai, S.; Nakahara, F., Photocatalytic hydrogen-production with Cd(S, Se) solid-solution particles—determining factors for the highly efficient photocatalyst. *Chem. Phys. Lett.* **1984,** *109* (1), 105-109.
125. Frame, F. A.; Carroll, E. C.; Larsen, D. S.; Sarahan, M.; Browning, N. D.; Osterloh, F. E., First demonstration of CdSe as a photocatalyst for hydrogen evolution from water under UV and visible light. *Chem. Commun.* **2008,** (19), 2206-2208.
126. Harris, C.; Kamat, P. V., Photocatalytic events of CdSe quantum dots in confined media. electrodic behavior of coupled platinum nanoparticles. *Acs Nano* **2010,** *4* (12), 7321-7330.

127. Zhou, Z. H.; Shi, J. W.; Wu, P.; Li, M. T.; Guo, L. J., First-principles study on absolute band edge positions for II-VI semiconductors at (110) surface. *Chem. Phys. Lett. 513* (1-3), 72-76.
128. Gerischer, H., The impact of semiconductors on the concepts of electrochemistry. *Electrochim. Acta* **1990,** *35* (11-12), 1677-1699.
129. Alonso-Tellez, A.; Robert, D.; Keller, N.; Keller, V., A parametric study of the UV-A photocatalytic oxidation of H_2S over TiO_2. *Appl. Catal. B-Environ.* **2012,** *115*, 209-218.
130. Portela, R.; Suarez, S.; Rasmussen, S. B.; Arconada, N.; Castro, Y.; Duran, A.; Avila, P.; Coronado, J. M.; Sanchez, B., Photocatalytic-based strategies for H_2S elimination. *Catal. Today* **2010,** *151* (1-2), 64-70.
131. Canela, M. C.; Alberici, R. M.; Jardim, W. F., GaS-phase destruction of H_2S using TiO_2/UV-VIS. *J. Photochem. Photobiol. A-Chem.* **1998,** *112* (1), 73-80.
132. Tambwekar, S. V.; Subrahmanyam, M., Photocatalytic generation of hydrogen from hydrogen sulfide: An energy bargain. *Inter. J. Hydrogen Energy* **1997,** *22* (10-11), 959-965.
133. Boragarello E, K. K., Gratzel M, Visible light induced generation of hydrogen from hydrogen sulfide in cadmium sulfide dispersions with hole transfer catalysis by ruthenium(IV) oxide. *Helv Chim Acta* **1982,** *65*, 243-248.
134. Szynkarczuk, J.; Komorowski, P. G.; Donini, J. C., Redox reactions of hydrosulfide ions on the platinum-electrode. 1. the presence of intermediate polysulfide ions and sulfur layers. *Electrochim. Acta* **1994,** *39* (15), 2285-2289.
135. Bard, A. J.; Parsons, R.; Jordan, J., Standard potentials in aqueous solution. New York and Basel, 1985.
136. Hara, K.; Sayama, K.; Arakawa, H., Photocatalytic hydrogen and oxygen formation over SiO_2-supported RuS_2 in the presence of sacrificial donor and acceptor. *Appl. Catal. A-Gen.* **1999,** *189* (1), 127-137.
137. Tang, J. W.; Ye, J. H., Correlation of crystal structures and electronic structures and photocatalytic properties of the W-containing oxides. *J. Mater. Chem.* **2005,** *15* (39), 4246-4251.
138. Ohmori, T.; Takahashi, H.; Mametsuka, H.; Suzuki, E., Photocatalytic oxygen evolution on alpha-Fe_2O_3 films using Fe^{3+} ion as a sacrificial oxidizing agent. *Phys. Chem. Chem. Phys.* **2000,** *2* (15), 3519-3522.
139. Kim, W.; Tachikawa, T.; Majima, T.; Choi, W., Photocatalysis of dye-sensitized TiO_2 nanoparticles with thin overcoat of Al_2O_3: Enhanced activity for H_2 production and Dechlorination of CCl_4. *J. Phys. Chem. C* **2009,** *113* (24), 10603-10609.
140. Minero, C.; Piccinini, P.; Calza, P.; Pelizzetti, E., Photocatalytic reduction/oxidation processes occurring at the carbon and nitrogen of tetranitromethane. *New J. Chem.* **1996,** *20* (11), 1159-1164.
141. Nadtochenko, V.; Denisov, N.; Gorenberg, A.; Kozlov, Y.; Chubukov, P.; Rengifo, J. A.; Pulgarin, C.; Kiwi, J., Correlations for photocatalytic activity and spectral features of the absorption band edge of TiO_2 modified by thiourea. *Appl. Catal. B-Environ.* **2009,** *91* (1-2), 460-469.
142. Ferry, J. L.; Glaze, W. H., Photocatalytic reduction of nitroorganics over illuminated titanium dioxide: Electron transfer between excited-state TiO_2 and nitroaromatics. *J. Phys. Chem. B* **1998,** *102* (12), 2239-2244.
143. Kandiel, T. A.; Dillert, R.; Bahnemann, D. W., Enhanced photocatalytic production of molecular hydrogen on TiO_2 modified with Pt-polypyrrole nanocomposites. *Photochem. Photobiol. Sci.* **2009,** *8* (5), 683-690.
144. Deki, S.; Nishikawa, H.; Mizuhata, M., Fabrication of Pt nanoparticles-polypyrrole composite for electrocatalyst. *Electrochem.* **2004,** *72* (6), 415-417.
145. Frank, A. J.; Honda, K., Polymer-modified electrodes, catalysis and water-splitting reactions. *J. Photochem.* **1985,** *29* (1-2), 195-204.
146. Cooper, G.; Noufi, R.; Frank, A. J.; Nozik, A. J., Oxygen evolution on tantalum polypyrrole platinum anodes. *Nature* **1982,** *295* (5850), 578-580.

147. Kandiel, T. A.; Dillert, R.; Robben, L.; Bahnemann, D. W., Photonic efficiency and mechanism of photocatalytic molecular hydrogen production over platinized titanium dioxide from aqueous methanol solutions. *Catal. Today* **2011,** *161* (1), 196-201.
148. Kandiel, T. A.; Ismail, A. A.; Bahnemann, D. W., Mesoporous TiO_2 nanostructures: a route to minimize Pt loading on titania photocatalysts for hydrogen production. *Phys. Chem. Chem. Phys.* **2011,** *13* (45), 20155-20161.
149. Karakitsou, K. E.; Verykios, X. E., Effects of altervalent cation doping of TiO_2 on its performance as a photocatalyst for water cleavage. *J. Phys. Chem.* **1993,** *97* (6), 1184-1189.
150. Junwang Tang, H. Q., and Jinhua Ye, Photocatalytic Properties and Photoinduced Hydrophilicity of Surface-Fluorinated TiO_2. *Chem. Mater. 2007, 19, 116-122* **2007**.
151. Jitputti, J.; Pavasupree, S.; Suzuki, Y.; Yoshikawa, S., Synthesis and photocatalytic activity for water-splitting reaction of nanocrystalline mesoporous titania prepared by hydrothermal method. *J. Sol. State Chem.* **2007,** *180* (5), 1743-1749.
152. Ekambaram, S., Photoproduction of clean H_2 or O_2 from water using oxide semiconductors in presence of sacrificial reagent. *J. All. Comp.* **2008,** *448* (1-2), 238-245.
153. Jitputti, J.; Suzuki, Y.; Yoshikawa, S., Synthesis of TiO_2 nanowires and their photocatalytic activity for hydrogen evolution. *Catal. Commun.* **2008,** *9* (6), 1265-1271.
154. Rosseler, O.; Shankar, M. V.; Du, M. K. L.; Schmidlin, L.; Keller, N.; Keller, V., Solar light photocatalytic hydrogen production from water over Pt and Au/TiO_2(anatase/rutile) photocatalysts: Influence of noble metal and porogen promotion. *J. Catal.* **2010,** *269* (1), 179-190.
155. Highfield, J. G.; Chen, M. H.; Nguyen, P. T.; Chen, Z., Mechanistic investigations of photo-driven processes over TiO_2 by in-situ DRIFTS-MS: Part 1. Platinization and methanol reforming. *Energy Environ. Sci.* **2009,** *2* (9), 991-1002.
156. Kandiel, T. A.; Ivanova, I.; Bahnemann, D. W., Long-term investigation of the photocatalytic hydrogen production on platinized TiO_2: an isotopic study. *Energy Environ. Sci.* **2014,** *7*, 1420-1425.
157. Yasui, S.; Itoh, K.; Ohno, A.; Tokitoh, N., Kinetic deuterium isotope effect in single-electron transfer occurring from tributylphosphine to viologens. *Chem. Lett.* **2001,** (10), 1056-1057.

Electrochemical and Optical Characterization of Materials Band Structure

Suman Parajuli and Mario A. Alpuche-Aviles

1 Introduction

The use of semiconductors (SCs) in solar energy conversion is a direct consequence of the band structure of the materials [1–5]. The relationship between optical and electronic properties of semiconductors enables the conversion of light into electrical or chemical energy. To harvest the potential of solar energy conversion, the different electrochemical and optical properties of the semiconductor must be optimized and this remains a challenge. In this chapter, we present a combination of methods for the experimental characterization of optical and electrochemical properties using a synergist approach in the context of photoelectrochemical production of solar fuels. When light interacts with a semiconductor, a fundamental transition is said to occur; when the photon energy is enough to promote an electron from the valance band (VB) to the conduction band (CB), this is the band-to-band transition (also known as a fundamental absorption) [6]. For solar fuels, a semiconductor should have a bandgap of sufficiently low energy to collect most of the solar spectra while being able to provide sufficient driving force to, for example, split water into hydrogen and oxygen (Table 1).

In this chapter we explain common approaches for the characterization of the bandgap (E_g) and the energy of the conduction (E_{CB}) and valence band (E_{VB}) energies. We note that these parameters are not independent of each other, but rather, are linked by the band structure of the semiconductor, and this fundamental relationship can be used to gain deep understanding of a semiconductor band structure from relatively simple experiments. The band energies correspond to the thermodynamic driving force towards the reaction of interest. For example, in water splitting the valance band energy position will be the driving force towards water oxidation while the conduction band will be the driving force towards H^+ reduction.

S. Parajuli • M.A. Alpuche-Aviles (✉)
Department of Chemistry, University of Nevada Reno, Reno, NV 89557, USA
e-mail: malpuche@unr.edu

B. Viswanathan et al. (eds.), *Materials and Processes for Solar Fuel Production*,
Nanostructure Science and Technology 174, DOI 10.1007/978-1-4939-1628-3_4

Table 1 Summary of the techniques discussed in this review

Property	Technique	Comments
E_g	Optical (e.g., UV Vis)	Absorbance and transmittance methods
	Photocurrent	Photocurrent dependence on wavelength
Band edge (E_{CB} or E_{VB})	Mott–Schottky	Extrapolation of the $1/C_{SC}$ dependence with electrochemical potential
	Photocurrent onset	Extrapolation to the potential of zero photoelectrochemical current
Type (n-type or p-type)	Photocurrent	n-type photooxidizes
		p-type photoreduces
	Mott–Schottky	Sign of the slope of the $1/C_{SC}$ dependence with electrochemical potential

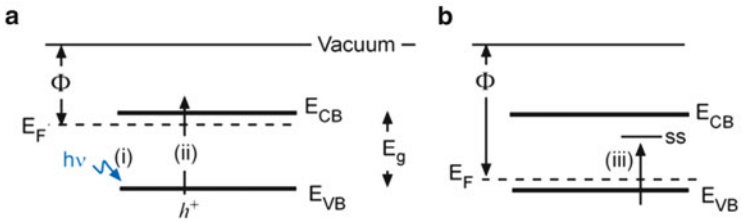

Fig. 1 Schematic diagram of the energy levels in a semiconductor (**a**) an n-type SC and (**b**) the material as in (**a**) but p-type. The figure shows the fundamental optical transition (ii) that occurs upon illumination: photon absorption (i) promotes an electron (e^-) from VB to CB leaving a hole (h^+) in VB. (iii) indicates a transition from the VB to a surface state (ss). Φ = work function, E_F = Fermi level, E_g = bandgap, E_{CB} = conduction band edge, E_{VB} = valence band edge

Because it is often difficult to characterize each of these bands independently, the energy of these positions is determined from the relationship:

$$E_g = E_{CB} - E_{VB} \quad (1)$$

Figure 1 shows the relationships between the different energy levels of interest in a semiconductor. Note that when the material is heavily doped with electrons, i.e., the n-type material, the E_F and E_{CB} are similar (Fig. 1a); for a p-type material, $E_F \approx E_{VB}$ (Fig. 1b). Experimentally, this relationship can be exploited to estimate independently the values of E_{CB} and E_{VB}, although this requires synthetic control of the material doping. Figure 1b also shows the presence of surface states (ss), i.e., energy levels at the surface that have energies different from the states in the bulk of the semiconductor, within the "forbidden," bandgap region.

A word of caution is appropriate about the different scales used in the study of semiconductors. In electrochemistry, the measurements are usually performed with respect to a reference system, such as the Ag/AgCl reference electrode and then they are converted to the standard scale of the normal hydrogen electrode (NHE),

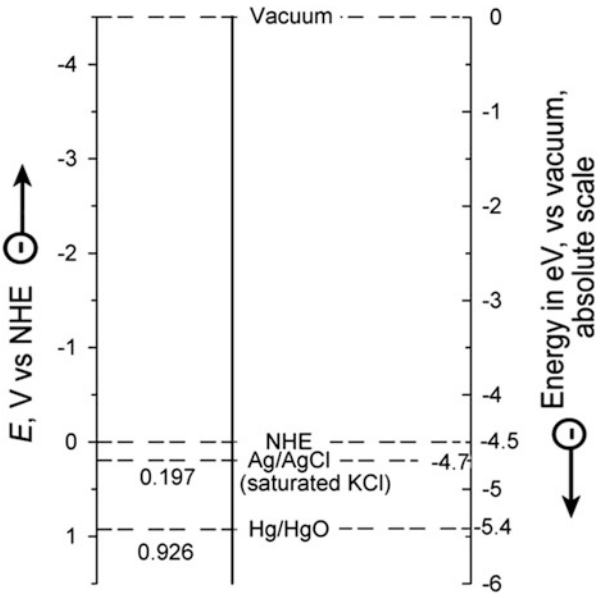

Fig. 2 Comparison of the electrochemical and absolute potential scales. The chart shows the values of the normal hydrogen electrode (NHE), and of two common references used in practice: Ag/AgCl in saturated KCl, and Hg/HgO (used for alkaline solutions)

using equivalencies from tables [4]. In studies of semiconductor in vacuum, the energy of the bands, E_{CB} and E_{VB}, are reported in electron volts, eV, with respect to vacuum, i.e., with vacuum being 0 and lower energies assigned to negative values in eV, e.g., the work function of gold is ca. –5 eV. The consequence of these different definitions is that the solid state scale and the electrochemical scale move in opposite directions. Because the electrochemical scale follows the electrostatic convention, the negative direction in electrochemistry is the higher energy direction, i.e., the positive direction in the solid scale with respect to vacuum. Figure 2 shows the different directions of these scales, and for comparison, the figure shows three points of practical importance: (1) the value of the NHE, which in practice is not frequently used, it is usually replaced by (2) the more practical Ag/AgCl reference, or by (3) the Hg/HgO reference electrode recommended for alkaline solutions [4].

We present a compilation of optical and electrochemical techniques that can be used to characterize the band structure of semiconductor materials in the research for solar fuels. The values of E_{CB} and E_{VB} can be found from electrochemical measurements while E_g is often determined from optical measurements that can also provide additional information about the band structure of the material. Because optical properties can be complicated by the presence of impurities and the so-called traps that can present optical transitions that do not result in band-to-band transitions, electrochemical measurements complement optical measurements by determining which transition results in carriers that can be used to drive reactions across the semiconductor–liquid interface.

2 Optical Characterizations

Optical methods are some of the simplest ways to probe the electronic structure of a semiconductor. Careful measurement of optical properties yields the critical bandgap energy E_g, in addition, the optical properties report on the type of electronic transition that results in photon absorption. The band-to-band transitions must follow certain selection rules that result in different types of transitions: direct-allowed, direct-forbidden, indirect-allowed, etc. Thus, optical measurements can also provide additional information on the band structure of the material [3, 6, 7]. The experimental procedure involves measuring the absorption coefficient, α, defined as [1, 7]:

$$\alpha = \frac{1}{d} \ln \frac{I_o}{I} \tag{2}$$

where $\alpha =$ absorption coefficient, $d =$ thickness of the sample, $I_o =$ incident light intensity, and $I =$ transmitted light intensity. A simple procedure to obtain an approximation of α is to measure the absorbance, A, of a film of known thickness:

$$\alpha = \frac{2.303}{d} A \tag{3}$$

Note that Eq. (2) is the definition of α and Eq. (3) is obtained from the algebraic definition of absorbance. However, application of Eq. (3) from a simple absorbance measurement without corrections from reflectance and scattering provides only approximate results. The calculation of α should be obtained from measurements of film transmittance and reflectance [1, 7]. It is usual to perform these measurements under normal incidence conditions with an integrating sphere. From the equation and a fit to the wavelength dependence of transmittance and reflectance one can obtain α and the refractive index of the material n, also wavelength dependent. In practice, researchers often use Eq. (3), e.g., when absorbance is fitted to a transition-type equation, with the implied approximation that there are no losses of reflectance in the film, or that in suspensions of nanoparticles, the scattering and reflectance is minimal. This approximation would be acceptable if light is efficiently absorbed by the material, i.e., if photon energy, hv, is much larger than the bandgap, E_g, $hv \gg E_g$. The wavelength dependence of α can be used to determine the bandgap and the type of electronic transition that occurs in the semiconductor upon photon absorption.

A plot of α as a function of the photon energy, hv, yields curves that are characteristic of the different types of transition. Near the absorption edge, i.e., at energies where photons are efficiently absorbed to promote an electron from the valence band to the conduction α should vary with respect to hv according to [3, 6, 7]:

Table 2 Transition types and their γ coefficients for Eq. (4)

Transition type	γ	Notes	Ref.
Direct allowed	1/2	$\alpha = 10^4$–10^6 cm^{-1}	[1, 7]
Direct forbidden	3/2	$\alpha < 10^4$ cm^{-1} for E_g ca. 1 eV	[7, 8]
Indirect allowed	2	$\alpha < 10^4$ cm^{-1}	[7, 8]
Indirect forbidden	3		[8]
Indirect transition to exciton	1/2	Exciton: a bound electron–hole pair moving through the crystal as a particle (a quasiparticle)	[3]

$$\alpha \sim \left(h\upsilon - E_g\right)^{\gamma} \tag{4}$$

where γ is a constant that depends on the type of electronic transition in the semiconductor. Equation (4) takes different forms depending on the type of transition, e.g., direct or indirect, but in general, predict an exponential increase in the rate of photon absorption once $h\nu > E_g$. Thus a simple plot of absorbance vs. photon energy is often used to estimate the value of E_g. A more precise measurement for E_g will require a strict measurement of α and its wavelength dependence to then fit the curve to a form of Eq. (3). Table 2 shows a compilation of theoretical values of γ.

The α values for direct allowed transitions result in strong values of α of the order of 10^4–10^6 cm^{-1}. Because of these high absorption coefficients, these materials are of interest in solar energy conversion applications: they are very effective at absorbing light. Here, we briefly describe the basic characteristics of direct bandgap transitions.

When the transition is direct, the absorption of a photon happens with conservation of the momentum of the electron promoted from the valance band to the conduction band. Strictly speaking, the assumption is that the electron wavevector is conserved after absorption of the photon to promote the electron from the CB to the VB, and that the wavevector (or momentum) of the photon is much smaller than the valence band or conduction band electron's wavevector [6]. The result is that the absorption coefficient, α, has some of the strongest values reported in the order of 10^4–10^6 cm^{-1}. The dependence of α on photon energy ($h\nu$) follows Eq. (5) [7, 8]:

$$\alpha = B_a \frac{\left(h\upsilon - E_g\right)^{1/2}}{h\nu} \tag{5}$$

where B_a is a constant that depends on the material, typically of the order of 10^4 cm^{-1}.

In some cases, the quantum mechanical selection rules do not allow the transition to be direct, even though the conduction band minimum and the valence band maximum are aligned in the k-space. The transitions are said to be direct forbidden, and they follow the expression [7, 8]:

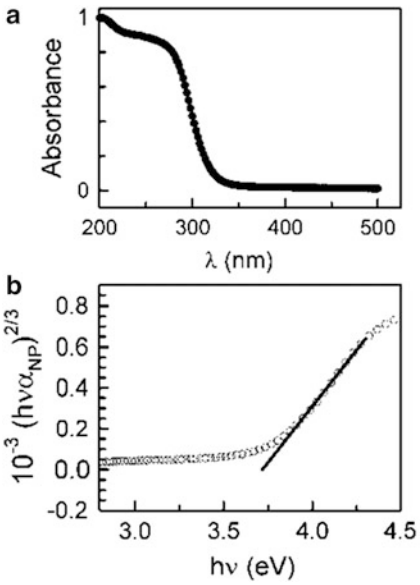

Fig. 3 (**a**) Absorbance of film of Zn_2SnO_4 nanoparticles. The absorbance spectrum was corrected for scattering losses. (**b**) Calculated values of α for the data in (**a**) showing a fit of Eq. (5) with $E_g = 3.7$ eV (——) to the experimental data (∘). Adapted with permission from Ref. [9], *J Am Chem Soc* 2009, *131*, 3216. Copyright 2009, American Chemical Society

$$\alpha = B_f \frac{\left(h\upsilon - E_g\right)^{3/2}}{h\nu} \tag{6}$$

B_f in Eq. (6) is a constant that depends on the material, as is B_a in Eq. (5). The values of B_f are in the order of 10^4 cm^{-1} [7, 8] but note that the shape of Eq. (6) makes the value of α change more slowly with photon energy due to the necessary change in momentum of the electron promoted from the CB to the VB.

Zinc stannate, Zn_2SnO_4, is an example of a material with absorption coefficients that fit Eq. (6) [9, 10] as shown in Fig. 3. The bandgap was determined to be 3.7 eV with a direct-forbidden absorption. The experimental data fitted the direct-forbidden case best than any other model. Calculations also predict that the transition will be direct forbidden [10] because the VB is derived mostly from O p and Sn 4d states while the CB minimum is mostly derived from O 2*s* and Zn 4*s* states which make the transition forbidden [10].

Figure 3 also illustrates that at $h\nu \gg E_g$ the deviation from theory becomes more apparent, a common problem with fitting theory to data. In the derivation of Eqs. (5) and (6) and other equations in the literature [3, 6–8] the main assumptions are that (1) there is one electron in the conduction band and one hole in the valence band; this is the so-called one-electron approximation [6] that neglects charge interactions. Another assumption is (2) that the energy of the bands are parabolic; this assumption holds well generally only near the absorption edge, i.e., when $h\nu \approx E_g$. Thus the one-particle approximation does not hold at photon energies, $h\nu \gg E_g$ where the density of states is not parabolic and the interaction between charges becomes important. For example, the excitons, quasiparticles that result from

electron–hole pairs bound by Coulomb attraction can move as a unit through the crystal and their occurrence is not included in the theory described above [1, 6].

3 Position of the Conduction Band and Valence Band Edges

The position of the band edges is of fundamental importance: the CB edge defines the reducing power of the photogenerated electrons while the VB edge defines the oxidation power of the holes. In addition, the majority carriers become readily available for electrochemical reactions when the surface becomes degenerated (metal-like), either by doping the material or under electrochemical control. Thus, the band positions determine electrochemical reactions, including photo-induced reactions, and are therefore fundamental to energy conversion.

3.1 Mott–Schottky Method

The traditional electrochemical method to determine the band edge position is the so-called Mott–Schottky measurement. It is relatively straightforward for bulk materials and the details of the measurements have been reported [1, 2, 11]. For stable single crystals, the Mott–Schottky equation (Eq. 7) gives the change in the capacitance at the space charge region as a function of the electrochemical potential. Briefly, an electrode is prepared in a solution with supporting electrolyte and the capacitance C_{SC} is measured as a function of the electrochemical potential with respect to a reference. The capacitance is usually measured with impedance techniques and in the absence of complications the plot of $1/C_{SC}^2$ should be linear with frequency as predicted by Eq. (7). A fit to Eq. (1) provides the flat band potential, E_{fb}, the type of semiconductor from the sign of the slope (positive for *n*-type) and the doping concentration, N_D [1, 2, 4]:

$$\frac{1}{C_{SC}^2} = \frac{2}{qA^2 N_D \varepsilon \varepsilon_0}\left[E - E_{fb} - \frac{k_B T}{q}\right] \tag{7}$$

where A is the surface area, q the elementary charge, ε the dielectric constant of the semiconductor, and ε_0 the permittivity of free space. Note that if A and ε are known, the technique also yields the doping concentration from the slope of the curve. Several aspects can complicate this measurement; surface states can cause deviations from the linear behavior predicted by Eq. (7). In addition, the slope should be independent of frequency [4]. The value of E_{fb} is of interest because it provides an

approximation to E_{CB}. Strictly speaking, E_{fb} is related to the band edge by Eq. (8) for an *n*-type semiconductor [8]:

$$E_{CB} = E_{fb} + \frac{k_B T}{q} \ln\left(\frac{N_D}{N_C}\right) \tag{8}$$

where N_D is the density of states of the donor and N_C is the densities of states near the conduction band edge (within a few $k_B T$ from the top of the CB). For a semiconductor within $1 \times k_B T$, N_C is in the order of 1×10^{19} cm^{-3} [1], while a somewhat typical doping would be in the order of $N_D = 1 \times 10^{17}$ cm^{-3} [1]; if N_D approaches N_C, the semiconductor approaches the degenerated state where its behavior becomes more like a metal. This means that the difference between E_{CB} would be in the order of 0.1 V more negative with respect to E_{fb}. Because of these complications, the term $k_B T/q = 0.025$ V in Eq. (7) is usually not significant when one considers the uncertainty of the measurement due to N_C. Also, note that in the usual formulation of Eq. (8) the flat band potential (E_{fb}) is replaced by the Fermi level, E_F [1, 8], and therefore the implied assumption made here and in the flat band potential measurements is that $E_{fb} = E_F$.

The Mott–Schottky equation allows for the measurement of one band edge, e.g., for an *n*-type material, the method yields E_{CB}. The value of E_{VB} can be calculated from E_{CB} and the bandgap, E_g, given that:

$$E_g = E_{CB} - E_{VB} \qquad (9, \text{Eq.}(1), \text{restated})$$

Alternatively, the material can be made with a *p*-type to obtain E_{VB} from the Mott–Schottky method, although this approach requires extensive material preparation. There have been attempts to use the Mott–Schottky method on mesoscopic materials and on films of NPs. However, to the best of our knowledge, the theoretical framework to extend the application to these systems is lacking, and the extension of these measurements must be done with caution. For example, the value of the surface area A in Eq. (7) is not well defined when one uses porous materials. An alternative to the Mott–Schottky method is the use of the photocurrent onset method described below.

3.2 Electrochemical Photocurrent

The photocurrent onset method is also used to measure the flat band potential, E_{fb}. When possible, this method can be combined with the Mott–Schottky equation to study the effect of surface states and of electrochemical background reactions that may interfere with E_{fb} measurements. In this method, a photocurrent is observed when the illumination source is larger than E_g. To study *n*-type semiconductors, a so-called hole scavenger is used, such as methanol or acetate. Under illumination, this scavenger provides electrons to the VB of the semiconductor and it is said that,

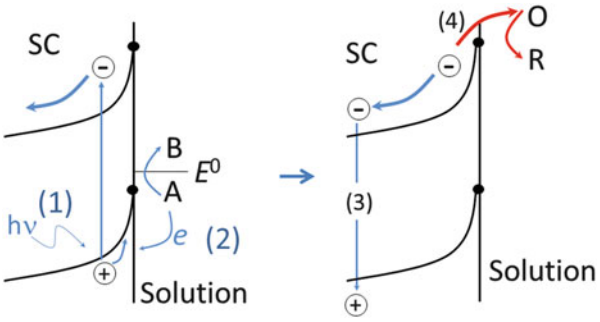

Fig. 4 Schematic representation of an SC under illumination in the reverse biased condition. After photon absorption (1), a hole scavenger, A, is oxidized (reaction 2). This allows free electrons to travel through the material. Two competing paths for electron collection are shown: electronic recombination (3) and an electrochemical back reaction (4)

for example, "holes oxidize the methanol." This facilitates electron transport through the CB. The process is shown in Fig. 4 where the sample is illuminated while in solution and (1) a photon is absorbed and this generates an electron–hole pair, e^- to h^+. The holes are strong oxidizing agents and oxidize the hole scavenger, A, (2) to leave free electrons in the CB; these electrons are then free to travel across the semiconductor material and can be detected with the potentiostat. Note that for electrons to be collected at the potentiostat they must survive reaction (3) the electronic recombination from band to band and (4) the so-called back reaction to the electrolyte.

In a bulk semiconductor, the electrons are driven across the material by the field created due to the applied bias on electrochemical potential; this is the reversed-bias regime that is characterized by bending the conduction and valence bands. In the absence of bias with respect to the E_{fb}, there is no photocurrent; if the direction of the bias now resembles the forward bias regime, the SC surface becomes degenerated and no photocurrent is observed either, under these conditions, the surface becomes more like a metallic electrode and faradaic background processes are usually observed. Figure 5a shows a schematic of the response for an ideal electrode. E_{fb} should ideally be the onset of the photocurrent, and for an *n*-type semiconductor, only photooxidations are observed. Although ideal behavior is rarely observed, the photocurrent can be used to determine the E_{fb} from the photocurrent onset, the semiconductor type from the direction of the photocurrent: *n*-type semiconductor photooxidizes while *p*-type photo reduces; in addition, the wavelength dependence of the photocurrent can also be used to measure the fundamental band-to-band transition. A more realistic expectation is shown in Fig. 5b, where background currents are seen both in the dark and under illumination. The background currents in the dark are usually assigned to surface states, i.e., because their energy levels can have energies within the bandgap "forbidden" region; these energies are different from the states in the bulk of the semiconductor that make the CB and VB. Surface states can be populated during electrochemical

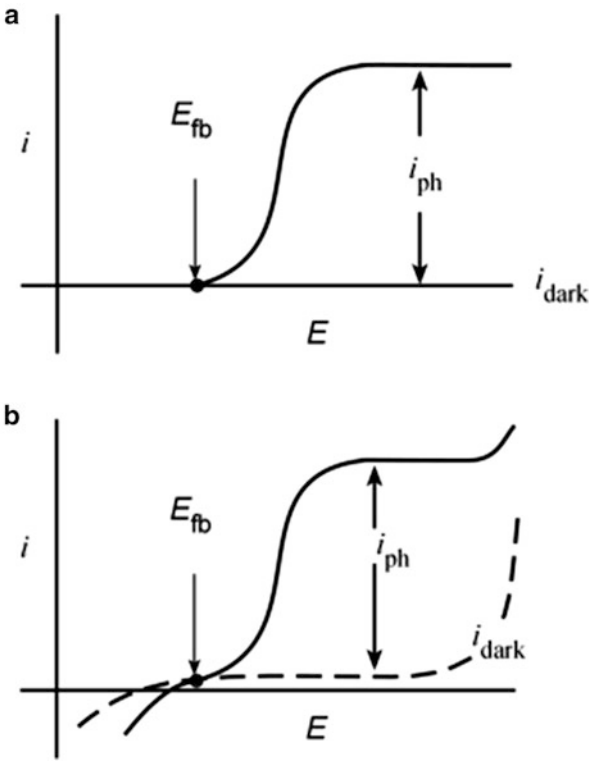

Fig. 5 (**a**) Schematic photoelectrochemical behavior of an ideal SC under illumination. In the dark, there are no currents or background reactions. Under illumination a photocurrent, i_{ph}, is observed; the photocurrent onset is in the ideal situation, the flat band potential, E_{fb} (**b**) Schematic of a more realistic response showing background currents

experiments and may even be able to undertake electrochemical reactions at potentials corresponding to the "forbidden region" of the bandgap [12]. Another interesting feature of these experiments is that sometimes the photocurrent can reverse signs around E_{fb} [13]. This has been attributed to complications due to the surface carrier concentration as the SC approaches the degenerate condition near E_{fb} [13]. Also, during illumination, the SC surface can increase its temperature and this can cause convection of the solution near the surface and increase the conductivity of the SC [14].

3.3 Photocurrent Onset Method

The ideal response in Fig. 5a is not usually observed and one sees background currents, both in the dark and under illumination, as shown schematically in Fig. 5b. In practice, the current in the dark and under illumination is used to discriminate the photocurrent i_{ph} from faradaic background processes. A typical setup is shown in Fig. 6, similar to the one reported before [5, 15]. This is a standard three-electrode cell modified for the photoelectrochemical experiment. The working electrode is the SC of interest and is illuminated through a silica window with a light source of

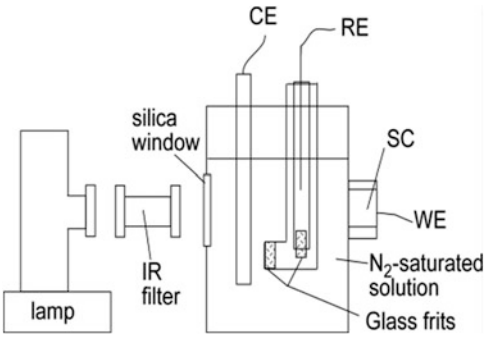

Fig. 6 Experimental setup used for photocurrent measurements in our laboratory. The illumination source is a broad spectrum source (e.g., a Xe lamp) with a filter (water) to minimize heating from the IR component. The cell is closed and the solution is saturated with N_2 (or Ar) to remove O_2; during the experiments, the cell is kept under an inert gas blanket. The working electrode (WE) is the semiconductor and is mounted with an O-ring to define the area exposed to solution. The reference electrode (RE) is usually a Ag/AgCl electrode and the counter electrode (CE) a graphite rod. The CE is usually enclosed in a fritted junction (not shown) similar to the RE

broad spectrum (e.g., Xe lamp). Note that the reference electrode, usually a Ag/AgCl electrode is kept in a compartment that is separated from the working electrode compartment by a fritted glass junction. This is preferable because reference electrodes can often leak ions, e.g., Ag^+ from AgCl or Hg^{2+} from the calomel electrode. Because these measurements are very sensitive to the conditions of the interface, these precautions avoid complications from Ag deposition on the surface of the SC electrode. For similar reasons, the counter electrode is usually a graphite rod (to avoid problems with the dissolution of metals like Pt). Also, the counter electrode is kept in a fritted glass compartment (not shown in Fig. 6 for simplicity).

With real semiconductors, the photocurrent deviates from the data shown in Fig. 5a. In the dark, there are usually currents that are observed, even at potentials that correspond to the forbidden region. These currents are usually attributed to surface states. Also, at sufficiently large biases currents are often observed. Even in the reverse bias condition, at sufficiently large bias, e.g., positive electrochemical potentials with respect to E_{fb}, current flows and the electrode is said to "break down" and tunneling processes are said to take effect, analogous to diode break down [5]. In the forward bias direction, e.g., electrochemical potentials more negative than E_{fb}, the SC becomes essentially an electrode capable of reducing species in solution (e.g., O_2 or H^+). The main implication of background currents is that they make determination of the onset potential difficult. Thus, in practice, one usually defines the photocurrent "onset" as some fraction of the background current. One approach to help discriminate photocurrent from background currents in the dark is to chop the illumination source to determine the onset of the photocurrent, i.e., E_{fb} [4, 13]. Extrapolation from the photocurrent squared (Eq. 10) [13, 16] is used to avoid ambiguity of defining a photocurrent onset; this approach is sometimes referred to as the "Butler method":

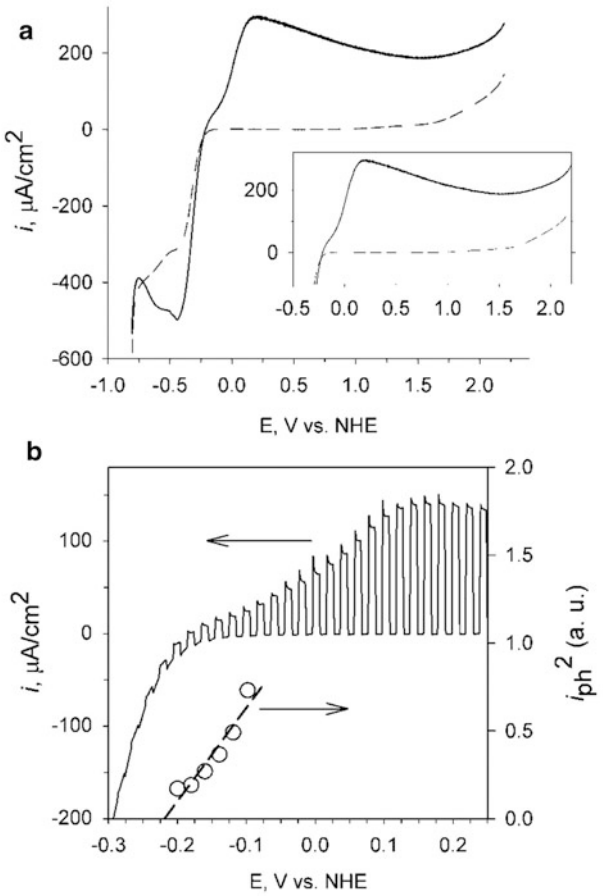

Fig. 7 Experimental photocurrent measurements for TiO_2 anatase nanoparticles film (3.2 μm thick) measured in our laboratory in 1.0 M KNO_3 at pH = 2. Details of the experimental setup are shown in Fig. 6. (**a**) Linear sweep voltammetry experiments at a scan rate, $v = 10$ mV/s. The insert in (**a**) shows the detail of the currents under illumination (——) and in the dark (- - -) near E_{fb}. (**b**) corresponds to a chopping light experiment ($\nu = 1$ mV/s) while simultaneously chopping light on and off for 10 s each (——). The difference between currents under illumination and in the dark is used to plot i_{ph}^2 (- - -) on the right axis of (**b**). Anodic currents are shown as positive

$$i_{ph}{}^2 \sim (E - E_{fb}) \tag{10}$$

One usually starts by running a potential scan for an electrode made of the semiconductor material in the dark and under illumination at a relatively fast scan, $v = 10$ mV/s (e.g., Fig. 7a) with the difference between the current in the dark and under illumination one can estimate the onset potential. To refine the photocurrent onset measurement, the light is chopped on and off (10 s each) while scanning the potential at a slower rate, e.g., $v = 1$ mV/s as shown in Fig. 7b. The

photocurrent usually presents small transients or spikes and then decays to a quasi-steady state value. One then samples this quasi-steady state photocurrent and accounts for the difference with the dark current extrapolated to the same potential. The photocurrent is used to extrapolate to $i_{ph}^2 = 0$ (Eq. 10) as shown in Fig. 7b. The method can readily be applied to different kinds of substrates including single crystals, NP films on inert substrates (e.g., doped SnO_2), and even on pressed pellets of the materials. Note that the experimental data suffer from problems with discrimination of the photocurrent onset. Faradaic currents due to states near the CB edge (e.g., negative current in Fig. 7a) compete with the main band-to-band transitions and can shift the photocurrent onset from the value of the true flat band potential.

It should be noted that the value of the band edges is often a strong function of solution conditions, most notably pH. In particular, metal oxide electrodes usually present a pH dependence of E_{CB} with a slope of 0.059 V/pH [1]. This is the result of H^+ and OH^- ions at equilibrium on the surface of the material setting the final energy of the bands. This is often not a problem because the potentials of H^+ reduction and of H_2O oxidation are also pH dependent. Redox mediators in solution can also have a strong effect on E_{fb} when they adsorb strongly on the surface [17, 18]. However, in working with novel materials, one must verify this dependence as surface states can pin the value of the band edges, this effect is known as surface pinning [1, 19]. The net effect of surface pinning will be a change on the driving force towards the electrochemical reaction of interest. In addition, chalcogenide semiconductors display a dependence on the band edges with the concentration of the chalcogenide ion in solution, e.g., CdS will have a E_{fb} that will depend on S^- concentration, in addition to the pH dependence [20].

In general, the measurement of band edge properties in solution must be approached with caution as with other interfacial property measurements. As pointed out above, pH, surface states, electrolyte concentration, and also the history of the surface can have an appreciable effect on the band edge measurement. The best approach is to perform the measurements in a solution that most closely follows the conditions such as pH of the final application, and to perform replicates of the measurements to assess the reproducibility of the interface.

3.4 Bandgap from Photoelectrochemical Current Measurements

The optical bandgap responsible for the photocurrent can be determined from the photocurrent dependence with illumination wavelength. To achieve this, the setup described in Fig. 6 is modified by adding a monochromator to select the illumination wavelength. For this measurement, the electrochemical potential is set to a value where the photocurrent is independent of potential, thus minimizing complications from background currents. Care must be taken in "normalizing" the

Scheme 1 Direct ECL. Adapted with permission from *Nano Lett*. 2002, 2, 1315–1319 [27]. Copyright 2002, American Chemical Society

$$QD + ne^- \rightarrow QD^{\cdot -}$$
$$QD - ne^- \rightarrow QD^{\cdot +}$$
$$QD^{\cdot -} + QD^{+} \rightarrow QD^{*}$$

photocurrent due to the complicated power vs. wavelength dependence of the light source and of the monochromator throughput. The "normalized" photocurrent dependence typically yields a graph where the onset is used to calculate E_g. The wavelength dependence can also be used to probe the nature of the photocurrent transitions; for example, in the doping of TiO_2 with C the method yielded a shift from the 3.2 eV of anatase to ca. 2.2 eV [21].

4 Electrogenerated Chemiluminescence of Quantum Dots

Quantum dots (QDs) have gained attraction due to their size-dependent properties [22] and reproducibility [23]. While there is interest in these semiconductors in the energy field, there is also interest in the use of QDs in the analytical field. In this regard, electrogenerated chemiluminescence (ECL) bridges the gap between using electrochemistry to characterize SC materials and the use of SC materials for chemical analysis. Although advances in this field have focused on the use of QD for bioanalysis [24], the experiments in the field are of relevance to the characterization of the QD energetics [25, 26] and open the door to study energy transfer processes by ECL. We provide a brief description of ECL for CdSe quantum dots; CdSe is of interest because QDs can be prepared with very narrow size distribution and their surface can be passivated.

In ECL electrochemical reactions generate an excited state. The excited state in turn relaxes to the ground state by emitting light. In a semiconductor, the excited state can be thought of as the same excited state that is generated after light absorption. Two main avenues for ECL experiments are discussed here: the direct ECL and the use of a coreactant. In the direct ECL experiment, shown in Scheme 1, the QD is constantly reduced and oxidized, so that the excited state is formed by the reaction of the oxidized quantum dot, $QD^{\bullet +}$, and the reduced species ($QD^{\bullet -}$). The oxidized and reduced forms are generated by alternating the electrochemical potential from a positive to a negative region. This normally requires large potential windows to address the CB and VB, i.e., the window must be $>E_g$ of the QD.

Bard and co-workers [27] reported the ECL behavior from CdSe nanocrystals (NCs) synthesized by Peng's [28] method for the first time in CH_2Cl_2 with tetra-*n*-butylammonium perchlorate (TBAP) as supporting electrolyte. CdSe NCs produced ECL when scanned between +2.3 to −2.3 V using a Ag wire quasi-reference

$$DBAE - e^- \rightarrow DBAE^{\bullet +}$$
$$DBAE^{\bullet +} - H^+ \rightarrow DBAE^{\bullet}$$
$$QD + DBAE^{\bullet} \rightarrow QD^{\bullet -} + P1$$
$$QD - e^- \rightarrow QD^{\bullet +}$$
$$QD^{\bullet +} + QD^{\bullet -} \rightarrow QD^{*} + QD$$
$$QD^{\bullet +} + DBAE^{\bullet} \rightarrow QD^{*} + P1$$
$$QD^{*} \rightarrow QD + h\nu\ (625\ nm)$$

Where: DBAE = $(n\text{-}Bu)_2NCH_2CH_2OH$,
$DBAE^{\bullet +} = (n\text{-}Bu)_2N^{\bullet +}CH_2CH_2OH$
$DBAE^{\bullet} = (n\text{-}Bu)_2NC^{\bullet}HCH_2OH$
$P1 = (n\text{-}Bu)_2N^{+}{=}CHCH_2OH$
PEG = polyethylene glycol

Scheme 2 Oxidative-reduction route of ECL emission from a well-passivated QD = CdSe/ZnS/PEG with DBAE coreactants. Adapted from Ref. [47], *Phys. Chem. Chem. Phys.* 2010, *12*, 10073. Reproduced by permission of the PCCP Owner Societies

$$QD + e^- \rightarrow QD^{\bullet -}$$
$$S_2O_8^{2-} + e^- \rightarrow SO_4^{2-} + SO_4^{\bullet -}$$
$$QD^{\bullet -} + SO_4^{\bullet -} \rightarrow QD^{*} + SO_4^{2-}$$
$$QD^{*} \rightarrow QD + h\nu$$

Scheme 3 Reductive-oxidation route of ECL emission from QDs with $S_2O_8^{2-}$ coreactant. Reprinted with permission from Ref. [48], *Anal. Chem.* 2012, *84*, 2811. Copyright 2012 American Chemical Society

electrode. Light emission occurred when chemically reduced species ($R^{\bullet -}$) collide with oxidized species ($R^{\bullet +}$) producing excited states (R*) in ion annihilation process. They reported that the species $R^{\bullet +}$ is more stable than $R^{\bullet -}$which was evidenced by the larger light emission where cathodic scanning followed anodic scanning. To generate ECL from the direct route, the electrochemically generated reduced species and oxidized species have to be stable so that they can form the excited state, QD^*, through ion annihilation process [29]. Addition of coreactants can help overcome the poor stability of electrochemically generated species to form excited state or in many cases can help solve the problem of small potential window of some solvents [4]. Because of this, in aqueous systems the use of a coreactant is preferred [30].

When a coreactant is used, a more complicated mechanism is in effect (Schemes 2 and 3). A molecule in solution is oxidized, to form an intermediate that will be an effective reducing agent. The rapid reactions between the coreactant and semiconductor generate the semiconductor excited state that can relax through

Table 3 Coreactants reported for ECL detection of CdSe quantum dots

Coreactants	Potential[a] V vs. NHE	Type of ECL	Ref.
Dibutylaminoethanol (DBAE)[b]	0.80 V (ox)	Oxidative-reduction	[46]
Tripropylamine (TPrA)[b]	0.85 V (ox)	Oxidative-reduction	[46]
Hydrogen peroxide (H_2O_2)[c]	−0.70 V (red)	Reductive-oxidation	[47]
Potassium persulfate ($K_2S_2O_8$)	−0.80 V (red)	Reductive-oxidation	[35]

[a]Formal electrochemical potentials for either oxidation (ox) or reduction (red) of the coreactants. These were converted to NHE using data from the references
[b]These coreactants have been reported for CdSe/ZnS
[c]ECL mechanism of H_2O_2 coreactant is described in Ref. [47]

the emission of light. One approach to generate ECL of QDs is to immobilize QDs on the electrode surface. To achieve light emission, different coreactants have been used, including H_2O_2 [31–33], $S_2O_8^{2-}$ [34, 35], and O_2 (Ref. [36]) upon cathodic scanning. Analytical applications of QDs include immunoassay-based ECL detection of biomolecules [34, 37–39] in cellular imaging [40], DNA hybridization analysis [41], and monitoring of specific biorecognition [42–44]. QDs are emerging as an alternative to the use of ruthenium complexes as emitters in conventional ECL immunosensors [45, 46]. Table 3 shows a list of coreactants used for CdSe.

There are two routes for coreactant-based ECL, namely, oxidative-reduction and reductive-oxidation routes depending on the nature of coreactants [24]. (1) QDs can produce ECL upon anodic scanning with the coreactants such as tri-*n*-propyl amine (TPrA) and dibutylaminoethanol (DBAE), this route is called oxidative reduction where QDs and the coreactants get electrochemically oxidized to form oxidized species. The coreactant produces a strongly reductive radical which reduces $QD^{\bullet+}$ (the oxidized form of QDs); this generates the excited species of QDs, QD^* which eventually emits light (Scheme 2). In the reductive-oxidation route, the coreactants such as H_2O_2 and $K_2S_2O_8$ are electrochemically reduced upon cathodic scanning to produce the reduced species; these species chemically produce very strong oxidizing species which interact with $QD^{\bullet-}$ (reduced form of QDs); this forms QD^* which emits light (Scheme 3).

4.1 ECL from CdSe Quantum Dots

Bo et al. [29] have used potassium persulfate ($K_2S_2O_8$) as a coreactant to generate ECL with CdSe. The potential is cycled from 0.1 V and −1.2 V vs. Ag/AgCl where both $S_2O_8^{2-}$ and CdSe get electrochemically reduced to form $SO_4^{\bullet-}$ and $CdSe^{\bullet-}$, respectively, which interact to produce CdSe* that emits light. The ECL emission occurs at −1.1 V at a carbon paste working electrode vs. Ag/AgCl reference and Pt counter electrode with 0.1 M KCl. $S_2O_8^{2-}$ gets reduced at −1.0 V and CdSe at −1.1 V. The emission of light at −1.1 V is consistent with CdSe reduction. Ju group [33] used hydrogen peroxide (H_2O_2) to generate ECL emission from thioglycolic

acid-capped CdSe quantum dots. They proposed that on cathodic scanning electrons are injected into CdSe from the electrode. The electrode eventually generates $OH^{\bullet}$ from H_2O_2. The $OH^{\bullet}$ radical being a strong oxidant injects a hole (h^+) onto CdSe. The annihilation of hole and electron injected CdSe produces CdSe* which emits light at −1.114 V vs. Ag/AgCl. In their experiment, CdSe was immobilized on paraffin-impregnated graphite electrode (PIGE). CdSe QDs with nitrogen-doped carbon nanotubes produce enhanced ECL with H_2O_2 as coreactant [49]. The enhancement was five times compared to pure CdSe QDs, three times compared to CdSe composited with carbon nanotubes (CNTs). The authors assigned this enhancement to a decrease in potential barrier for electron injection into CdSe QDs. On anodic scanning, CdSe produced ECL with SO_3^{2-} as coreactant [30] in air-saturated Tris-buffer at indium tin oxide (ITO) electrode. During anodic scanning, ${SO_3}^{2-}$ oxidized to SO_3^- species which then reacts with dissolved oxygen to produce ${O_2}^{\bullet -}$. The ${O_2}^{\bullet -}$ injects an electron into the CdSe. The oxidized form of CdSe and the reduced form collide to yield the excited state which emits light.

Teng et al. [50] developed a novel strategy for enhancement of ECL by combining CdSe QDs with graphene oxide (GO)-chitosan (CHIT). The CdSe QDs/GO-CHIT composite-based ECL sensor demonstrated high ECL intensity, stability, and biocompatibility. The CdSe QDs gets reduced to $CdSe^{\bullet -}$ and $S_2O_8^{2-}$ to form ${SO_4}^{\bullet -}$ on cathodic scanning. ${SO_4}^{\bullet -}$ is strong oxidant and produces CdSe* from $CdSe^{\bullet -}$. The amine groups in CHIT molecules can facilitate radical generation and GO acts as a medium for electron transfer between CdSe QDs and the glassy carbon working electrode. This CdSe QDs/GO-CHIT sensor was used to detect cytochrome C with ECL quenching method. The energy transfer between the excited state and the cytochrome C caused the decrease in ECL intensity. Cytochrome C could be detected as low as 1.5 μM. The ECL intensity was enhanced by 20-fold when 3-aminopropyl-triethoxysilane (APS) as a cross-linker was conjugated to CdSe QDs-CNTs-CHIT compared to CdSe QDs-CNTs-CHIT [51]. Combination of carbon nanotubes (CNTs) and poly (diallyldimethylammonium chloride) (PDDA) on CdSe QDs film greatly enhances the ECL intensity of CdSe and $S_2O_8^{2-}$ system [52]. The ECL intensity from the CdSe QDs-CNTs was threefold higher than that from the CdSe QDs film. More porous structure, larger surface area, and better conductivity of the CdSe QDs-CNTs composite film contributed to higher intensity. Sensitive detection of human IgG (HIgG) was reported by Ling et al. [53] by PDDA-protected graphene-CdSe QDs (P-GR-CdSe QDs) composites immunosensor. The P-GR-CdSe QDs composite film shows high ECL intensity, fast response, good electronic conductivity and stability.

Xiao et al. [54] successfully fabricated graphene oxide sheets-polyaniline-CdSe QDs (GO-PANi-CdSe QDs)-based immunosensor for the detection of cytochrome C with $S_2O_8^{2-}$ coreactant. The GO-PANi-CdSe QDs nanocomposite was immobilized onto the surface of glassy carbon electrode (GCE). The ECL intensity of GO-PANi-CdSe QDs nanocomposites is over four times higher than that of pure CdSe QDs. The GO-PANi-CdSe QDs nanocomposites film has larger surface area and the amine group of the nanocomposites facilitates the radical generation and electron transfer during ECL reaction.

The ECL of CdSe QDs in aqueous solvent was reported by Ju and co-workers [31]. A thin film of CdSe QDs on PIGE produces two ECL peaks at −1.2 V and −1.5 V vs. Ag/AgCl. The electron transfer reaction of electrochemically reduced individual CdSe QDs and oxidant coreactants such as H_2O_2 or reduced dissolved O_2 in solution produces the ECL peak at −1.2 V whereas electrochemically reduced assembly of CdSe produces second ECL peak at −1.5 V.

Core-shell type quantum dots such as CdSe/ZnS and CdSe/CdS have been used as ECL label in biosensors. Lynn et al. [55] have used CdSe/ZnS QDs to detect glutathione (GSH) using H_2O_2 as coreactant. The Nafion-CdSe/ZnS QDs composite was immobilized on GCE and potential scanned from 0 V to −2.0 V. This composite film did not generate ECL with $S_2O_8^{2-}$ coreactant since Nafion effectively excluded the coreactant. GSH detection was based on ECL quenching as it is $OH^{\bullet}$ scavenger. The CdSe/ZnS QDs immobilized on a support of graphene-CdS QDs-alginate (G-CdS QDs-AL) on GCE scavenges ECL produced by G-CdS QDs-AL composite on GCE [56]. Detection of cancer biomarker has been realized by ECL quenching. Miao group [46] has used sandwich type immunoassay of CdSe/ZnS QDs and C-reactive protein (CRP) to detect it using 2-(dibutylamino) ethanol (DBAE) as coreactant. Electrogenerated chemiluminescence resonance energy transfer (ECRET) has been realized with CdSe/ZnS QDs and cyanine dye (Cy5) and biomolecule as a linker [57]. CdSe/ZnS QDs-DNA-Cy5 conjugate was scanned in the cathodic direction with $S_2O_8^{2-}$ as coreactant and ECL spectrum showed two emission peaks due to emission from excited CdSe/ZnS QDS at 590 nm and emission from Cy5 at 675 nm suggesting the energy transfer from exited CdSe/ZnS QDs to Cy5. In CdSe/ZnS QDs-DNA-luminol composite, where luminol acts as a donor ECRET is observed between luminol and QDs in the presence of H_2O_2 coreactant. Excited state luminol either emit at 460 nm or transfer energy to proximal CdSe/ZnS QDs which emit at 665 nm [58]. Lei et al. [59] reported the fabrication of solid state ECL sensor based on core-shell CdSe/ZnS QDs self-assembled film on GC for the first time. The ECL emission has been obtained with $S_2O_8^{2-}$ and H_2O_2 coreactants. Zhang group [60] used dendrimers-CdSe/ZnS QDs nanocomposites to detect cancer cells with $S_2O_8^{2-}$ coreactant.

Acknowledgements This work was partially supported by NSF Career Award CHE-1255387 and by UNR startup funds for M.A.A.-A.

References

1. Memming, R. *Semiconductor Electrochemistry*; Wiley-VCH: Weinheim, Federal Republic of Germany, 2001.
2. Morrison, S. R. *Electrochemistry at Semiconductor and Oxidized Metal Electrodes*; Plenum Press: NY, 1980.
3. Sze, S. M.; Kwow, K. N. *Physics of Semiconductor-Devices*; Wiley-Interscience: Hoboken, New Jersey, 2007.

4. Bard, A. J.; Faulkner, L. R. *Electrochemical Methods: Fundamentals and Applications*; 2nd ed.; John Wiley & Sons: New York, 2000.
5. Haram, S. K. Semiconductor Electrodes In *Handbook of Electrochemistry*; Zoski, C. G., Ed.; Elsevier: Amsterdam, The Netherlands, 2007, pp. 329–389.
6. Basu, P. K. *Theory of Optical Processes in Semiconductors*; Oxford University Press: New York, 1997.
7. Pankove, J. I. *Optical Processes in Semiconducting Thin-Films*; Dover Publications, Inc: New York, 1971.
8. Smith, R. A. *Semiconductors*; 2nd ed.; Cambridge University Press: Cambridge, Great Britain, 1978.
9. Alpuche-Aviles, M. A.; Wu, Y. Y. Photoelectrochemical Study of the Band Structure of Zn_2sno_4 Prepared by the Hydrothermal Method. *J. Am. Chem. Soc.* **2009**, *131*, 3216–3224.
10. Segev, D.; Wei, S.-H. Structure-Derived Electronic and Optical Properties of Transparent Conducting Oxides. *Phys. Rev. B: Condens. Matter Mater. Phys.* **2005**, *71*, 125129/125121–125111.
11. Finklea, H. O. Titanium Dioxide (TiO_2) and Stronium Titanate ($SrTiO_3$) In *Semiconductor Electrodes*; 1 ed.; Finklea, H., O, Ed.; Elsevier: Amsterdam, 1988; Vol. 55, pp. 43–145.
12. Bard, A. J.; Fan, F. R. F.; Gioda, A. S.; Nagasubramanian, G.; White, H. S. On the Role of Surface-States in Semiconductor Electrode Photoelectrochemical Cells. *Faraday Discuss. Chem. Soc.* **1980**, *70*, 19–31.
13. Finklea, H. O. Semiconductor Electrode: Concepts and Terminology In *Semiconductor Electrodes*; Finklea, H., O, Ed.; Elsevier: Amsterdam, 1988, pp. 1–42.
14. Bard, A. J.; Kohl, P. A. In *Semiconductor Liquid-Junction Solar Cells*; Heller, A., Ed.; The Electrochemical Society: Airlie, VA, 1977; Vol. 77-3, pp. 222–230.
15. Jaeger, C. D.; Fan, F. R. F.; Bard, A. J. Semiconductor Electrodes. 26. Spectral Sensitization of Semiconductors with Phthalocyanine. *J. Am. Chem. Soc.* **1980**, *102*, 2592–2598.
16. Butler, M. A. Photoelectrolysis and Physical Properties of the Semiconducting Electrode WO_3. *J. Appl. Phys.* **1977**, *48*, 1914–1920.
17. Fan, F. R. F.; Bard, A. J. Semiconductor Electrodes. 36. Characteristics of N-$MoSe_2$, N-WSe_2 and P-WSe_2 Electrodes in Aqueous-Solution. *J. Electrochem. Soc.* **1981**, *128*, 945–952.
18. Turner, J. A.; Parkinson, B. A. The Application of Chronocoulometry to the Study of Adsorption at the Semiconductor Electrolyte Interface. *J. Electroanal. Chem.* **1983**, *150*, 611–617.
19. Bard, A. J.; Bocarsly, A. B.; Fan, F. R. F.; Walton, E. G.; Wrighton, M. S. The Concept of Fermi Level Pinning at Semiconductor/Liquid Junctions. Consequences for Energy Conversion Efficiency and Selection of Useful Solution Redox Couples in Solar Devices. *J. Am. Chem. Soc.* **1980**, *102*, 3671–3677.
20. Finlayson, M. F.; Wheeler, B. L.; Kakuta, N.; Park, K. H.; Bard, A. J.; Campion, A.; Fox, M. A.; Webber, S. E.; White, J. M. Determination of Flat-Band Position of Cds Crystals, Films, and Powders by Photocurrent and Impedance Techniques—Photoredox Reaction Mediated by Intragap States. *J. Phys. Chem.* **1985**, *89*, 5676–5681.
21. Park, J. H.; Kim, S.; Bard, A. J. Novel Carbon-Doped Tio_2 Nanotube Arrays with High Aspect Ratios for Efficient Solar Water Splitting. *Nano Lett.* **2005**, *6*, 24–28.
22. Alivisatos, A. P. Semiconductor Clusters, Nanocrystals, and Quantum Dots. *Science* **1996**, *271*, 933–937.
23. Ding, Z.; Quinn, B. M.; Haram, S. K.; Pell, L. E.; Korgel, B. A.; Bard, A. J. Electrochemistry and Electrogenerated Chemiluminescence from Silicon Nanocrystal Quantum Dots. *Science* **2002**, *296*, 1293–1297.
24. Miao, W. Electrogenerated Chemiluminescence In *Handbook of Electrochemistry*; Zoski, C. G., Ed.; Elsevier: Amsterdam, The Neatherlands, 2007, pp. 541–590.
25. Myung, N.; Bae, Y.; Bard, A. J. Effect of Surface Passivation on the Electrogenerated Chemiluminescence of Cdse/Znse Nanocrystals. *Nano Lett.* **2003**, *3*, 1053–1055.

26. Myung, N.; Bae, Y.; Bard, A. J. Enhancement of the Photoluminescence of Cdse Nanocrystals Dispersed in Chcl3 by Oxygen Passivation of Surface States. *Nano Lett.* **2003**, *3*, 747–749.
27. Myung, N.; Ding, Z.; Bard, A. J. Electrogenerated Chemiluminescence of Cdse Nanocrystals. *Nano Lett.* **2002**, *2*, 1315–1319.
28. Aldana, J.; Wang, Y. A.; Peng, X. Photochemical Instability of Cdse Nanocrystals Coated by Hydrophilic Thiols. *J. Am. Chem. Soc.* **2001**, *123*, 8844–8850.
29. Liu, B.; Ren, T.; Zhang, J.-R.; Chen, H.-Y.; Zhu, J.-J.; Burda, C. Spectroelectrochemistry of Hollow Spherical Cdse Quantum Dot Assemblies in Water. *Electrochem. Commun.* **2007**, *9*, 551–557.
30. Liu, X.; Guo, L.; Cheng, L.; Ju, H. Determination of Nitrite Based on Its Quenching Effect on Anodic Electrochemiluminescence of Cdse Quantum Dots. *Talanta* **2009**, *78*, 691–694.
31. Zou, G.; Ju, H. Electrogenerated Chemiluminescence from a Cdse Nanocrystal Film and Its Sensing Application in Aqueous Solution. *Anal. Chem.* **2004**, *76*, 6871–6876.
32. Ding, S.-N.; Xu, J.-J.; Chen, H.-Y. Enhanced Solid-State Electrochemiluminescence of Cds Nanocrystals Composited with Carbon Nanotubes in H2o2 Solution. *Chem. Commun.* **2006**, 3631–3633.
33. Jiang, H.; Ju, H. Electrochemiluminescence Sensors for Scavengers of Hydroxyl Radical Based on Its Annihilation in Cdse Quantum Dots Film/Peroxide System. *Anal. Chem.* **2007**, *79*, 6690–6696.
34. Jie, G.; Liu, B.; Pan, H.; Zhu, J.-J.; Chen, H.-Y. Cds Nanocrystal-Based Electrochemiluminescence Biosensor for the Detection of Low-Density Lipoprotein by Increasing Sensitivity with Gold Nanoparticle Amplification. *Anal. Chem.* **2007**, *79*, 5574–5581.
35. Jie, G.; Huang, H.; Sun, X.; Zhu, J.-J. Electrochemiluminescence of Cdse Quantum Dots for Immunosensing of Human Prealbumin. *Biosens. Bioelectron.* **2008**, *23*, 1896–1899.
36. Jiang, H.; Ju, H. Enzyme-Quantum Dots Architecture for Highly Sensitive Electrochemiluminescence Biosensing of Oxidase Substrates. *Chem. Commun.* **2007**, 404–406.
37. Qian, J.; Zhang, C.; Cao, X.; Liu, S. Versatile Immunosensor Using a Quantum Dot Coated Silica Nanosphere as a Label for Signal Amplification. *Anal. Chem.* **2010**, *82*, 6422–6429.
38. Liu, X.; Zhang, Y.; Lei, J.; Xue, Y.; Cheng, L.; Ju, H. Quantum Dots Based Electrochemiluminescent Immunosensor by Coupling Enzymatic Amplification with Self-Produced Coreactant from Oxygen Reduction. *Anal. Chem.* **2010**, *82*, 7351–7356.
39. Lin, D.; Wu, J.; Yan, F.; Deng, S.; Ju, H. Ultrasensitive Immunoassay of Protein Biomarker Based on Electrochemiluminescent Quenching of Quantum Dots by Hemin Bio-Bar-Coded Nanoparticle Tags. *Anal. Chem.* **2011**, *83*, 5214–5221.
40. Michalet, X.; Pinaud, F. F.; Bentolila, L. A.; Tsay, J. M.; Doose, S.; Li, J. J.; Sundaresan, G.; Wu, A. M.; Gambhir, S. S.; Weiss, S. Quantum Dots for Live Cells, in Vivo Imaging, and Diagnostics. *Science* **2005**, *307*, 538–544.
41. Wang, J.; Liu, G.; Merkoci, A. Electrochemical Coding Technology for Simultaneous Detection of Multiple DNA Targets. *J. Am. Chem. Soc.* **2003**, *125*, 3214–3215.
42. Yuan, J.; Guo, W.; Wang, E. Utilizing a CdTe Quantum Dots-Enzyme Hybrid System for the Determination of Both Phenolic Compounds and Hydrogen Peroxide. *Anal. Chem.* **2008**, *80*, 1141–1145.
43. Liu, J.; Lee, J. H.; Lu, Y. Quantum Dot Encoding of Aptamer-Linked Nanostructures for One-Pot Simultaneous Detection of Multiple Analytes. *Anal. Chem.* **2007**, *79*, 4120–4125.
44. Mukundan, H.; Xie, H.; Price, D.; Kubicek-Sutherland, J. Z.; Grace, W. K.; Anderson, A. S.; Martinez, J. S.; Hartman, N.; Swanson, B. I. Quantitative Multiplex Detection of Pathogen Biomarkers on Multichannel Waveguides. *Anal. Chem.* **2010**, *82*, 136–144.
45. Zhan, W.; Bard, A. J. Electrogenerated Chemiluminescence. 83. Immunoassay of Human C-Reactive Protein by Using $Ru(bpy)_3^{2+}$-Encapsulated Liposomes as Labels. *Anal. Chem.* **2007**, *79*, 459–463.
46. Wang, S.; Harris, E.; Shi, J.; Chen, A.; Parajuli, S.; Jing, X.; Miao, W. Electrogenerated Chemiluminescence Determination of C-Reactive Protein with Carboxyl CdSe/ZnS Core/Shell Quantum Dots. *Phys. Chem. Chem. Phys.* **2010**, *12*, 10073–10080.

47. Choi, J.-P.; Bard, A. J. Electrogenerated Chemiluminescence (Ecl) 79. Reductive-Oxidation Ecl of Tris(2,2′-Bipyridine) Ruthenium(Ii) Using Hydrogen Peroxide as a Coreactant in Ph 7.5 Phosphate Buffer Solution. *Anal. Chim. Acta* **2005**, *541*, 143–150.
48. Jie, G.; Yuan, J. Novel Magnetic Fe_3O_4@CdSe Composite Quantum Dot-Based Electrochemiluminescence Detection of Thrombin by a Multiple DNA Cycle Amplification Strategy. *Anal. Chem.* **2012**, *84*, 2811–2817.
49. Guo, L.; Liu, X.; Hu, Z.; Deng, S.; Ju, H. Electrochemiluminescence of CdSe Quantum Dots Composited with Nitrogen-Doped Carbon Nanotubes. *Electroanalysis* **2009**, *21*, 2495–2498.
50. Wang, T.; Zhang, S.; Mao, C.; Song, J.; Niu, H.; Jin, B.; Tian, Y. Enhanced Electrochemiluminescence of CdSe Quantum Dots Composited with Graphene Oxide and Chitosan for Sensitive Sensor. *Biosens. Bioelectron.* **2012**, *31*, 369–375.
51. Jie, G.; Zhang, J.; Wang, D.; Cheng, C.; Chen, H.-Y.; Zhu, J.-J. Electrochemiluminescence Immunosensor Based on Cdse Nanocomposites. *Anal. Chem.* **2008**, *80*, 4033–4039.
52. Jie, G.; Li, L.; Chen, C.; Xuan, J.; Zhu, J.-J. Enhanced Electrochemiluminescence of CdSe Quantum Dots Composited with Cnts and Pdda for Sensitive Immunoassay. *Biosens. Bioelectron.* **2009**, *24*, 3352–3358.
53. Li, L.-L.; Liu, K.-P.; Yang, G.-H.; Wang, C.-M.; Zhang, J.-R.; Zhu, J.-J. Fabrication of Graphene-Quantum Dots Composites for Sensitive Electrogenerated Chemiluminescence Immunosensing. *Adv. Funct. Mater.* **2011**, *21*, 869–878.
54. Hu, X.-W.; Mao, C.-J.; Song, J.-M.; Niu, H.-L.; Zhang, S.-Y.; Huang, H.-p. Fabrication of GO/Pani/CdSe Nanocomposites for Sensitive Electrochemiluminescence Biosensor. *Biosens. Bioelectron.* **2013**, *41*, 372–378.
55. Dennany, L.; Gerlach, M.; O'Carroll, S.; Keyes, T. E.; Forster, R. J.; Bertoncello, P. Electrochemiluminescence (ECL) Sensing Properties of Water Soluble Core-Shell CdSe/Zns Quantum Dots/Nafion Composite Films. *J. Mater. Chem.* **2011**, *21*, 13984–13990.
56. Guo, Z.; Hao, T.; Wang, S.; Gan, N.; Li, X.; Wei, D. Electrochemiluminescence Immunosensor for the Determination of Ag Alpha Fetoprotein Based on Energy Scavenging of Quantum Dots. *Electrochem. Commun.* **2012**, *14*, 13–16.
57. Li, L.; Hu, X.; Sun, Y.; Zhang, X.; Jin, W. Electrochemiluminescence Resonance Energy Transfer between Quantum Dots (QDs) as the Donor and Cy5 Dye Molecules as the Acceptor in QD-Cy5 Conjugates with Biomolecules as the Linker. *Electrochem. Commun.* **2011**, *13*, 1174–1177.
58. Li, M.; Li, J.; Sun, L.; Zhang, X.; Jin, W. Measuring Interactions and Conformational Changes of DNA Molecules Using Electrochemiluminescence Resonance Energy Transfer in the Conjugates Consisting of Luminol, DNA and Quantum Dot. *Electrochim. Acta* **2012**, *80*, 171–179.
59. Bao, L.; Sun, L.; Zhang, Z.-L.; Jiang, P.; Wise, F. W.; Abruna, H. D.; Pang, D.-W. Energy-Level-Related Response of Cathodic Electrogenerated-Chemiluminescence of Self-Assembled CdSe/ZnS Quantum Dot Films. *J. Phys. Chem. C* **2011**, *115*, 18822–18828.
60. Jie, G.; Wang, L.; Yuan, J.; Zhang, S. Versatile Electrochemiluminescence Assays for Cancer Cells Based on Dendrimer/CdSe-ZnS-Quantum Dot Nanoclusters. *Anal. Chem.* **2011**, *83*, 3873–3880.

New Cu(I)-Based *p*-Type Semiconducting Metal Oxides for Solar-to-Fuel Conversion: Investigation and Challenges

Upendra A. Joshi

1 Introduction

As the oil reserve is depleting, more and more efforts are focused on the renewable energy [1]. Hydrogen is considered as a new energy carrier of the coming centuries as it can be produced from most abundant source (water) and its utilization is environment friendly. The photoelectrochemical solar-to-fuel conversion (photoelectrochemical cell, PEC) is a promising way to produce fuels from sunlight. This concept has generated intense research over the past few decades in the field of semiconducting photoelectrodes, such as for the photon-driven reduction of water or carbon dioxide [2–7]. Much research efforts are focused on developing visible active photoelectrode (through bandgap engineering) which has a significant portion in the solar spectrum [8, 9]. The use of metal oxides as photoelectrodes, typically *n*-type, is very well studied owing to their photostability and conductivity. The *p*-type metal oxide electrode can act as a photocathode in a PEC cell system, which in turn carries out reduction of water to generate hydrogen using solar radiation. The chalcogenide-based *p*-type semiconductor to date has highest efficiency with outstanding optoelectronic properties but limited corrosion resistance [10–12]. Metal oxide semiconductors, by contrast, can exhibit superior corrosion resistance and can be made visible active, but are typically difficult to dope as *p*-type with a high mobility of carriers. A relatively smaller number of *p*-type metal oxide photoelectrodes have been discovered so far which absorb visible light and can be used as a photocathode, among them Cu_2O [13–15], metal-doped Fe_2O_3 [16, 17], $CaFe_2O_4$ [18, 19], Rh-doped $SrTiO_3$ [20], and *N*-doped ZnO [21] are known to date. Copper oxide is one of the most abandoned elements on earth, unlike chalcogenide it is environment friendly and can be a

U.A. Joshi (✉)
Department of Chemical Engineering, University of South Carolina, Columbia, SC 29208, USA
e-mail: upendra.joshi@gmail.com; joshiu@mailbox.sc.edu

B. Viswanathan et al. (eds.), *Materials and Processes for Solar Fuel Production*, Nanostructure Science and Technology 174, DOI 10.1007/978-1-4939-1628-3_5

potential candidate as a photoelectrode owing its relatively smaller bandgap which absorbs visible light. Most extensively studied metal oxide photocathode for PEC application is *p*-type Cu_2O, but its tendency to photocorrode remains a significant drawback. Recent efforts successfully showed that Cu_2O can be stabilized using surface coating of Al_2O_3, ZnO, and TiO_2 preventing photoreduction of Cu_2O to Cu metal but still long-term activity is outlying [22].

In this chapter, we aim to put together the research effort made, so far, to develop copper-based *p*-type photocathode materials for PEC applications, with a view of providing a good reference and inspiring new concepts to develop *p*-type semiconductor photoelectrode. Starting with a brief overview about to-date known copper-based semiconductor photoelectrode metal oxide materials and photocatalysts, we gave in-depth understanding of the crystal structure, electronic structure, and effect of doping on the photoelectrochemical solar-to-fuel conversion.

2 Cu (I)-Based Photoelectrode and Photocatalysts: Current Status

Cuprous oxide (Cu_2O) is a nonstoichiometric defect *p*-type semiconductor and its potential for the design of solar cells have been recognized in 1920 well before silicon, germanium, and other potential semiconducting materials were discovered [23]. Owing to low bandgap (~2 eV) *p*-type semiconductor, it can generate up to 14.7 mA/cm^2 photocurrent (theoretically) under AM 1.5. Recently it has been explored as photocatalyst to generate hydrogen [24]. However there are relatively few studies about Cu_2O as photocathode and reported photocurrent values (1 mA/cm^2) are far less than theoretical value [25, 26]. As reduction potential of Cu_2O to Cu metal lies between the conduction band and valence band positions of Cu_2O, under photo illumination it can easily reduce to Cu metal and hence unstable. Although recent efforts show that the Cu_2O can be stabilized by nano-size layer of TiO_2 and Al_2O_3, the overall activity remains for 1 h.

Delafossites are another Cu (I)-based *p*-type semiconductor oxides which were extensively studied for transparent conducting oxide (TCO) application but relatively less reported as photocathode for PEC application. Kawazoe et al. [27] first reported the electrical conductivity of *p*-type $CuAlO_2$ for TCO. Following their work, Brahimi [28] reported the photocatalytic hydrogen evolution over $CuAlO_2$/TiO_2 heterojunction. A *p*-type $CuYO_2$ has been studied by Trari et al. [29] and reported photoelectrochemical activity for hydrogen generation. The addition of Ca increases the *p*-type characteristics of $CuYO_2$. Similarly, oxidized $CuYO_2$ to produce super oxides such as $CuYO_{2.25}$ and $CuYO_{2.5}$ shows higher photocatalytic activity compared to non-oxide samples, attributing the partial oxidation of Cu^+ in the $CuYO_2$ lattice [30]. A *p*-type $CuCrO_2$ delafossite with smaller bandgap (2.12 eV) has been studied photoelectrochemically [31]. Photocatalytic reduction of CO_2 to CO was carried out over $CuGaO_2$ and $CuGa_{1-x}Fe_xO_2$ delafossite,

however no reports about photoelectrochemical hydrogen production using this material [32]. Very recently Read et al. [33] reported $CuFeO_2$ delafossite for photoelectrochemical hydrogen production. Similarly, bare $CuFeO_2$ and $CuFeO_2$/SnO_2 heterojunction has been reported for visible light-induced photocatalytic hydrogen generation. Ca-doped $CuMnO_2$ and *p*-$CuMnO_2$/*n*-Cu_2O heterojunction was reported as a photocatalysts for hydrogen generation under alkaline condition.

Various Cu (II) oxides with spinel structure have been studied for photocatalytic hydrogen production. $CuMn_2O_4$ has a very narrow bandgap (1.4 eV) and can be utilized as a photocatalysts under visible light in an aqueous sulfide containing solution. The highest hydrogen evolution rate (0.26×10^{-2} mL/mg/h) was obtained over platinized $CuMn_2O_4$ under visible light compared to non-platinized sample [34]. Similarly, $CuFe_2O_4$ has been studied for the photocatalytic hydrogen evolution under visible light. The higher reaction rate is obtained over sol–gel synthesized photocatalyst compared to solid state and coprecipitation method. The study suggests that this catalyst is stable for 40 h [35]. The band structure and origin of stability is not clear but $CuFe_2O_4$ spinel is more stable compared to $CuFeO_2$ delafossite. Various other spinel structures such as $CuCr_2O_4$, $CuAl_2O_4$, and $CuCo_2O_4$ have been studied for photocatalytic hydrogen production under visible light, among them $CuCo_2O_4$ has the highest activity [36]. The tetragonal $SrCu_2O_2$ also reported as a *p*-type semiconductor with large bandgap (3.3 eV) for TCO applications [37]. Wang et al. [38] studied the heterojunction of WO_3/$SrCu_2O_2$ for photocatalytic hydrogen production.

3 New Class of Cu(I)-Based Metal Oxide Semiconductors

In this research area, our efforts have been focused on the investigation of new *p*-type semiconductors that comprise both early and late transition metals. Our research efforts have sought to investigate the reduction of the bandgap sizes of early transition-metal oxides via the incorporation of transition metals with d^{10} electron configurations, that is, specifically Cu^+. For example, a number of new Cu^+/Nb^{5+} and Cu^+/Ta^{5+} metal oxides reveal tunable and significantly reduced optical bandgap sizes in the range of ~2.4–1.2 eV within many structurally flexible networks [39]. These combinations yield the reduction of bandgap sizes via the use of Nb(V) or Ta(V) cations (empty d^0 orbitals) that form the conduction band states in early transition-metal oxides, together with a Cu(I) cation (filled d^{10} orbitals) that can form high-energy valence band states. For example, the isoelectronic substitution of Cu(I) for the Na cation in the $NaNbO_3$ photocatalyst decreases its bandgap size from ~3.4 to ~2.0 eV via the creation of a new higher energy valence band consisting of the filled Cu d^{10} orbitals, as found in $CuNbO_3$. For the UV-photocatalyst $Na_2Ta_4O_{11}$, the isoelectronic substitution of Cu^+ for Na^+ results in the site-differentiated solid solution $(Na_{1-x}Cu_x)_2Ta_4O_{11}$ with an accompanying modification of the bandgap transition and size from ~4.0 to 2.65 eV [40]. This new class of niobate and tantalate (based on d^{10} and d^0 configuration) phases has been

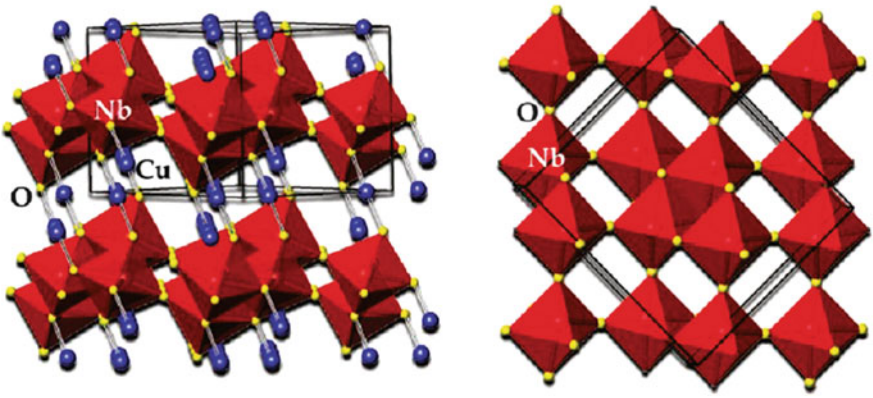

Fig. 1 Crystal structure of $CuNbO_3$. Reprinted with permission from J. Phys. Chem. C. Ref. [41]. Copyright (2011) American Chemical Society

investigated and their photoelectrochemical properties tested for the solar-to-fuel conversion [41–43]. The following section summarizes various copper niobates and copper tantalate metal oxide semiconductors with their crystal structure, electronic structure, and photoelectrochemical properties for solar-to-fuel conversion.

3.1 Crystal Structure, Electronic Structure, and Photoelectrochemical Properties

3.1.1 $CuNbO_3$

The monoclinic crystal structure of $CuNbO_3$ with C2/m space group symmetry has been described previously based on single crystal investigation [44]. The polyhedral structural view of $CuNbO_3$ is presented in Fig. 1. The structure contains stepped NbO_3 layers, which consist of edge-shared NbO_6 octahedra combined into Nb_4O_{16} groups. Each group is roughly parallel to [-101] plane and shares its corner oxygen atoms with other Nb_4O_{16} groups so that staircase-like NbO_3 layers appear down [001] as shown in Fig. 1 (left). These groups are similar to those observed in Na_3NbO_4 [45]. Copper atoms are situated between layers so that they linearly coordinate between two oxygen atoms from upper and lower Nb_4O_{16} groups, (blue spheres in Fig. 1 left). As it was indicated earlier [46], the staircase-layers of $CuNbO_3$ could be derived from layers of ReO_3-type structures so that in each layer the neighboring planar squares cornered by NbO_6 undergo the 45° rotation.

To understand the origin of the photon-driven bandgap transitions in $CuNbO_3$, electronic structure calculations were performed on the geometry-optimized structure based on density functional theory (DFT) within the CASTEP program package. The calculated total and partial electronic densities-of-states and bandgap size

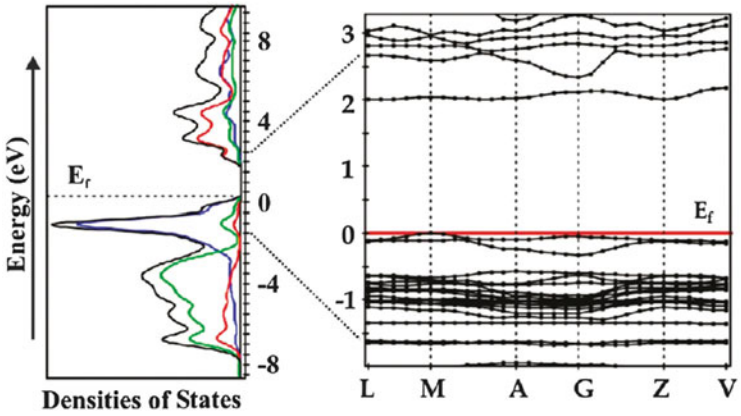

Fig. 2 On the *left*, the calculated electronic densities-of-states (DOS) of $CuNbO_3$ using CASTEP, including the total DOS (*black*), and the projected orbital contributions from Cu d-orbitals (*blue*), Nb d-orbitals (*red*), and O *p*-orbitals (*green*). On the right, the band structure k-space diagram for a narrower energy range falling within a few eV above and below the Fermi level (E_f). Reprinted with permission from J. Phys. Chem. C. Ref. [41]. Copyright (2011) American Chemical Society

are shown in Fig. 2 (left). The uppermost energy of $CuNbO_3$ valence band comprises filled Cu-based d-orbitals (blue line) mixed to a small extent with the filled O-based *p*-orbitals at lower energies, whereas the conduction band comprises empty Nb-based d-orbitals (red line) that are increasingly mixed at higher energies with empty O-based *p*-orbitals (green line). Thus, the lowest energy bandgap transitions are found to be a metal-to-metal charge transfer (MMCT) between Cu (d^{10})- to Nb (d^0)-based crystal orbitals. Analogous alkali-metal niobates are found to exhibit bandgap transition primarily from oxygen-to-niobium with higher sizes, for example, $NaNbO_3$ at 3.4 eV [47]. Thus, the isoelectronic substitution of Cu^+ for Na^+ has resulted in the insertion of a higher energy valence band based of the $3d^{10}$ orbitals of the former into new copper niobate phase.

Figure 2 (right) shows a plot of band-structure diagram for crystal orbitals as defined in its primitive space group setting within few electron volts. The lowest energy indirect transitions stemming from $k = M$ to L or M to Z, whereas the lowest energy direct bandgap transitions are at the $k = M$ vector just ~0.04 eV higher. This situation arises because of the flatness of the lowest energy conduction band crystal orbital located at ~2 eV in Fig. 2 (right). The flatness of this particular band leads to a higher effective mass and lower charge mobility of the excited electrons. This arises because the effective mass is inversely proportional to the rate of change of the band energy in *k*-space (i.e., $m \times R\ (\partial E)^2/\partial^2 k$).

Photocurrent measurements on $CuNbO_3$ were carried out using a three-electrode PEC. The $CuNbO_3$ working electrode was prepared by drop-coating $CuNbO_3$ slurry in ethanol over 2 cm^2 area. Figure 3 shows cyclic voltammetry scan from 0.2 V to −0.6 V vs. standard calomel electrode (SCE) under visible-light illumination. The photocathodic response is a clear evidence of the *p*-type conductivity in $CuNbO_3$.

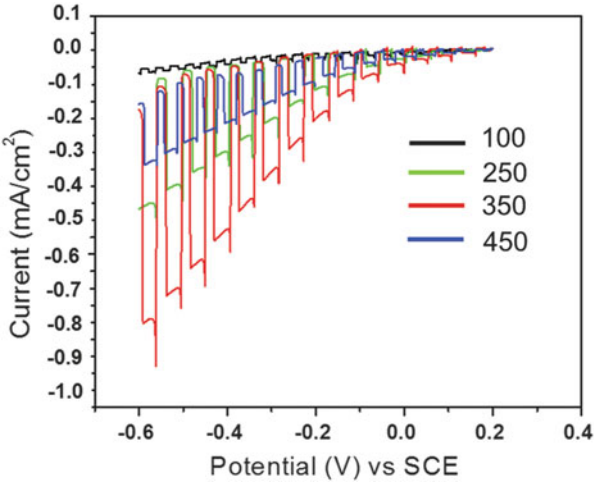

Fig. 3 Effect of oxidation temperature on the photocurrent of $CuNbO_3$ electrode

The electrode achieves a cathodic photocurrent density of -0.10 mA/cm^2 at -0.6 V applied bias versus SCE (after subtracting dark current, for non-oxidized samples not shown). Conversely, no photoanodic current is observed. The onset potential of the photocathodic current was observed at ~+0.10 V versus SCE, which corresponds to +0.35 V versus the reversible hydrogen electrode (RHE, at pH 6.3).

It is clearly evident that as the oxidation temperature increases the photocurrent response increases and it reaches maximum at 350 °C. Above 350 °C the photocurrent decreases. The XRD analysis shows that the $CuNbO_3$ phase is stable till 350 °C and above that the decomposition occurs, hence the activity decreases. As the oxidation increases more and more oxygen impurities inserted into the crystal enhance the *p*-type conductivity. The detailed understanding of the origin of *p*-type conductivity is discussed in Sect. 4. The chronoamperometry experiment shows that $CuNbO_3$ is stable at least for an hour. As electron excitation in $CuNbO_3$ from Cu (d^{10}) to Nb (d^0) orbital, final electron density resides at Nb hence prevent copper reduction to Cu metal (which is case in Cu_2O) and higher stability.

3.1.2 $CuNb_3O_8$

Another copper-containing niobate phase which can be easily obtained by stoichiometric reaction of Cu_2O and Nb_2O_5 at 750 °C for 1 day is $CuNb_3O_8$. The $CuNb_3O_8$ is crystallized as monoclinic structure with $P2_1/c$ space group symmetry. In earlier work of Marinder et al. [48] $CuNb_3O_8$ was described as mixed-valence compound with averaged atomic position of Cu^+ and Cu^{2+}, although there are contradictions in the literature about copper valence. It has been reported that $CuNb_3O_8$ is isostructural with $LiNb_3O_8$. There are striking similarities between the copper and the lithium compound. The octahedral environment of the niobium atoms is nearly the same in both compounds. The niobium–oxygen distances in the three types of

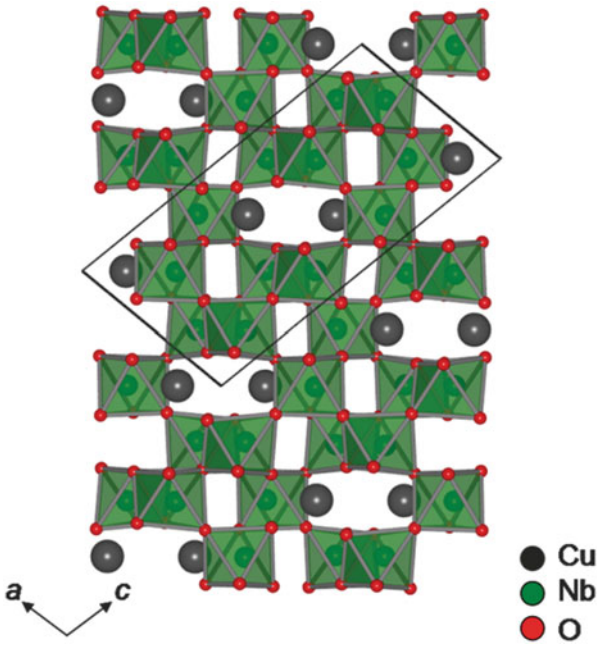

Fig. 4 The crystal structure of $CuNb_3O_8$

NbO_6 octahedra exhibit an even smaller range of variation than in $LiNb_3O_8$. Similar to $CuNbO_3$, the $CuNb_3O_8$ structure also consists of NbO_6 octahedra. Although in contrast to staircase-like layers of clustered NbO_6 octahedra, it can be described in terms of layers of identically oriented 1D zigzag chains of Nb- or/and Cu-centered NbO_6 octahedra, which share their edges and propagate along [010]. Packard oxygen and planar Nb/Cu atomic layers run parallel to [101] plane and alternate so that every ninth of them reproduces itself along [101] direction, Fig. 4. The atomic environment of Cu is a distorted octahedral.

To investigate the origin of the photon-driven bandgap excitations in $CuNb_3O_8$, electronic structure calculations were performed on the geometry-optimized structure based on DFT within the CASTEP program package. As shown in Fig. 5 the calculated band structures confirm the indirect band transition in $CuNb_3O_8$. However, the relative flatness of the bands also yields a direct bandgap transition only a little higher in energy. Figure 5 bottom (5a) shows electron density plots of the highest valence band states and the lowest conduction band states, that is, within 0.5 eV of each of the band edges. The conduction band edge mainly consists of one type of Nb atom d^0 orbitals (nonbonding), whereas the valence band edge consists primarily of Cu(I) d^{10} orbitals mixed with O 2*p* orbitals (σ^* interactions). Thus, similar to $CuNbO_3$, the lowest energy bandgap transition is an MMCT between Cu (I) and Nb(V). Figure 5 bottom (5b) shows the electron density plots of the valence and conduction band states further away from the band edge by an additional 0.5 eV. These show that the next highest conduction band states consist of d orbital contributions from all niobium atoms and the next lowest valence band states

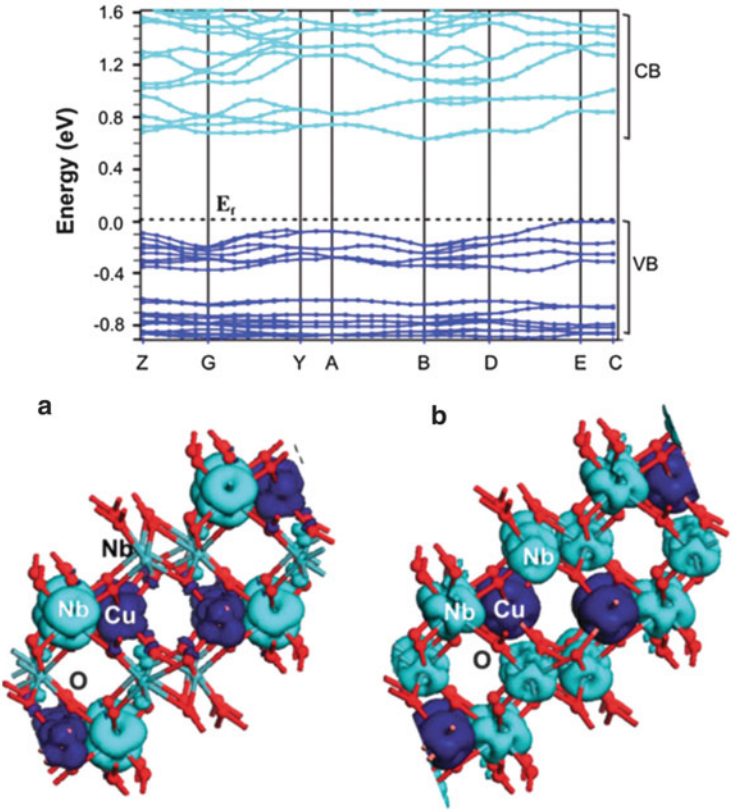

Fig. 5 *Top*: Calculated band structure diagram for $CuNb_3O_8$, with conduction and valence bands colored *light* and *dark blue*, respectively. *Bottom*: (**a**) Electron density plot of valence (*dark blue*) and conduction band (*light blue*) states within 0.5 eV of the band edge. (**b**) The same plot for valence and conduction band states within 0.5−1.0 eV of the band edge. O, Cu, and Nb atoms are *red*, *blue*, and *light blue*, respectively. Reprinted with permission from J. Phys. Chem. Lett. Ref. [42]. Copyright (2012) American Chemical Society

consist of filled copper d^{10} orbitals (weak $\sigma\pi$-to-$p\pi$ interactions to O 2*p* orbitals). Photoelectrochemical hydrogen generation was carried out on $CuNb_3O_8$ working electrode using Pt counter and SCE as a reference in a three-electrode cell. Figure 6 shows a linear-sweep cyclic voltammogram of the polycrystalline $CuNb_3O_8$ film electrode, under chopped visible-light irradiation. The photocathodic current increases with the applied bias voltage (+0.44 to −0.35 V plotted versus RHE), which is representative of typical *p*-type semiconductor behavior. The electrode film achieves a cathodic photocurrent density of −0.40 mA/cm^2 at a −0.35 V applied bias versus RHE, after subtraction of the dark current.

The onset potential of the photocurrent is estimated at ∼0.30 V vs. RHE (pH = 6.3). The estimated indirect bandgap of $CuNb_3O_8$ using UV–Vis spectroscopy is 1.26 eV, whereas direct bandgap is 1.47 eV. The *p*-type dopant

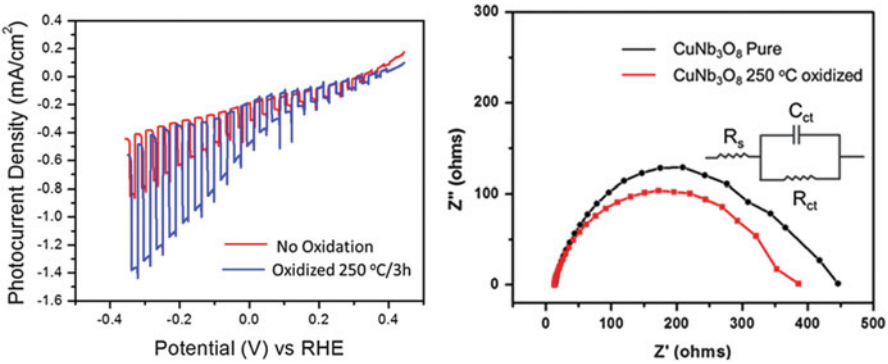

Fig. 6 *Left*: Effect of oxidation temperature on the photocurrent of $CuNb_3O_8$ electrode, *Right*: Electrochemical impedance spectra of $CuNb_3O_8$

concentration was found $\sim 7.2 \times 10^{15}$ cm^{-3}. Overall hole mobility was ~145 cm^2/V s. Under irradiation, the electrons in the $CuNb_3O_8$ film are excited into Nb-based crystal orbitals, which can lead to increased stability against photocorrosion as compared to *p*-type Cu_2O. The overall Faradaic efficiency for hydrogen evolution was 62 %. It is clearly shown in Fig. 6 that the photocurrent is higher for the 250 °C oxidized films compared to non-oxidized films. To investigate more about the origin of the high photocurrent in oxidized samples, we carried out electrochemical impedance spectroscopy (EIS). Figure 6 (right) shows EIS spectra measured under simulated solar light illumination and presented in Nyquist diagram in the frequency range of 100 kHz–100 MHz for bare pure $CuNb_3O_8$ and 250 °C oxidized film electrodes. The Nyquist plot can be interpreted in terms of the equivalent circuit as displayed in the inset. In the plot, symbols indicate the experimental results and the lines represent fitting results by using an equivalent circuit. Here, the EIS data were measured using a three-electrode cell system, thus the arc in Nyquist plot indicates the charge transfer kinetics on the working electrode. The fitted values of R_{ct} were 125 and 96 Ω for pure $CuNb_3O_8$ and oxidized $CuNb_3O_8$, respectively. The efficient charge transfer at the interface between photoelectrode/electrolyte hinders the charge recombination and induces the facile charge transport of electrons through the films. The large R_{ct} value for pure $CuNb_3O_8$ indicates that the charge transfer characteristics of non-oxidized $CuNb_3O_8$ are poor. Thus, the oxidized films show a very good efficiency of charge transfer compared to pure non-oxidized $CuNb_3O_8$ film electrodes.

3.1.3 $Cu_3Ta_7O_{19}$

$Cu_3Ta_7O_{19}$ crystallizes in a hexagonal structure with P63/m space group symmetry. Polyhedral view down [110] is shown in Fig. 7 (top). The structure contains layers of edge-shared TaO_7 pentagonal bipyramids. These layers stack along *c*-axis, sharing apex oxygen atom and forming double layers. These alternate with layers

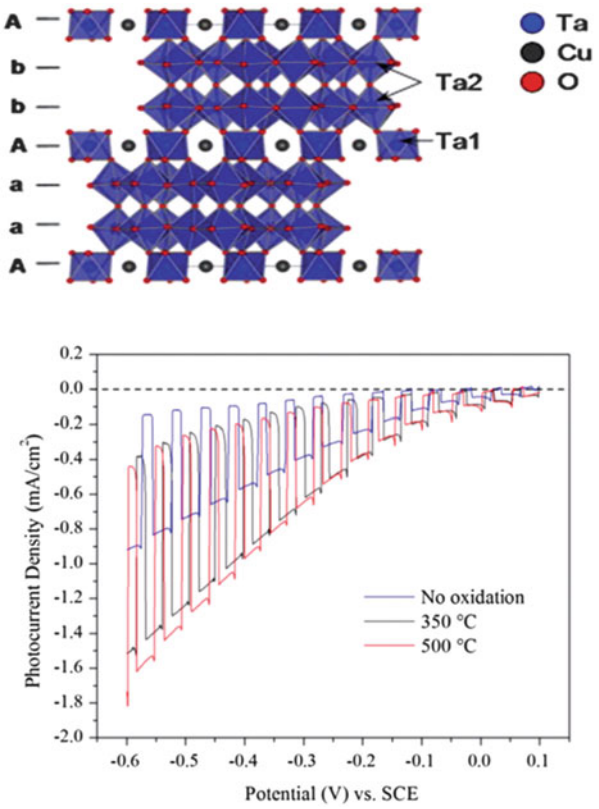

Fig. 7 *Top*: The crystal structure of $Cu_3Ta_7O_{19}$. *Bottom*: Effect of oxidation on the photoresponse of $Cu_3Ta_7O_{19}$ film electrode. *Bottom* figure reprinted with permission from J. Phys. Chem. C. Ref. [43]. Copyright (2012) American Chemical Society

of TaO_6 octahedra and linearly coordinated Cu^+. The TaO_6 octahedra are formed from the apical oxygen atoms from three edge-shared pentagonal bipyramids both above and below. Electronic structures were calculated based on plane-wave DFT methods from the geometry-optimized crystal structures reported for $Cu_3Ta_7O_{19}$, Cu(I)−tantalate compounds. The calculated band structure for $Cu_3Ta_7O_{19}$ (not shown) predicts the highest carrier mobilities within the 2D plane defined by $k = \mathrm{K} \rightarrow \mathrm{G} \rightarrow \mathrm{M}$ in the plane of the TaO_7 layers, but a lower mobility for the reciprocal directions along $k = \mathrm{L} \rightarrow \mathrm{M} \rightarrow \mathrm{K}$ between the layers.

The DOS calculations further confirm that the electron density for lowest energy conduction band state located on TaO_7 layers, whereas for highest energy valence band state it is situated on TaO_6/Cu layers. Thus, electron density in these layers represents the primary transition between filled Cu d^{10} and empty Ta d^0-based crystal orbitals which are lowest energy bandgap transition between the valence and conduction bands. The conduction band states are found to occur over both the TaO_7 in the double layers and the isolated TaO_6 octahedra, while valence band states are shown to reside predominantly on Cu (I) ions. Additional minor contributions arise from the bridging oxygen ligands between the edge-linked TaO_7 polyhedra, showing that excited electrons into this band would migrate within the

2D layers of this structure. There are no direct Cu-O−Cu bridges to facilitate hole transport within the isolated Cu(I)/TaO_6 layer of the structure, while there are shared Cu−O−Ta bridging interactions that would facilitate a charge transfer transition to the tantalate layer. The direct Cu−Cu distances are ∼3.10 Å within these structures.

The *p*-type behavior of $Cu_3Ta_7O_{19}$ is evident by photocathodic response in the cyclic voltammogram (Fig. 7 bottom). The photoelectrochemical measurement shows that the conduction band position of $Cu_3Ta_7O_{19}$ is negative enough compared to the water reduction potential and hence it can reduce water to hydrogen. The photocurrent response at −0.6 V vs. SCE was −0.75 mA/cm^2 in non-oxidized films. It is worth to mention that a relative low dark current is observed compared to $CuNbO_3$ or $CuNb_3O_8$. The oxidation of $Cu_3Ta_7O_{19}$ at different temperatures shows a higher photocurrent compared to non-oxidized samples, suggesting the *p*-type doping into the matrix.

3.1.4 $Cu_5Ta_{11}O_{30}$

The $Cu_5Ta_{11}O_{30}$ also crystallizes in a hexagonal structure with P62c space group symmetry. The $Cu_5Ta_{11}O_{30}$ structure consists of alternating single and double layers of the TaO_7 units in contrast to stacking of double layers of TaO_7 units in $Cu_3Ta_7O_{19}$ structure. Figure 8 shows the crystal structure of $Cu_5Ta_{11}O_{30}$. The conduction band states are found to occur only on TaO_7 octahedra double layers, the single layers of TaO_7 in $Cu_5Ta_{11}O_{30}$ do not contribute to these conduction band states, whereas valence band states are found on Cu(I)/TaO_6 layers. These layers represent primarily a transition between filled Cu d^{10} and empty Ta d^0-based crystal orbitals which are lowest energy bandgap transition between the valence and conduction bands.

Photoelectrochemical measurement shows (Fig. 8 bottom) *p*-type characteristics of $Cu_5Ta_{11}O_{30}$ phase with photocurrent reaching as high as −0.2 mA/cm^2 at −0.6 V applied bias vs. SCE without oxidation. The pronouns effect of oxidation is observed on the photocurrent. The saturation of photocurrent (−2 mA/cm^2) was observed ∼−0.6 V vs. SCE for the oxidized films at 350 °C. It is worth to mention that the dark current is also considerably reduced after oxidation of films. The conduction band of $Cu_5Ta_{11}O_{30}$ is more dispersed compared to $Cu_3Ta_7O_{19}$ and copper niobate phases hence higher photocurrent is obtained. As $Cu_5Ta_{11}O_{30}$ have alternating single and double layers of TaO_7 units, which facilitate the charge separation and migration effectively, the photocurrent is high. The lack of these layers in $CuNbO_3$ and $CuNb_3O_8$ and less dispersion of valence band give low photocurrent.

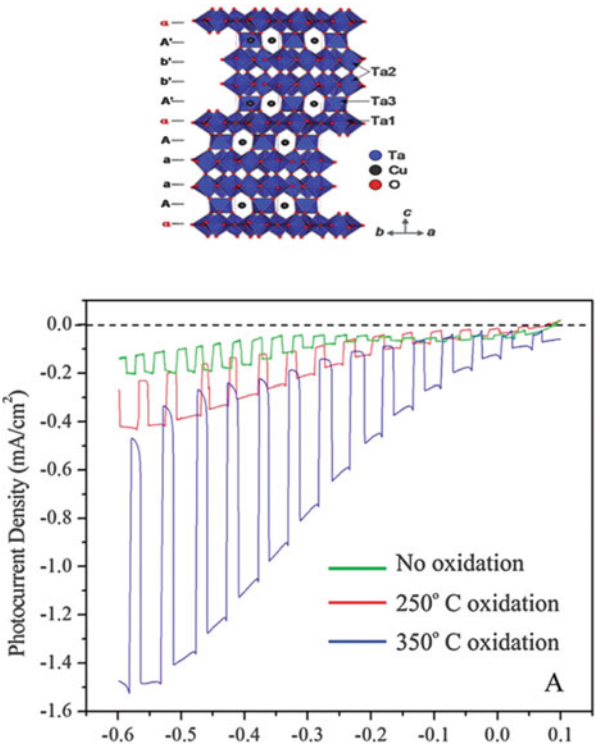

Fig. 8 *Top*: The crystal structure of $Cu_5Ta_{11}O_{30}$. *Bottom*: The effect of oxidation on the photoresponse of $Cu_5Ta_{11}O_{30}$ film electrode. *Bottom* figure reprinted with permission from J. Phys. Chem. C. Ref. [43]. Copyright (2012) American Chemical Society

4 The Origin of *p*-Type Conductivity in Copper Niobates, Copper Tantalates, and Future Challenges

Naturally occurring cation-deficient metal oxides are hole conductors and hence *p*-type. In broad term any oxide can be a cation deficient if its cation is oxidizable (i.e., can have more positive oxidation number). The cation deficiency could occur via metal vacancies, and/or oxygen interstitials, and/or oxygen antisites creating a hole and hence *p*-type conductivity. In case of Cu_2O, it has been reported that the origin of *p*-type conductivity is in cation deficiency, accommodated mostly by Cu vacancies (V_{cu}) rather than oxygen interstitials (O*i*). The stable concentration of V_{cu} is found to be ~10^{20} cm^{-3}, thus naturally making it *p*-type conductor. Delafossite structures are well-known *p*-type semiconductors but suffers from very low hole conductivity. The origin of *p*-type conductivity in delafossite is also reported due to copper vacancies. In case of copper niobates and copper tantalates intrinsic *p*-type conductivity conformed by photoelectrochemical measurements, the nature and origin of *p*-type conductivity is under investigation. The overall *p*-type photocurrent is less in case of non-oxidized copper niobates and copper tantalates due to the lack of Cu-O-Cu linkage as seen in Cu_2O. The photocurrent in $Cu_3Ta_7O_{19}$ and $Cu_5Ta_{11}O_{30}$ is high suggesting the high hole conductivity may be due to favorable

mixing of 5d states on tantalum cation in the Cu–O–Ta–O–Cu linkages and well-dispersed valence band. In case of $CuNbO_3$ and $CuNb_3O_8$ the valence band is not dispersed; hence, then hole mobility is low owing to low photocurrent. In all copper niobates and copper tantalate phases, the oxidized sample shows higher photocurrent. The oxidation of these phases forms a mixture of Cu(I)/Cu(II) at the surface of films, in term increases the Cu(I) vacancies and hence high photocurrent.

To investigate furthermore on the origin of *p*-type conductivity in the copper niobates and tantalates, we carried out Cu^{2+} doping into $CuNb_3O_8$. The partial substitution of Cu^{2+} doping will create Cu^{1+} vacancies, if Cu^{2+} is accommodated in Cu^{1+} site. The results after doping with Cu^{2+} show no photoelectrochemical activity suggesting that the Cu^{2+} doping has an adverse effect on the activity. However, the oxidation of doped samples show the higher photoresponse compared to the non-oxidized samples and pure $CuNb_3O_8$. This suggests that the oxidation step is inevitable to all the samples under study and after oxidation only high photoactivity was observed. These results clearly indicate that the possible origin in enhanced activity is either due to oxygen interstitials or formation of CuO on the surface which in turn forms *p*–*n* junction (e.g., $CuO/CuNb_3O_8$). To check the possibility of oxygen interstitials, one has to do thorough XRD and TGA analysis and investigate the oxygen percent in the sample before oxidation and after oxidation. This work is undergoing and detailed results will be published soon. The primary results suggest that the oxygen percentage is increasing, but the overall cell volume decreasing suggests that the copper is leaching out on the surface. The copper which is out of the structure gets oxidized to form CuO. Hence confirm the second possibility of formation of *p*–*n* junction.

The key challenge in the development of new *p*-type semiconductor metal oxide is the overall conductivity and stability. As *p*-type conductivity is originates in the cation vacancies/or oxygen interstitial, which is very difficult to create and hence *p*-type metal oxide with high conductivity are difficult to make compare to metallic or chalcogenide *p*-type semiconductors. Furthermore, the cation vacancies can be easily occupied by adding atom impurities, surface defects, or the oxygen dangling bonds created due to the absence of cation can be easily stabilized by impurity, hence *p*-type conductivity decreases rapidly. Doping with other cation having different oxidation state can be another approach to improve the overall stability of *p*-type semiconductor metal oxides, but phase segregation is a problem before achieving desire conductivity value. An ideal *p*-type semiconductor with similar conductivity values as *n*-type semiconductor is still a challenge for scientists and engineers.

5 Summary

This chapter summarizes the current state of copper-based *p*-type semiconductors for solar-to-fuel conversion. The new class of *p*-type metal oxide semiconductors for photoelectrochemical solar-to-fuel conversion based upon combination of early

(Nb^{5+}, Ta^{5+}) and late transition metal (specifically Cu^{+}) has been introduced. Incorporation of Cu (d^{10}) orbitals into the structure creates new high-energy valence band states, hence reduces the bandgap into visible region. Various copper niobates (such as $CuNbO_3$ and $CuNb_3O_8$) and tantalates (such as $Cu_3Ta_7O_{19}$ and $Cu_5Ta_{11}O_{30}$) have been investigated as a photocathode for the PEC application. The photoelectrochemical properties were investigated and correlated with crystal structures and electronic structures. The positive effect of oxidation of the niobate and tantalate shows a higher photocurrent.

References

1. Kamat PV (2007) Meeting the clean energy demand: Nanostructure architectures for solar energy conversion. J. Phys. Chem. C 111(7): 2834-2860.
2. Walter MG, Warren EL, McKone JR, Boettcher SW, Mi Q, Santori EA, Lewis NS (2010) Solar water splitting cells. Chem. Rev. 110 (11): 6446-6473.
3. Chen X, Shen S, Guo L, Mao SS (2010) Semiconductor-based photocatalytic hydrogen generation. Chem. Rev. 110 (11): 6503-6570.
4. Osterloh F (2008) Inorganic materials as catalysts for photochemical splitting of water. Chem. Mater. 20(1): 35-54.
5. Kumar B, Llorente M, Froehlich J, Dang T, Sathrum A, Kubiak CP (2012) Photochemical and photoelectrochemical reduction of CO_2. Annu. Rev. Phys. Chem. 63: 541-69.
6. Barton EE, Rampulla DM, Bocarsly AB (2008) Selective solar-driven reduction of CO_2 to methanol using a catalyzed p-GaP based photoelectochemical cell. J. Am. Chem. Soc. 130: 6342-6344.
7. Cole EB, Lakkaraju PS, Rampulla DM, Morris AJ, Abelev E, Bocarsly AB (2010) Using a one-electron shuttle for the multielectron reduction of CO_2 to methanol: Kinetics, mechanistic and structural insights. J. Am. Chem. Soc. 132: 11539-11551.
8. Kubacka A, García MF, Colón G (2012) Advanced nanoarchitectures for solar photocatalytic applications. Chem. Rev. 112: 1555-1614.
9. Kudo A, Miseki Y (2009) Heterogeneous photocatalytic materials for water splitting. Chem. Soc. Rev. 38: 253-278.
10. Khaseley O, Turner JA (1998) A monolithic photovoltaic-photoelectrochemical device for hydrogen production via water splitting. Science 280: 425-427.
11. Bard AJ (1980) Photoelectochemistry. Science 207: 139-144.
12. Sun J, Liu C, Yang P (2011) Surfactant-free, large-scale, solution-liquid-solid growth of gallium phosphide nanowires and their use for visible-light-driven hydrogen production from water reduction. J. Am. Chem. Soc. 133: 19306-19309.
13. Nian J-N, Hu C-C, Teng H (2008) Electrodeposited p-type Cu_2O for H_2 evolution from photoelectrolysis of water under visible light illumination. Int. J. Hydrogen Energy 33: 2897-2903.
14. McShane CM, Choi K-S (2009) Photocurrent enhancement of n-type Cu2O electrodes achieved by controlling dendritic branching growth. J. Am. Chem. Soc. 131: 2561-2569.
15. Nakaoka K, Ueyama J, Ogura K (2004) Photoelectrochemical behavior of electrodeposited CuO and Cu_2O thin films on conducting substrate. J. Electrochem. Soc. 151: C661-C665.
16. Ingler WB, Baltrus JP Jr., Khan SUM (2004) Photoresponse of p-type zinc-doped iron (III) oxide thin films. J. Am. Chem. Soc. 126: 10238-10239.
17. Leygraf C, Hendewerk M, Somorjai GA (1982) Photocatalytic production of hydrogen from water by a p- and n-type polycrystalline iron oxide assembly. J. Phys. Chem. 86: 4484-4485.

18. Matsumoto Y, Omae M, Sugiyama K, Sato E (1987) New photocathode materials for hydrogen evolution: $CaFe_2O_4$ and $Sr_7Fe_{10}O_{22}$. J. Phys. Chem. 91: 577-581.
19. Ida S, Yamada K, Matsunaga T, Hagiwara H, Matsumoto Y, Ishihara T (2010) Preparation of p-type $CaFe_2O_4$ photocathodes for producing hydrogen from water. J. Am. Chem. Soc. 132: 17343-17345.
20. Iwashina K, Kudo A (2011) Rh-doped $SrTiO_3$ photocatalyst electrode showing cathodic photocurrent for water splitting under visible-light irradiation. J. Am. Chem. Soc. 133: 13272-13275.
21. Chavillon B, Cario L, Renaud A, Tessier F, Chevire F, Boujtita M, Pellegrin Y, Blart E, Smeigh A, Hammarstrom L, Odobel F, Jobic S (2012) P-type nitrogen doped ZnO nanoparticles stable under ambient conditions. J. Am. Chem. Soc. 134: 464-470.
22. Paracchino A, Laporte V, Sivula K, Grätzel M, Thimsen E (2011) Highly active oxide photocathode for photoelectrochemical water reduction. Nature Mater. 10: 456-461.
23. Walter HB. (1951) The copper oxides rectifier, In Review of Modern Physics, pp. 203-208.
24. Hara M, Kondo T, Komoda M, Ikeda S, Shinohara K, Tanaka A, Kondo JN, Domen K (1998) Cu_2O as a photocatalyst for overall water splitting under visible light irradiation. Chem. Commun. 3: 357-358.
25. de Jongh PE, Vanmaekelbergh D, Kelly JJ (2000) Photoelectrochemistry of deposited Cu_2O. J. Electrochem. Soc. 147: 486-489.
26. Siripala W, Ivanovskaya A, Jaramillo TF, Baeck SH, McFarland EW (2003) A Cu_2O/TiO_2 heterojunction thin film cathode for photoelectrocatalysis. Sol. Energy Mater. Sol. Cells 77: 229-237.
27. Kawazoe H, Yasukawa M, Hyodo H, Kurita M, Yanagi H, Hosono H (1997) P-type electrical conduction in transparent thin films of $CuAlO_2$. Nature 389: 939-942.
28. Brahimi R, Bessekhouad Y, Bouguelia A, Trari M (2007) $CuAlO_2/TiO_2$ heterojunction applied to visible light H_2 production. J. Photochem. Photobio A 186: 242-247.
29. Trari M, Bouguelia A, Bessekhouad Y (2006) p-type $CuYO_2$ as hydrogen photocathode. Sol. Ener. Mater. & Sol. Cell. 90: 190-202.
30. Younsi M, Saadi S, Bouguelia A, Aider A, Trari M (2007) Synthesis and characterization of oxygen rich delafossite $CuYO_{2+x}$—application of H_2 photo production. Sol. Ener. Mater. & Sol. Cell 91: 1102-1109.
31. Boumaza S, Bouarab R, Trari M, Bouguelia A (2009) Hydrogen photo-evolution over the spinel $CuCr_2O_4$. Energ. Conv. Manag. 50: 62-68.
32. Lekse JW, Underwood MK, Lewis JP, Matranga C (2012) Synthesis, characterization, electronic structure, and photocatalytic behavior of $CuGaO_2$, and $CuGa_{1-x}Fe_xO_2$ ($x = 0.05$, 0.10, 0.15, 0.20) delafossites. J. Phys. Chem. C 116: 1865-1872.
33. Read CG, Park Y, Choi K-S (2012) Electrochemical synthesis of p-type $CuFeO_2$ electrodes for use in a photoelectrochemical cell. J. Phys. Chem. Lett. 3: 1872-1876.
34. Bessekhouad Y, Trari M (2002) Photocatalytic hydrogen production from suspension of spinel powders AMn_2O_4 (A = Cu and Zn). Inter. J. Hydro. Energ. 27: 357-362.
35. Yang H, Yan J, Lu Z, Cheng X, Tang Y (2009) Photocatalytic activity evolution of tetragonal $CuFe_2O_4$ nanoparticles for the H_2 evolution under visible light irradiation. J. Alloy. Compd. 476: 715-719.
36. Saadi S, Bouguelia A, Trari M (2006) Photoassisted hydrogen evolution over spinel CuM_2O_4 (M = Al, Cr, Mn, Fe, and Co). Renewable Energy 31: 2245-2256.
37. Kudo A, Yanagi H, Hosono H, Kawazoe H (1998) $SrCu_2O_2$: A p-type semiconductor oxide with wide band gap. Appl. Phys. Lett. 73: 220-222.
38. Wang G, Wu C, Song B, Wang Y (2011) Synthesis and photocatalytic activity of $SrCu_2O_2$ for water decomposition to hydrogen. Adv. Mater. Rese. 239: 2914-2918.
39. Joshi UA, Palasyuk A, Arney D, Maggard PA (2010) Semiconducting oxides to facilitate the conversion of solar energy to chemical fuels. J. Phys. Chem. Lett. 1: 2719-2726.

40. Palasyuk O, Palasyuk A, Maggard PA (2010) Site-differentiated solid solution in $(Na_{1-x}Cu_x)_2Ta_4O_{11}$ and its electronic structure and optical properties. Inorg. Chem. 49: 10571-10578.
41. Joshi UA, Palasyuk AM, Maggard PA (2011) Photoelectrochemical investigation and electronic structure of a p-type $CuNbO_3$ photocathode. J. Phys. Chem. C 115: 13534-13539.
42. Joshi UA, Maggard PA (2012) $CuNb_3O_8$: A p-type semiconducting metal oxide photocathode. J. Phys. Chem. Lett. 3: 1577-1581.
43. Fuoco L, Joshi UA, Maggard PA (2012) Preparation and photoelectrochemical properties of p-type $Cu_5Ta_{11}O_{30}$ and $Cu_3Ta_7O_{19}$ semiconducting polycrystalline films. J. Phys. Chem. C 116: 10490-10497.
44. Wahlström E, Marinder B-O. (1977) Phase analysis studies in copper-niobium-oxygen system. Inorg. Nucl. Chem. Letters 13: 559-564.
45. Meyer G, Hoppe R (1974) Na_3NbO_4, das erste orthoniobat mit inselstruktur: $Na_{12}[Nb_1O_{16}]$. *Naturwiss* **1974**, *61*, 501.
46. Marinder B-O, Wahlström E (1984) $CuNbO_3$- a structure with stepped NbO_3 layers. Chemica Scripta 23: 157-160.
47. Li G, Kako T, Wang D, Zuo Z, Ye J (2008) Synthesis and enhanced photocatalytic activity of $NaNbO_3$ prepared by hydrothermal and polymerized complex methods. J Phys. Chem. Sol. 69: 2487-2491.
48. Marinder B-O, Werner P-E, Wahlstroem E, Malmros G (1980) Investigation on a new copper niobate oxide of $LiNb_3O_8$ type using chemical analysis and x-ray powder diffraction analysis. Acta Chem. Scand. A. 34: 51-56.

Theoretical Modeling of Oxide-Photocatalysts for PEC Water Splitting

Muhammad N. Huda

1 Introduction

Theoretical modeling of materials by *first principle* theories is a powerful tool to guide and explain experimental challenges for rapid discovery of any functional material [1]. Because of the guidance and explanations that can be gained by theoretical efforts, the expensive and time-consuming laboratory trial-and-error processes can be replaced by a quicker theory-experiment feedback loop. In addition, theoretical study can play a crucial role in selecting appropriate materials from available database and to design composite functional systems [2]. Recent developments of computational power and algorithm enable theorists to compute/simulate materials of practical sizes with realistic approximations. In this chapter, some of the metal-oxide materials that we have studied recently will be reviewed. The goal of this chapter is not so much to discuss the theory or methodology-related challenges in order to study such materials, rather to highlight the relevant physical or chemical insights that can be gained from the theoretical/computational studies. For reviews of the electronic structure theory-related issues, the reader may consult several good review articles [3–6].

In order to have a focused goal to study the metal-oxides, we will mainly concentrate on their applications as photocatalysts. Photoelectrochemical (PEC) splitting of water by solar light is considered to be the most desirable "green" method for hydrogen production [7–9]. This has attracted great attentions since the demonstration of water splitting by a TiO_2 photoanode illuminated with ultraviolet light over four decades ago by Fujishima and Honda [10]. As a result, TiO_2 has enjoyed much popularity as a photocatalyst in the PEC communities. However,

M.N. Huda (✉)
Department of Physics, University of Texas at Arlington, Box 19059, Arlington, TX 76019, USA
e-mail: huda@uta.edu

B. Viswanathan et al. (eds.), *Materials and Processes for Solar Fuel Production*, Nanostructure Science and Technology 174, DOI 10.1007/978-1-4939-1628-3_6

under visible-light illumination TiO_2, with a bandgap over 3 eV, does not show much photoactivity. To meet the necessary energy requirements for water splitting by absorbing the visible range of the solar spectra, the desired photocatalyst must be a semiconductor which is stable in aqueous solutions, has bandgap around 2.0 eV, and the positions of its band edges must be matched with the water-splitting reduction potentials with proper band edge properties [11]. In addition, low cost photocatalysts consist of earth abundant elements are desirable for a successful commercial PEC hydrogen production. In general, naturally occurring semiconductors do not satisfy all these constraints simultaneously. New methods and technology must be developed to engineer such semiconductors. Metal-oxides are found to stable, and can meet most of the criteria through suitable electronic structure modification. Theoretical studies can contribute most in this endeavor.

It is to be noted that a suitable bandgap alone may not ensure good photocurrent activity if the charge carriers mobility in the photocatalysts is poor [12]. In transition metal-oxides, the presence of the localized 3*d* metal orbitals near the band edges, such as near valence band maximum (VBM) and/or conduction band minimum (CBM), increase the charge carriers' effective masses. These 3*d* bands result in a very flat band structures at the VBM or CBM. So, though metal-oxides are sometimes preferable because of their stability, these may suffer from high resistivity, such as in α-Fe_2O_3 or $CuWO_4$. On the other hand, a conducting semiconductor with good carrier mobility does not automatically guarantee to have a better optical transition at the minimum direct bandgap. Due to the crystal structures, certain symmetry conditions of the crystals may prohibit an optical transition at the minimum bandgap, for example, in Cu_2O and $CuAlO_2$ [13]. However, theoretical studies can help improve the situations. It has been shown that by breaking the symmetry of the delafossite, such as in $CuYO_2$, by means of appropriate alloying or doping, the optical absorption can be improved at this smallest direct gap [14]. Hence, while doping or alloying a photocatalyst to band engineering its gap and band edge positions, the carrier mobility and optical absorption issues need to be taken into careful considerations.

The most common method used for bandgap reduction of metal-oxides is the incorporation of impurities, such as C and N [15–17]. However, it has been argued that although impurities can reduce the bandgap, their incorporation also leads to poor photocurrent. This is because the partially occupied or unoccupied impurity bands which are created due to doping can act as carrier traps for photo-generated carriers [18]. It has been demonstrated that passive donor–acceptor co-doping may suppress the recombination and yet maintain a reduced bandgap. These "non-isovalent compound" alloying could be an excellent choice for bandgap engineering due to the large band offsets that can exist between the compounds [19, 20]. Compound alloying poses several critical problems, including choosing the appropriate host and alloying semiconductors, the alloying approach, and the alloying concentration. A thorough theoretical understanding of the non-isovalent alloying physics is necessary to prescreen the potential alloying materials for a given purpose.

On the other hand, the availability of both *n*-type and *p*-type semiconductors is often desirable for photocatalysts [21]. Oxides, in general, are found to be *n*-type semiconductors because of high electronegativity of O 2*p* orbitals. As the upper part of the valence band usually consists of O 2*p* band hybridized with metal d bands, high electronegativity of O 2*p* band pushes down the VBM. For effective and sustainable *p*-type doping in oxides, higher VBM is necessary. In metal-oxides, this can be achieved by selecting metals with relatively higher *d*-orbital position. In several theoretical studies, the doping rule for desired type of conductivity has been explained extensively [22, 23]. Among the transition metals, Cu 3*d* has the highest energy. Hence, Cu-based oxides are more likely to be doped with *p*-type carriers. However, Cu_2O is not stable in aqueous solutions, though its bandgap is in the right range. Recently, Cu delafossites, $CuMO_2$ (M = group III-A (group 13) and III-B (group 3) elements), have received great attention due to their unique properties such as stability in most aqueous solutions and *p*-type conductivity with excellent hole mobility [24, 25]. The *p*-type conduction here is due to the fact that their VBM is composed of hybridized Cu-*d* and O 2*p* antibonding orbitals. PEC response for some Cu delafossites has already been demonstrated [26, 27].

2 A Brief Computational Detail

The theoretical results of metal-oxide materials reviewed in the rest of the chapter were obtained by density-functional theory (DFT) calculations. Local density approximation (LDA) or generalized gradient approximation (GGA) to DFT and the projected augmented wave (PAW) basis as implemented in the Vienna ab initio simulation package (VASP) were used [28–30]. To correct the DFT-LDA/GGA underestimation of electron correlation in the cation 3*d* bands, DFT + U method has been used in general [31, 32]. This usually improves the value of the calculated bandgap as compared against the experimental value. It should be noted that the choice of the value of U cannot be determined uniquely within the present methodology. The choice of U for the metal cation such as in Cu- or Zn-based oxides has been discussed in our previous papers [20, 33]. In the following, some general features of few metal-oxides are presented. These discussions are based on the bulk crystalline phase of these oxides, as significant fundamental insights can be gained by studying the bulk phases. In fact, a good understanding of the bulk phase can lead to the appropriate defect study or interface study to further tune the photocatalysts' electronic properties. For the sake of brevity, defects discussions will be very cursory. In almost all of the following cases, the structural parameters and the choice of ground state crystal symmetry were found to be agreed well with known experimental results. For specific details of a particular oxide, the reader my consult the original references as will be mentioned below.

3 Some Representative Oxides

1. ZnO: It is one of the most studied binary oxides having partially filled 3*d* band in their valence band. The presence of this 3*d* band, which is hybridized with O 2*p* band, determines the minority carrier transport for this *n*-type material. Minority carrier transport is crucial for the splitting of oxygen from water. In addition, ZnO is also well known for its difficulty in *p*-type doping [34]. Significant efforts have been made, but *p*-type doping in ZnO is still difficult to stabiliz. Successful *p*-type doping in ZnO requires a shallow delocalized acceptor level. A donor/acceptor level due to doping can be considered delocalized if its wave function is not strictly localized only on the dopant atom, and electrons/holes transport from the dopant atom to neighboring sites does not require much activation energies. In general, doping destroys the local symmetry, and the chemical mismatch between the host and dopant may result in deep defect levels in the bandgap. To reduce these effects and to overcome the difficulty in *p*-type doping of ZnO, many approaches have been theoretically proposed [35–40]. A recent DFT study has offered details on the electronic state of the acceptor levels; explored whether a shallow acceptor level is effectively delocalized and in what electronic configuration it manifests [41]. For efficient photocatalysts, it is important to examine these doping characteristics to facilitate the delocalization of carriers.

DFT + U band structure of pristine ZnO is shown in Fig. 1, where 0.00 eV refers to the highest occupied band, i.e., top of the valence band (also known as Fermi level). The calculated bandgap is 1.67 eV and is a direct gap at Γ-point. In comparison, the experimental bandgap is 3.25 eV which can absorb light only at the UV region. This underestimation of the bandgap is a typical feature of DFT calculations. On the other hand, several characteristics of this band structure can give insights into the fundamental features of ZnO. Two interesting features can be noted from the band structures immediately; first, the conduction band is more dispersive than the valence band. This implies that electron conduction is much less resistive (less effective mass) than the hole conduction. Secondly, the VBM is not very flat either, which shows rather larger O 2*p* contribution compared to Zn 3*d* orbital. The highly localized part of Zn 3*d* band is seen below −6 eV. These features made ZnO a good conducting semiconductor once the photo-excited carriers are generated. However, it is known that ZnO is not stable in electrolyte due to photo-corrosion. Hence, the main challenges in ZnO are to stabilize it and to reduce the bandgap.

Reduction of bandgap by doping has been tried, for example, by nitrogen substitutional doping at O-site [42]. Even though these doping reduce bandgap, photocurrent was found not to be increased as expected [15]. In fact, the occurrence of localized levels in the bandgap due to doping is responsible for it. These localized states act as charge trapping centers and increase recombination rate. This may be avoided by clever doping strategies, such as random alloys [19]. For example, isovalent pair alloying, such as Ga–N pair alloying in ZnO was found to be energetically more favorable and uplift the VBM at higher energy, which can

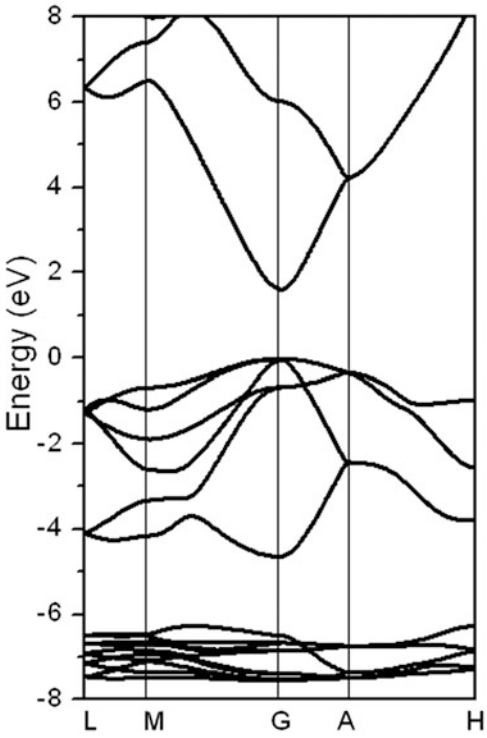

Fig. 1 Band structure of ZnO with GGA + U, where $U_{eff} = 7$ eV was applied to Zn-*d* band

reduce the overall bandgap and facilitate further *p*-type doping [20, 43]. Similar effect can be obtained by Al–N pair alloying in ZnO, where the bandgap reduction was found to be by 0.5 eV. Even though in both cases, the bandgap remained direct, the *N*-related levels on top of valence band are shallower for Ga–N alloying in ZnO. It has been further shown that nitrogen doping on (Ga–N)-cluster doped ZnO create shallower acceptor levels compared to nitrogen doped ZnO. Some theoretical insights of the doping-based band engineering will be discussed in the next oxide.

2. WO_3: WO_3 is a class of oxides which are, unlike ZnO, relatively more stable in aqueous solution. The 5*d* orbital in WO_3 is not very localized, hence this represent a different class of metal-oxides than TiO_2 or ZnO. The monoclinic WO_3 can be considered as a deformed perovskite structure, such as ABO_3 where the A ions are missing and B is replaced by W which are sixfold coordinated. The WO_3 structure can also be considered as consisting of W-O-W-like chains, where the chains are connected across the W atoms, as seen in Fig. 2. This pseudo low-dimensional structure of WO_3 has given rise to many interesting properties, including superconductivity. The inter-chain O–O interactions are rather weak.

The band structure presented in Fig. 3a was calculated by LDA of density functional theory (LDA-DFT) [44]. Here we see that there are two nearly degenerate states at the conduction-band minima (CBM). The VBM at Γ point also splits due to the distorted arrangement of the W-O octahedrons. Also, at B → Γ segment

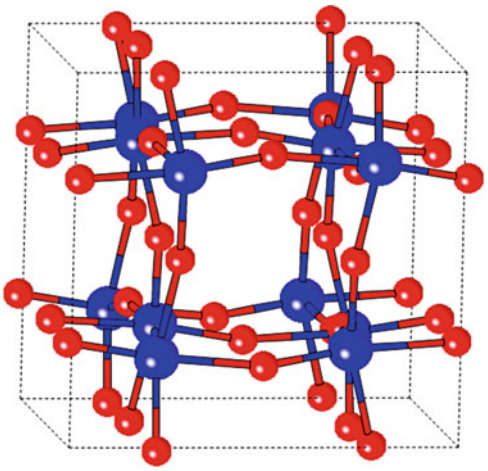

Fig. 2 Monoclinic structure of WO_3 unit cell is shown here, where W and O atoms are represented by blue and red balls, respectively [44]. This figure is copyrighted to American Physical Society

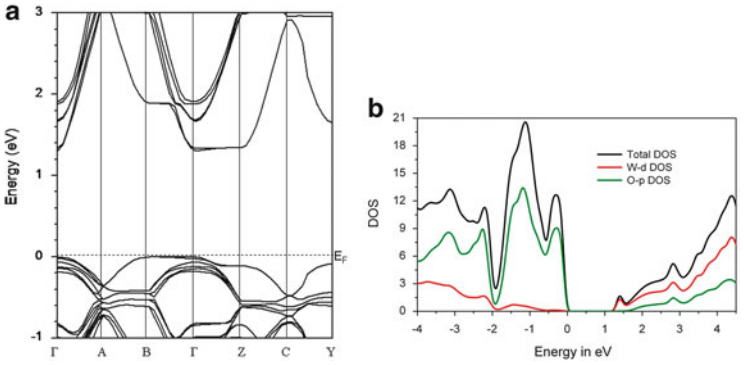

Fig. 3 (**a**) Band structure plot is shown along the high symmetry points; and (**b**) density of state (DOS) for both total, and site and angular momentum decomposed partial DOS plots for monoclinic WO_3 [44]. Top of the valence band is set to zero eV, and refers to as Fermi level. Partial DOS plots are amplified several times for better visibility. This figure is copyrighted to American Physical Society

of the valance band is flat, implying very high effective masses for the holes along the W-O-W chain in the x-direction, which constitutes tightly bound core-like electronic behavior along that direction on the zone boundary. Similar high effective masses were found for electrons in the $\Gamma \rightarrow Z$ direction. This has some interesting consequences in electronic behavior of WO_3, such as conduction being highly prohibitive in those directions. The bandgap of WO_3 was found to be pseudo-direct at the Γ point and is 1.31 eV, much less than the experimental bandgap of 2.6 eV. This underestimation of bandgap is a consequence of the LDA functional used in our calculation.

Beside these flat bands, there is also a highly dispersive part of the bands along other symmetry points near the Fermi level (0 eV). This simultaneous presence of highly dispersive and non-dispersive bands around the Fermi level indicates the potential of superconductivity which belongs to the highly correlated regime. It is important to note, highly correlated electrons can give rise to fundamentally insulating behavior, especially in case of some 3*d* transition metal-oxides, which are not suitable for photocatalytic applications [12]. Figure 3b shows the total and partial density of states (DOS). The sharp rise of the valence-band DOS at the Fermi level is due to the flat bands found in the band structure as discussed earlier. The partial DOS are amplified for clarity. This shows that, as expected for a metal-oxide semiconductor, the valence band of WO_3 mainly consists of O 2*p* bands, while its conduction band has predominantly W5*d* character. The heavy presence of the O *p* band near the Fermi level is responsible for the VBM being lower in energy (assuming reference level of 0 eV at Fermi level). In fact, the onset of *p*-*d* hybridized band in the valence band starts from about 0.6 eV below the top of the valence band. This is one of the reasons for the lower position of CBM with respect the H_2 redox potential. Hence, WO_3 cannot drive the hydrogen evolution part of the water-splitting reactions.

To understand the basic principles and mechanism of the band engineering strategies by doping, we discuss some insights on band structure modification from the theoretical point of view. First we discuss one nitrogen atom substitution per WO_3 unit cell (***N-doping***), which gives ~4 % N impurity. Substitution of a nitrogen atom at oxygen site is not expected to cause significant changes in structural properties, because the size mismatch is minimal and the difference in electronegativity is small, with N has the less electronegativity. This implies that upon substitution, the N 2*p* band would be situated above the VBM which is mainly consists of O *p*. In addition, as can be seen from the total DOS plot in Fig. 4 (upper panel), the one less electron in a *N* atom compared to an O atom introduces a hole state on top of the valence band. However, it can be argued that this hole state is very localized and may not be very stable [18].

The partial DOS in Fig. 4 (lower panel) shows that the partially filled bands are mainly from the N 2*p* states. These N 2*p* bands are hybridized with the neighboring W 5*d* bands, and very slightly with the nearest O 2*p* bands. The unaffected O 2*p* bands started from 0.40 eV below the Fermi level. This indicates that the top of the valence bands of WO_3 can be raised up in energy due to the *N* substitution. Also, the bandgap is reduced from 1.31 to 1.04 eV for the spin-up bands and 0.89 eV for spin-down bands. The lowering of bandgap by *N* doping has also been observed by experiment [16]. It is important to note, these types of systems with large partially filled DOS at Fermi level are very unstable. It has been found, a further relaxation with a larger super-cell and with same N concentration split the partially occupied band at Fermi level into two occupied and unoccupied bands with a gap of 0.5 eV, and the system became ferromagnetic [18]. Some more complex *N*-doping in WO_3 was also considered. It has been found that 2 N substitutions at the two closest O substitutional sites are energetically more favorable than only one *N* substitution. Furthermore, the lowest formation energy (higher solubility) for the *N*-impurities has been found for N_2 interstitial doping (Fig. 5) at both O- and W-rich growth

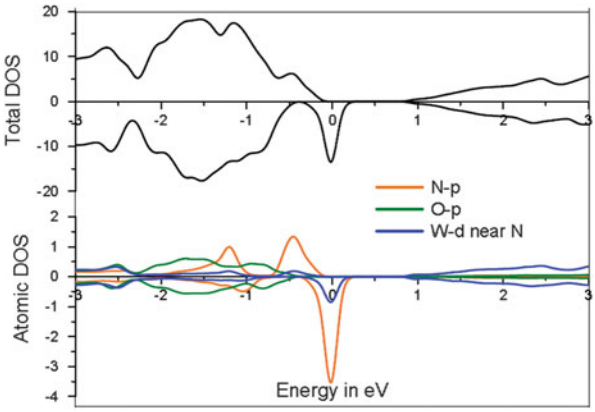

Fig. 4 Total DOS (*upper panel*) and partial DOS (*lower panel*) for WO_3 with ~4 % N impurity [13]. Fermi levels for all the DOS plot here are set to zero. High density of states of half-filled N 2*p* band is clearly seen at the Fermi level [44]. This figure is copyrighted to American Physical Society

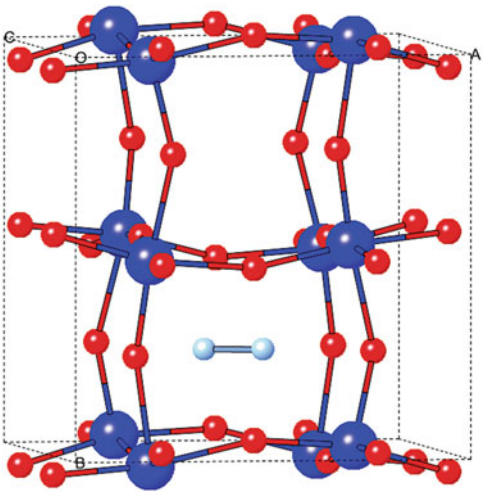

Fig. 5 Interstitial N_2 doping in WO_3 unit cell is shown here, where W, O, and N atoms are represented by *blue*, *red*, and *light blue balls*, respectively [45]. This figure is copyrighted to Elsevier

environments. This suggests that, *N* doping in WO_3 is more likely to be found as an *N*-dimer in the interstitial site. Interestingly, the calculated bandgap of WO_3 with such interstitial doping is 0.22 eV higher than that of pristine WO_3 [44, 45].

Metal substitutions: Let us first consider two simple cases here, one with no *d*-band and another with a metal isovalent to W. The substitution of a simple metal, Al, which has no *d*-orbitals, in place of W would result in a highly mismatched condition. First, Al's *p*-orbitals have some contribution deep in the valance bands, which may not have a significant effect on the valence band-edges. Secondly, because Al lacks *d*-electrons, the *d*-bands near CBM in WO_3 remained almost unaltered. However, due to the mismatch of the oxidation states between Al and W, there is an unoccupied and localized O 2*p* band on top of VBM at the spin down channel; this may act as a charge trap center. There is also a partially unoccupied O 2*p* band at the spin up channel as well, however, is not very dominant at all. The overall bandgap was reduced by 0.05 eV compared to pristine WO_3.

Let us then consider Mo substitution, which is isovalent to W. From the DFT band diagram in an earlier publication, [44] one can see that the band profile of Mo-substituted WO_3 remains the same as undoped WO_3, except for a partly unoccupied Mo *s*-band just around the Fermi level. This is probably due to the fact that the atomic Mo *s*-orbital is higher in energy than the W 5*d* and O 2*p* orbitals. Except for this *s*-band, the VBM and CBM remain the same, with a bandgap of 1.32 eV, which is again almost the same as pure WO_3.

Next, we'll discuss briefly a ***transition-metal substitution*** and its effect on the electronic structure of WO_3. For example, Ta and Hf atoms have shallower *d*-bands compared to W, which would contribute to bands at higher energy in the conduction bands. For Ta atom substitution at W site, two facts need to be considered: first, Ta has only one less 5*d* electron compared to the W atom; and second, Ta differs in electronegativity by 0.86 pauling from W. So, a hole state would be present on top of the valence band. The bandgaps were calculated to be 1.21 and 1.12 eV for the spin-up and spin-down band, respectively [44]. The valence band-edge consists of O 2*p* bands which are near the Ta atom, as expected. The CBM remained almost the same, where the Ta-*d* bands were formed about 0.6 eV behind the conduction band-edge. This indicates that with optimal Ta substitution, the conduction band could also be raised slightly.

To avoid the charge-mismatch situation as found in the previous doping examples, an example of ***co-doping*** scenario in WO_3 will be discussed. It can be argued that co-doping can reduce the recombination centers in the materials, and hence would also help to increase the conduction of the charge carriers. For example, for N substitutional doping if one W atom which is bonded to a N atom is replaced by a Re atom, then the Re-N would be isovalent to W-O, so no hole states would be expected. The valence band would be completely filled, and, in fact, the valence band-edge has found to be an admixture of N 2*p* and O 2*p* bands, with a contribution from Re-*d* bands [44]. It has been shown that VBM also moved up by 0.19 eV compared to the pure WO_3 valence band. However, the CBM came down slightly by about 0.09 eV due to this co-doping, an effect which is not desirable for water splitting. The minimum bandgap, 1.03 eV, in this case was found to be indirect.

3. $CuWO_4$: We now move from the binary to ternary metal-oxides. $CuWO_4$ represent an oxide where the two cations provide the chemistry for both the 3*d* and 5*d* orbitals, respectively [46]. Due to the higher energy for Cu 3*d* orbital, this is usually dominant in the top of the valence band. Copper tungstate, $CuWO_4$ or cuproscheelite, a *n*-type semiconductor with an indirect bandgap 2.3 eV, [47] crystallizes in a triclinic structure with symmetry $P\overline{1}$. In the structure of $CuWO_4$, four distinct oxygen atoms (refer here as O_1, O_2, O_3, and O_4) occupy four different sites, and both Cu and W are surrounded by six oxygen atoms to form CuO_6 and WO_6 octahedra [48]. These two different edge sharing octahedra form infinite zigzag chains.

The two possible antiferromagnetic (AFM) arrangements in $CuWO_4$ can be considered: (a) electrons with different spins along "a" direction referred as AFM1 and (b) electrons with the same spins along "a" direction referred as AFM2. The lattice optimization process determines that $CuWO_4$ adopts AFM2

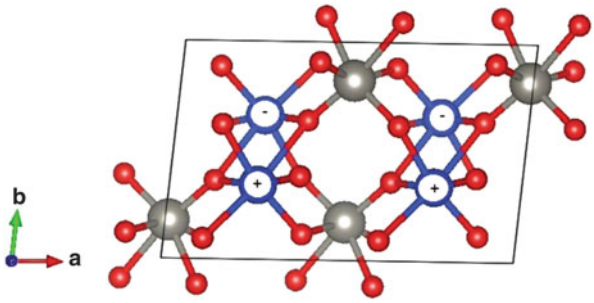

Fig. 6 Crystal structure of $CuWO_4$. Blue, gray, and red spheres represent Cu, W, and O, respectively. The "+" and "−" indicate the up and down spin on Cu atoms, which shows a layer-by-layer antiferromagnetic (AFM) arrangement [46]. This figure is copyrighted to American Institute of Physics

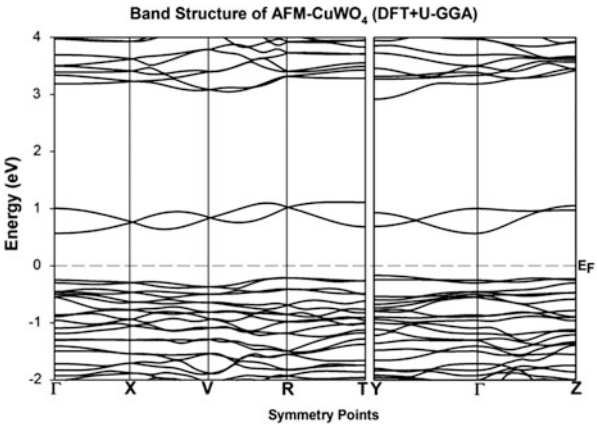

Fig. 7 DFT + U-GGA electronic band structure calculation of AFM triclinic $CuWO_4$ [46]. This figure is copyrighted to American Institute of Physics

triclinic phase as ground state in both DFT-GGA and DFT-GGA + U cases (Fig. 6). The DFT-GGA + U optimized AFM2 triclinic lattice parameters are: $a = 4.653685$ Å, $b = 5.80990$ Å, $c = 4.88819$ Å, $\alpha = 91.4936°$, $\beta = 91.7646°$, and $\gamma = 84.3218°$.

The DFT + U-GGA band structure calculation, as shown in Fig. 7, produces an insulating solution. The valence band along $\Gamma \rightarrow X$ and $X \rightarrow V$ regions are very flat suggesting higher effective mass of holes. The conduction band is divided into two regions. The first region contains only two bands which are dispersive throughout the all symmetry points. These are considered to be unoccupied mid-gap states. On the other hand, conduction bands of the second region are flat along $\Gamma \rightarrow X$, and $R \rightarrow T$, however, little dispersive along the other symmetry points. DFT + U-GGA partial DOS plot in Fig. 8 shows that the top of valence band (VB) is dominated by Cu $3d$ being hybridized with O $2p$. On the other hand, bottom of the conduction band is also composed of O $2p$, W $5d$, and Cu $3d$ orbitals, with very high dominance of the latter. The bottom of the next higher unoccupied conduction band is mostly consists of W $5d$ and O $2p$ bands.

Figure 9 shows the optical absorption spectrum of AFM $CuWO_4$ optimized in DFT + U-GGA scheme. The DFT + U-GGA absorption spectrum shows that the

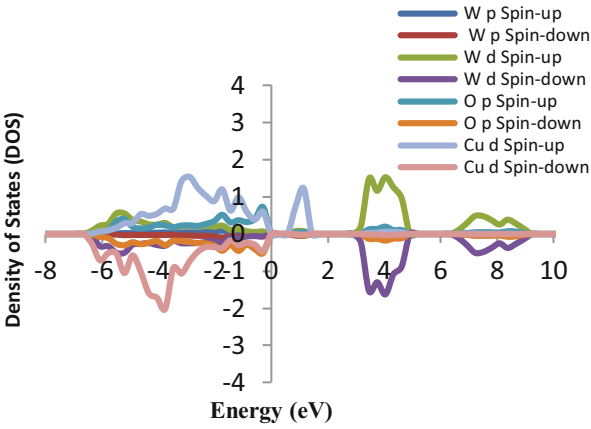

Fig. 8 DFT + U-GGA electronic partial density of states of $CuWO_4$. The mid-gap band is clearly dominated by the Cu-*d* orbital [46]. This figure is copyrighted to American Institute of Physics

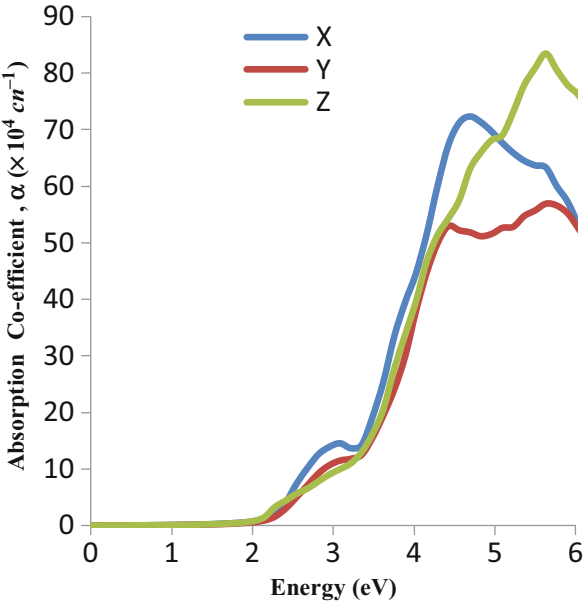

Fig. 9 Optical absorption curve for DFT + U-GGA-optimized AFM $CuWO_4$

first optical gap is at about 2.1 eV which does not correspond to the bandgap calculated in electronic band structure as shown in Fig. 7. This indicates that electron transition does not occur between the top of the valence band and bottom of the conduction band which are dominated by Cu 3*d* and W 5*d*, respectively, since *d*-*d* transition is forbidden. Hence, the origin of the optical gap can be attributed to the electron transfer from occupied O 2*p* states within the valence band to the unoccupied Cu 3*d* mid-bands (first part of CB). Another peak is observed at 4.7 eV in absorption spectrum is attributed to the electron transfer from redistributed

occupied O 2*p* states to unoccupied W 5*d* states (second part of CB) or from the top the valence band to higher unoccupied O 2*p* states in the conduction band. However, in spite of the relatively good optical absorption, the presence of flat band at the VBM and the antiferromagnetism in $CuWO_4$ indicates high resistivity [12].

4. $Bi_2Ti_2O_7$: Bismuth titanate is another ternary oxide with a mix of post-transition metal and transition metal. Conductivity of this oxide is supposed to be better than $CuWO_4$. Whereas in transition metal Ti *d*-orbital get prominent in the valence band, it is the Bi-*p* and -*s* orbitals that contribute the most on top of the valence band and in the bottom of the conduction band [49]. One can consider $Bi_2Ti_2O_7$ (BTO) as being developed from alloying, rather than doping, of TiO_2 with Bi_2O_3. In stoichiometric pyrochlore crystal structure bismuth titanate exists as $Bi_2Ti_2O_7$. Bi occupies the A site with +3 oxidation state and Ti occupies the B sites with +4 oxidation state to form stoichiometric $A_2B_2O_7$ pyrochlore. In recent studies, the choice of bismuth as the element for the A site of the pyrochlore has been shown to be photoactive [50, 51]. Using a *p*-block element such as bismuth has been reported to show high electron mobility as well as improved photocatalytic activity compared with TiO_2 [52]. In Bi, 6s orbital helps to shift the valence band upward to reduce the bandgap. Generally, Bi^{3+} cation in the BTO pyrochlore structure shows distorted Bi_2O network [53]. This disorder is due to the static displacement, by the lone pair of electrons in the Bi^{3+} cation. Similar to $BiVO_4$, in BTO the 3+ charge state of Bi results in a lone pair which is composed of $6s^2$ electrons. The interaction of this lone pair with the adjacent O atom results into unique electronic and structural properties.

Figure 10 shows the band structure of BTO which has a direct bandgap of 2.6 eV. For comparison, for TiO_2, theoretical calculations and experimental results have shown an indirect bandgap of 3.2 eV [54, 55]. The estimates in the valence band of $Bi_2Ti_2O_7$ vary from −5 eV to 0 eV, and the conduction band from 2.6 to 4.3 eV. The bandgap is estimated from the separation energy levels between the highest VB and the lowest CB. The band characteristics at the points L, X and W show similar features. Similar observations have been noted for $Ca_2Nb_2O_7$ and $Ca_2Ta_2O_7$ in pyrochlores [56]. The direct bandgap materials are likely to be more efficient in a photocatalytic process as it promotes minimization of recombination losses due to trapping of the excited electrons as they transit from the valence band to the conduction band. This shows that BTO will be useful for photocatalytic applications.

The partial density of states (PDOS) of BTO was also analyzed. BTO shows a reduced bandgap of 0.4 eV compared to TiO_2 (Fig. 11) in the total DOS. This provides a quantitative estimate of the extent of bandgap reduction. There are clear and distinct peak formation noticed in the energy range between −8.0 eV to −11 eV. The presence of an interband in the valence band of BTO is due to the contribution from the 6s lone pair electrons of the Bi atom. Thus, the combination of 2*p* orbitals and 6s orbitals of BTO contribute to the reduction of the bandgap. The interband formed by the occupied Bi 6s orbitals shifts the valence band towards the conduction band, which in turn leads to visible light activity and assist with a facile electron transfer process.

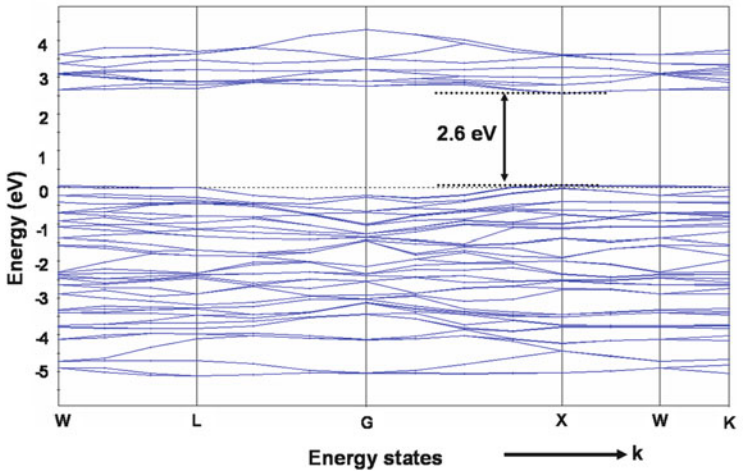

Fig. 10 The electronic band diagram of the BTO pyrochlore crystal along the *k*-vector [49]. This figure is copyrighted to American Chemical Society

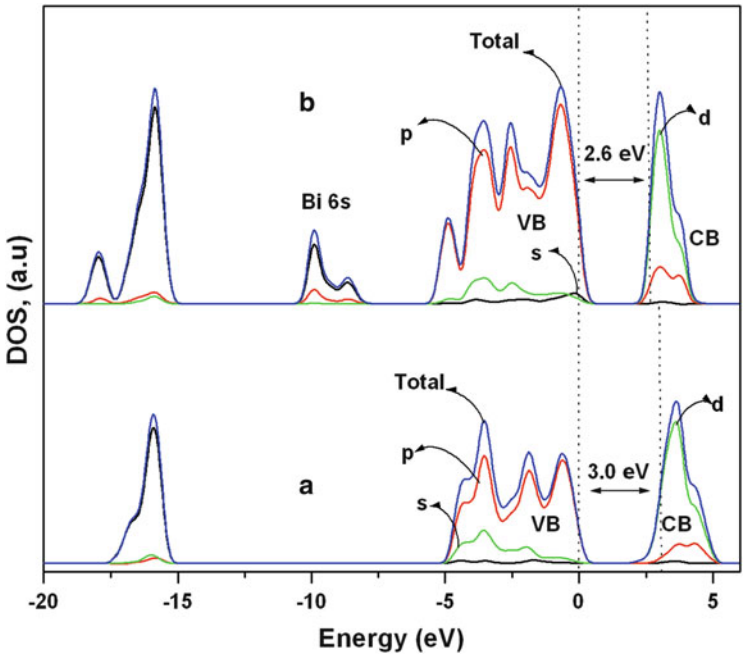

Fig. 11 Comparison of total density of states of (**a**) TiO_2 and (**b**) BTO pyrochlore, where BTO shows contribution from 6*s* orbitals of Bi in the valence band [49]. This figure is copyrighted to American Chemical Society

The characteristics of the conduction band are important to study the efficiency of photocatalytic process. In case of BTO pyrochlore, the conduction band is mainly derived from the 3*d* bands of Ti atom along with additional contribution from Bi atom. Since, Bi contributes the *p*-character of BTO, we further examined the VB in detail. It is noted that the contribution of s orbital from Bi plays an important role in the VB. The shift in the conduction of BTO is due to the combined effect of empty *d*-orbitals of the Ti atom and Bi 6*p* states. To compare the percentage of *p*-character in the conduction band with TiO_2, the PDOS was calculated. From the analysis it is found that the percentage of *p*-character was raised in BTO (21.68 %) by 7 % compared to TiO_2 (14.32 %). These analyses can facilitate the further doping studies at the Bi or Ti-sites in BTO.

5. Cu-delafossites: As a third set of ternary oxides, we will take an example of *p*-type oxides. Delafossites structures can accommodate a host of transition metal and non-transition metal in their ABO_2 structure. In addition, the strong localization of the holes at VBM due to the Coulomb interactions is reduced by the metal-induced covalent bonding. This implies higher holes conductivity through the Cu–O channel along the *c*-direction of the crystal. Due to their *p*-type nature, these materials are resistive against the oxidative corrosion. Some recent experimental studies showed that $CuM^{IIIB}O_2$, where $M^{IIIB} = Sc$, Y and La, are stable in solution and is capable of H_2 evolution from water [26, 27].

These delafossites are also important for the use of transparent conductive oxides (TCO) [57]. The discovery of transparent *p*-type $CuAlO_2$ thin films has stimulated extensive study on the group-IIIA delafossite oxide family, $CuM^{IIIA}O_2$ ($M^{IIIA} = B$, Al, Ga, In). However, the $CuM^{IIIA}O_2$ family do not exhibit direct bandgaps. Their fundamental bandgaps, i.e., from VBM to CBM, are significantly smaller than their reported optical bandgaps. This is because, the absorption of photons with energy of the minimum direct bandgap at brillouin zone center is very weak due to the inversion symmetry of the delafossite structures, an effect also observed in other oxide systems. From optical absorption calculation it has been predicted that by appropriate alloying, this absorption can be improved [58]. In addition, due to the highly delocalized lower conduction band minima in these delafossites, unwanted *n*-type carrier concentration is possible which may be detrimental to *p*-type conductivity. On the other hand $CuM^{IIIB}O_2$ ($M^{IIIB} = Sc$, Y, La) may turn out to be also good *p*-type TCO materials.

We have found that the $CuM^{IIIA}O_2$ and $CuM^{IIIB}O_2$ delafossites behave significantly differently, due to the different crystal structures and electronic configurations for group-IIIA and -IIIB elements [33]. The differences can be summarized as: (a) The $CuM^{IIIA}O_2$ family prefers rhombohedral symmetry, whereas the $CuM^{IIIB}O_2$ family prefers the hexagonal symmetry. (b) The $CuM^{IIIA}O_2$ family has indirect bandgaps with large difference between the direct and indirect bandgaps. However, this difference for $CuScO_2$ is very small (0.219 eV). The difference even diminishes for $CuYO_2$ and $CuLaO_2$. (c) The bandgap anomalies observed in the $CuM^{IIIA}O_2$ family are not found in $CuM^{IIIB}O_2$. The understanding of the bandgap behaviors of these group-III cuprate-delafossites provides a unique way to design materials with the desirable band structures.

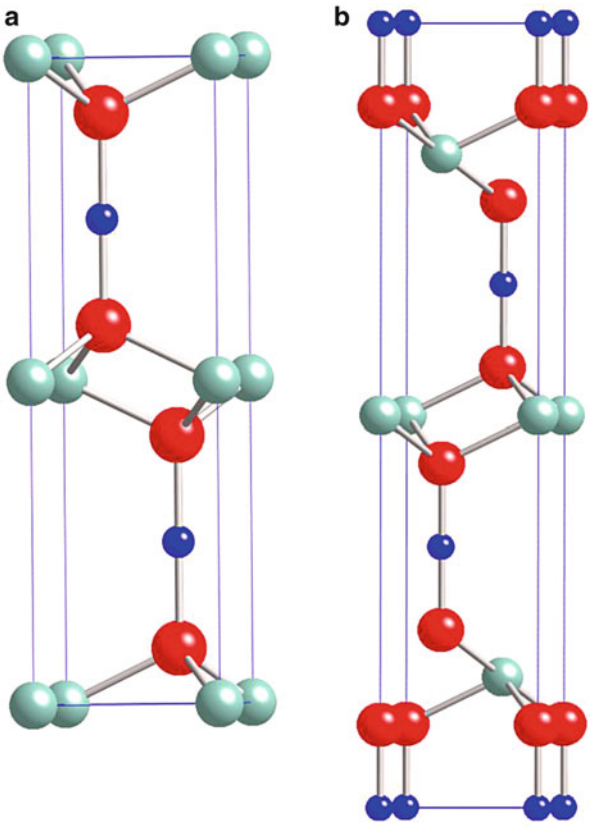

Fig. 12 (**a**) Hexagonal and (**b**) rhombohedral stacking of the delafossite structures are shown here. The *blue* and the *red* are copper and oxygen atoms, respectively. The *light green* atoms could be any one from the group IIIA or IIIB from the periodic table

The group-IIIA and -IIIB delafossite structures can have either $P6_3/mmc$ (#194) or $R\bar{3}m$ (#166) space group symmetry. For example, $CuAlO_2$ is experimentally recognized to be in the rhombohedral group ($R\bar{3}m$), whereas $CuYO_2$ has been reported to be in the hexagonal group ($P6_3/mmc$). In both symmetries, O and Cu form linear bonding structure along the *c*-axis which is considered to be the main channel for the hole transport, whereas O-*M* (*M* = group-IIIA and -IIIB) bonds form distorted octahedra. The difference between these two structures is the stacking sequence of the O-*M* octahedron layers, as shown in Fig. 12. The calculated lattice constants for both the rhombohedral and hexagonal unit cells agree well with the available experimental values.

For example [33], for hexagonal $CuYO_2$ we found the energy per formula unit is lowered by 0.034 eV than the rhombohedral structure. These differences are 0.050 and 0.015 eV per formula unit for $CuScO_2$ and $CuLaO_2$, respectively. On the other hand, the group-IIIA prefers the $R\bar{3}m$ structure. For example, the energy per formula unit for $CuAlO_2$ structure in $R\bar{3}m$ symmetry is 0.027 eV lower than the hexagonal structure. For $CuGaO_2$ and $CuInO_2$ this difference is 0.006 eV and 0.232 eV, respectively. However, it should be pointed out that the energy differences between the rhombohedral and hexagonal structures are small except for $CuInO_2$. It is

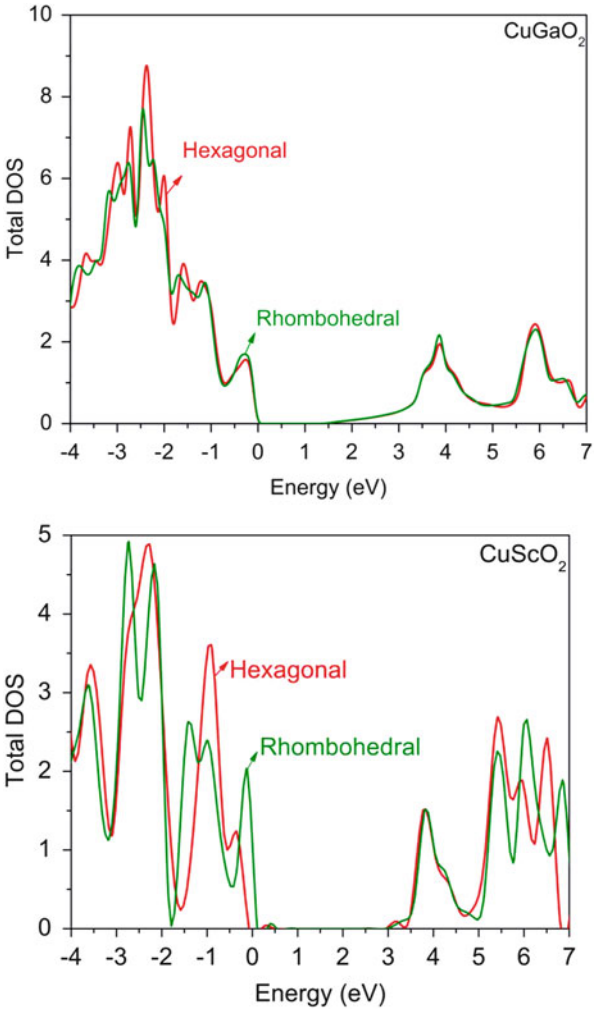

Fig. 13 Total Dos plots for $CuGaO_2$ and $CuScO_2$ in $P6_3/mmc$ (*red line*) and $R\bar{3}m$ symmetry (*green line*). Structural differences have little impact on the electronic structures of these two delafossites [33]. This figure is copyrighted to American Physical Society

possible that the synthesized materials may exhibit either of these two symmetry groups, or a mixed symmetry structure.

From Fig. 12, it is clear that the rhombohedral and hexagonal structures differ only in stacking sequence and are symmetrically similar. So it is expected that a given delafossite in these two symmetries would have similar electronic characters. It is known that, in the case of Cu(I)-oxide-based structure the VBM is composed of hybridized Cu-*d* and O 2*p* antibonding type band. So for the two families of delafossites in both of the two symmetries, this antibonding VBM is a common feature. The antibonding nature of the valence band edge is the main reason for the relatively higher mobility of holes, compared to the other oxides (such as ZnO). Figure 13 shows the calculated total DOS plot for two representative delafossites: (a) $CuGaO_2$ and for (c) $CuScO_2$ in both hexagonal and rhombohedral symmetries. The overall features of the DOS plots are almost the same within the same group of

delafossite. The electronic difference between the two groups is chemical in nature, rather than structural. From Fig. 13a, we see that for $CuGaO_2$, both the hexagonal and rhombohedral symmetries have similar DOS features near the top part of the valence band. The presence of unoccupied Ga-*s* band is seen around 6 eV above the Fermi level, and a long *s*-band tail at the bottom of the conduction band is seen in Fig. 13a. Very minor *d*-band contribution due to Ga in the valence band part of the DOS has almost no influence. On the other hand, the presence of a lone 3*d* electron due to Sc appears to have more influence on the valence band structure between the two symmetries for $CuScO_2$ (Fig. 13b). The unoccupied Sc-*d* band is mainly seen in the conduction band from 5 eV (Fig. 13b). The electron density at the Fermi level has a more pronounced and localized peak for the rhombohedral symmetry than that of the hexagonal one. This type of high DOS near the Fermi level may be responsible for its structural transition from rhombohedral to a relatively lower symmetry hexagonal structure. In case of this type of transition, as the rearrangements took place among the occupied energy levels, the energy gain is not much. However here the bonding DOS (bottom of the valence band) increased slightly compared to the antibonding DOS (top of the valence band) for the hexagonal structure. This is responsible for the slight energy gain for the hexagonal phase relative to the rhombohedral phase of $CuScO_2$. We also have calculated the Madelung energy to see if the electrostatic energy has any role in determining the symmetry of the delafossites, as it does in the case of ZnO. In ZnO, the wurtzite structure is stabilized over the zinc-blend one due to the gain in the electrostatic energy [59]. However, though in case for group IIIA the rhombohedral structures gain energy due to this electrostatic interaction between the ions, for group IIIB hexagonal structure do not have the electrostatic favorability over the rhombohedral one.

6. $AgBiW_2O_8$: Finally we will briefly describe a quaternary metal-oxide. Though multiple cation systems provide more tuning flexibilities of their electronic properties such as bandgaps, these are challenging to synthesize and characterize experimentally. In sulfides, Cu_2ZnSnS_2 (CZTS) is one of the most popular examples for photovoltaic absorber materials nowadays, which was developed in part to improve upon $Cu(In,Ga)S_2$ [60]. However, single phase synthesis and stabilization of these types of materials are highly challenging [61]. In addition defects or impurities formations in CZTS can trigger phase separations into smaller binary or ternary compounds. For example, CZTS can be often found to coexist with ZnS and Cu_2SnS_3. However, thermodynamically "clever" methods can be designed to synthesize these ternary materials which coexist only with benign lower order phases. Theoretical analysis by first principle theories can provide important guidance in this regard [61].

Motivation for studying $AgBiW_2O_8$ came in order to band engineer WO_3 to modify its electronic structure [62]. This modification is mainly twofold: as discussed in Sect. 3.2, WO_3 has an experimental bandgap of 2.7 eV which is higher than the ideal water-splitting energy, as well as its conduction band edge is below the hydrogen reduction potential. It has been found that alloying WO_3 with Ag and Bi can uplift its CBM. From the DOS calculation [62], it has been found that Ag 4*d*

band which sits on top of the valence band helps to uplift the VBM. This in turn uplifts the conduction band due to hybridization. From theoretical point of view, to analyze the structure further, its crystal structure needs to be known a priori. By exploring mineral database by appropriate chemical descriptors, followed by configurational optimizations by density functional theory, we have predicted that $AgBiW_2O_8$ would have wolframite crystal structure [62]. Among other possibilities, scheelite and fergusonite structures were 0.69 and 0.28 eV higher in energy, respectively. From band structure calculations, it did have an indirect gap, however, the difference between this indirect gap and smallest direct gap is 0.06 eV. Optical absorption calculations confirmed that electron photoexcitation at the minimum direct gap is possible as well. Overall, the measured bandgap remains same as WO_3, which is about 2.6 eV. To reduce the bandgap, similar quaternary oxides has been proposed theoretically with detail stability analysis, such as $CuBiW_2O_8$ [46], which is yet to be tested in laboratory. Compared to $AgBiW_2O_8$, the bandgap reduction in $CuBiW_2O_8$ is by 0.58 eV, which is significant, even though bandgap remained indirect. However, optical absorption is very high near the gap, and the CBM is above the hydrogen reduction potential. So far $CuBi_2O_8$ has shown potentials to be a good photocatalysts.

4 Summary

Here we have discussed the recent theoretical studies of some of the representative metal-oxides which were mainly performed by our groups. The goal was to show that the insight that can be gained from the theoretical studies not only help in identifying the fundamental issues, but also can guide the experimental approaches. Despite the limitations due to the theoretical or computational approximations, the electronic structure calculations can provide the fundamental understanding of these oxide systems and can guide studies for further tuning of these oxides for a desired functionality. From binary oxides to ternary oxides, the main limitations are the lower valence band created by the high electronegativity of O atoms, higher bandgap and resistivity. A combination of cations, such as a combination of various *d*-orbitals from cations, may help raise the top of the valence band. Highly delocalized s or *p*-bands from cation can also help to raise the valence band, such as in case of Bi containing oxides. Cu 3*d* can do the same as well; however, the presence of the localized 3*d* band may increase the effective mass of the holes. It is important to note that mismatch doping may create highly localized defect levels, which can create strain on the crystal structure during its growth process. Hence, alloying would be a better strategy for tuning the bandgaps. In contrast to doping, alloying may require the prediction of new alloy crystal structures. To identify new alloy structures of complex oxides is nevertheless challenging both theoretically and experimentally. However, a careful alloying can also help to move the conduction band edge upward where necessary. For example, alloying Bi and Ag or Cu in WO_3 can move the conduction band edge over the hydrogen reduction potential.

So, an intelligent design approach to predict complex oxides with suitable doping/alloying may provide a better photocatalyst than those already exist in the laboratory.

Acknowledgements The author would like to thank the coauthors with whom most of the original works reviewed here were performed. The author also gratefully acknowledges the funding from the National Science Foundation (NSF) and from the National Renewable Energy Laboratory (NREL) where most of the original researches were performed.

References

1. Cohen, M. L. Conceptual progress for explaining and predicting semiconductor properties. *Journal of Materials Research* **2011**, *26*, 2815-2825.
2. Fischer, C. C.; Tibbetts, K. J.; Morgan, D.; Ceder, G. Predicting crystal structure by merging data mining with quantum mechanics. *Nat Mater* **2006**, *5*, 641-646.
3. Cramer, C. J.; Truhlar, D. G. Density functional theory for transition metals and transition metal chemistry. *Physical Chemistry Chemical Physics* **2009**, *11*, 10757-10816.
4. Neugebauer, J.; Hickel, T. Density functional theory in materials science. *Wiley Interdisciplinary Reviews: Computational Molecular Science* **2013**, *3*, 438-448.
5. Van de Walle, C. G.; Neugebauer, J. First-principles calculations for defects and impurities: Applications to III-nitrides. *Journal of Applied Physics* **2004**, *95*, 3851-3879.
6. Huang, P.; Carter, E. A. Advances in Correlated Electronic Structure Methods for Solids, Surfaces, and Nanostructures. *Annual Review of Physical Chemistry* **2008**, *59*, 261-290.
7. Bak, T.; Nowotny, J.; Rekas, M.; Sorrell, C. C. Photo-electrochemical hydrogen generation from water using solar energy. Materials-related aspects. *International Journal of Hydrogen Energy* **2002**, *27*, 991-1022.
8. Lewis, N. S.; Nocera, D. G. Powering the planet: Chemical challenges in solar energy utilization. *Proceedings of the National Academy of Sciences* **2006**, *103*, 15729-15735.
9. Miller, E. L.; Gaillard, N.; Kaneshiro, J.; DeAngelis, A.; Garland, R. Progress in new semiconductor materials classes for solar photoelectrolysis. *International Journal of Energy Research* **2010**, *34*, 1215-1222.
10. Fujishima, A.; Honda, K. Electrochemical Photolysis of Water at a Semiconductor Electrode. *Nature* **1972**, *238*, 37-38.
11. Gratzel, M. Photoelectrochemical cells. *Nature* **2001**, *414*, 338-344.
12. Huda, M. N.; Al-Jassim, M. M.; Turner, J. A. Mott insulators: An early selection criterion for materials for photoelectrochemical H[sub 2] production. *Journal of Renewable and Sustainable Energy* **2011**, *3*, 053101.
13. Nie, X. L.; Wei, S. H.; Zhang, S. B. Bipolar doping and band-gap anomalies in delafossite transparent conductive oxides. *Physical Review Letters* **2002**, *88*, 066405.
14. Huda, M. N.; Yan, Y.; Walsh, A.; Wei, S.-H.; Al-Jassim, M. M. Symmetry-breaking-induced enhancement of visible light absorption in delafossite alloys. *Applied Physics Letters* **2009**, *94*, 251907.
15. Ahn, K.-S.; Yan, Y.; Al-Jassim, M. Band gap narrowing of ZnO:N films by varying rf sputtering power in O[sub 2]/N[sub 2] mixtures. *Journal of Vacuum Science & Technology B: Microelectronics and Nanometer Structures* **2007**, *25*, L23-L26.
16. Cole, B.; Marsen, B.; Miller, E.; Yan, Y.; To, B.; Jones, K.; Al-Jassim, M. Evaluation of Nitrogen Doping of Tungsten Oxide for Photoelectrochemical Water Splitting. *The Journal of Physical Chemistry C* **2008**, *112*, 5213-5220.
17. Di Valentin, C.; Finazzi, E.; Pacchioni, G.; Selloni, A.; Livraghi, S.; Paganini, M. C.; Giamello, E. N-doped TiO2: Theory and experiment. *Chemical Physics* **2007**, *339*, 44-56.

18. Huda, M. N.; Yan, Y.; Wei, S.-H.; Al-Jassim, M. M. Exchange-induced negative-U charge order in N-doped WO_3: A spin-Peierls-like system. *Physical Review B* **2009**, *80*, 115118.
19. Ahn, K.-S.; Yan, Y.; Shet, S.; Deutsch, T.; Turner, J.; Al-Jassim, M. Enhanced photoelectrochemical responses of ZnO films through Ga and N codoping. *Applied Physics Letters* **2007**, *91*, 231909.
20. Huda, M.; Yan, Y.; Wei, S.-H.; Al-Jassim, M. Electronic structure of ZnO:GaN compounds: Asymmetric bandgap engineering. *Physical Review B* **2008**, *78*, 195204.
21. Nozik, A. J. Photochemical diodes. *Applied Physics Letters* **1977**, *30*, 567-569.
22. Zhang, S. B.; Wei, S. H.; Zunger, A. Microscopic Origin of the Phenomenological Equilibrium "Doping Limit Rule" in *n*-Type III-V Semiconductors. *Physical Review Letters* **2000**, *84*, 1232-1235.
23. Wei, S.-H. Overcoming the doping bottleneck in semiconductors. *Computational Materials Science* **2004**, *30*, 337-348.
24. Ingram, B. J.; González, G. B.; Mason, T. O.; Shahriari, D. Y.; Barnabè, A.; Ko, D.; Poeppelmeier, K. R. Transport and Defect Mechanisms in Cuprous Delafossites. 1. Comparison of Hydrothermal and Standard Solid-State Synthesis in CuAlO2. *Chemistry of Materials* **2004**, *16*, 5616-5622.
25. Buljan, A.; Llunell, M.; Ruiz, E.; Alemany, P. Color and conductivity in Cu2O and CuAlO2: A theoretical analysis of d(10)center dot center dot center dot d(10) interactions in solid-state compounds. *Chemistry of Materials* **2001**, *13*, 338-344.
26. Saadi, S.; Bouguelia, A.; Derbal, A.; Trari, M. Hydrogen photoproduction over new catalyst CuLaO2. *Journal of Photochemistry and Photobiology a-Chemistry* **2007**, *187*, 97-104.
27. Younsi, M.; Saadi, S.; Bouguelia, A.; Aider, A.; Trari, M. Synthesis and characterization of oxygen-rich delafossite CuYO2 + x—Application to H2-photo production. *Solar Energy Materials and Solar Cells* **2007**, *91*, 1102-1109.
28. Kresse, G.; Furthmüller, J. Efficiency of ab-initio total energy calculations for metals and semiconductors using a plane-wave basis set. *Computational Materials Science* **1996**, *6*, 15-50.
29. Kresse, G.; Furthmuumlller, J. Efficient iterative schemes for ab initio total-energy calculations using a plane-wave basis set. *Physical Review B* **1996**, *54*, 11169.
30. Gajdoscaron, M.; Hummer, K.; Kresse, G.; Furthm; uuml; ller, J.; Bechstedt, F. Linear optical properties in the projector-augmented wave methodology. *Physical Review B* **2006**, *73*, 045112.
31. Dudarev, S. L.; Botton, G. A.; Savrasov, S. Y.; Humphreys, C. J.; Sutton, A. P. Electron-energy-loss spectra and the structural stability of nickel oxide: An LSDA + U study. *Physical Review B* **1998**, *57*, 1505-1509.
32. Anisimov, V. I.; Zaanen, J.; Andersen, O. K. Band theory and Mott insulators: Hubbard U instead of Stoner I. *Physical Review B* **1991**, *44*, 943.
33. Huda, M. N.; Yan, Y.; Walsh, A.; Wei, S.-H.; Al-Jassim, M. M. Group-IIIA versus IIIB delafossites: Electronic structure study. *Physical Review B* **2009**, *80*, 035205.
34. Zhang, S. B.; Wei, S.-H.; Zunger, A. A phenomenological model for systematization and prediction of doping limits in II–VI and I–III–VI[sub 2] compounds. *Journal of Applied Physics* **1998**, *83*, 3192-3196.
35. Yamamoto, T.; Katayama-Yoshida, H. Solution Using a Codoping Method to Unipolarity for the Fabrication of p-Type ZnO. *Japanese Journal of Applied Physics* **1999**, *38*, L166.
36. Yan, Y.; Zhang, S. B.; Pantelides, S. T. Control of Doping by Impurity Chemical Potentials: Predictions for p-Type ZnO. *Physical Review Letters* **2001**, *86*, 5723.
37. Wang, L. G.; Zunger, A. Cluster-Doping Approach for Wide-Gap Semiconductors: The Case of *p*-Type ZnO. *Physical Review Letters* **2003**, *90*, 256401.
38. Yan, Y.; Li, J.; Wei, S.-H.; Al-Jassim, M. M. Possible Approach to Overcome the Doping Asymmetry in Wideband Gap Semiconductors. *Physical Review Letters* **2007**, *98*, 135506.
39. Li, J.; Wei, S.-H.; Li, S.-S.; Xia, J.-B. Design of shallow acceptors in ZnO: First-principles band-structure calculations. *Physical Review B* **2006**, *74*, 081201.

40. Liu, L.; Xu, J.; Wang, D.; Jiang, M.; Wang, S.; Li, B.; Zhang, Z.; Zhao, D.; Shan, C.-X.; Yao, B.; Shen, D. Z. *p*-Type Conductivity in N-Doped ZnO: The Role of the NZn-VO Complex. *Physical Review Letters* **2012**, *108*, 215501.
41. Huda, M. N.; Yan, Y.; Al-Jassim, M. M. The delocalized nature of holes in (Ga, N) cluster-doped ZnO. *Journal of Physics: Condensed Matter* **2012**, *24*, 415503.
42. Yan, Y.; Ahn, K. S.; Shet, S.; Deutsch, T.; Huda, M.; Wei, S. H.; Turner, J.; Al-Jassim, M. M.: Band gap reduction of ZnO for photoelectrochemical splitting of water - art. no. 66500H. In *Solar Hydrogen and Nanotechnology II*; Guo, J., Ed.; Proceedings of the Society of Photo-Optical Instrumentation Engineers (Spie), 2007; Vol. 6650; pp. H6500-H6500.
43. Huda, M. N.; Deutsch, T. G.; Sarker, P.; Turner, J. A. Electronic structure study of N, O related defects in GaP for photoelectrochemical applications. *Journal of Materials Chemistry A* **2013**, *1*, 8425-8431.
44. Huda, M. N.; Yan, Y. F.; Moon, C. Y.; Wei, S. H.; Al-Jassim, M. M. Density-functional theory study of the effects of atomic impurity on the band edges of monoclinic WO_3. *Physical Review B* **2008**, *77*, 195102.
45. Janáky, C.; Rajeshwar, K.; de Tacconi, N. R.; Chanmanee, W.; Huda, M. N. Tungsten-based oxide semiconductors for solar hydrogen generation. *Catalysis Today* **2013**, *199*, 53-64.
46. Sarker, P.; Prasher, D.; Gaillard, N.; Huda, M. N. Predicting a new photocatalyst and its electronic properties by density functional theory. *Journal of Applied Physics* **2013**, *114*, 133508.
47. Ruiz-Fuertes, J.; Errandonea, D.; Segura, A.; Manjón, F. J.; Zhu, Z.; Tu, C. Y. Growth, characterization, and high-pressure optical studies of $CuWO_4$. *High Pressure Research* **2008**, *28*, 565-570.
48. Forsyth, J. B.; Wilkinson, C.; Zvyagin, A. I. The antiferromagnetic structure of copper tungstate, $CuWO_4$. *Journal of Physics: Condensed Matter* **1991**, *3*, 8433.
49. Murugesan, S.; Huda, M. N.; Yan, Y.; Al-Jassim, M. M.; Subramanian, V. Band-Engineered Bismuth Titanate Pyrochlores for Visible Light Photocatalysis. *The Journal of Physical Chemistry C* **2010**, *114*, 10598-10605.
50. Kudo, A.; Hijii, S. H-2 or O-2 evolution from aqueous solutions on layered oxide photocatalysts consisting of Bi3+ with 6 s(2) configuration and d(0) transition metal ions. *Chemistry Letters* **1999**, 1103-1104.
51. Kako, T.; Zou, Z.; Ye, J. Photocatalytic oxidation of 2-propanol in the gas phase over cesium bismuth niobates under visible light irradiation. *Research on Chemical Intermediates* **2005**, *31*, 359-364.
52. Ikarashi, K.; Sato, J.; Kobayashi, H.; Saito, N.; Nishiyama, H.; Inoue, Y. Photocatalysis for water decomposition by RuO2-dispersed ZnGa2O4 with d(10) configuration. *Journal of Physical Chemistry B* **2002**, *106*, 9048-9053.
53. Hector, A. L.; Wiggin, S. B. Synthesis and structural study of stoichiometric BiTi2O7 pyrochlore. *Journal of Solid State Chemistry* **2004**, *177*, 139-145.
54. Kavan, L.; Gratzel, M.; Gilbert, S. E.; Klemenz, C.; Scheel, H. J. Electrochemical and photoelectrochemical investigation of single-crystal anatase. *Journal of the American Chemical Society* **1996**, *118*, 6716-6723.
55. Mo, S. D.; Ching, W. Y. Electronic and Optical-Properties of 3 Phases of Titanium-Dioxide—Rutile, Anatase, and Brookite. *Physical Review B* **1995**, *51*, 13023-13032.
56. Zhang, L. W.; Fu, H. B.; Zhang, C.; Zhu, Y. F. Effects of Ta5+ substitution on the structure and photocatalytic behavior of the Ca2Nb2O7 photocatalyst. *Journal of Physical Chemistry C* **2008**, *112*, 3126-3133.
57. Vidal, J.; Trani, F.; Bruneval, F.; Marques, M. A. L.; Botti, S. Effects of Electronic and Lattice Polarization on the Band Structure of Delafossite Transparent Conductive Oxides. *Physical Review Letters* **2010**, *104*, 136401.
58. Huda, M. N.; Yan, Y.; Walsh, A.; Wei, S.-H.; Al-Jassim, M. M. Symmetry-breaking-induced enhancement of visible light absorption in delafossite alloys. *Applied Physics Letters* **2009**, *94*, 251907.

59. Takeuchi, S.; Suzuki, K. Stacking Fault Energies of Tetrahedrally Coordinated Crystals. *physica status solidi (a)* **1999**, *171*, 99-103.
60. Walsh, A.; Chen, S.; Wei, S.-H.; Gong, X.-G. Kesterite Thin-Film Solar Cells: Advances in Materials Modelling of Cu2ZnSnS4. *Advanced Energy Materials* **2012**, *2*, 400-409.
61. Pranab, S.; Al-Jassim, M. M.; Huda, M. N. Theoretical study of the stability of single phase kesterite-Cu2ZnSnS4. *To be published* **2014**.
62. de Tacconi, N. R.; Timmaji, H. K.; Chanmanee, W.; Huda, M. N.; Sarker, P.; Janáky, C.; Rajeshwar, K. Photocatalytic Generation of Syngas Using Combustion-Synthesized Silver Bismuth Tungstate. *ChemPhysChem* **2012**, *13*, 2945-2955.

Photo-Fuel-Cells: An Alternative Route for Solar Energy Conversion

Maria Antoniadou and Panagiotis Lianos

1 Introduction and Cell Operation Principles

The limited reserves of fossil fuels and the environmental problems they create by their processing and utilization has incited a great effort for broader use of renewable sources of energy. In addition to the standard photovoltaic devices and the solar heating systems, research is recently focusing on alternative processes and devices with more favorable environmental impact. Such an alternative route is traced by the so-called photo-fuel-cells (PFCs) [1, 2], also sometimes called Photoactivated Fuel Cells [3]. PFCs are photoelectrochemical cells similar to the original and most celebrated water-splitting apparatus proposed by Fujishima and Honda [4]. A PFC is made of a photoanode electrode carrying a photocatalyst, a cathode electrode supporting a reduction electrocatalyst and an electrolyte. Anode and cathode electrodes are externally electrically connected while internal conductivity is assured through the electrolyte. Figure 1 gives a typical design of a PFC. The operation of a PFC is briefly described by the following procedure. The photocatalyst on the anode electrode is excited by absorption of photons generating electron–hole (e^-–h^+) pairs. Holes mediate oxidation of the fuel while electrons are channeled through the external circuit to the cathode electrode, where they mediate reduction reactions. The reactions taking place at the two electrodes depend on the type of the photocatalyst, the pH, the fuel and the presence or absence of O_2. Reactions are summarized in Table 1 and discussed here below.

M. Antoniadou
Department of Chemical Engineering, University of Patras, University campus, 26500 Patras, Greece

P. Lianos (✉)
Department of Chemical Engineering, University of Patras, University campus, 26500 Patras, Greece

FORTH/ICE-HT, P.O. Box 1414, 26504 Patras, Greece
e-mail: lianos@upatras.gr

B. Viswanathan et al. (eds.), *Materials and Processes for Solar Fuel Production*, Nanostructure Science and Technology 174, DOI 10.1007/978-1-4939-1628-3_7

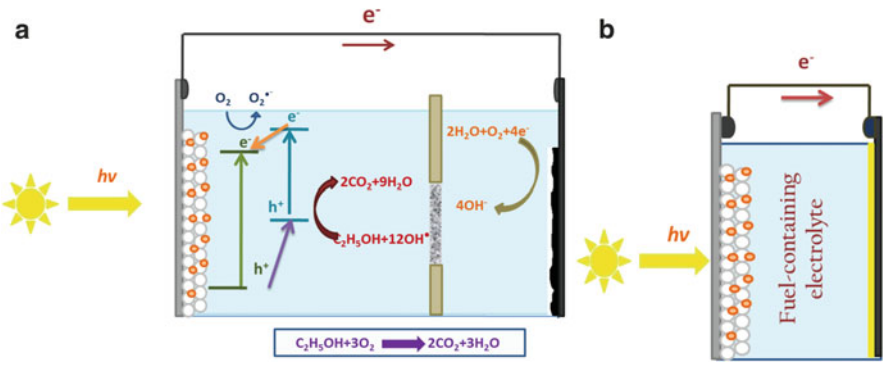

Fig. 1 (**a**) Basic design of a two-compartment photo-fuel-cell also illustrating some oxidation and reduction reactions. On the *left* is the anode carrying the nanostructured photocatalyst and the photosensitizer also acting as window for light entrance. On the *right* is the (*black*) cathode supporting the electrocatalyst and exposed to the ambient atmosphere. In the middle is the ion transfer membrane. (**b**) A version of the cell where ion transfer membrane and cathode are stuck in a membrane-electrode assembly

The most popular photocatalyst is nanocrystalline titania (nc-TiO_2), thanks to the easiness of its synthesis in nanocrystalline form, its stability, and its commercial availability at reasonable prices. Because of its large bandgap and the fact that it absorbs only UVA radiation ($\lambda < 390$ nm), it is necessary to sensitize titania by visible light in order to exploit a large portion of the solar radiation at the surface of the earth. Dye-sensitizers of titania and other oxide photocatalysts have been employed in dye-sensitized solar cells, in combination with nonaqueous electrolytes [5]. Such sensitizers do not function in PFCs. Tiny nanocrystalline metal sulfide semiconductors (Quantum Dots, QDs) have been used as sensitizers in Quantum-Dot-sensitized solar cells [6]. QD sensitizers do function in the presence of aqueous electrolytes; therefore, they have been also employed in water splitting [7] applications as well as with PFCs [8]. The present work also employs QDs as sensitizers of nc-TiO_2. The fuel used in a PFC can be any organic substance that may be considered a waste. An important advantage of photocatalysts is that they demonstrate no specificity towards the photodegradable substance. Therefore, any organic substance or mixture of substances that is found in surplus or it is a pollutant may be used as a fuel, thus offering a double environmental benefit, i.e., producing renewable electricity with pollutant photodegradation. One characteristic example is the case of glycerol, which is now produced in surplus as a by-product of biodiesel. Glycerol has been used as a fuel in PFCs [3]. Other products of biomass, for example, alcohol mixtures that may be too costly to refine, may also be employed as fuel in PFCs. The choice of a fuel is further discussed later. The value of the pH is another major parameter affecting PFC efficiency. Photodegradation of the organic substances by metal oxide photocatalysts is more effective at high pH, i.e., in the presence of abundant OH^- ions that lead to abundant $^{\bullet}OH$ radicals. For this reason, PFCs usually function with alkaline electrolytes. Finally, operation of a PFC depends on the presence or not of O_2. Oxygen

Table 1 Typical reactions taking place in a PFC employing ethanol as model fuel

Photoanode	
(1) *Reactions induced by absorption of UV photons* (*radiation mainly absorbed by the majority species,* i.e., *nc-TiO$_2$*) $TiO_2 \xrightarrow{h\nu} e^- + h^+$ (I) • Fate of the photogenerated electrons: Most electrons flow in the external circuit. Some may interact with O_2: $O_2 \xrightarrow{+e^-} O_2^{\bullet -} \xrightarrow{+H^+} HO_2^{\bullet} \xrightarrow{+e^-} HO_2^- \xrightarrow{+H^+} H_2O_2 \xrightarrow{+e^-} {}^{\bullet}OH + OH^-$ (II) • Fate of the photogenerated holes $C_2H_5OH + 3H_2O + 12\ h^+ \rightarrow 2CO_2 + 12H^+$(low pH) (III) $OH^- + h^+ \rightarrow OH^{\bullet}$ and $C_2H_5OH + 12OH^{\bullet} \rightarrow 2CO_2 + 9H_2O$ (high pH) (IV) • Intermediate steps may involve interaction of the fuel with photogenerated holes in the valence band of titania or holes injected into the valence band of the sensitizer $C_2H_5OH + 2\ h^+ \rightarrow CH_3CHO + 2H^+$ or $C_2H_5OH + h^+ \rightarrow C_2H_5O^{\bullet} + H^+$ (V)	
(2) *Reactions induced by absorption of visible light* (*exclusive excitation of the photosensitizer*) • Excited electrons are rapidly injected into the conduction band of TiO_2. Some may interact with O_2 forming superoxide radical and following the scheme of reaction (II). Most electrons flow through the external circuit. Holes at the valence band of the photosensitizer may go through reactions (III)–(V) depending of the nature of the photosensitizer Other schemes may also be possible	
Cathode	
Inert environment (*no O_2 present*)	*Aerated electrolyte or cathode exposed to ambient air*
• Low pH (potential: 0.00 V at pH = 0) $2H^+ + 2e^- \rightarrow H_2$ (VI) • High pH (potential: −0.83 V at pH = 14) $2H_2O + 2e^- \rightarrow H_2 + 2OH^-$ (VII)	• Low pH (potential: 1.23 V at pH = 0) $2H^+ + \frac{1}{2}\ O_2 + 2e^- \rightarrow H_2O$ (VIII) • High pH (potential: 0.40 V at pH = 14) $H_2O + \frac{1}{2}O_2 + 2e^- \rightarrow 2OH^-$ (IX)
Overall cell reactions (combination of anode and cathode reactions)	
• Absence of oxygen (ethanol reforming): $C_2H_5OH + 3H_2O \rightarrow 2CO_2 + 6H_2$ (X) • Presence of oxygen (ethanol oxidation): $C_2H_5OH + 3O_2 \rightarrow 2CO_2 + 3H_2O$ (XI)	

affects, for example, the availability of free electrons, since it may act as electron scavenger. At the cathode electrode oxygen affects the type of reduction reactions. Therefore, the presence or absence of oxygen is a crucial factor for PFC operation, as it will be further discussed below.

The cell operation reactions, summarized in Table 1 (also partly exposed in Fig. 1a), are detailed as follows. Reactions in Table 1 are designed for ethanol, which is employed in this work as a model fuel. When UV light is shined on the photocatalyst (for example, nc-TiO_2), the oxide semiconductor, which is the majority species, is excited generating e^-–h^+ pairs (reaction (I)). Electrons may be partly retained in the presence of O_2 leading to formation of superoxide ${}^{\bullet}O_2$ and through them to ${}^{\bullet}OH$ radicals, which add to the degradation capacity towards the organic fuel (reaction (II)). The potential of superoxide radical formation is −0.33 V vs. SHE, which is hard to realize by electrons in the conduction band of titania (about −0.2 V vs. SHE). However, the electronegativity of the conduction band may be raised in the presence of the fuel, which retains holes and liberates more

electrons. Furthermore, oxygen adsorbed on titania has a different potential for superoxide radical formation than free oxygen and it does become an electron scavenger as it is experimentally observed. Therefore, the procedure of reaction (II) may be possible but to a limited degree. The majority of free electrons flow through the external circuit. The type of reactions induced by photogenerated holes depend on solution pH. At low pH, holes mediate the generation of hydrogen ions H^+ according to reaction (III). Reaction (III) represents a simplified scheme. In reality, reaction proceeds by steps, where the following route usually prevails [2]:

$$\text{Ethanol} \rightarrow \text{Acetaldehyde} \rightarrow \text{Acetic acid} \rightarrow CO_2 + H_2O \tag{1}$$

Most of these intermediate reactions are endothermic. The energy input comes from the photogenerated holes. The Gibbs free energy change for reaction (III) is positive; therefore, the overall balance is endergonic and is mediated by photogenerated holes. The same holds true for all reactions associated with chemical substances of the general composition $C_xH_yO_z$, which are generalized by the following scheme [2]:

$$C_xH_yO_z + (2x - z)H_2O + (4x + y - 2z)h^+ \rightarrow xCO_2 + (4x + y - 2z)H^+ \tag{2}$$

At high pH, a lot of $^{\bullet}OH$ radicals are formed by interaction of OH^- with holes.

$$OH^- + h^+ \rightarrow {}^{\bullet}OH \tag{3}$$

Therefore, photocatalytic degradation should be visualized with their participation. In reality, ethanol photodegradation still follows the route of Eq. (1) through intermediate acetaldehyde formation, as it has been previously detected and analyzed [9]. However, the number of hydrogen ions should be limited at high pH or completely eliminated by interacting with OH^- and producing water. Thus at high pH the photocatalytic degradation of ethanol should be represented by reaction (IV) while a more general scheme equivalent to Eq. (2) should be defined by the following equation:

$$C_xH_yO_z + (4x + y - 2z){}^{\bullet}OH \rightarrow xCO_2 + (2x + y - 2z)H_2O \tag{4}$$

Equation (4) is in essence equivalent to Eq. (2) if we assume that $H^+ + OH^- \rightarrow H_2O$ and $H_2O + h^+ \rightarrow H^+ + {}^{\bullet}OH$. The only difference is that hydrogen ions survive only at low OH^- concentration.

As seen in Table 1, reactions taking place at the cathode electrode are less complicated and are independent of what is the fuel or the photocatalyst. It is seen that in the absence of oxygen, hydrogen is produced by reduction of hydrogen ions at low pH or by reduction of water at high pH. In the presence of O_2, reactions proceed with the participation of the latter. Of course, no hydrogen is produced in that case. The electrochemical potentials for the reduction reactions are given in Table 1. The variation of the potential with pH follows the general rule [2].

$$\Delta V(\mathrm{V}) = -0.059 \times \Delta\mathrm{pH} \tag{5}$$

The values of these potentials define the conditions of PFC operation. The conduction band level of nanocrystalline titania lies at about −0.2 V vs. SHE at pH zero [10] or about −1 V at high pH. Then the potential difference with the cathode is ideally no more than 0.2 V in the absence of oxygen. This difference, taking into account also the inevitable losses, is not sufficient to provide drive for cell operation. Consequently, a bias is necessary in that case, which can be applied either externally or chemically. If the anode is in an alkaline environment and the cathode in acidic environment, a chemical forward bias is provided [11] according to Eq. (5). Thus a PFC can produce hydrogen only under bias. On the contrary, when the cathode electrode is in an aerated environment, a potential difference of around 1.4 V is established between the anode and the cathode electrode. Indeed, experimental data have repeatedly fulfilled this expectation [8, 11, 12]. PFCs then operating in the presence of oxygen produce high voltage and operate without bias, similarly to solar cells. Obviously, in that case a PFC can be used as a device to produce electricity consuming organic wastes and being activated by absorption of light.

The overall reactions obtained by taking into account reactions taking place at both the anode and the cathode electrode are expressed by reactions (X) and (XI) of Table 1. It is seen that these overall reactions are independent of the pH but depend on the presence of oxygen. In the absence of oxygen ethanol is photocatalytically reformed producing H_2 while in the presence of oxygen ethanol is photocatalytically "burned" and mineralized. We have previously found that the presence of O_2 accelerates mineralization of ethanol [9, 13] at the expense of the current flowing in the external circuit. The corresponding overall scheme for substances of the general composition $C_xH_yO_z$ is given by

$$\mathrm{C}_x\mathrm{H}_y\mathrm{O}_z + \left(x + \frac{y}{4} - \frac{z}{2}\right)\mathrm{O}_2 \rightarrow x\mathrm{CO}_2 + \frac{y}{2}\mathrm{H}_2\mathrm{O} \tag{6}$$

The Gibbs free energy change ΔG^0 for such a reaction has been calculated and listed in Table 2 for a few substances of the type $C_xH_yO_z$. The overall balance is exergonic ($\Delta G^0 < 0$). The corresponding standard potential was calculated by the following equation:

$$E^0 = \frac{\Delta G^0}{-nF} \tag{7}$$

where n is the number of electron moles involved in the reaction and F is the Faraday constant 96.486 kC mol^{-1}, while ΔG^0 is given in kJ mol^{-1}. n and E^0 are also listed in Table 2. The number of electrons (and holes) is equal to $n = (4x + y - 2z)$, i.e., equal to the number of holes involved in reactions (2) and (4) or to 4 electrons per oxygen molecule involved in reaction (6). Thus all potentials are positive and their range is limited between 1.12 and 1.21 V with respect to the

Table 2 Calculated Gibbs free energy change and standard potential for reaction (5) and for a few organic substances of the general composition $C_xH_yO_z$

Name	Chemical composition	Number of electrons	ΔG^0(kJ mol^{-1})	E^0 (V)
Methanol	CH_3OH	6	−702	1.21
Ethanol	C_2H_5OH	12	−1,325	1.14
n-propanol	C_3H_7OH	18	−1,965	1.13
n-butanol	C_4H_9OH	24	−2,595	1.12
n-pentanol	$C_5H_{11}OH$	30	−3,249	1.12
Glycerol	$C_3H_8O_3$	14	−1,656	1.22
Sorbitol	$C_6H_{14}O_6$	26	−3,084	1.23
Acetic acid	CH_3COOH	8	−873	1.13

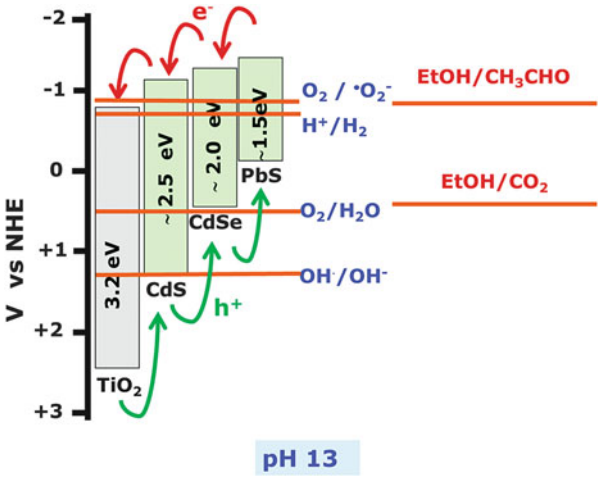

Fig. 2 Approximate energy levels of a few semiconductors together with some characteristic redox potentials. The values of the bandgap for CdS, CdSe, and PbS are higher than those corresponding to bulk semiconductors because of the quantum confinement effect. Values are adapted to data in Refs. [2, 14–16]. The depicted values correspond to pH 13. They were negatively shifted with respect to the values that correspond to pH = 0, according to Eq. (5). Thus at pH = 0 the potential of H^+/H_2 is zero

standard hydrogen potential. The corresponding value for ethanol is +1.14 V and is depicted in Fig. 2 as $EtOH/CO_2$ level. Figure 2 shows energy levels of a few semiconductors and redox reactions. It reveals that for holes found at the valence band level of titania the oxidation power is high enough to carry out all listed reactions. However, in the presence of a sensitizer, holes are injected into the higher lying level of the sensitizer and then their oxidative power dramatically decreases. Thus only CdS valence band level is still oxidative enough to realize ethanol oxidation. Comparison of energy levels in Fig. 2 may be an oversimplification.

Thus reaction (V), which is the first step of ethanol oxidation, with ΔG^0 equal to 34.8 kJ mol^{-1} and corresponding $E^0 = -0.18$ V (see Fig. 2) is in principle feasible in the presence of any of the depicted semiconductors. However, reaction (V) means that ethanol molecules are adsorbed on the semiconductor, while interactions with $^{\bullet}OH$ occur in the liquid phase. It is obvious that these interactions are fairly complicated. Obviously, mineralization of the fuel is encouraged by photocatalysts with high enough oxidation capacity.

When visible light is shined on the photoanode, only the photosensitizer is excited, since titania does not absorb in the Visible. Electrons are rapidly injected into the conduction band of titania (cf. Fig. 2) and follow the routes related to reaction (II). The fate of the holes in the valence band of the photosensitizer depends on the valence band potential, as already discussed. Photocatalytic degradation of alcohols using oxide photocatalysts has been extensively studied, however, rare data or no data at all exist for combined titania-QD photocatalysts. The reason is that such systems are considered to be unstable but this conclusion is still questioned as it will be discussed later [8]. Unquestionably, more work is necessary on such combined photocatalysts to clarify what actually takes place.

The PFC configuration depicted in Fig. 1a assumes that the cell is divided into two compartments, the anode and the cathode compartment, separated by an ion transfer membrane. The fuel is then introduced in the anode compartment while reduction reactions are limited in the cathode compartment. In such two compartment cells, a chemical bias may be applied by introducing an alkaline electrolyte in the anode and an acidic electrolyte in the cathode compartment. The cell of Fig. 1b is essentially a two-compartment cell where the ion transfer membrane is assembled with the cathode electrode. The latter is exposed to the ambient, thus it always functions in the presence of oxygen. A membrane-electrode assembly may, for example, be obtained by hot-pressing a plastic membrane like nafion on a carbon cloth electrode. The electrocatalyst is sandwiched between the membrane and the electrode. An acid-functionalized nafion membrane assembled with the cathode electrode and introduced in a PFC functions only in conduct with an acidic electrolyte [17, 18]. In a typical two-compartment cell as the one depicted in Fig. 1a, a glass frit or a similar material, may be used as an ion transfer membrane. Ion transfer membranes for PFCs have not been particularly studied and remain a technological challenge.

2 Cell Construction

As already said, the major components of a PFC are the photoanode electrode carrying the photocatalyst and the cathode electrode carrying the reduction electrocatalyst. In most cell configurations, for example, those of Fig. 1, photoanode may also play the role of cell window. For this reason, the photoanode electrode is usually based on a transparent conductive oxide like Fluorine-doped Tin Oxide glass (FTO).

2.1 Construction of the Photoanode

In our works, photoanodes always carried nc-TiO_2 sensitized by metal sulfide QDs. nc-TiO_2 was deposited first and was followed by the sensitizer. Nanocrystalline titania was always deposited in two layers, a bottom thin compact layer that facilitates stable attachment on and good electrical conduct with the FTO glass and a thick top open structure, which allows deep electrolyte penetration thus increasing active interface [8]. The bottom layer was synthesized by the sol–gel method while the top layer was applied by using a paste made of Degussa P25 nanoparticles. A densely packed nanocrystalline titania layer was first deposited on a patterned FTO electrode, cleaned by sonication in acetone, isopropanol, and ethanol, according to the following procedure [8, 19]: 3.5 g of the nonionic surfactant Triton X-100 was mixed with 19 mL ethanol. Then 3.4 mL glacial acetic acid (AcOH) and 1.8 mL of Titanium Tetraisopropoxide were added under vigorous stirring. After a few minutes stirring, the film was deposited by dipping and then it was left to dry in air for a few minutes. Finally, it was calcined at 550 °C. The temperature ramp was 20°/min up to 550 °C and the sample was left for about 10 min at that temperature. The procedure was repeated once more. Each layer gave a thin nanostructured film of about 170 nm thickness, as measured by its FE-SEM profile [19]. On the top of this compact nanostructured layer commercial Degussa P25 was deposited. For this purpose, a paste of titania P25 was prepared according to Ref. [20]. The paste was applied by screen printing using a 90 mesh screen. It was finally calcined again at 550 °C. The thickness of the top layer was about 3.4 μm as measured by its FE-SEM profile [19]. The procedure was repeated once more so that the final nc-TiO_2 film was about 7.5 μm thick. The active area of the film was 1 cm^2 (1 cm × 1 cm).

CdS, ZnS, CdS-ZnS composites and PbS QDs were deposited on nc-TiO_2 films by Successive Ionic Layer Adsorption and Reaction (SILAR method) [8, 19, 21]. For this purpose, two aqueous solutions were used, one containing 0.1 mol L^{-1} $Cd(NO_3)_2.4H_2O$, $Zn(NO_3)_2.6H_2O$ or $Pb(ClO_4)_2.3H_2O$ or their mixtures and the second containing 0.1 mol L^{-1} $Na_2S.9\ H_2O$. Freshly prepared titania electrode was immersed for 5 min in the metal salt solution, then copiously washed with triple-distilled water, then immersed for 5 min in the $Na_2S.9H_2O$ solution and finally washed again. This sequence corresponds to one SILAR cycle. Optimization led to a choice of 10 SILAR cycles for the deposition of CdS or combined ZnS-CdS QDs and only 2 cycles for PbS, which is fast adsorbed on nc-TiO_2. Higher number of SILAR cycles overloads titania and has adverse effects on its performance. Optimization was carried out by measuring the electric characteristics of the cells made by these sensitized photoanodes. The electrode with deposited QD@nc-TiO_2 film was first left to dry in an N_2 stream and then it was put for a few minutes in an oven at 100 °C. Finally, it was annealed for a few minutes in an inert atmosphere (N_2) at 400 °C.

CdSe QDs cannot be deposited by the above SILAR method but instead a Chemical Bath Deposition (CBD) procedure was employed. It was similar to that

employed by other researchers [22, 23] and involves the following steps: An aqueous solution of 0.08 mol L^{-1} Se powder was first prepared in the presence of 0.2 mol L^{-1} Na_2SO_3 by continuous stirring and refluxing at 80 °C. The procedure lasted about 15 h and was carried out overnight. The obtained solution, denoted in the following as sol A, actually aimed at the formation of sodium selenosulphate (Na_2SeSO_3), which is a precursor for slow Se^{2-} release. Two more aqueous solutions were then prepared, containing 0.08 mol L^{-1} $CdSO_4 \cdot {}^8/_3$ H_2O (sol B) and 0.12 mol L^{-1} nitrilotriacetic acid trisodium salt (sol C), respectively. Sol B was mixed with an equal volume of sol C and the obtained mixture was stirred for a few minutes. The combination of sol B with sol C leads to the formation of a complex, which is used as precursor for slow release of Cd^{2+}. Finally, two parts of this last mixture were mixed with one part of sol A and the thus obtained final mixture was used for CBD. Thus, the final concentration of $Se^{2-}$and Cd^{2+} ions was 0.08/3 mol L^{-1}. The idea of the above procedure is to make a mixture of precursors, which slowly release selenium and cadmium ions so as to make them react after adsorption on the substrate. Thus the electrodes with substrate films were dipped in this final solution. Subsequently, they were put in a refrigerator at 5 °C for 4 h or left at ambient temperature for several hours. The choice of temperature or residence time is dictated by the substrate. It was observed that nc-TiO_2/FTO electrodes where QD seeds were first deposited by the SILAR method needed only 4 h and low temperature to adsorb substantial quantities of CdSe and be deeply colored while more than 24 h were required in the absence of the first QD layer. The procedure was accelerated when the CBD was done at ambient temperature.

2.2 Construction of the Cathode Electrode

The cathode electrode was made of carbon cloth with deposited carbon black and Pt [12]: 0.246 g of carbon black was mixed with 8 mL of distilled water by vigorous mixing in a mixer (about 2,400 r.p.m.) until it became a viscous paste. This paste was further mixed with 0.088 mL polytetrafluorethylene (Aldrich, Teflon 60 % wt. dispersion in water) and then applied on a carbon cloth cut in the necessary dimensions. This has been achieved by first spreading the paste with a spatula, preheating for a few minutes at 80 °C and finally heating also for a few minutes in an oven at 340 °C. Subsequently, the catalytic layer was prepared as follows: 1 g of Pt/carbon black electrocatalyst (30 % on Vulcan XC72) was mixed with 8 g of nafion perfluorinated resin (5 wt% solution in lower aliphatic alcohols and water, Aldrich) and 15 g of a solution made of 7.5 g H_2O and 7.5 g isopropanol. The mixture was ultrasonically homogenized and then applied on the previously prepared carbon cloth bearing carbon black. The electrode was then heated at 80 °C for 30 min and the procedure was repeated as many times as necessary to load about 0.5 mg of Pt/cm^2. The active dimensions of the cathode electrode were $3 \times 4 = 12$ cm^2.

2.3 Description of the Reactor

The reactor was made of Plexiglas and comprised two compartments of orthogonal shape separated by a silica frit (ROBU, Germany, porosity SGQ 5, diameter 25 mm, thickness 2 mm). Both compartments contained the same aerated electrolyte. The capacity of the anode compartment was 10 mL and that of the cathode compartment was 2 mL. The fuel (ethanol), when necessary, was added only in the anode compartment. Irradiation by simulated solar light was made by employing an Osram XBO 450 W Xe source. Light was filtered for the IR radiation using a circulating water filter. The intensity of radiation at the position of the photocatalyst was 75 mW cm^{-2}. In all cases, the exciting radiation passed through the glass-FTO electrode, which played the role of window. The active area of the photoanode was 1 cm^2. Electrical connections were made by means of an auto-adhesive copper ribbon and wires soldered on the ribbon.

In some cases, instead of the two-compartment cell described above and schematically illustrated in Fig. 1a, we used the modified configuration illustrated in Fig. 1b. In that case, a polymer ion exchange membrane was assembled with the counter electrode by heating the assembly up to about 120 °C under pressure. The cell closes on one side by the photoanode-window and on the other side by the membrane-cathode assembly [24]. The cathode is exposed to ambient air. The Pt/carbon black electrocatalyst is on the side that touches the membrane. Between the photoanode and the membrane is the electrolyte with fuel. We used a nafion membrane (N117, Ion Power, Inc., USA) functionalized in hot sulphuric acid.

3 Cell Operation and Optimization

The operation of a PFC is affected by the four major parameters already mentioned in the Introduction, namely, the type of photocatalyst, the fuel, the electrolyte pH, and the presence or absence of oxygen. These parameters will be further analyzed in the following paragraphs.

3.1 Choice of Photocatalyst and Sensitizer

A review of the recent literature reveals that the most popular photocatalyst is nanoparticulate titania. Other oxides, for example, ZnO are also popular since they offer some possibilities not provided by nc-TiO_2. For example, ZnO films can be obtained at low temperature, therefore, they may be used with flexible plastic electrodes [25, 26], contrary to titania, which is functional only when heated at high temperature. In addition, ZnO can be easily synthesized in exemplary single-dimensional nanostructures, like nanorods [27], which offer large interface and

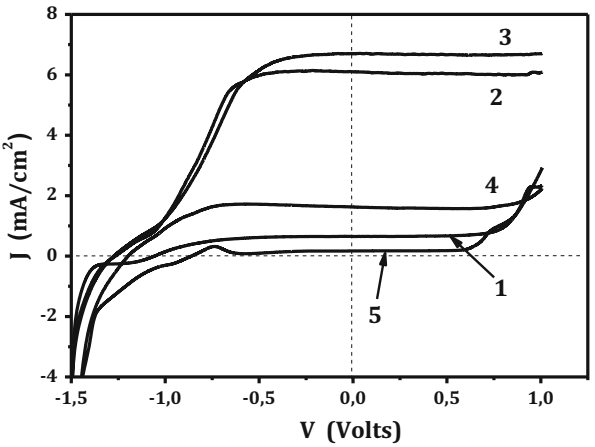

Fig. 3 JV curves recorded with an unbiased two-compartment cell using a photoanode made of nc-TiO_2/FTO and various QD photosensitizers: (1) ZnS; (2) CdS; (3) 25 % ZnS-75 % CdS; (4) CdSe; and (5) PbS. A 0.5 mol L^{-1} aqueous NaOH electrolyte was used in all cases. The anode compartment also contained 1 mol L^{-1} ethanol

efficient electron hole separation. Even with these advantages taken into account, nanoparticulate titania has led to the construction of solar cells with unsurpassed efficiency. Thus the champion (dye-sensitized) solar cells are based on photoanodes made of mixtures of TiO_2 nanoparticles [28] of two or three different sizes. Our own experience has also persuaded us that the most efficient PFCs should rely on nanoparticulate titania. Thus nc-TiO_2 films were deposited on FTO electrodes according to the procedure described in Sect. 2.1. The next step was to choose the QD sensitizer in order to make visible-light responsive cells. We have studied four different II–VI semiconductors: ZnS, CdS, CdSe, and PbS. Figure 3 shows current–voltage curves for PFCs employing photoanodes carrying an nc-TiO_2 film functionalized with the above semiconductors, alone or in combinations. The highest short-circuit current density (i.e., value of J at $V = 0$) and the highest open-circuit voltage (i.e., value of V at $J = 0$) was obtained with a combination of 25 % ZnS-75 % CdS (curve 3), while pure CdS (curve 2) gave a bit lower but comparable values. For higher percentages of ZnS, both current and voltage dropped. Both values extensively dropped in the presence of CdSe (curve 4) and became dramatically low in the presence of PbS (curve 5). Similar variation was demonstrated, as expected, also by the value of the maximum power density generated by the cell in each case (not shown). The presence of CdSe and PbS had similar detrimental effects also when these materials were combined with CdS. The explanation of this behavior [8] can be given in terms of the diagram of Fig. 2. Even though, CdSe and PbS have small energy bandgaps and they can absorb a higher portion of the incident light, their high-lying valence band decreases their oxidative power. Therefore, they cannot effectively oxidize the fuel and they thus produce less electric power. Indeed, the current density decreased, as seen in Fig. 3, when the valence band moved to less positive potentials, as seen in Fig. 2. Pure ZnS also generated low electric power (curve 1), which is close to that obtained with pure nc-TiO_2, i.e., in the absence of a sensitizer, even though, ZnS valence band is more oxidative than that of CdS [2, 8]. This drop of current is due to a different

reason. ZnS is a large bandgap semiconductor [2, 8] and absorbs only UV light. Therefore, it cannot act as a sensitizer, i.e., it absorbs less photons and behaves as if it were pure titania alone. Nevertheless, a small percentage of ZnS added to CdS beneficially affected the cell performance [8] (i.e., curve 3). The above results briefly show that a QD sensitizer may be well combined with nc-TiO_2 as long as it does not destroy the oxidative power of the combined photocatalyst. Thus a medium bandgap sensitizer such as 25 % ZnS-75 % CdS or pure CdS [8] is functional but low bandgap semiconductors like CdSe or PbS are not applicable to PFCs. A question of stability then arises at this point. Mixtures of CdS with ZnS may successfully act as visible-light sensitizers of titania but how stable are they? A brief review of literature reveals that metal sulfide semiconductors can survive only in the presence of sulfide or polysulfide electrolytes, which repair any loss due to self-oxidation by photogenerated holes. Degradation of metal sulfide semiconductors occurs when photogenerated holes are not rapidly removed causing oxidation of S^{2-} to S, thus destroying the semiconductor. Removal of holes is, however, realized in the presence of a sacrificial agent. We have previously shown [8] that the presence of ethanol in an alkaline electrolyte satisfactorily preserved the photosensitization action for several hours, while in the absence of ethanol this action fainted in a few minutes. The low currents obtained in the case of CdSe and PbS became even lower in the course of time, obviously due to the degradation effect, since ethanol could not act as a sacrificial agent in their case.

3.2 Choice of Fuel

Any organic substance or mixture of substances may be used as a fuel in a PFC, since as we have already said, photocatalysts do not demonstrate any specificity towards the photodegradable material. Research is usually carried out with model fuels like ethanol, methanol, and glycerol, since they produce the highest electric power. Indeed, the electric power generated by a PFC under the same illumination conditions differs from one fuel to another. Table 3 lists data, which concern a few characteristic organic substances of the type $C_xH_yO_z$, that is, alcohols, polyols, sugars and organic acids, which are products of biomass and therefore renewable. The JV_{max} values of Table 3 were obtained with a pure nc-TiO_2 photoanode to avoid any complication or doubt arising in the presence of a QD sensitizer. JV_{max} is the maximum value of the product $J \times V$ calculated by tracing the current–voltage curve that characterizes cell function. The highest JV_{max} value was obtained with the shortest chain alcohol, i.e., methanol, and it dropped as the aliphatic chain length increased. A relatively high value was obtained also in the presence of glycerol and acetic acid. The data of Table 3 then reveal a clear-cut inverse relation between the size of the molecule and the electric yield of the cell. Smaller molecules of each category may produce more electric power. Thus methanol and ethanol as well as glycerol and acetic acid are more powerful fuels than substances of larger molecular weight. Substances containing other elements beyond C, H, and

Table 3 Maximum power density generated by a PFC employing substances of the general composition $C_xH_yO_z$ as fuel. Fuel concentration was 1 mol L^{-1}

Name	Chemical composition	JV_{max} (mW cm^{-2})
Methanol	CH_3OH	0.71
Ethanol	C_2H_5OH	0.63
n-propanol	C_3H_7OH	0.60
n-butanol	C_4H_9OH	0.52
n-pentanol	$C_5H_{11}OH$	0.42
Glycerol	$C_3H_8O_3$	0.61
Sorbitol	$C_6H_{14}O_6$	0.50
Acetic acid	CH_3COOH	0.66

Electrolyte was 0.5 mol L^{-1} NaOH. The photoanode carried an nc-TiO_2 film without sensitizer

O and presumably more difficult to degrade produce less electric power as well [11].

3.3 Choice of pH

pH value in both the anode and the cathode compartment does affect cell operation, as already discussed in Sect. 1. Use of a glass frit as ion transfer membrane allows electrolyte of any pH to be introduced in any of the two cell compartments. When a nafion membrane was used instead of a glass frit, it was necessary to introduce an electrolyte of low pH in at least one of the two compartments, in order to preserve its cation transfer functionality. In that case, the acidic electrolyte is introduced in the cathode compartment in order to apply a forward bias, according to Eq. (5). As a matter of fact, we never ran the anode at acidic pH, since, as already said, photocatalytic degradation of organic substances is more effective at high pH. In addition, we have observed a failure of the nc-TiO_2 film, which was detached from the FTO electrode at low pH. PFCs then normally run either at alkaline conditions in both compartments [3, 8, 16] or at alkaline in the anode and acidic in the cathode compartment [15]. In this last case, thanks to the chemical forward bias, the open-circuit voltage was higher [15] than when the electrolyte was the same in both compartments [12]. Indeed, as seen in Fig. 3, the data of which correspond to alkaline electrolyte in both compartments, the maximum open-circuit voltage was around 1.2 V, while in the case of Ref. [11], where an acidic electrolyte was introduced in the cathode compartment, the open-circuit voltage climbed up to 1.8 V.

3.4 Presence or Not of Oxygen

The presence of O_2 affects, as already said, the reactions in both compartments. Oxygen in the anode compartment may retain some electrons and decrease current. In the cathode compartment, hydrogen can be produced only in the absence of oxygen (Eqs. (VI) and (VII) of Table 1), but in that case the electric potential drive is too weak to run the cell without bias. In the presence of oxygen, the cell runs without external bias similarly to a solar cell. Of course, there is a basic difference from the latter since PFCs function by consuming a fuel while typical solar cells function in a cyclic manner. The necessity to consume a fuel has been repeatedly demonstrated in previous works [3, 12]. Thus both current and electric potential dramatically dropped when the fuel was removed. Water itself is photocatalytically split in a PFC. Thus it behaves as a fuel and produces some current and voltage [12]. However, both these parameters largely increased even in the presence of a small quantity of organic fuel. The fuel plays a dual role that defines the necessity of its presence for cell operation. The fuel is photocatalytically oxidized, mainly, by retaining photogenerated holes. Thus electrons are liberated to make the external current. In addition, fuel consumption creates intermediate species that facilitate the flow of charge and provide internal ionic conductivity. Of course, the electrolyte provides the ionic species but their preservation, for example, through reactions (VI) to (IX) of Table 1, is necessary in order to provide continuous operation.

4 Efficiency Issues

The calculation of cell efficiency in the case of PFCs is more complicated [29] than in the case of regular solar cells. The reason is that, in addition to the solar input, efficiency calculations must take into account the chemical energy liberated by the oxidized fuel plus the value of any applied bias. We presently list a number of models [2] for calculating cell efficiency, which are simple and unambiguously represent what they are designed for. One clear way to calculate cell efficiency is by External Quantum Efficiency (EQE) as expressed by Incident Photon to Current conversion Efficiency (IPCE). EQE of a solar cell is the ratio of the number of charge carriers produced by the cell over the number of photons incident on the cell. IPCE is one way to express EQE. IPCE is a measure of the effectiveness of the cell to convert the incident photons of a monochromatic radiation into electric current [2, 29]. It is given by the following equation:

$$\mathrm{IPCE} = \frac{1,240 \times J_{sc}(\mathrm{mA/cm^2})}{\lambda(\mathrm{nm}) \times P(\mathrm{mW/cm^2})} \tag{8}$$

where J_{sc} is the short-circuit current density and P the incident radiation intensity at a given wavelength λ. IPCE is a pure number without units. The number 1,240

carries the matching units. By recording IPCE at different wavelengths, it is possible to judge the effectiveness of the cell with respect to the spectral response of a photocatalyst or a system of combined photocatalysts or a sensitized catalyst. The value of IPCE is expected to vary between 0 and 1.

In the case when the cell is used to produce a solar fuel, for example, hydrogen, the efficiency η can be calculated by the following equation [29]:

$$\eta = \frac{\Delta G^0 \times R}{P} \tag{9}$$

where ΔG^0 is the standard Gibbs free energy change for the photodegradable substance multiplied by the rate R of fuel formation in moles/s and divided by the incident radiation power. Instead of ΔG^0 we can use the corresponding potential, calculated by Eq. (7)

$$\eta = \frac{E \times I}{P} \tag{10}$$

where I is the current involved in the decomposition process. The safest way to calculate I should correspond to the quantity of fuel produced. Thus if, for example, the device produces 2 μ mol/min of hydrogen [12], since two electrons correspond to one H_2, we expect that the corresponding current will be $I = 2(\text{electrons/molecule}) \times (2 \times 10^{-6}\ \text{mol/60 s}) \times 6{,}023 \times 10^{23}\ (\text{molecules/mol}) \times 1.602 \times 10^{-19}\ (\text{C/electron}) = 6.4$ mA. In the case when a bias voltage V_{app} is applied, then Eq. (10) should be substituted by the following equation:

$$\eta = \frac{\left(E - V_{\text{app}}\right) \times I}{P} \tag{11}$$

This last model for measuring efficiency has been applied in several cases [30–32]. The model of Eqs. (10) and (11) is simple and clear. Caution is only necessary to properly define E in each case.

5 Conclusions

PFCs constitute an alternative means of solar energy conversion, with simultaneous photocatalytic degradation of water-soluble wastes. PFCs are mainly designed to produce electricity but they can also be used for solar hydrogen production. In that case, the cells run only under bias. Chemical bias may be applied by introducing an alkaline electrolyte in the anode and an acidic electrolyte in the cathode compartment. Photoanodes based on nanocrystalline titania can be functionalized in the visible with QD sensitizers. In this respect, only medium energy gap semiconductors, like CdS and combined ZnS-CdS, have enough oxidative capacity to degrade

the fuel. Small bandgap semiconductors, like CdSe and PbS do not have this capacity and they are no use for PFCs. Stability of cell operation is assured only in the presence of QDs, which are capable of degrading the fuel. In the opposite case, the photoanode is unstable and cell operation fails. Any organic substance or mixture of substances may be used as fuel. However, small molecules of the $C_xH_yO_z$ category, i.e., small alcohols, polyols, and organic acids have demonstrated the highest electric power generation efficiency. The efficiency of a PFC may be well represented by its IPCE spectrum [8]. In cases when the cell is used to produce a solar fuel, like hydrogen, the efficiency can be calculated by simple models like that of Eq. (11).

Acknowledgements This research has been co-financed by the European Union (European Social Fund—ESF) and Greek national funds through the Operational Program "Education and Lifelong Learning" of the National Strategic Reference Framework (NSRF)—Research Funding Program: Thales. MIS379320. Investing in knowledge society through the European Social Fund.

References

1. Kaneko, M.; Nemoto, J.; Ueno, H.; Gokan, N.; Ohnuki, K.; Horikawa, M.; Saito, R.; Shibata, T. Photoelectrochemical reaction of biomass and bio-related compounds with nanoporous TiO_2 film photoanode and O_2-reducing cathode. *Electrochem. Commun.* **2006,** 8, 336-340.
2. Lianos, P. Production of electricity and hydrogen by photocatalytic degradation of organic wastes in a photoelectrochemical cell: The concept of the Photofuelcell: A review of a re-emerging research field. *J. Hazardous Mater*, **2011**, 185, 575-590.
3. Antoniadou, M.; Lianos, P. A photoactivated fuel cell used as an apparatus that consumes organic wastes to produce electricity. *Photochem. Photobiol. Sci*. **2011**, 10, 431-435.
4. Fujishima, A.; Honda, K. Electrochemical Photolysis of Water at a Semiconductor Electrode. *Nature* **1972,** 238, 37-38.
5. Hagfeldt, A.; Boschloo, G.; Sun, L.; Kloo, L.; Pettersson, H. Dye-Sensitized Solar Cells. *Chem. Rev*. **2010**, 110, 6595-6663.
6. Ruhle, S.; Shalom, M.; Zaban, A. Quantum-Dot-Sensitized Solar Cells. *ChemPhysChem* **2010**, 11, 2290-2304.
7. Chouhan, N.; Yeh, C.L.; Hu, S-F.; Liu, R-S.; Chang, W-S.; Chen, K-H. Photocatalytic CdSe QDs-decorated ZnO nanotubes: an effective photoelectrode for splitting water. *Chem. Commun*. **2011**, 47, 3493-3495.
8. Antoniadou, M.; Kondarides, D.I.; Dionysiou, D.D.; Lianos, P. Quantum Dot Sensitized Titania Applicable as Photoanode in Photoactivated Fuel Cells. *J. Phys. Chem. C* **2012**, 116, 16901-16909.
9. Panagiotopoulou, P.; Antoniadou, M.; Kondarides, D.I.; Lianos, P. Aldol condensation products during photocatalytic oxidation of ethanol in a photoelectrochemical cell. *Appl. Catal. B* **2010**, *100*, 124-132.
10. Yu, H.; Irie, H.; Hashimoto, K. Conduction Band Energy Level Control of Titanium Dioxide: Toward an Efficient Visible-Light-Sensitive Photocatalyst. *J. Am. Chem. Soc*. **2010,** 132, 6898-6899.
11. Antoniadou, M.; Lianos, P. Near Ultraviolet and Visible light photoelectrochemical degradation of organic substances producing electricity and hydrogen. *J. Photochem. Photobiol. A* **2009**, 204, 69-74.

12. Antoniadou, M.; Lianos, P. Production of electricity by photoelectrochemical oxidation of ethanol in a PhotoFuelCell. *Appl. Catal. B* **2010**, 99, 307-313.
13. Antoniadou, M.; Panagiotopoulou, P.; Kondarides, D.I.; Lianos, P. Photocatalysis and photoelectrocatalysis using nanocrystalline titania alone or combined with Pt, RuO_2 or NiO co-catalysts. *J. Appl. Electrochem.* **2012**, *42*, 737-743.
14. Kawai, M.; Kawai, T.; Naito, S.; Tamaru, K. The mechanism of photocatalytic reaction over Pt/TiO_2: Production of H_2 and aldehyde from gaseous alcohol and water. *Chem. Phys. Lett.* **1984,** *110*, 58-62.
15. Lee, Y-L.; Chi, C-F.; Liau S-Y. CdS/CdSe Co-Sensitized TiO_2 Photoelectrode for Efficient Hydrogen Generation in a Photoelectrochemical Cell. *Chem. Mater.* **2010**, 22, 922-927.
16. Kim, H.S.; Jeong, N.C.; Yoon, K.B. Photovoltaic Effects of CdS and PbS Quantum Dots Encapsulated in Zeolite Y. *Langmuir* **2011**, 27, 14678-14688.
17. Seger, B.; Kamat, P.V. Fuel Cell Geared in Reverse: Photocatalytic Hydrogen Production Using a TiO_2/Nafion/Pt Membrane Assembly with No Applied Bias. *J. Phys. Chem. C* 2009, 113, 18946-18952.
18. Seger, B.; Lu, G.Q.M.; Wang, L. Electrical power and hydrogen production from a photo-fuel cell using formic acid and other single-carbon organics. *J. Mater. Chem.* **2012**, 22, 10709-10715.
19. Balis, N.; Dracopoulos, V.; Stathatos, E.; Boukos, N.; Lianos P. A Solid-State Hybrid Solar Cell Made of nc-TiO_2, CdS Quantum Dots, and P3HT with 2-Amino-1-methylbenzimidazole as an Interface Modifier. *J. Phys. Chem. C* **2011**, *115*, 10911-10916.
20. Ito, S.; Chen, P.; Comte, P.; Nazeeruddin, M. K.; Liska, P.; Pechy P.; Gratzel M. Fabrication of screen-printing pastes from TiO_2 powders for dye-sensitised solar cells. *Prog. Photovolt: Res. Appl,* **2007**, *15*, 603-612.
21. Pathan H. M.; Lokhande C. D. Deposition of metal chalcogenide thin films by successive ionic layer adsorption and reaction (SILAR) method. *Bull. Mater. Sci.* **2004**, 27, 85-111.
22. Shen, Q.; Kobayashi, J., Diguna L.J.; Toyoda, T. Effect of ZnS coating on the photovoltaic properties of CdSe quantum dot-sensitized solar cells. *J. Appl. Phys.* **2008**, *103*, 0843041-5.
23. Gorer, S.; Hodes, G. Quantum Size Effects in the Study of Chemical Solution Deposition Mechanisms of Semiconductor Films. *J. Phys. Chem.* **1994**, *98*, 5338-5346.
24. Antoniadou, M.; Kondarides, D.I.; Labou, D.; Neophytides, S.; Lianos, P. An efficient photoelectrochemical cell functioning in the presence of organic wastes. *Sol. Energy Mater. Sol. Cells* 2010, *94*, 592-597.
25. Krebs, F.C.; Thomann, Y.; Thomann, R.; Andreasen, J.W. A simple nanostructured polymer/ZnO hybrid solar cell—preparation and operation in air. *Nanotechnology* **2008**, *19*, 424013-424025.
26. Sondergaard, R.R.; Makris, T.; Lianos, P.; Manor, A.; Katz, E.A.; Gong, W.; Tuladhar, S.M.; Nelson, J.; Tuomi, R.; Sommeling, P.; Veenstra, S.C.; Rivaton, A.; Dupuis, A.; Teran-Escobar, G.; Lira-Cantu, M.; Sapkota, S.B.; Zimmermann, B.; Wurfel, U.; Matzarakis, A.; Krebs, F.C. The use of polyurethane as encapsulating method for polymer solar cells—An inter laboratory study on outdoor stability in 8 countries. *Sol. Energy Mater. Sol. Cells*, **2012**, *99*, 292-300.
27. Xu, J.; Yang, X.; Yang, Q-D.; Wong, T-L.; Lee, S-T.; Zhang, W-J.; Lee, C-S. Arrays of CdSe sensitized ZnO/ZnSe nanocables for efficient solar cells with high open-circuit voltage. *J. Mater. Chem.* **2012**, *22*, 13374-13379.
28. Kalyanasundaram, K.; Gratzel, M. Themed issue: nanomaterials for energy conversion and storage. *J. Mater. Chem.* **2012**, *22*, 24190-24194.
29. Varghese, O.K.; Grimes, C.A. Appropriate strategies for determining the photoconversion efficiency of water photoelectrolysis cells: A review with examples using titania nanotube array photoanodes. *Solar Energy Materials and Solar Cells* **2008**, *92*, 374-384.
30. Tode, R.; Ebrahimi, A.; Fukumoto, S.; Iyatani, K.; Takeuchi, M.; Matsuoka, M.; Lee, C.H.; Jiang, C-S.; Anpo, M. Photocatalytic Decomposition of Water on Doublelayered Visible

Light-responsive TiO_2 Thin Films Prepared by a Magnetron Sputtering Deposition Method. *Catal. Lett.* **2010**, *135*, 10-15.

31. Mohapatra, S.K.; Misra, M.; Mahajan, V.K.; Raja, K.S. Design of a Highly Efficient Photoelectrolytic Cell for Hydrogen Generation by Water Splitting: Application of TiO_2-xCx Nanotubes as a Photoanode and Pt/TiO_2 Nanotubes as a Cathode. *J. Phys. Chem. C* **2007**, *111*, 8677-8685.
32. Matsuoka, M.; Kitano, M.; Fukumoto, S.; Iyatani, K.; Takeuchi, M.; Anpo, M. The effect of the hydrothermal treatment with aqueous NaOH solution on the photocatalytic and photoelectrochemical properties of visible light-responsive TiO_2 thin films. *Catal. Today* **2008**, *132*, 159-164.

Simultaneous Photodegradation and Hydrogen Production with TiO_2/Pt/CdS Using UV–Visible Light in the Presence of a Sacrificial Agent and a Pollutant

Aaron Peterson, Winn Wilson, Bratindranath Mukherjee, and Vaidyanathan (Ravi) Subramanian

1 Introduction

Light and water are clean, abundant, and universally available and hence of immense interest as clean energy resources. Bringing them together for clean fuel (hydrogen) production is a sustainable and logical approach to perennial energy generation [1–3]. TiO_2 is a photocatalyst of interest and has been studied in aiding water splitting for reasons that include wide ranging pH stability, non-toxicity, and good photoactivity in the presence of UV light [4–6]. The hydrogen generation mechanism on TiO_2 can be summarized as follows [7–10]:

$$\mathrm{TiO_2} \overset{\text{Sunlight}}{\rightarrow} \mathrm{TiO_2}(e_{cb} + h_{vb}) \tag{1}$$

$$2\mathrm{H_2O} \overset{\mathrm{TiO_2}(e_{cb}+h_{vb})}{\rightarrow} 2\mathrm{H_{2,\,anode}} + \mathrm{O_{2,\,cathode}} \tag{2}$$

Photoillumination causes electron–hole generation and separation (Eq. (1)). It is followed by a hole-enabled water oxidation and an electron-enabled hydrogen formation (Eq. (2)). If particulate TiO_2 is used, the redox reaction occurs at different locations in the same particle. Several reviews have discussed photocatalytic water splitting in general [11, 12] and the specific benefits of using TiO_2 [13].

There are two essential requirements for TiO_2 to fulfill in order to perform water splitting and produce hydrogen, efficiently: separating photogenerated charges and absorbing light over a broad range. In theory, TiO_2 can photocatalytically perform

A. Peterson • B. Mukherjee • V. (Ravi) Subramanian (✉)
Department of Chemical and Materials Engineering, University of Nevada, MS-388, LME-309, 1664-N Virginia Street, Reno, NV 89557, USA
e-mail: ravisv@unr.edu

W. Wilson
Civil and Environmental Engineering, University of Nevada, MS-388, LME-309, 1664-N Virginia Street, Reno, NV 89557, USA

B. Viswanathan et al. (eds.), *Materials and Processes for Solar Fuel Production*, Nanostructure Science and Technology 174, DOI 10.1007/978-1-4939-1628-3_8

water splitting, but is limited in its absorbance and charge separation capabilities. Charge separation can be achieved using metal centers that function as sinks for the photogenerated electrons and aid in keeping it away from holes [8]. Further, the addition of visible light receptors such as chalcogenides can aid with enhancing light absorbance and the quantum efficiency of the overall process [14–16]. Thus, a TiO_2-based photocatalyst with these primary entities (metals and light harvesters) as additives can be built to efficiently perform photocatalytic water splitting.

There have been a few studies examining the role of metal and light harvesters on TiO_2. Among metals, most studies have focused on Pt group metals or PGMs [17–22] while chalcogenides as size tunable visible light harvesters have garnered significant attention [23–28]. CdS is a chalcogenide that has been used with Pt to promote photocatalysis [14, 29, 30]. Most studies have focused on the commercially available Degussa P25 [31, 32] as the TiO_2 source while a few have explored sol–gel-based TiO_2 [20, 33, 34]. A study comparing the various forms of contacting CdS, Pt, and TiO_2 has been reported [29, 35]. After examining various approaches to combine TiO_2, Pt, and CdS; having Pt and CdS deposits juxtaposed adjacently to one another decorating the TiO_2 surface appears to be an optimal arrangement as it can be expected to promote both hole-mediated oxidation and electron-mediated reduction, effectively. Elsewhere, it has been mentioned that a core-shell architecture comprising Au core-CdS shell on TiO_2 is highly efficient in artificial photosynthesis [22]. In another related report, the application of Degussa P25 with Pt and CdS to form a nanocomposites film to produce hydrogen from pollutants has been reported [14]. The present work is significantly different from the aforementioned one, in that (a) instead of sacrificial agents an actual pollutant has been tested, viz., colored compound (azo-dye) and (b) instead of commercial P25, the applicability of an IH-TiO_2 with 100 % anatase phase and higher area is reported.

This work presents a systematic study of the effects of (a) PGM metals, (b) a representative visible light chalcogenide-type harvester, (c) a corrosion inhibitor on the photocatalytic hydrogen generation, and (d) the role of pollutants as electrolyte additives in hydrogen generation. A unique approach to synthesizing TiO_2 with 100 % anatase content and use it as a base to first deposit metal followed by chalcogenide is presented. The effects of Ag, Au, and Pt as the electron shuttling agent and the chalcogenide CdS as the light harvester on the photocatalytic water splitting are examined. Since CdS is involved, prevention of its hole-driven corrosion assumes a significant challenge. To this end, the effect of a stabilizing agent that scavenges the holes has been examined using two approaches. Firstly, the role of a sulfide ion containing sacrificial agent has been probed. Secondly, a strategy to perform hole-mediated oxidation of an aquatic pollutant as an approach to (a) delay CdS corrosion and (b) facilitate photodegradation of the pollutant, simultaneously, has also been presented.

2 Experimental Section

The TiO_2–PGM–chalcogenide composites were synthesized as follows:

2.1 TiO_2 Synthesis

In-house nanoparticulate TiO_2 was synthesized using a wet chemical approach. In a typical step a mixture of 5 mL of titanium propoxide (Sigma-Aldrich) and 0.6 mL of hydrofluoric acid (40 wt/v%) were taken in a Teflon®-lined autoclave and diluted to 30 mL with DI water. Diluted HF was taken with the goal to accelerate the hydrolysis of Ti precursor, creating large number of nucleation sites and hence smaller particle size. The autoclave is sealed and heated in the oven at 190 °C for 24 h. The resulting TiO_2 is rinsed multiple times with DI water and ethanol to remove impurities. For comparative studies, commercial TiO_2 was obtained from Degussa® corporation (Generic name: Degussa P25) and used without any modification.

2.2 Pt, Ag, Au Deposition

Pt and Au deposition on either P25 or the as-prepared TiO_2 was performed by mixing 1 mg Pt salt or Au salt/mL with 20 % or 5 % HCl in solution, respectively. A quantity that would give 1 wt% coverage on TiO_2 was used. These mixtures were stirred on a hot plate at 80 °C until all the excess water was evaporated. A 1 M $NaBH_4$ solution was then added to the dried samples to ensure the metal ions are reduced to nanoparticles. Aqueous Ag ions were reduced by UV-assisted photogenerated electrons for a loading of 1 wt% on TiO_2. The solution was later stirred at 80 °C until all the excess water was evaporated off.

2.3 CdS Deposition

A two-step approach was adapted to ensure the deposition of CdS on TiO_2. The preliminary TiO_2-*M* (*M* = Pt, Au, or Ag) powders were immersed in 0.1 M NaOH aqueous solution for 1 h to enhance the number of basic sites on the TiO_2 surface. After this base treatment, the slurries were centrifuged and the excess solution was poured off. The CdS was deposited at room temperature by stirring the pretreated TiO_2-*M* (*M* = Pt, Au, or Ag) powders in 10 mM solution of $Cd(NO_3)_2$ and thioacetamide. Calculated amount of $Cd(NO_3)_2$ and thioacetamide was taken to ensure 10 % CdS loading on the catalyst surface. It is anticipated that the surface

hydroxyl groups on TiO_2 promotes selective deposition of CdS presumably through intermediate formation of $Cd(OH)_2$. A similar procedure was followed with P-25–PGMs. Further, separate experiments were conducted with identical CdS content. To ensure that the CdS content was the same, known concentration of CdS was deposited on both IH-TiO_2-*M* and P25-*M*.

2.4 Techniques Used for the Characterization of the Composites

The characterization of the various catalysts was carried out using a series of instruments. A Philips 12045 BX-ray diffractometer (XRD) was used at a scan rate of 0.4°/min to identify the phase of the synthesized materials. A Micrometrics 2720 Chemisorb Single point Brunauer-Emmett-Teller (BET) surface area analyzer was used to determine the surface area of the photocatalyst. A Shimadzu UV-2501PC spectrophotometer was used to perform UV–Vis diffuse reflectance measurements (DRUV-vis) and determine the absorbance responses of the photocatalysts.

2.5 Film Preparation and Measurements

A suspension of the Degussa® P25 TiO_2 and the IH-TiO_2 of same loading in DI water was used to prepare the films using an established procedure [36]. The P25 and IH-TiO_2 nanoparticulate coatings were prepared on conducting glass slides by syringing out identical volumes of suspension, drop casting them, and performing a mild annealing in an oven at ~300 °C. The photoelectrochemical measurements involved two specific studies: voltage (J/t) measurements and Mott-Schottky analysis. Both these measurements were performed using an Autolab® PGSTAT 30 Potentiostat and Galvanostat under illumination using a ~90 mW/cm^2 collimated UV–Vis light. Our earlier work provides complete details on the protocols for performing ($I - t/V - t$) [37] and MS analysis [38, 39].

2.6 Photocatalytic Measurements

A gas chromatograph equipped with TCD detector (SRI 8610C) was used to quantitatively and qualitatively estimating hydrogen production under UV–Vis illumination. The setup comprised a 500 mL Pyrex vessel with 500 mg of catalyst and was run with and without sacrificial agents. The catalyst dispersion was bubbled with nitrogen for 30 min prior to running the experiment. It was then

sealed and the outlet was fed to a downward displacement gas collection system. The light source was a 500 W Xenon lamp with an output equal to one sun. The light consists of ~10 % UV, and the rest visible/infrared. The sacrificial agent was made of either 0.1 M Na_2S and 0.02 M Na_2SO_3 or the pollutant, methyl orange (MO)—40 μM. A schematic of the setup is shown elsewhere [40, 41]. The photocatalysis was carried out under ambient conditions of temperature and pressure.

2.7 Actinometry Measurements

Quantum yield for methyl orange dye degradation is measured using ferrioxalate actinometer using the procedure reported elsewhere [42]. Briefly, 0.6 M of potassium ferrioxalate solution was irradiated by a xenon light source for 90 s and photoreduced Fe^{2+} concentration is estimated by measuring the absorbance of Fe^{2+} phenanthroline complex at 510 nm. The number of photons entering the reaction system is determined to be 5.376×10^{16}/s using a method discussed elsewhere [43]. Further, at working white light condition, quantum yield for photocomplexation of Fe^{2+} is taken 1.2 and molar absorptivity is that of the Fe^{2+} phenanthroline complex measured from the slope of the Fe^{2+} complex absorbance calibration curve.

3 Results

3.1 Surface and Photoelectrochemical Characterization

3.1.1 Surface Area Measurements

Table 1 indicates that the surface area of IH-TiO_2 is ~60 % larger compared to the P25. Smaller particle sizes are desirable as they offer higher surface area per gram of the photocatalyst. This smaller particle size and greater surface area has a number of activity implications that are detailed in later sections. Further, smaller particle sizes can be useful for the immobilization of the visible light harvesters as well as the metal centers in a mutually synergistic manner. Such a trilateral arrangement could prove to be useful for photoinduced charge separation and redox photocatalysis. Preliminary analysis of the samples using XRD and EDS was performed (Sect. 3.1.2) to obtain additional details of the photocatalyst surface.

Table 1 Quantitative analysis of the metal content in the TiO_2-Pt-CdS was performed using EDS

		Metal loading			Rate constant, k_{MO} (min^{-1})[a]		Rate, (mL/g/h)[b]	
Surface Area (m^2/g)		Pt (At.%)	Au (At.%)	Ag (At.%)	No Pt/CdS	Pt/CdS	No Pt/CdS	With Pt/CdS
P-25 TiO_2	53 ± 4 %	0.79	0.85	0.81	0.0041	0.017	–	0.25
IH-TiO_2	130 ± 4 %	0.8	0.78	0.75	0.0063	0.036	–	4.6

The table lists the comparative data of the different element content in a representative set of samples [M = Pt,Au, or Ag]. The columns in the second half at the far end provide rate information on MO photodegradation and hydrogen generation

[a]MO photodegradation

[b]Hydrogen generation

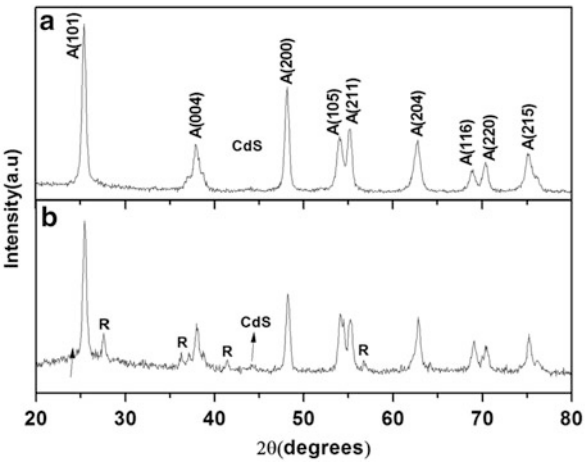

Fig. 1 The XRD of the (**a**) IH-TiO_2-Pt-CdS and (**b**) P25-Pt-CdS indicating the formation of crystalline TiO_2 is shown. The (hkl) values associated with the different anatase peaks are also shown in the figure (Note "A"—anatase, "R"—rutile)

3.1.2 XRD and EDS Analysis

XRD analysis was performed on the samples during various stages of synthesis. XRD of representative samples with CdS and Pt is shown in Fig. 1. The IH-TiO_2 is exclusively in anatase crystal structure (JCPDS #21-1272). The anatase phase has been shown to have a higher photoactivity compared to the mixed anatase/rutile crystal structure [44–46]. The CdS peaks can also be observed in the XRD of the IH-TiO_2-CdS-Pt. The primary CdS peak (111) overlaps with the anatase TiO_2 peak, but the next CdS peak has no overlap with TiO_2 or metal and can be seen at $2\theta = 43°$. This corresponds to (220) (JCPDS #65-2887). The XRD of the P25-CdS-Pt structure shows the anatase and rutile peaks as well as the peaks for CdS. Since Pt loading is less than 1 wt%, EDS analysis was carried out is required to determine its concentration. The EDS results of all metal loaded IH-TIO_2 were performed over identical areas and the results are shown in Table 1. Recollect that

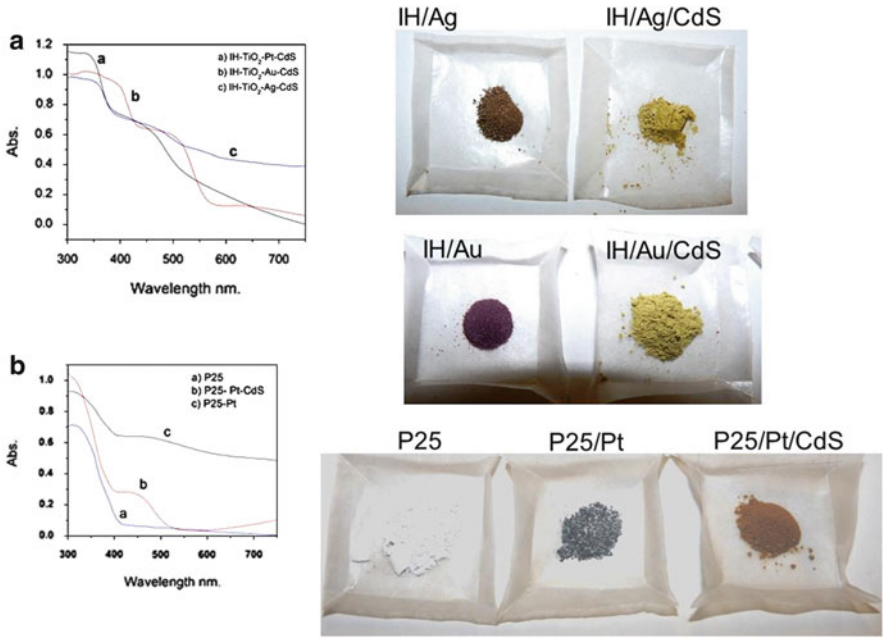

Fig. 2 Diffuse reflectance UV–Visible spectra of other samples prepared in this study are shown. This includes (**a**) IH-TiO_2-based and (**b**) P25-based samples. The photographs of the different samples are also shown in the figure

the metal loading intended during synthesis was ~1 wt% while the EDS tests showed the metal loading was 0.79, 0.85, and 0.81 wt%. This result indicates that the PGM loading is very close to the desired levels.

3.1.3 Diffuse Reflectance

Diffuse reflectance measurements are used to obtain the absorbance profiles of the samples. As shown in Fig. 2, the Pt and CdS deposits appear of the same color on Degussa-P25. The addition of Au nanoparticle turns the IH-TiO_2 to dark red/violet and creates a blue/green composite, while the addition of Ag nanoparticles results in a gray/brown color while CdS addition results in a dark yellow composite. From the EDS data of Table 1 and a comparison of the absorbance of the CdS on IH-TiO_2 with P25, a higher and efficient distribution of CdS on IH-TiO_2 is evident. The pictures and corresponding absorbance spectra of other samples are shown in Fig. 2.

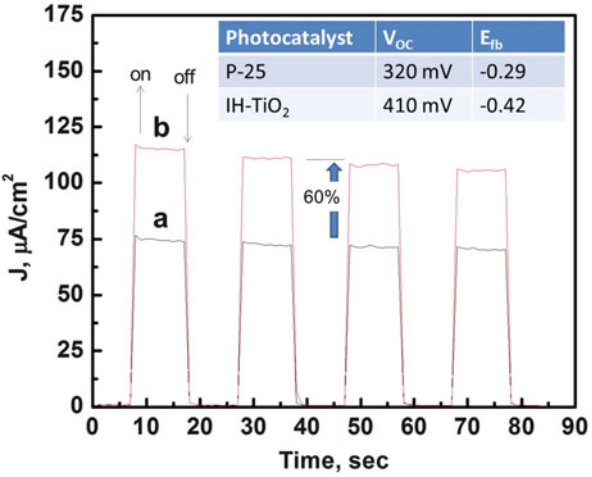

Fig. 3 The photocurrent measurements of the (**a**) commercial (Degussa® P25) and the (**b**) IH-TiO_2 are shown. The *inset* shows the stabilized values of the chronopotentiometry (V_{OC}/t) and the values of the flat band potential E_{fb} for both TiO_2

3.1.4 Photoelectrochemical Analysis

Figure 3 shows a representative *I*/*t* result of the P25 and IH-TiO_2. The insert table shows that both photocurrent and photovoltage are higher with the IH-TiO_2 compared to the P25 for the same loading. This is attributed to the higher surface area provided by the film by virtue of smaller particle sizes. Further, Mott-Schottky analysis indicates that IH-TiO_2 shows a flatband potential of −0.42 V whereas P25 shows a flatband potential of −0.29 V (Fig. 3 insert). The more negative flatband potential for IH-TIO_2 implies the presence of larger band bending at the TiO_2—electrolyte interface aiding better charge separation compared to P25. Thus, both photoelectrochemical measurements indicate the usefulness of the IH-TiO_2 as an effective photocatalyst that promote high charge generation, separation, and available for utilization. The next section examines the applicability of the IH-$TiiO_2$ as a base material for photocatalysis.

3.2 Photocatalytic Hydrogen Generation

The applicability of the composites to photo-assisted hydrogen generation from water has been evaluated by performing slurry-based reactions in the presence of two classes of sacrificial agents: (a) a commonly known sulfur-stabilizing polysulfide as a sacrificial compound—Na_2S,+Na_2SO_3 [47], and (b) a common aquatic pollutant that belongs to the azo-dye family group [14]—methyl orange (MO). These results are discussed below.

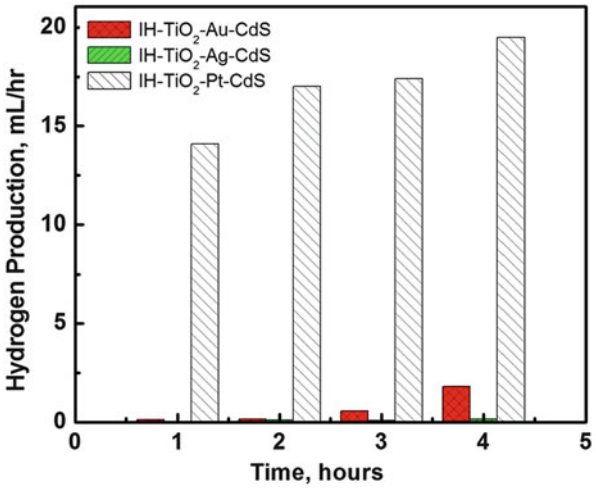

Fig. 4 The hydrogen yield obtained in the presence of the different IH-TiO_2-based photocatalysts with Au, Ag, and Pt followed by CdS deposits. The experiments were conducted in the presence of a polysulfide solution as a sacrificial agent using UV–Vis illumination (Deaeration using N_2 for 30 min, 0.1 M Na_2S + 0.2 M Na_2SO_3)

3.2.1 Photocatalytic Hydrogen Generation with Polysulfide as the Sacrificial Agent

Effects of PGM in IH-TiO_2/*M*/CdS (*M* = Pt,Ag,Au) Photocatalysis

Photocatalytic hydrogen generation was tested with both the metal and the chalcogenide on the IH-TiO_2. As a first screening step, the focus was on the contribution of the PGMs to photocatalytic water splitting. The tests were performed comparing the hydrogen production rates of IH-TiO_2-Pt-CdS, IH-TiO_2-Au-CdS, and IH-TiO_2-Ag-CdS samples in the presence of sacrificial agent (0.1 M Na_2S, 0.02 M Na_2SO_3). The preliminary results shown in Fig. 4 indicate that IH-TiO_2-Pt-CdS had the highest production rate, while IH-TiO_2-Au-CdS was less and IH-TiO_2-Ag-CdS was the lowest. Further, the hydrogen production rate is noted to steadily increase over the duration of the experiment. It is to be noted that during the photocatalysis, the IH-TiO_2-Ag-CdS samples particularly become visibly darker during prolonged irradiation.

Comparison of the Pt-Based Catalysts on Photocatalytic Hydrogen Evolution in DI Water

Since Pt was found to be most favorable among the PGMs, the results discussed here on focus only on Pt. A series of tests were performed comparing the photocatalytic activities of IH-TiO_2-Pt-CdS, IH-TiO_2-CdS, and P25-Pt-CdS. Photocatalytic hydrogen evolution was tested without any sacrificial agent, just

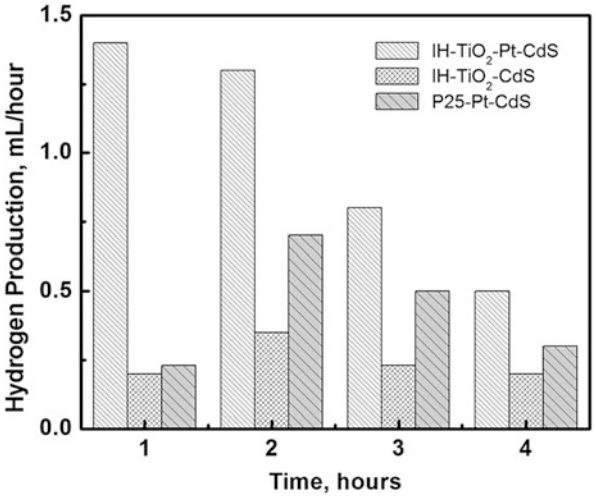

Fig. 5 The hydrogen generation obtained in the presence of the different types of TiO_2 including IH-TiO_2 and P25 containing Pt and CdS deposits. The experiments were conducted in DI water using UV–Vis illumination (500 mg photocatalyst, Deaeration using N_2 for 30 min, No polysulfides were used)

for baseline information. Figure 5 shows the results obtained using these three catalysts. The IH-TiO_2-Pt-CdS has the highest hydrogen production rate of 1.4 mL/h. However, the main aspect to note is the decrease in the hydrogen generation with time. This type of observation is well known as (a) firstly very low water splitting occur without sacrificial agents and (ii) CdS corrosion drives the hydrogen generation albeit for a short duration.

Comparison of the Pt-Based Catalysts on Photocatalytic Hydrogen Evolution in Aqueous Na_2S/Na_2SO_3

The photocatalytic activities of the different IH-TiO_2 supported photocatalysts were further examined in the presence of the Na_2S/Na_2SO_3 (results not shown). It is observed that ~18.5 mL of hydrogen can be produced per hour once the system is operating at a steady state. While overall trend in the catalysts performance is similar to the trend seen in Fig. 5 (i.e., IH-TiO_2-Pt-CdS > P25-Pt-CdS > IH-TiO_2-CdS), two key differences can be observed: (a) at least one-order higher hydrogen generation rate with all the photocatalysts in the presence of Na_2S/Na_2NO_3 and (b) unlike the results in Fig. 5, the hydrogen generation rate does not decrease even after 4 h of continuous illumination. The sacrificial agent is expected to protect the CdS from a predominantly hole-mediated corrosion [48, 49]. Furthermore, the IH-TiO_2-based photocatalyst shows at least a twofold enhancement in hydrogen generation compared to the Degussa P25-based photocatalyst. Thus, in the presence of the polysulfide as a sacrificial agent, the IH-TiO_2-based samples demonstrate a higher photoactivity than the P25-based samples.

3.2.2 Photocatalytic Hydrogen Generation with Methyl Orange as the Sacrificial Agent

Need for Replacing Stabilizers With Pollutants

The presence of Na_2S/Na_2SO_3 is shown to greatly increase the activity of TiO_2 with CdS and Pt. However, using Na_2S/Na_2SO_3 as a sacrificial additive has limitations: it (a) has to be exclusively introduced with the purpose to remove holes to stabilize CdS, (b) will require monitoring on a regular basis as it will be consumed (potentially forming S deposits on CdS) [31], and (c) offers no additional value from an energy production or environmental benefit standpoint. Alternatively, should this additive be a pollutant, the added advantage of its decontamination, besides hole scavenging, can also be realized. The quantum yield under exactly same illumination condition (reactor volume exposed and distance of photocell from light source) is found to be 12.45 %. To test the applicability of a pollutant-assisted photocatalytic hydrogen production in the presence of CdS deposits the organic pollutants MO was used to replace Na_2S/Na_2SO_3.

Photocatalytic Hydrogen Generation in the Presence of MO

MO is a colored compound that belongs to the azo-dye family group and is often used in the textile industry as a dying agent [50]. A significant amount of the unused MO is released as waste into the adjoining water bodies destabilizing the fragile aquatic ecosystem. To mitigate this issue, photodegradation has been considered as a possible pathway to destroy MO [37] and similar colored dyes [51]. MO photodegradation has been well studied by our group [37, 52] as well as by others [53–55].

Blank experiments performed with no photocatalyst and light illumination to examine the photobleaching of MO was carried out and indicated no measureable change (Fig. 6). Figure 7 shows the results of the UV–Vis illumination of a dye solution in the presence of the IH-TiO_2/Pt/CdS composite. The change in the dye concentration was tracked by monitoring the decrease in the peak dye absorbance at 465 nm as shown in Fig. 7a. The conversion of the dye is noted to occur over a period of 50 min of continuous illumination.

Estimation of the Kinetic Parameters

The photodegradation of MO can be fitted to a pseudo first-order rate expression: $-r = k[\mathrm{MO}]^n$, where r is rate of consumption of the MO, [MO] is MO concentration, and n is the order of reaction ($n = 1$) as shown in Fig. 7b. The rate constant values corresponding to the different photocatalysts are reported in Table 1. In studies on hydrogen generation kinetics involving TiO_2/CdS, the focus has been on the hydrogen yield from sulfide-based electrolytes alone [56, 57]. We have chosen to apply the general rigorous approach of using the differential form of the power

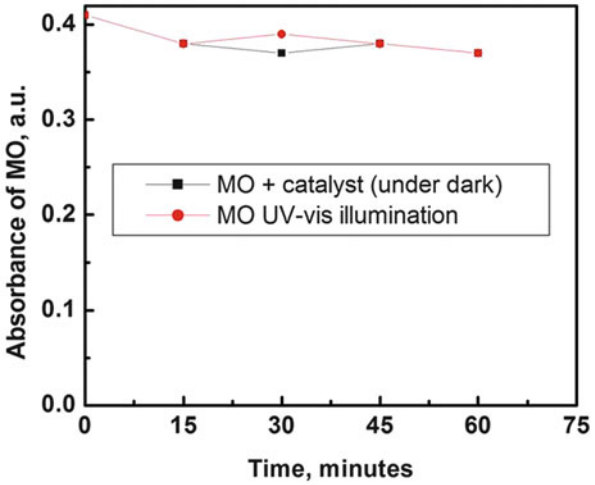

Fig. 6 Baseline experiments to demonstrate activity of MO in the absence of light and absence of photocatalyst

law model [58] to estimate the rate parameters. The hydrogen generation rate is also shown in Table 1. The values are higher with the IH-TiO_2 and are reflective of the trend noted with MO degradation indicating that higher MO degradation leads to greater hydrogen yields.

The rate-limiting step(s) can be any one of the following: dye concentration, catalyst loading, light intensity, or charge transfer from photocatalyst to surrounding electrolyte across the catalyst-electrolyte double layer. In an unrelated system, it has been shown that these parameters can influence photocatalytic reactions and conversion yields [36]. Other parameters such as catalyst size, adsorption mechanism, and light type can also critically influence the photo conversion process in such systems. [59] Performing optimization of these parameters is essential to get deeper insights into the role of each of these contributing factors.

4 Discussions

An analysis of the observations and results presented in Sect. 3 is discussed below.

4.1 Pt, Au, and Ag Noble Metal Ad-Atoms

The addition of a noble metal reduces electron–hole recombination since the metal functions as electron sinks [19, 21, 60]. To facilitate electron–hole separation, three noble metals Ag, Au, and Pt were individually tested and Pt was noted to be the most effective while Au and Ag were less effective. The IH-TiO_2 with Au as well as Ag indicated a gradual change in color following photoillumination. Such a color change

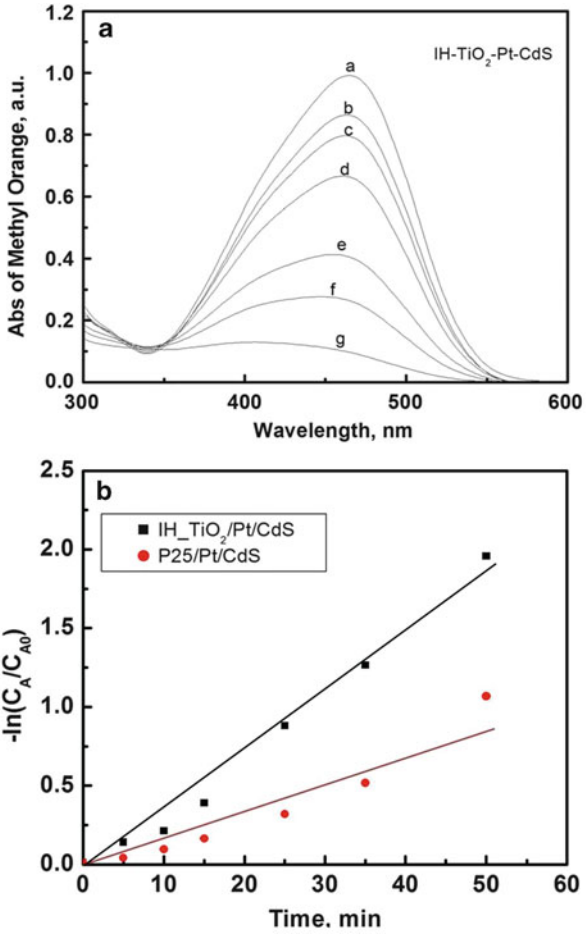

Fig. 7 (**a**) *Top*. The absorbance spectra of the MO solution was monitored at the end of (*a*) 0, (*b*) 5, (*c*) 10, (*d*) 15, (*e*) 25, (*f*) 35, and (*g*) 50 min to determine the fractional conversion of the methyl orange dye during the simultaneous production of hydrogen. (**b**) *Bottom*. A pseudo-first order linearized kinetic model was applied to the absorbance data to determine the rate constant. The linear fit indicates that the photodegradation follows the first order kinetics

indicates possible undesirable side reaction which could be the basis for the observed lowering in photoactivity. In fact, it has been shown that Au at the interface with an oxide semiconductor exists in a dynamic equilibrium with its oxidation states [61–63]. Photogenerated holes oxidize Au while the electron reduce them resulting in the existence of a dynamic equilibrium as shown below [62]:

$$\mathrm{Au} \xrightarrow{nh^+} \mathrm{Au}^{n+} \tag{3}$$

$$\mathrm{Au}^{n+} \xrightarrow{ne^-} \mathrm{Au} \tag{4}$$

Such a dynamic interface can function as trap centers consuming photogenerated electrons and holes resulting in reduced availability of these charges for redox reactions. Likewise, variation in Ag-Ag_2O ratio under illumination in a related study suggests the presence of a dynamic metal–metal ion interface [64]. Further, oxidation of Ag to Ag ions can lead to the formation of Ag_2O or Ag_2S [64–66]. These in situ reactions could decrease the role the Ag particles are expected to play, i.e., preventing e^-/h^+ recombination.

4.2 Mechanism of the Photocatalytic Hydrogen Generation

The UV–Vis illumination will produce electron–hole pairs in the composite across the valence and conduction bands, respectively, of the TiO_2 and CdS. The holes participate in multiple reactions including water oxidation (rxn-1), hydroxyl radical formation (rxn-2), and in the oxidation of the polysulfide (rxn-3) or the pollutant MO/4-CP (rxn-4) resulting in intermediate degradation products. It is to be noted that the oxidizing power of the holes from TiO_2 can lead to the formation of hydroxyl radicals. Every step that participates in hole utilization directly facilitate ensuring the longevity of the CdS deposits on the TiO_2 surface. The favorable energetics between the TiO_2 and CdS allows for the transfer of the photogenerated electrons from the CdS to the TiO_2. Electrons can be drawn to the Pt sites due its electron affinity. These charges will then participate in reactions leading to hydrogen generation (rxn-5). The protons can also yield hydroxyl radicals (rxn-6). The different steps that occur on the composite surface are summarized in Scheme 1.

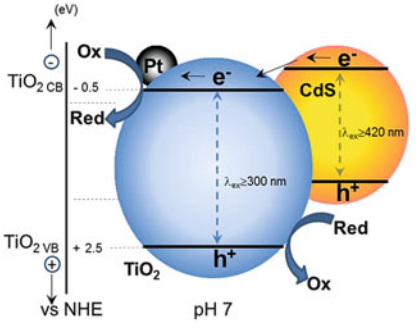

Redox reactions	
$H_2O+2h^+ \rightarrow 2H^+ + ½O_2$	1
$OH + h^+ \rightarrow OH^•$	2
$2S^{2-} + 2h^+ \rightarrow S_2^{2-}$	3
$MO \rightarrow h^+/(OH^•) \rightarrow$ Intermediates	4
$2H^+ + 2e^- \rightarrow H_2$	5
$H^+ + HO_2^• \rightarrow 2OH^•$	6
$O_2 + e^- \rightarrow O_2^{•-}$	7

Scheme 1 The figure shows the process of photocatalytic hydrogen evolution with simultaneous stabilization of the CdS via either hole scavenging by the polysulfides or the pollutant MO. The common redox reactions that occur on the surface of the composite photocatalyst under aerated and deaerated conditions are shown in the adjacent table

5 Conclusion

This work presents a wet chemical approach to synthesis anatase-only TiO_2, incorporate PGMs, and subsequently deposit a chalcogenide to form a unique high surface area nanocomposite. Optical, microstructural, and photoelectrochemical studies have shown that the IH-TiO_2 has a particle size of 20 nm, demonstrates 60 % higher surface area compared to the commercial TiO_2, and exhibits superior photoelectrochemical responses (e.g., 60 % increase in photocurrent) indicating that it is a promising base material for preparing visible light active composites. Among the three PGMs studied for photocatalytic hydrogen generation, Pt of ~0.79 wt% on IH-TiO_2 is noted to be most useful: attributable at least in part to its known stability relative to other PGMs during photocatalysis. MO can be used as a replacement for polysulfide stabilizers with the dual benefit of its photodegradation as well as hydrogen generation. Hydrogen generation with all the catalysts over various time intervals in the presence of MO increases with time.

Acknowledgements RSV thanks the Department of Energy and the Office of the Vice-President for Research at the University of Nevada, Reno junior faculty research startup for funding this project. RSV would also like to thank Degussa® Corporation for samples of P25.

References

1. Ni, M.; Leung, M. K. H.; Leung, D. Y. C.; Sumathy, K., A review and recent developments in photocatalytic water-splitting using TiO2 for hydrogen production. *Renw. Sust. Energy. Rev.* 2007, *11* (3), 401-425.
2. Park, H.; Holt, J. K., Recent advances in nanoelectrode architecture for photochemical hydrogen production. *Energy and Environmental Science* 2010, *3* (8), 1028-1036.
3. Ma, Y.; Xu, Q.; Zong, X.; Wang, D. G.; Wu, G. P.; Wang, X.; Li, C., Photocatalytic H-2 production on Pt/TiO2-SO42- with tuned surface-phase structures: enhancing activity and reducing CO formation. *Energy and Environmental Science* 2012, *5* (4), 6345-6351.
4. Fujishima, A.; Rao, T. N.; Tryk, D. A., Titanium dioxide photocatalysis. *Journal of Photochemistry and Photobiology C* 2000, *1* (1), 1-21.
5. Gerischer, H., Photocatalysis in Aqueous-Solution with Small Tio2 Particles and the Dependence of the Quantum Yield on Particle-Size and Light-Intensity. *Electrochimica Acta* 1995, *40* (10), 1277-1281.
6. Tran, P. D.; Wong, L. H.; Barber, J.; Loo, J. S. C., Recent advances in hybrid photocatalysts for solar fuel production. *Energy and Environmental Science* 2012, *5* (3), 5902-5918.
7. Aroutiounian, V. M.; Arakelyan, V. M.; Shahnazaryan, G. E., Metal oxide photoelectrodes for hydrogen generation using solar radiation-driven water splitting. *Sol. Energy* 2005, *78* (5), 581-592.
8. Tang, J.; Durrant, J. R.; Klug, D. R., Mechanism of Photocatalytic Water Splitting in TiO2. Reaction of Water with Photoholes, Importance of Charge Carrier Dynamics, and Evidence for Four-Hole Chemistry. *Journal of the American Chemical Society* 2008, *130* (42), 13885-13891.
9. Alexander, B. D.; Kulesza, P. J.; Rutkowska, L.; Solarska, R.; Augustynski, J., Metal oxide photoanodes for solar hydrogen production. *J. Mater. Chem.* 2008, *18* (20), 2298-2303.

10. Rajeshwar, K., Hydrogen generation at irradiated oxide semiconductor-solution interfaces. *J. Appl. Electrochem.* 2007, *37* (7), 765-787.
11. Maeda, K.; Domen, K., Photocatalytic Water Splitting: Recent Progress and Future Challenges. *The Journal of Physical Chemistry Letters 1* (18), 2655-2661.
12. Chen, X.; Shen, S.; Guo, L.; Mao, S. S., Semiconductor-based Photocatalytic Hydrogen Generation. *Chem. Rev.* 2010, *110* (11), 6503-6570.
13. Cowan, A. J.; Tang, J.; Leng, W.; Durrant, J. R.; Klug, D. R., Water Splitting by Nanocrystalline TiO2 in a Complete Photoelectrochemical Cell Exhibits Efficiencies Limited by Charge Recombination. *The Journal of Physical Chemistry C 114* (9), 4208-4214.
14. Daskalaki, V. M.; Antoniadou, M.; Li Puma, G.; Kondarides, D. I.; Lianos, P., Solar Light-Responsive Pt/CdS/TiO2 Photocatalysts for Hydrogen Production and Simultaneous Degradation of Inorganic or Organic Sacrificial Agents in Wastewater. *Environmental Science & Technology* 2010, *44* (19), 7200-7205.
15. Lee, Y.-L.; Chi, C.-F.; Liau, S.-Y., CdS/CdSe Co-Sensitized TiO2 Photoelectrode for Efficient Hydrogen Generation in a Photoelectrochemical Cellâ€. *Chem. Mater.* 2009, *22* (3), 922-927.
16. Li, G.-S.; Zhang, D.-Q.; Yu, J. C., A New Visible-Light Photocatalyst: CdS Quantum Dots Embedded Mesoporous TiO2. *Environmental Science & Technology* 2009, *43* (18), 7079-7085.
17. Chiarello, G. L.; Aguirre, M. H.; Selli, E., Hydrogen production by photocatalytic steam reforming of methanol on noble metal-modified TiO2. *Journal of Catalysis 273* (2), 182-190.
18. Awazu, K.; Fujimaki, M.; Rockstuhl, C.; Tominaga, J.; Murakami, H.; Ohki, Y.; Yoshida, N.; Watanabe, T., A Plasmonic Photocatalyst Consisting of Silver Nanoparticles Embedded in Titanium Dioxide. *Journal of the American Chemical Society* 2008, *130* (5), 1676-1680.
19. Choi, H.; Chen, W. T.; Kamat, P. V., Know Thy Nano Neighbor. Plasmonic versus Electron Charging Effects of Metal Nanoparticles in Dye-Sensitized Solar Cells. *ACS Nano 6* (5), 4418-4427.
20. Qi, L.; Yu, J.; Jaroniec, M., Preparation and enhanced visible-light photocatalytic H2-production activity of CdS-sensitized Pt/TiO2 nanosheets with exposed (001) facets. *Physical Chemistry Chemical Physics 13* (19), 8915-8923.
21. Subramanian, V.; Wolf, E. E.; Kamat, P. V., Catalysis with TiO2/gold nanocomposites. Effect of metal particle size on the Fermi level equilibration. *Journal of the American Chemical Society* 2004, *126* (15), 4943-4950.
22. Tada, H.; Mitsui, T.; Kiyonaga, T.; Akita, T.; Tanaka, K., All-solid-state Z-scheme in CdS-Au-TiO2 three-component nanojunction system. *Nat Mater* 2006, *5* (10), 782-786.
23. Peng, Z. A.; Peng, X. G., Formation of high-quality CdTe, CdSe, and CdS nanocrystals using CdO as precursor. *Journal of the American Chemical Society* 2001, *123* (1), 183-184.
24. Robel, I.; Subramanian, V.; Kuno, M. K.; Kamat, P. V., Quantum dot solar cells. Harvesting light energy with CdSe nanocrystals molecularly linked to mesoscopic TiO2 films. *J. Amer. Chem. Soc.* 2006, *128* (7), 2385-2393.
25. Zlateva, G.; Zhelev, Z.; Bakalova, R.; Kanno, I., Precise Size Control and Synchronized Synthesis of Six Colors of CdSe Quantum Dots in a Slow-Increasing Temperature Gradient. *Inorganic Chemistry communication* 2007, *46*, 6212-6214.
26. Kongkanand, A.; Tvrdy, K.; Takechi, K.; Kuno, M.; Kamat, P. V., Quantum dot solar cells. Tuning photoresponse through size and shape control of CdSe-TiO2 architecture. *Journal of the American Chemical Society* 2008, *130* (12), 4007-4015.
27. Weller, H., Quantized Semiconductor Particles - a Novel State of Matter for Materials Science. *Advanced Materials* 1993, *5* (2), 88-95.
28. Li, L. S.; Hu, J. T.; Yang, W. D.; Alivisatos, A. P., Band gap variation of size- and shape-controlled colloidal CdSe quantum rods. *Nano Letters* 2001, *1* (7), 349-351.
29. Park, H.; Choi, W.; Hoffmann, M. R., Effects of the preparation method of the ternary CdS/TiO2/Pt hybrid photocatalysts on visible light-induced hydrogen production. *J. Mater. Chem.* 2008, *18* (20), 2379-2385.

30. Park, H.; Kirn, Y. K.; Choi, W., Reversing CdS Preparation Order and Its Effects on Photocatalytic Hydrogen Production of CdS/Pt-TiO2 Hybrids Under Visible Light. *J. Phys. Chem. C*. 2011, *115* (13), 6141-6148.
31. Daskalaki, V. M.; Antoniadou, M.; Puma, G. L.; kondarides, D. I.; Lianos, P., Solar light-responsive Pt/CdS/TiO2 photocatalysts for hydrogen production and simultaneous degradation of inorganic or organic sacrificial agents in wastewater. *Environmnetal Science and Technology* 2010, *44* (19), 7200-7205.
32. Lu, H. Q.; Zhao, J. H.; Li, L.; Gong, L. M.; Zheng, J. F.; Zhang, L. X.; Wang, Z. J.; Zhang, J.; Zhu, Z. P., Selective oxidation of sacrificial ethanol over TiO2-based photocatalysts during water splitting. *Energy and Environmental Science* 2011, *4* (9), 3384-3388.
33. Kim, J.; Monllor-Satoca, D.; Choi, W., Simultaneous production of hydrogen with the degradation of organic pollutants using TiO2 photocatalyst modified with dual surface components *Energy and Environmental Science* 2012, *5* (6), 7647-7656.
34. Patsoura, A.; Kondarides, D. I.; Verykios, X. E., Enhancement of photoinduced hydrogen prodcution from irradiated Pt/TiO2 suspensions with simultaneous degradation of azo-dyes. *Appl. Catal. B-Environ.* 2006, *64*, 171-179.
35. Jang, J. S.; Choi, S. H.; Kim, H. G.; Lee, J. S., Location and State of Pt in Platinized CdS/TiO2 Photocatalysts for Hydrogen Production from Water under Visible Light. *The Journal of Physical Chemistry C* 2008, *112* (44), 17200-17205.
36. Subramanian, V.; Kamat, P. V.; Wolf, E. E., Mass-transfer and kinetic studies during the photocatalytic degradation of an azo dye on optically transparent electrode thin film. *Industrial & Engineering Chemistry Research* 2003, *42* (10), 2131-2138.
37. Smith, Y.; Kar, A.; Subramanian, V. R., Investigation of Physicochemical Parameters That Influence Photocatalytic Degradation of Methyl Orange over TiO2 Nanotubes. *Industrial & Engineering Chemistry Research* 2009, *48* (23), 10268-10276.
38. Raja, K.; Smith, Y.; Kondamudi, N.; Manivannan, A.; Misra, M.; Subramanian, V., CO2 Photoreduction in the Liquid Phase over Pd-Supported on TiO2 Nanotube and Bismuth Titanate Photocatalysts. *Electrochemical and Solid State Letters* 2010, *14* (5), F5-F8.
39. Mukherjee, B.; Peterson, A.; Subramanian, V., 1D CdS/PbS heterostructured nanowire synthesis using cation exchange. *Chem. Comm.* 2012, *48*, 2415-2417.
40. Jaeger, V.; Wilson, W.; Subramanian, V., Photodegradation of methyl orange and 2,3-butanedione on titanium-dioxide nanotube arrays efficiently synthesized on titanium coils. *Applied Catalysis B: Environmental* 2011, *110* (0), 6-13.
41. Murugesan, S.; Huda, M. N.; Yan, Y.; Al-Jassim, M. M.; Subramanian, V., Band-engineered bismuth titanate pyrochlores for visible light photocatalysis. *J. Phys. Chem. C*. 2010, *114* (23), 10598-10605.
42. Hatchard, C. G.; Parker, C. A., A New Sensitive Chemical Actinometer. II. Potassium Ferrioxalate as a Standard Chemical Actinometer. *Proceedings of the Royal Society of London. Series A. Mathematical and Physical Sciences* 1956, *235* (1203), 518-536.
43. Gomes Silva, C.; Juárez, R.; Marino, T.; Molinari, R.; García, H., Influence of Excitation Wavelength (UV or Visible Light) on the Photocatalytic Activity of Titania Containing Gold Nanoparticles for the Generation of Hydrogen or Oxygen from Water. *Journal of the American Chemical Society* 2010, *133* (3), 595-602.
44. Toyoda, M.; Nanbu, Y.; Nakazawa, Y.; Hirano, M.; Inagaki, M., Effect of crystallinity of anatase on photoactivity for methylene blue decomposition in water. *Applied Catalysis B-Environmental* 2004, *49* (4), 227-232.
45. Sivalingam, G.; Nagaveni, K.; Hegde, M. S.; Madras, G., Photocatalytic degradation of various dyes by combustion synthesized nano anatase TiO2. *Applied Catalysis B-Environmental* 2003, *45* (1), 23-38.
46. Chan, C. K.; Porter, J. F.; Li, Y. G.; Guo, W.; Chan, C. M., Effects of calcination on the microstructures and photocatalytic properties of nanosized titanium dioxide powders prepared by vapor hydrolysis. *Journal of the American Ceramic Society* 1999, *82* (3), 566-572.

47. Jang, J. S.; Ji, S. M.; Bae, S. W.; Son, H. C.; Lee, J. S., Optimization of CdS/TiO2 nano-bulk composite photocatalysts for hydrogen production from Na2S/Na2SO3 aqueous electrolyte solution under visible light (lambda > =420 nm). *Journal of Photochemistry and Photobiology a-Chemistry* 2007, *188* (1), 112-119.
48. Lee, Y.-L.; Chang, C.-H., Efficient polysulfide electrolyte for CdS quantum dot-sensitized solar cells *J. Power Sources* 2008, *185* (1), 584-588.
49. Chakrapani, V.; Baker, D.; Kamat, P. V., Understanding the Role of the Sulfide Redox Couple (S2-/S-n(2-)) in Quantum Dot-Sensitized Solar Cells *J. Amer. Chem. Soc.* 2011, *133* (24), 9607-9615.
50. Baiocchi, C.; Brussino, M. C.; Pramauro, E.; Prevot, A. B.; Palmisano, L.; Marci, G., Characterization of methyl orange and its photocatalytic degradation products by HPLC/UV-VIS diode array and atmospheric pressure ionization quadrupole ion trap mass spectrometry. *International Journal of Mass Spectrometry* 2002, *214* (2), 247-256.
51. Stathatos, E.; Petrova, T.; Lianos, P., Study of the efficiency of visible-light photocatalytic degradation of basic blue adsorbed on pure and doped mesoporous titania films. *Langmuir* 2001, *17* (16), 5025-5030.
52. Kar, A.; Smith, Y. R.; Subramanian, V., Improved Photocatalytic Degradation of Textile Dye Using Titanium Dioxide Nanotubes Formed Over Titanium Wires. *Environmental Science & Technology* 2009, *43* (9), 3260-3265.
53. Arabatzis, I. M.; Stergiopoulos, T.; Andreeva, D.; Kitova, S.; Neophytides, S. G.; Falaras, P., Characterization and photocatalytic activity of Au/TiO2 thin films for azo-dye degradation. *Journal of Catalysis* 2003, *220* (1), 127-135.
54. Bao, N. Z.; Feng, X.; Yang, Z. H.; Shen, L. M.; Lu, X. H., Highly efficient liquid-phase photooxidation of an azo dye methyl orange over novel nanostructured porous titanate-based fiber of self-supported radially aligned H2Ti8O17 center dot 1.5H(2)O nanorods. *Environmental Science & Technology* 2004, *38* (9), 2729-2736.
55. Comparelli, R.; Fanizza, E.; Curri, M. L.; Cozzoli, P. D.; Mascolo, G.; Passino, R.; Agostiano, A., Photocatalytic degradation of azo dyes by organic-capped anatase TiO2 nanocrystals immobilized onto substrates. *Applied Catalysis B-Environmental* 2005, *55* (2), 81-91.
56. Priya, R.; Kanmani, S., Batch slurry photocatalytic reactors for the generation of hydrogen from sulfide and sulfite waste streams under solar irradiation. *Sol. Energy* 2009, *83* (10), 1802-1805.
57. Hatchard, S., N.; Upadhyay, S. N.; Sinha, A. S. K., Kinetics of reduction of water to hydrogen by visible light on alumina supported Pt–CdS photocatalysts. *Int. J. Hydrogen. Energ.* 2009, *24* (1), 130-137.
58. Fogler, H. S.; Gurmen, M. N., *Elements of chemical reaction engineering*. Prentice hall: 2006; Vol. 2nd.
59. Kansal, S. K.; Singh, M.; Sud, D., Studies on photodegradation of two commercial dyes in aqueous phase using different photocatalysts. *Journal of Hazardous Materials,* 2007, *141* (3), 581-590.
60. Tian, Y.; Tatsuma, T., Mechanisms and Applications of Plasmon-Induced Charge Separation at TiO2 Films Loaded with Gold Nanoparticles. *Journal of the American Chemical Society* 2005, *127*, 7632-7637.
61. Lahiri, D.; Subramanian, V.; Shibata, T.; Wolf, E. E.; Bunker, B. A.; Kamat, P. V., Photoinduced transformations at semiconductor/metal interfaces: X-ray absorption studies of titania/gold films. *Journal of Applied Physics* 2003, *93* (5), 2575-2582.
62. Subramanian, V.; Wolf, E. E.; Kamat, P. V., Influence of metal/metal ion concentration on the photocatalytic activity of TiO2-Au composite nanoparticles. *Langmuir* 2003, *19* (2), 469-474.
63. Subramanian, V.; Roeder, R. K.; Wolf, E. E., Synthesis and UV-visible-light photoactivity of noble-metal-SrTiO3 composites. *Industrial & Engineering Chemistry Research* 2006, *45* (7), 2187-2193.

64. Park, M. S.; Kang, M., The preparation of the anatase and rutile forms of Ag-TiO2 and hydrogen production from methanol/water decomposition *Materials Letters* 2008, *62* (2), 183-187.
65. Kuo, Y. L.; Chen, H. W.; Ku, Y., Analysis of silver particles incorporated on TiO2 coatings for the photodecomposition of o-cresol. *Thin Solid Films* 2007, *515* (7–8), 3461-3468.
66. Zhang, W. X.; Zhang, L.; Hui, Z. H.; Zhang, H. M.; Qian, Y. T., Synthesis of nanocrystalline Ag2S in aqueous solution *Solid State Ionics* 2000, *130* (1–2), 111-114.

Stability of the Nanoporous Bismuth Oxide Photoanodes for Solar Water Splitting

Kalyan Chitrada and K.S. Raja

1 Introduction

The search for semiconductor photocatalysts for commercially viable solar water-splitting process still continues in spite of the multidisciplinary research efforts put worth by the international community since the publication of the first report by Fujishima and Honda [1]. The basic requirements of photocatalysts for spontaneous water splitting are: (a) electron energy bandgap around 1.73 eV in order to absorb most of the visible light spectrum and drive the water splitting reaction, (b) appropriate band edge positions relative to the energy levels of the hydrogen and oxygen evolution reactions (OERs), and (c) stable against environmental degradation. Furthermore, the material should have high charge transport properties and low electron–hole recombination losses in order to exhibit high solar-to-hydrogen conversion efficiency.

Several binary transition metal oxides, such as TiO_2 [2], Fe_2O_3 [3], ZnO [4], and WO_3, and higher order mixed oxides [5–7], such as $CaBi_2O_4$ and $BiVO_4$, have been investigated as photo-electrocatalysts for water splitting. Non-oxide-based compound semiconductor materials such as CdTe, CdS, CdSe, and PbS have been investigated widely as photocatalysts individually or as quantum dot sensitizers in combination with oxide materials [8, 9]. If the energy level of the anodic or cathodic decomposition reaction of the semiconductor lies within the energy bandgap, then the material will be prone to photo corrosion [10]. Compound semiconductors that show *n*-type behavior have higher tendency for photo corrosion than their *p*-type counterparts. This phenomenon is attributed to the oxidation reaction of the holes at the surface of the *n*-type semiconductor that acts as a photoanode:

K. Chitrada • K.S. Raja (✉)
Chemical and Materials Engineering, University of Idaho, Moscow, ID 83844, USA
e-mail: ksraja@uidaho.edu

B. Viswanathan et al. (eds.), *Materials and Processes for Solar Fuel Production*,
Nanostructure Science and Technology 174, DOI 10.1007/978-1-4939-1628-3_9

$$MX + zh^{+} \rightarrow M^{z+} + X \quad (1)$$

On the other hand, *p*-type semiconductor materials act as photo cathode where the photo reaction is hydrogen ion reduction. Therefore, in general, the *p*-type material is cathodically protected during solar water splitting. TiO_2 shows higher photo stability than other metal oxide photocatalysts such as Fe_2O_3, ZnO, and WO_3. However, use of TiO_2 is limited by its wider bandgap that absorbs light at wavelengths shorter than 400 nm. Iron oxide is impaired by its short diffusion lengths for holes, and the conduction band minimum positioned at lower than the H_2/H_2O energy level. WO_3 will not be stable in high pH electrolytes. Because no single material is found to possess all the required properties for functioning as a sustainable photocatalyst material for solar water splitting, materials with novel compositions, unique morphologies, and hybrid nanostructures are being investigated.

In order to have highly mobile charge carriers, the widths of the conduction and valence bands require being wide. The chance of scattering of the charge carrier is more when the bandwidth is narrow. Recently the interest on bismuth-based materials is increasing because of the $6s^2$ configuration. Hybridization of Bi 6*s* and O 2*p* orbitals in bismuth oxides results in well-dispersed valence bands that show high mobility of holes [11]. Furthermore, bismuth oxide show high refractive index (2.9) and high dielectric constant that varies from 46 to 190 [12–15]. The high refractive index of the material helps utilize the light effectively for conversion of electron and hole pairs. The high dielectric constant ensures low electrostatic forces between the charge and its trap. Thus, the charge transport properties will be better with a high dielectric material.

Bismuth sesquioxide exists in different polymorphs depending on the synthesis conditions and thermal history. The monoclinic α-Bi_2O_3 is a stable phase at room temperature that shows a bandgap of 2.8 eV with *p*-type semiconductivity. The high temperature β-Bi_2O_3 becomes a metastable phase at room temperature with a tetragonal lattice structure, a bandgap of ~2.5 eV and an *n*-type semiconductivity. In spite of being a non-toxic material with appropriate bandgap and valence band edge position (+3.13 V vs. NHE), Bi_2O_3 shows only a low hydrogen evolution rate due to its lower conduction band edge position (+0.33 V vs. NHE). The general strategies employed to overcome these limitations are simultaneous doping and nano-sizing of the material. Most of the investigations are focused on the β-Bi_2O_3 because of its higher photoactivity than that of other polymorphs. However, being a metastable phase, the stability of the β-Bi_2O_3 is not investigated.

2 Synthesis and Characterization of Bi_2O_3 Polymorphs for Photocatalytic Applications

Yang et al. [12] investigated the photoelectrochemical properties of β-Bi_2O_3 nanoporous films prepared by wet chemical process using $Bi(NO_3)\cdot 5H_2O$ as bismuth source and triton X-100 and citric acid in ethanol as surfactant and complexing agent. The bismuth citrate complex was spin coated onto ITO and heat treated at different temperatures ranging from 350 to 550 °C. The optical absorption edges were observed at 2.7 eV and 3.26 eV. The conduction band minimum was composed of the hybridization of O 2*p* and Bi 6*p*. The two absorption edges could be attributed to the photon electron excitation of O 2*p* → Bi 6*p* and Bi 6*s* → Bi 6*p*. Photocatalytic studies were carried out in 1 M NaOH. IPCE and APCE were calculated at 0 V vs. Ag/AgCl. No photocurrents were reported but the reported IPCE was 10.5 % at 400 nm and 25.5 % at 350 nm.

Bi_2O_3 thin films were obtained by air oxidizing of the magnetron sputtered pure Bi layer at 250 °C for 1–3 h by Yang et al. [13]. The photoelectrochemical (PEC) studies were carried out in 0.5 M Na_2SO_3 solution. The reported photocurrent density was 0.45 mA/cm^2 at 1.23 V_{NHE} for which the reported APCE was 30 %. The onset of the photocurrent occurred at −0.15 V_{NHE}. The bandgap of the air oxidized Bi_2O_3 film increased with the decrease in the thickness (2.63 and 2.88 eV for 500 and 12 nm thickness, respectively).

Nanoporous Bi_2O_3 films were synthesized by electrochemical anodization in 0.3 wt% ammonium sulfate +5.0 wt% DI water in ethylene glycol at 30–50 °C by applying potentials in the range of 10–40 V [14]. The anodization time was 40 min. Water content of the ethylene glycol solution was observed to play a crucial role in the formation nanoporous structure. No regular nanoporous films were formed when the water content was below 4 wt%. The nanopores showed a diameter was as large as 400 nm for 5 wt% water content at 30 °C. Increasing the anodization temperature increased the diameter of the nanopores. The optimized anodization conditions was reported to be 0.3 wt% $(NH_4)_2SO_4$ + 5 wt% water in EG, 20 V, 40 °C, 40 min. The nanoporous Bi_2O_3 film formed under these conditions showed the tetragonal β-Bi_2O_3 phase after annealing at 200 °C. (PFD card 74-1374). Photocurrent measurements were carried out in 0.5 M Na_2SO_4 electrolyte. The observed dark currents were 0.013–0.032 μA/cm^2 at 0 V and 0.5 V_{SCE}, respectively, and photocurrents were 2.893 and 6.98 μA/cm^2 at 0 and 0.5 V_{SCE}, respectively.

Brezensinski et al. [15] synthesized β-Bi_2O_3 in two different routes and compared their properties. Poly(ethylene-co butylene)-block-poly(ethylene oxide) diblock copolymer (referred as KLE) was used as template to grow the nanoporous β-Bi_2O_3 film. Nanofibers of β-Bi_2O_3 were prepared by electrospinning of Bi $(NO_3)\cdot 5H_2O$ dissolved in acetylacetone and 2-methoxyethanol combined with polyvinyl butyral in methanol. All the materials were calcined at 400 °C. The KLE template β-Bi_2O_3 film showed high phase purity and high BET surface area as compared to electrospun β-Bi_2O_3 nanofiber mat. The nanostructure was found to be retained up to 450 °C of calcination. Higher temperature than 450 °C resulted in

restructuring of the nanowires and transformation of β to more stable α-Bi_2O_3. Low temperature calcination at 250 °C required about 12 h for cross linking of the amorphous structure JCPDS card for β-Bi_2O_3: 27-0050. Crystallization was observed to occur at the temperature window of 380–385 °C. The KLE-templated β-Bi_2O_3 showed an optical bandgap of 3.4 eV (~360 nm light) for the samples calcined at 400 °C. The KLE-templated β-Bi_2O_3 showed exceptional photocatalytic activity as compared to the TiO_2 thin film having similar bandgap and similar BET area.

Li et al. [16] reported the photoelectrochemical behavior of DC reactive magnetron sputtered Bi_2O_3 that was annealed at 300 °C for 2 h. PEC studies were carried out using 0.2 M Na_2SO_3 solution. It was observed that the electrode having Bi/Bi_2O_3 configuration showed better photoelectrochemical properties than the Bi_2O_3 electrode. It was suggested that the increased photocurrent density of Bi/Bi_2O_3 was due to the shift in the Fermi level of the Bi_2O_3. Therefore under equilibrium, the contact between Bi and Bi_2O_3 resulted in shift in the Fermi level of the Bi_2O_3. When the Bi_2O_3 was present without a BI substrate, no such Fermi level shift occurred and therefore photocurrent was low.

Qin et al. [17] reported formation of template-free nanotubes of β-Bi_2O_3 by a hydrothermal process of dissolving 0.375 mmol of $Bi(NO_3)_3{\cdot}5H_2O$ and urea (1.35 mmol) in ethylene glycol (25 mL) and heating it to 150 °C for 12 h. If the $Bi(NO_3)_3$/urea influences both the morphology of the final product (sheet vs. nanotube) and the chemistry (stoichiometry). Moreover, ethylene glycol also was found to be critical in achieving the nanotubes. If water was the solvent, then the product was not nanotube. The Bi_2O_3 and $(BiO)_2CO_3$ nanotubes were investigated for their waste water treatment capacity in terms of Cr(VI) ion removal. The Bi_2O_3 NTSs showed strong positive surface charge (zeta potential 38 mV in deionized water). The Cr(VI) adsorption peak showed a maximum at pH 5.0 and decreased at higher and lower pH values. The adsorption was poor at lower pH values ($pH < 3.0$) because of lower pH; the Cr 6+ was presented as uncharged H_2CrO_4. The nanotubular configuration showed higher photocatalytic activity than nanoparticle configuration in terms of photocatalytic degradation of RhB dye.

Schlensinger et al. [18] investigated the relation between the starting bismuth precursor materials and the final product. The starting bismuth precursor was in form of polynuclear bismuth oxide clusters composed of different numbers of $[Bi_6O_{8-X}]_{2(1+x)+}$ units. The polynuclear bismuth oxide clusters were hydrolyzed at room temperature and annealed at temperature lower than 400 °C. The β-Bi_2O_3 prepared by this route showed energy bandgaps between 2.36 and 2.53 eV. The photocatalyst showed promising results in the degradation of rhodamine B (RhB) dye.

Yu et al. [19] reported a simple template-free method for synthesis of flower-like Bi_2O_3 microspheres through a solvothermal process at 200 °C using Bi $(NO_3)_3{\cdot}5H_2O$ dissolved in ethylene glycol. The Bi_2O_3 contained predominantly cubic delta phase. The bandgap was 2.89 eV. The surface area of the nanosphere delta Bi_2O_3 was around 58.2 m^2/g as compared to 0.368 m^2/g of commercial Bi_2O_3 product.

Dutta et al. [20] prepared α-Bi_2O_3 by a simple wet chemical synthetic process by dissolving $Bi(NO_3)_3{\cdot}6H_2O$ in pH 10 solution by NH_4OH addition by high power ultrasonication. The hydrolyzed precipitate was vacuum dried. Doping the Bi_2O_3 with 1.2 % Eu^{3+} and/or 0.8 % Tb^{3+} resulted in β-Bi_2O_3 structure. Addition of PEG in the solution yielded nanorod structure [short chain polymer modified the morphology of final product]. The bandgap of the undoped α-Bi_2O_3 was about 3.81 eV. Doping of two rare earths red shifted the bandgap to 3.56 eV.

Li et al. [21] reported the electronic structure of α-Bi_2O_3 using XPS measurements and DFT calculations. The valence bands of α-Bi_2O_3 showed an energy width of about 7 eV that contained three knee points at binding energies of 2.4, 3.5, and 6.2 eV. In addition to the valence bandwidth, there was additional peak at 11.2 eV that was associated with Bi 6*s* states. The Bi^{3+} possesses an electronic configuration of $5d^{10}\ 6s^2 6p^0$, which prefers asymmetric coordination environment referred to as lone-pair effect. The asymmetry charge distribution was attributed to the interaction between *s* and *p* orbitals of cation and *p* orbitals of the anion.

Lei and Chen [22] calculated surface energies of different termination configurations of α-Bi_2O_3 using ab initio calculations. It is proposed that (010) plane is the most stable and (110) plane is the least stable. The second most stable plane is (111).

Matusumoto et al. [23] investigated the electronic structures of sesquioxides such as As_2O_3, Sb_2O_3, and Bi_2O_3. These oxides form highly distorted structures with large open spaces. The distorted structures are attributed to the presence of "lone pair" electrons in the outer orbital (for Bi^{3+}, it is 6*s*). The electrons were the top of valence band considered to contribute to the localized charge distribution (formation of lone pair). The low symmetry as the result of lone pair formation resulted in the bandgaps and semiconducting behavior of the sesquioxides.

Matsumoto et al. [24] investigated the electronic structures of the Bi_2O_3 by considering different defective configurations of oxide-ion vacancies arranged in different plane. Three possible arrays of vacancy sites of oxygen sublattice were considered aligned along either the <100>, <110>, or <111> direction. The symmetry was lowered by displacing the ions from their ideal lattice positions of cubic fluorite structure. Symmetry breaking in the <100> array model with $2 \times 2 \times 2$ super cell of defective cubic fluorite structure represented the β-Bi_2O_3 structure. The theoretical calculation of the bandgap indicated a value of 1.75 eV. The bandgap is of transition type.

Cheng et al. [11] investigated the electronic structures of the Bi_2O_3 polymorphs. The beta-Bi_2O_3 was synthesized by dissolving $Bi(NO_3)_3{\cdot}5H_2O$ in dilute HNO_3 and the solution was dropwise added to the excessive Na_2CO_3 solution to obtain $Bi_2O_2CO_3$ precipitates. The precipitate was calcined at 380 °C for 10 min to transform the precipitate into β-Bi_2O_3. The BET surface area of the β-Bi_2O_3 particles was 8.55 m^2/g; the room temperature photoluminescent peaks of β-Bi_2O_3 by excitation wavelength at 300 nm were weak indicating efficient charge separation or low charge recombination; the UV–Vis photo spectrum indicated a direct bandgap of 2.48 eV. The crystal structure of β-Bi_2O_3 showed tunnel structure at the center of the lattice. The tunnels are considered to provide the channels for the

transfers of the photogenerated electrons and holes. Moreover, the β-Bi_2O_3 exhibited a dispersive band structure (the width of band was 6 eV) that resulted in faster transfer of electrons and holes.

Xu et al. [25] prepared porous bismuth carbonate microflowers by urea assisted alcoholysis of bismuth nitrate. The as-prepared microflowers had surface area of 120 m^2/g. Upon thermal annealing at 500 °C for 1 h, the bismuth carbonate transformed into α-Bi_2O_3 whose surface area decreased to 25 m^2/g, the morphology also changed from microflowers to micronuts. Since surface area plays a crucial role in most of the catalytic reactions, a UV-irradiation process was developed to increase the surface area. UV irradiation was carried out to make Bi_2O_3 micronuts to rebloom for which the surface area increased from 25 to 95 m^2/g. The calcined α-Bi_2O_3 showed a bandgap value of 2.7 eV and UV-irradiated materials showed a bandgap of 2.4 eV. Furthermore, UV irradiation resulted in O ($2p$)–Bi^{3+} ($6p^0$) excitations and surface O($2p$)-Bi^{5+} ($6s^0$) transitions.

The stability of the Bi_2O_3 photocatalyst is considered to be affected by the oxidation reaction of Bi^{3+}. The Bi^{5+} formation could be attributed to reaction with oxygen in the solution during UV light illumination.

$$Bi^{3+} + 2\,h^+ \rightarrow Bi^{5+} \tag{2}$$

$$2H_2O + 4\,h^+ \rightarrow 4H^+ + O_2 \tag{3}$$

$$Bi_2O_3 + \frac{1}{2}\,O_2 \rightarrow Bi_2O_{4-x} \tag{4}$$

$$O_2 + e^- \rightarrow O^{2-} \tag{5}$$

The photogenerated super-oxide radicals with the strongest oxidation ability and sufficiently long life time can oxidize the Bi^{3+} to Bi^{5+} by forming Bi_2O_{4-x} at the surface.

3 Experimental

In the present investigation, Bi_2O_3 nanoporous films were synthesized by electrochemical anodization of commercial purity bismuth metal in the form of circular discs of 3 mm thick and 12.7 mm diameter in the electrolyte solutions containing 0.3 M citric acid. Anodization was carried out at various potentials ranging from 3 to 60 V for different time durations ranging from 0.5 to 2 h. Based on the morphology, thickness, and PEC behavior, the nanoporous oxides obtained by anodization at 60 V for 30 min were investigated further to evaluate the stability under continuous illumination. After anodization, the samples were thermally annealed at 200, 220, and 240 °C for 2–6 h. The annealing temperature was limited to 240 °C because of the low melting temperature of the bismuth metal substrate which supported the nanoporous bismuth oxide layer. The oxide layer was not

separated from the substrate since the bismuth substrate acted as a current collector for the Bi_2O_3 photoanode during the PEC experiments. It was observed that annealing at 200 °C for up to 6 h showed the presence of mixture of bismuth carbonate oxide ($Bi_2(CO_3)O_2$) and β-Bi_2O_3 phases. The proposed reactions of the formation of bismuth carbonate oxide during the anodization of bismuth in citric acid and further annealing in air can be given as:

Reactions on the anode:

$$Bi \rightarrow Bi^{3+} + 3e^- \tag{6}$$

$$Bi^{3+} + C_6H_8O_7 \rightarrow Bi(C_6H_5O_7) + 3H^+ \tag{7}$$

Reaction on the cathode:

$$3H^+ + 3e^- \rightarrow 3/2\, H_2 \tag{8}$$

During annealing at 200 °C in air:

$$2[Bi(C_6H_5O_7)] + 9O_2 \rightarrow Bi_2(CO_3)O_2 + 11CO_2 + 5H_2O \tag{9}$$

Annealing at 220 °C for 4 h resulted in decomposition of bismuth carbonate oxide phase and formation of predominantly the β-Bi_2O_3 phase, given by the reaction:

$$Bi_2(CO_3)O_2 \rightarrow Bi_2O_3 + CO_2 \tag{10}$$

Annealing at 240 °C resulted in complete disappearance of the bismuth carbonate oxide phase and formation of the metastable β-Bi_2O_3 and α-Bi_2O_3 phases. The effect of having only the β-Bi_2O_3 and mixtures α + β-Bi_2O_3 phases on the photo stability will be discussed in this chapter.

Potentiodynamic, potentiostatic, electrochemical impedance spectroscopy (EIS), and Mott-Schottky analysis studies were carried out with and without illuminated conditions. PEC studies were carried out using a three-electrode configuration with a 7.5 cm^2 flag-shaped platinum counter electrode, and a home-made Ag/AgCl reference electrode [calibrated as 199 mV vs. standard hydrogen electrode (SHE)]. The saturated Ag/AgCl electrode was prepared by anodizing a 1 mm in diameter, 10 cm long silver wire at 5 V for 15 min in a saturated KCl solution. The AgCl coated silver wire was immersed in the saturated KCl solution contained in a plastic pipette. The tip of the saturated KCl solution-filled pipette was sealed by a gel of agar. The agar gel was prepared by dissolving 1 g of agar in 20 mL of saturated KCl solution (~4.83 M at 25 °C) and cooking it at around 80 °C until a gel consistency was obtained. All the potentials in this investigation were measured with reference to the Ag/AgCl electrode dipped in the saturated KCl salt bridge, whose potential was measured to be +46 mV vs. saturated calomel electrode (SCE) at 24 °C and 199 mV vs. SHE. A home-made polyether ether ketone (PEEK) sample holder was used to electrically connect the sample with a potentiostat

(Gamry Instruments, model: Reference 600) by exposing 1 cm^2 of the active surface. The samples were illuminated using a solar simulator (SOLAR Light, Glenside, PA, USA, Model: 16S-300) with a 300 W xenon lamp, and an air mass global 1.5 filter that gave 1-sun intensity (100 mW/cm^2) at appropriate settings. Band pass filters (Edmund Optics) in the range of 400–700 nm at 50 nm intervals were used to obtain action spectra. The intensity of the light was measured using a pyranometer probe (SOLAR Light, USA, model: PMA 2144) and a radiometer (SOLAR Light, USA, model: PMA 2100). The samples were polarized at 0.2 V in 1 M KOH solution for constructing the Tauc plots. Potentiostatic measurements were carried out in 1 M KOH solution at 0.2 V. The photocurrents were recorded by illuminating the samples for 20 min. After 20 min of illumination, EIS measurements were carried out under light and dark (by interrupting the light and equilibrating the samples under dark condition for 20 min) conditions. EIS measurements were carried out under potentiostatic condition of 0.2 V by super imposing an *ac* signal of 10 mV and scanning the frequency from 0.1 MHz down to 0.1 Hz. Mott-Schottky (M-S) measurements were carried out at a frequency (f) of 3,000 Hz by scanning the potential of the sample from 0.5 to −0.6 V at 50 mV steps for every 2 s. The capacitance (C) of the space charge layer was calculated from the imaginary impedance (Z'') using the relation $C = -1/(2\pi f Z'')$. All potentials were applied with reference to an Ag/AgCl reference electrode. After completing the EIS and M-S measurements, the illumination of the sample resumed for another 20 min and the EIS and M-S measurements were repeated. Each 20 min of illumination constituted one cycle. Multiple illumination cycles were carried out on each annealing condition until the photocurrent density decreased to less than 0.05 mA/cm^2.

4 Results and Discussion

Morphology and structure: Figure 1a shows the nanoporous morphology of the oxide layer formed at 60 V for 30 min in citric acid electrolyte in the as-anodized condition. The diameters of the pores were in the range of 20–50 nm and total thickness of the film was less than 500 nm. It was observed that pore diameter and film thickness changed with the annealing at 240 °C for 2 h, as seen in Fig. 1b. Annealing at 240 °C resulted in growth of a thin planar oxide layer. The formation of the top planar layer was considered to occur in three stages: Stage 1. Widening of the rim of the nanopores and formation of oxide ridges; Stage 2. Coalescence of oxide ridges into islands (Fig. 1b); and Stage 3. Spreading of the islands into a thin continuous top layer. Occurrence of the stages 1 and 2 were observed in the samples annealed for 2 and 4 h. The area coverage of the oxide islands increased with annealing time and almost 50 % of the nanoporous oxide layer was covered with a thin top layer after 6 h of annealing. Ultrasonication of the samples in methanol for about 30 s was observed to remove the top oxide layer. The nanoporous oxide layer after removal of the top oxide layer showed almost similar dimensions as that of as

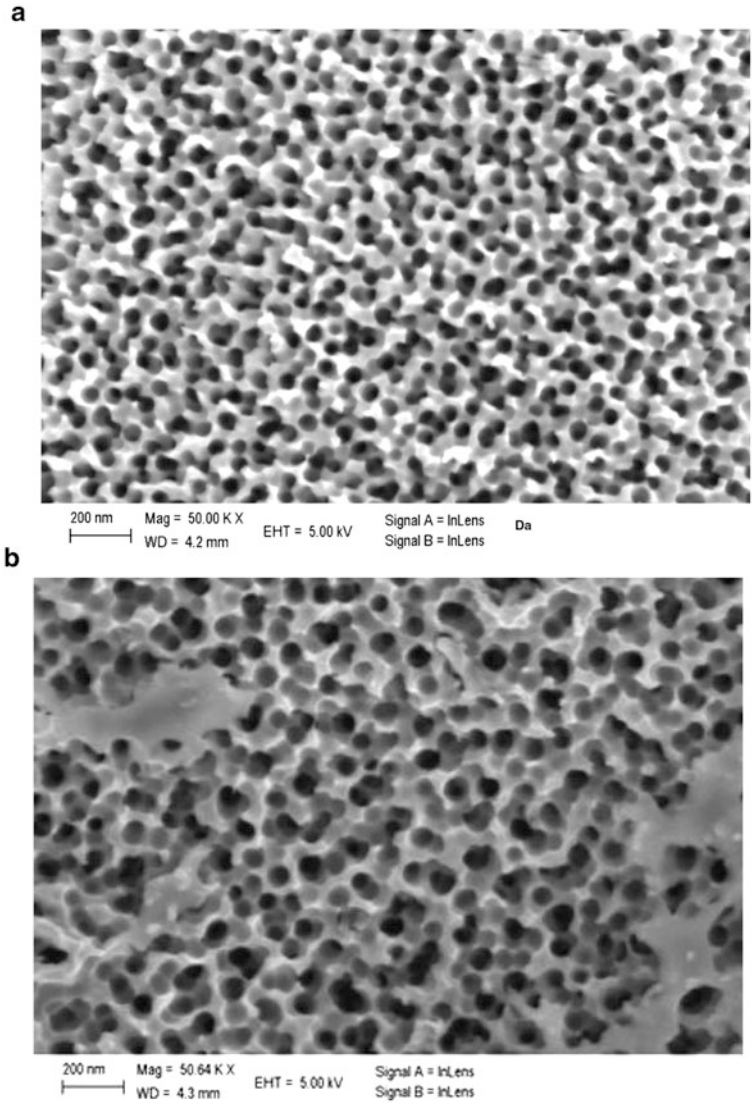

Fig. 1 FESEM images of the nanoporous morphology of the bismuth oxide synthesized by anodization of bismuth at 60 V for 30 min: (**a**) as-anodized condition; and (**b**) annealed at 240 °C for 2 h

anodized condition. Figure 2a, b shows the morphologies of the nanoporous oxide layer after removal of the top planar layer by ultrasonication.

Figure 3 shows the X-ray diffraction patterns of the nanoporous oxide layers after different annealing conditions. The samples annealed at 240 °C for 2 and 4 h showed predominantly β-Bi_2O_3. Annealing for 6 h showed a mixture of beta and

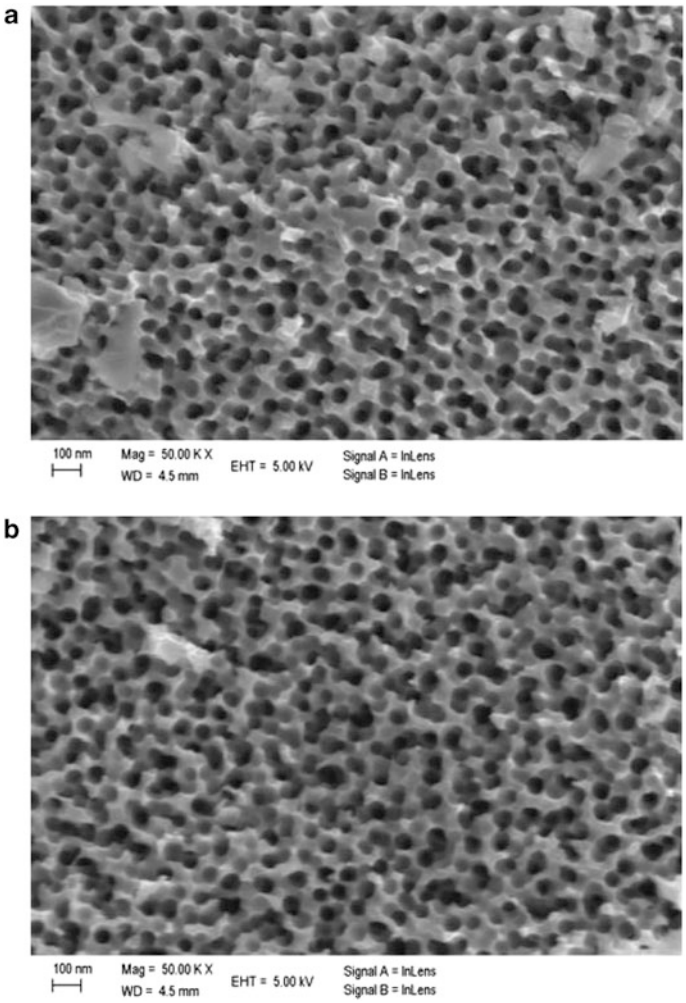

Fig. 2 FESEM images of the nanoporous morphology of the bismuth oxide synthesized by anodization of bismuth at 60 V for 30 min: (**a**) annealed at 240 °C for 4 h; and (**b**) annealed at 240 °C for 2 h

alpha phases of Bi_2O_3. The XRD peaks corresponding to α-Bi_2O_3 were not predominant and the phase content was roughly estimated to be less than 15 %. It should be noted that the α-Bi_2O_3 is considered as a *p*-type semiconductor. The nanopores of Bi_2O_3 containing both $\alpha + \beta$ phases showed enhanced photocatalytic activity that was attributed to an efficient charge separation and charge transfer across the $\alpha - \beta$ phase junction [26]. However, it should be noted that the *p*-*n* junction of $\alpha - \beta$ phases is advantageous for charge separation when used as a photocatalyst under open circuit conditions. When an external bias is applied to the

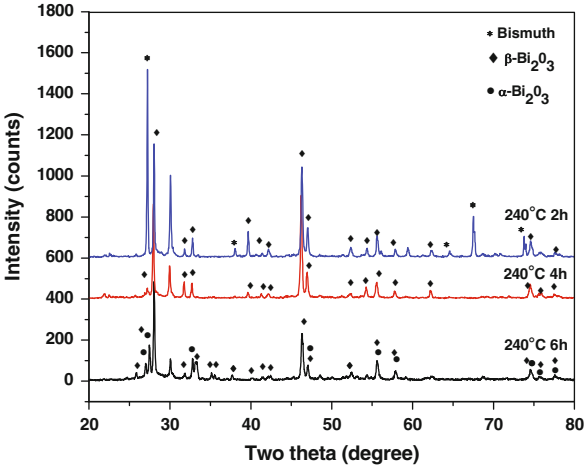

Fig. 3 X-ray diffraction patterns of the nanoporous bismuth oxide synthesized by anodization of bismuth at 60 V for 30 min and annealed at 240 °C for 2, 4, and 6 h. Increasing the annealing time increased the volume fraction of monoclinic α-Bi_2O_3

PEC cell, the presence of the *p-n* junction within a photo electrode (either photoanode or photo cathode) may not be helpful. This is because of the fact that the inherent electric field formed across the *p-n* junctions would be modified by the external applied electric field. How does the presence of *p*-type α-Bi_2O_3 along with β-Bi_2O_3 affect the PEC behavior will be discussed in the subsequent sections.

Optical characteristics: Figure 4 shows the UV–VIS diffuse reflectance spectroscopic results of the nanoporous Bi_2O_3 annealed at 240 °C for 4 and 6 h. A sharp absorbance shoulder was observed to take off at a wavelength of 500 nm corresponding to an energy level of 2.48 eV. This energy level is associated with the bandgap of β-Bi_2O_3. There were additional absorbance shoulders observed at energy levels of 2.8 and 3.02 eV. The absorbance at energy levels of 2.2–3.1 eV is usually attributed to the Bi^{3+} intra-ionic electronic transitions and charge transfer transitions between oxygen ligands and Bi^{3+} ions [27]. The minor absorbance shoulder observed at 2.8 eV could be attributed to the presence of β-Bi_2O_3 phase in the sample annealed at 240 °C for 6 h. The optical absorption coefficient of Bi_2S_3 has been reported to be around 2×10^5 cm^{-1} in the wavelength of 400–700 nm [28]. Similarly, the optical absorption coefficient of Bi_2O_3 has been reported to be in the range of 2×10^4–1×10^5 cm^{-1} in the wavelength range of 600–400 nm [29]. Based on the absorption coefficient, the required thickness of the Bi_2O_3 thin film to harvest the light having wavelengths of 600 nm and 400 nm would be about 5 μm and 1 μm, respectively. The presence of oxygen vacancies has been reported to shift the absorption spectra to longer wavelengths due to excitation of electrons from the donor levels of reduced Bi^{3+} to the conduction band [28].

Figure 5 shows the Raman spectra of the anodic nanoporous Bi_2O_3 annealed at 240 °C for 6 h before and after the PEC testing. The discussion in this section will focus on the Raman spectrum of the sample before the PEC testing. The spectrum consisted of three major Raman bands centered around 457, 312, and 91 cm^{-1}. Hardcastle et al. [30] reported the Raman frequencies of the displacements of

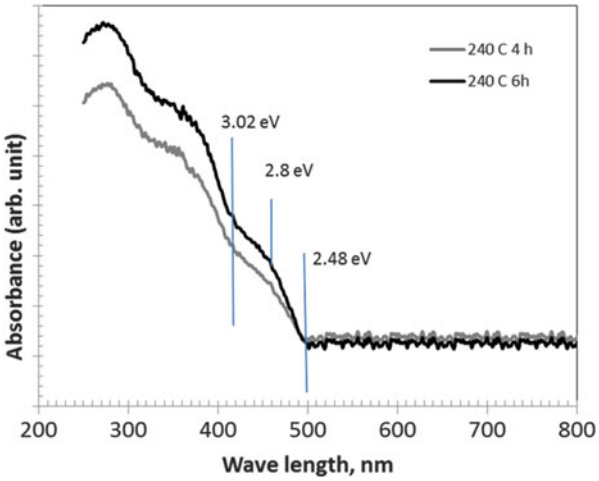

Fig. 4 Optical absorbance spectra (obtained from the UV–VIS diffuse reflectance spectroscopy) of the nanoporous bismuth oxide synthesized by anodization of bismuth at 60 V for 30 min and annealed at 240 °C for 4 and 6 h. Inflections of optical absorbance were observed at three different energy levels indicating optical transitions occurred due to multiple phases. Baseline corrections were applied by comparing the spectrum obtained using barium sulfate

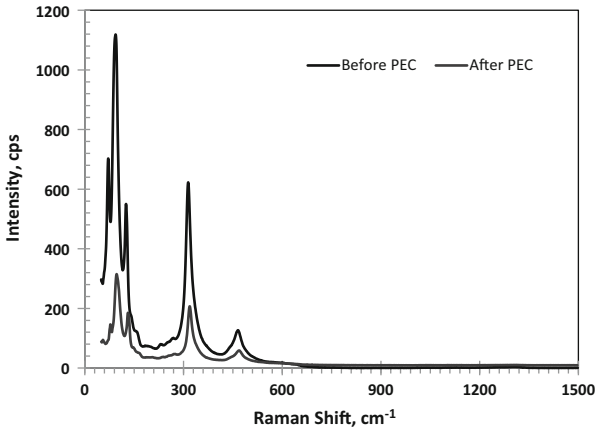

Fig. 5 Raman spectra of the anodic nanoporous Bi_2O_3 annealed at 240 °C for 6 h before and after the photoelectrochemical tests. The change in intensity implies decrease in the thickness of the oxide layer and modification of the surface morphology/roughness

oxygen atoms with respect to the bismuth atom that resulted in stretching of Bi–O bonds in the BiO_6 octahedra to be 462, 311, and 124 cm^{-1}. The Raman frequencies associated with α-Bi_2O_3 are reported to be 212, 278, 335, 410, 445, and 538 cm^{-1}. Based on the reported Raman frequencies, the Raman spectrum of Fig. 5 could be associated with the β-Bi_2O_3 phase. The Raman bands observed at lower frequencies

such as 90 and 70 cm^{-1} could be assigned to the E_g and A_{1g} vibration modes of Bi, respectively [31].

PEC behavior: Figure 6a shows the photocurrent densities of the annealed samples as a function of time under an external bias of 0.2 $V_{Ag/AgCl}$ in 1 M KOH. The observed spikes of the photocurrent density are associated with the starting of a new illumination cycle for every 20 min. The photocurrent decayed exponentially during the first 20 min of illumination. The rate of photocurrent decay was relatively slower in the subsequent 20-min illumination cycle than that of the first 20-min cycle. The sample annealed at 240 °C for 2 h showed slightly better PEC activity than the other two annealed conditions. The samples annealed at 240 °C for 4 h and 6 h showed almost similar decay behavior of photocurrent density. The initial trend of the photocurrent decay of the sample annealed at 240 °C for 6 h is given in Fig. 6b. It can be seen that the "half-life' of the photocurrent (time taken to reach the 50 % of the initial photocurrent density) of the sample was about 600 s. The exponential decay of the photocurrent during initial illumination conditions could be attributed to the faster recombination of electrons and holes. It is known that the photogenerated electrons and holes are separated by the electric field at the space charge layer. The electrons are extracted at the backside of the electrode and available for the hydrogen reduction reaction. The flow of these electrons is recorded as the photocurrent. The holes are consumed at the surface of the nanoporous Bi_2O_3 photoanode through the reaction (3) described in the earlier section. However, it is well established that bismuth-based oxides have low catalytic activity for OER [5, 7, 28]. The slower oxygen evolution kinetics of bismuth oxide resulted in accumulation of holes at the surface and lead to recombination losses. The rate of decay of the photocurrent density observed with the anodic nanoporous Bi_2O_3 was much faster than that of transition metal oxide photo electrodes such as TiO_2, Fe_2O_3, and WO_3.

Since annealing of the nanoporous anodic Bi_2O_3 was carried out in air, it was likely that a thermally oxidized layer could have formed in addition to the anodic oxide layer. The oxide layer due to thermal annealing could form either at the metal/anodic oxide layer interface or on top of the already existing anodic layer, depending on the transport numbers of the Bi^{3+} and O^{2-}. If the growth of the oxide layer is cation transport controlled, then the oxide will grow at the oxide/air interface. It is well known that the δ-Bi_2O_3, a high temperature phase has very high oxygen ion conductivity. Therefore, the air-oxidized layer would be predominantly formed at the metal/oxide interface. This is also evidenced from the predominantly nanoporous morphology of the oxide after annealing. In order to isolate the effect of thermally formed film on the photoactivity of anodic oxide layer, bismuth metal samples were thermally oxidized in air at 240 °C for 2, 4, and 6 h and their photocurrents were measured using the similar procedure followed for the anodic nanoporous oxide samples. Figure 6c shows the current densities of the samples with and without illumination when polarized at 0.2 $V_{Ag/AgCl}$ in 1 M KOH. The 2 h oxidized sample showed higher photocurrent density than the samples oxidized for longer time. Similar results were observed in the case of anodic oxide samples. The dark current density of the thermally oxidized samples (oxidized for

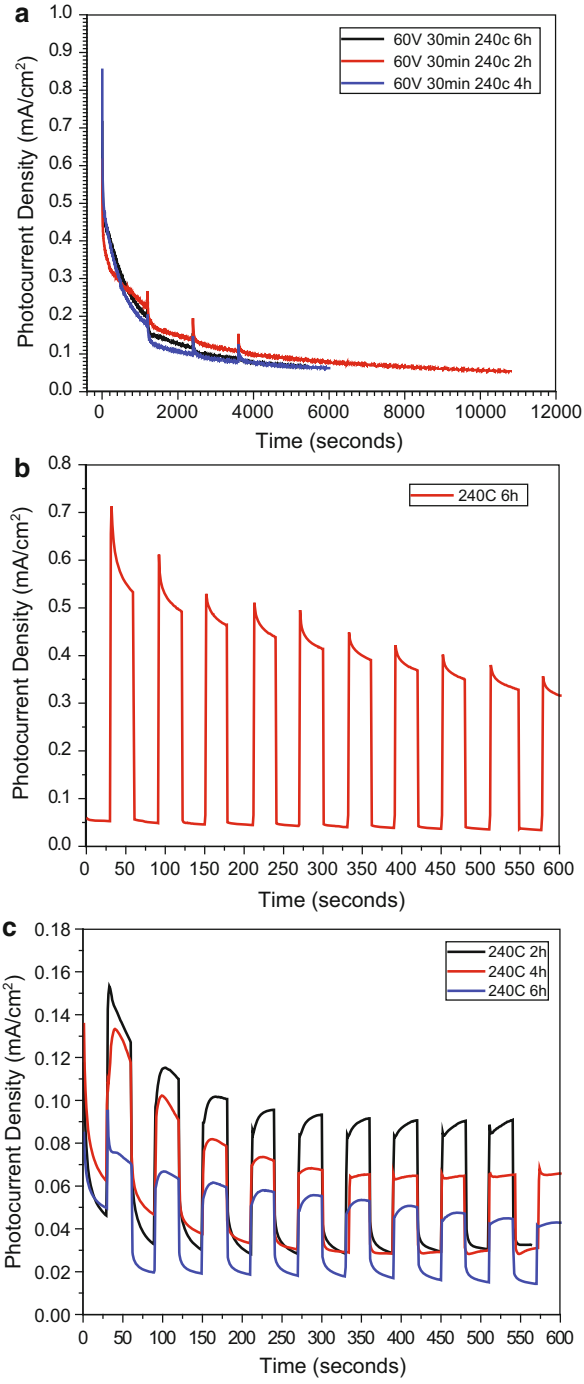

Fig. 6 (**a**) Photocurrent density of the nanoporous anodic Bi_2O_3 annealed at 240 °C for different times. The samples were polarized at 0.2 V Ag/AgCl in 1 M KOH solution and illuminated with a 1-sun intensity simulated solar light. (**b**) Photocurrent and dark current densities of the nanoporous anodic Bi_2O_3 annealed at 240 °C for 6 h. The samples were polarized at 0.2 V Ag/AgCl in 1 M KOH solution and illuminated with a 1-sun intensity simulated solar light. The light was interrupted at regular intervals to record the dark current. (**c**) Photocurrent and dark current densities of the thermally oxidized Bi_2O_3. Thermal oxidation was carried out at 240 °C for 2, 4, and 6 h. The samples were polarized at 0.2 V Ag/AgCl in 1 M KOH solution and illuminated with a 1-sun intensity simulated solar light. The light was interrupted at regular intervals to record the dark current

2 and 4 h) plateaued at around 30 μA/cm^2 which was lower than that of anodic nanoporous oxide (~50 μA/cm^2). The initial photocurrent density of the 2 h thermal oxidized sample was about 0.10 mA/cm^2 which was much lower than that of its anodic oxide counterpart (~0.68 mA/cm^2). After 500 s of illumination, the photocurrent densities of the thermal and anodic oxides were ~0.06 and ~0.36 mA/cm^2, respectively. Initially, both the samples revealed exponential decay of the photocurrent that could be due to accumulation of holes due to poor oxygen evolution kinetics and subsequent recombination losses. Interestingly, after 100 s of exposure to the test solution, the current density increased parabolically after illumination before reaching a steady state or decreasing. The thermally formed bismuth oxide was very thin and planar. Therefore, the surface area available for accumulation of holes was much smaller than that of the anodic nanoporous oxide. Once all the hole trapping sites were occupied, the excess holes generated by continuous illumination were participating in the OER. On the other hand, sites for electron and hole trapping were always available in the anodic oxide because of its large surface area. It is well established that large concentrations of oxygen vacancies and metal cation vacancies are available on the anodic oxide that act as electron and hole trapping sites, respectively. It was observed that the contribution of thermally oxidized layer to the photoactivity of annealed nanoporous anodic oxide was significantly less.

Figure 7a, b compares the surface morphologies of the anodic nanoporous Bi_2O_3 samples before and after the PEC test. It is clear the nanoporous morphology of the oxide layer has significantly changed after the PEC test. Furthermore, selective dissolution of oxide layer could also be observed that manifested into formation of discrete pits. The porosity level of the oxide appeared to have decreased significantly and the morphology of the oxide layer was turning out to be of sintered flakes. Figure 8 shows the Tauc plots of the post-PEC tested samples. The bandgap of the sample annealed at 240 °C for 4 h increased to 2.7 eV and the sample annealed at 240 °C for 6 h showed a bandgap of 2.75 eV. The increase in the bandgap of the samples suggested the possibility of increase in the volume fraction of α-Bi_2O_3. It should be noted that the α-Bi_2O_3 is the stable phase at room temperature whose bandgap is 2.8 eV and that shows *p*-type semiconductivity. Therefore, the exponential decrease in the photocurrent density of the samples containing metastable β-Bi_2O_3 could be attributed to the possible photo-assisted transformation of the α-Bi_2O_3 that had higher bandgap (therefore, harvesting smaller fraction of the simulated sunlight) and different semiconductivity. When *p*-type semiconducting phases are present within the matrix of *n*-type material, several local *p*-*n* junctions would be formed. These junctions would alter the electric field of the space charge layer of the photo electrode and affect the electron–hole separation. Furthermore, the α-Bi_2O_3 present along with the β-Bi_2O_3 could possibly act as traps for the holes. It should be noted that the holes need to be transported to the surface of the photoanode and participate in the water oxidation reaction to evolve oxygen as given in reaction (3). Trapping of holes by the α-Bi_2O_3 would manifest into decrease in the photocurrent. Figure 9 shows the XRD patterns of the post-PEC tested samples. By comparing the XRD results of the

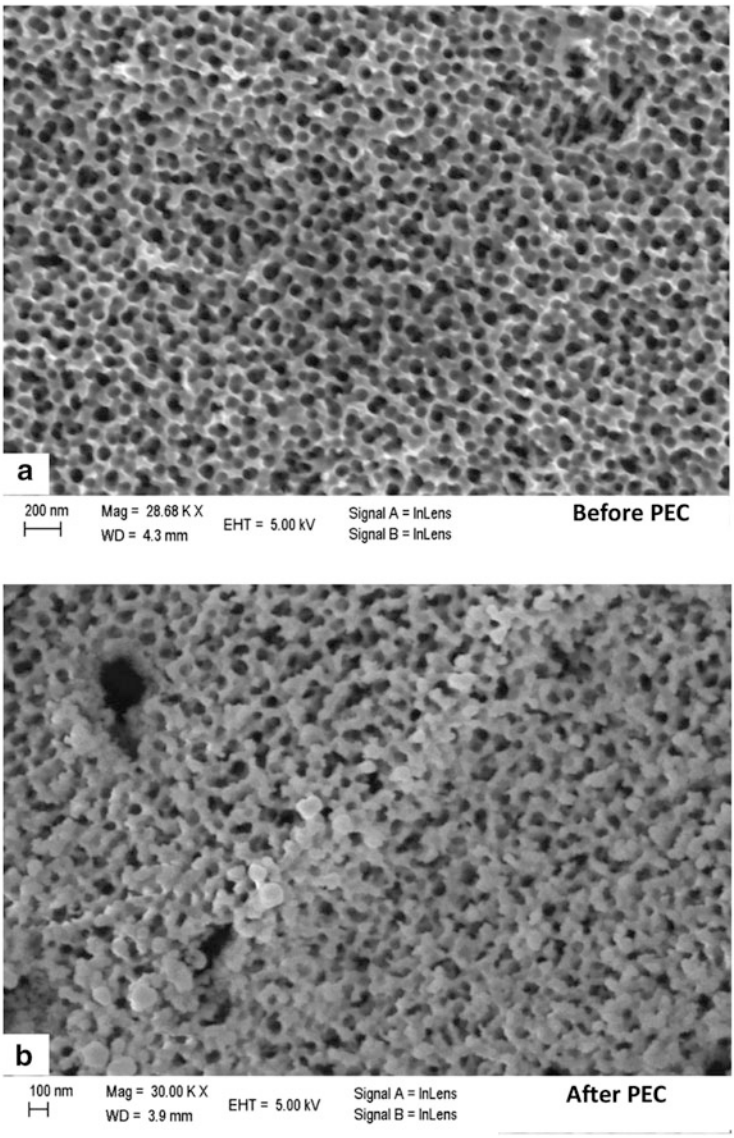

Fig. 7 FESEM images of the nanoporous morphology of the bismuth oxide synthesized by anodization of bismuth at 60 V for 30 min and annealed at 240 °C for 2 h: (**a**) before the PEC testing, and (**b**) after the PEC testing at 0.2 VAg/AgCl in 1 M KOH for ~3 h of illumination

samples before the PEC testing as given in Fig. 3, it was observed that the volume fraction of the α-Bi_2O_3 phase increased significantly after the PEC testing. It can be seen that the sample annealed at 240 °C for 6 h showed about 40 % of α-Bi_2O_3 after the long-term illumination under an external bias potential.

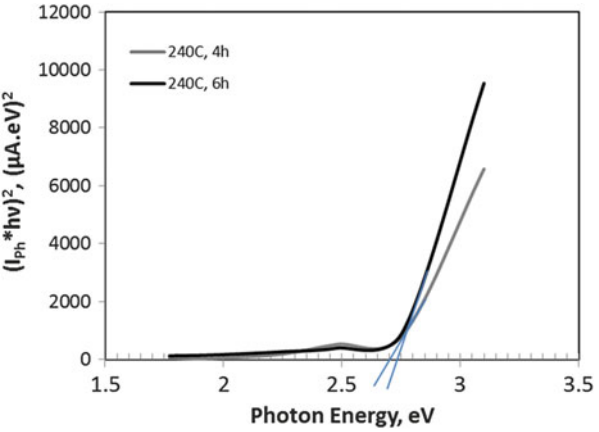

Fig. 8 Tauc plots of the nanoporous anodic Bi_2O_3 annealed at 240 °C for 2 and 4 h after long-term photoelectrochemical experiments. The bandgap values increased from 2.5 to >2.7 eV after >2 h of photo illumination

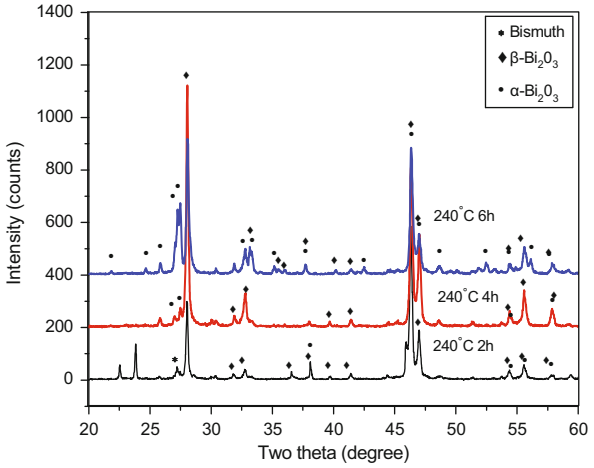

Fig. 9 XRD patterns of the nanoporous anodic Bi_2O_3 annealed at 240 °C for 2, 4, and 6 h after long-term photoelectrochemical experiments

Impedance spectroscopy: Figure 10a, b shows the impedance modulus of the sample annealed at 240 °C for 4 h under dark and illuminated conditions after the end of each 20-min illumination cycles. For comparison, the impedance modulus at 0.01 Hz could be considered. After the first cycle, the impedance under dark condition was about 5×10^4 Ω-cm^2. When illuminated the impedance was about 1.7×10^3 Ω-cm^2. The lower impedance under illumination could be attributed to the increased charge carrier density because of the photogenerated electron–hole pairs. The impedance increased almost by an order of magnitude to 3×10^5 Ω-cm^2 after the second cycle measured under dark condition. This increase in the impedance was commensurate with the significant decay in the photocurrent density between first and second 20-min illumination cycles. The impedance measured after subsequent illumination cycles increased with the number cycles even though the change was not very significant for both dark and illuminated conditions as seen in Fig. 10a, b which followed the trend of the photocurrent decay.

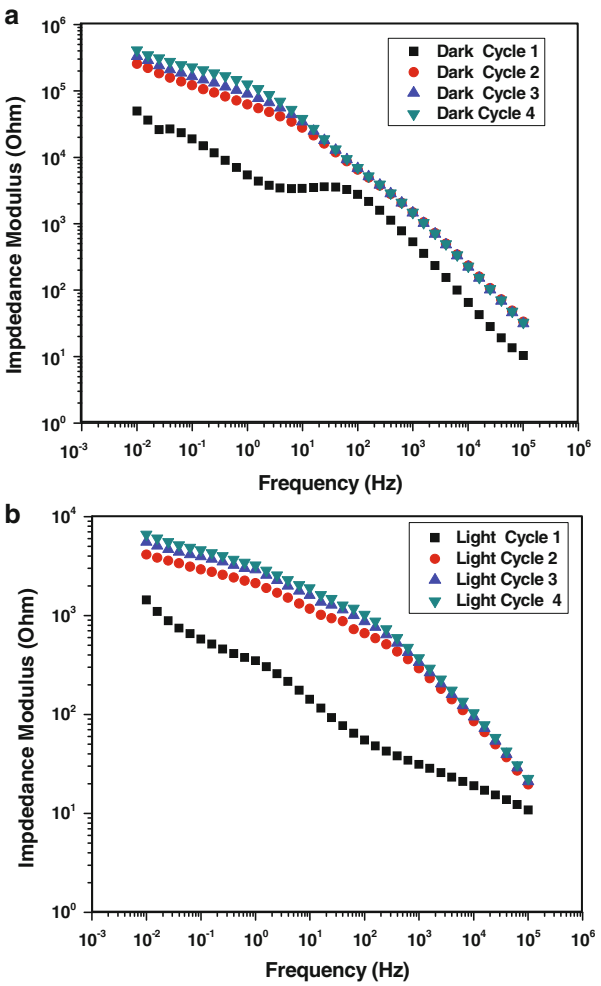

Fig. 10 Electrochemical impedance spectroscopy (Bode plots) of the anodic nanoporous Bi_2O_3 annealed at 240 °C for 4 h in 1 M KOH without (**a**) and with (**b**) illumination

Figure 11a, b shows the Mott-Schottky plots of the sample annealed at 240 °C for 4 h under dark and illuminated conditions, respectively. The plots showed two different regions. The region in the potential range of −0.5 to −0.3 V was considered as low band bending region that showed steeper slopes and hence lower charge carrier densities. The region at higher anodic potentials, considered as high band bending region, showed shallower slopes and therefore higher charge carrier densities. In order to compare the PEC behavior of the different annealed samples, only the low band bending region was considered. Table 1 summarizes the Mott-Schottky results of the sample annealed at 240 °C for 4 h. The flat band potential after cycle 1 under dark condition was −0.53 $V_{Ag/AgCl}$ and the potential shifted to slightly negative potential −0.59 $V_{Ag/AgCl}$ under illuminated condition. It is interesting to note that the flat band potentials of subsequent cycles under

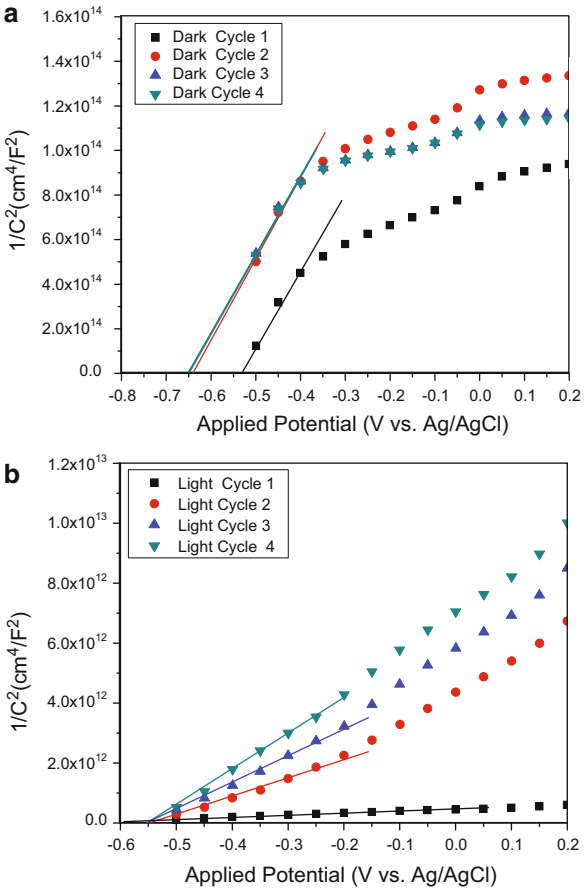

Fig. 11 Mott-Schottky of the anodic nanoporous Bi_2O_3 annealed at 240 °C for 4 h in 1 M KOH without (**a**) and (**b**) with illumination

Table 1 Summary of Mott-Schottky results of the anodic nanoporous Bi_2O_3 sample annealed at 240 °C for 4 h after different illumination cycles

Cycle	Flat band potential $V_{Ag/AgCl}$	Charge carrier density, cm^{-3}
Dark cycle 1	−0.53	9.35×10^{15}
Dark cycle 2	−0.64	8.53×10^{15}
Dark cycle 3	−0.66	9.45×10^{15}
Dark cycle 4	−0.66	9.45×10^{15}
Light cycle 1	−0.59	3.2×10^{18}
Light cycle 2	−0.54	5.56×10^{17}
Light cycle 3	−0.55	3.74×10^{17}
Light cycle 4	−0.55	2.43×10^{17}

Each cycle represents illumination of the sample using 1-sun intensity simulated solar light for 20 min under an applied potential of 0.2 $V_{Ag/AgCl}$ in 1 M KOH

illuminated condition were more positive than the flat band potentials of dark conditions. In fact, the flat band potentials did not change significantly with the increase in the number of illumination cycles.

Significance of the flat band potential: The flat band potential was determined from the intercept of potential axis of the Mott-Schottky plots where $1/C^2 = 0$. The flat band potential for an *n*-type material can be expressed as [32]:

$$E_{FB} = E_C + \Delta E_F + V_H + E_O \tag{11}$$

where E_{FB} is the flat band potential with respect to a reference electrode (Ag/AgCl in this case), ΔE_F is the difference between the Fermi level and majority carrier band edge (E_C), V_H is the potential drop across the Helmholtz layer, and E_O is the scale factor relating the reference electrode redox level to the absolute vacuum scale (−4.7 V for saturated Ag/AgCl). ΔE_F can be calculated using the standard relation:

$$\Delta E_F = kT \ln\left(\frac{N_D}{N_c}\right) \tag{12}$$

where k = Boltzmann constant, T = temperature, N_D = charge carrier density determined from the Mott-Schottky plot, and N_c = effective density of states in conduction band given by the relation:

$$N_c = (7.54\pi)\left(\frac{m_e E}{h^2}\right)^{3/2} \tag{13}$$

where m_e = equivalent mass of electrons, h = Planck's constant, E = energy range of the band considered. The effective mass of electrons in α-Bi_2O_3 is considered as 0.68 times the mass of electron. Considering the effective density of states in conduction band to be around 5×10^{22} cm^{-3}, the ΔE_F can be calculated in potential scale as: 0.4 V in dark condition and about 0.3 V for the illuminated condition. Using the relation (6), one can calculate the position of the conduction band edges of the anodic nanoporous Bi_2O_3 and analyze the energetics of the PEC water splitting process. If the flat band potential is measured at a pH corresponding to zero point of charge (pH_{ZPC}), then the V_H will be zero because of the absence of the absorption at the electrode interface. In case of the Bi_2O_3, the pH_{ZPC} has been reported [33] as 6.2. Therefore, significant adsorption of OH^- would be expected on the surface of the nanoporous oxide layer and the potential drop across the Helmholtz layer should be considered. Since the magnitude of V_H was a strong function of electrolyte and all the experiments were carried out in the same electrolyte, the contribution of V_H was not considered in the calculation of the band edges in this work. This is justifiable because the band edge variation were compared between different annealing conditions of similar material.

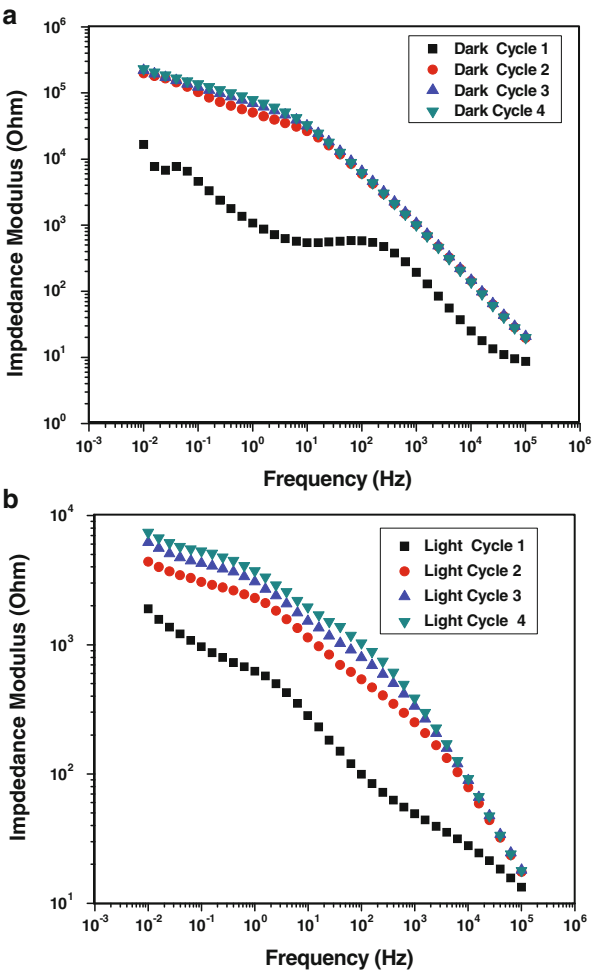

Fig. 12 Electrochemical impedance spectroscopy (Bode plots) of the anodic nanoporous Bi_2O_3 annealed at 240 °C for 6 h in 1 M KOH without (**a**) and with (**b**) illumination

From the positive slope of the Mott-Schottky plots, it can be concluded that the anodic nanoporous Bi_2O_3 showed *n*-type behavior. Therefore, the majority charge carriers will be electrons. The charge carrier density under the dark condition was in the order of 10^{16} cm^{-3}. The charge carrier could be associated with the oxygen vacancies that were inherently formed during anodization. It should be noted that the β-Bi_2O_3 has a distorted fluorite structure with 25 % of ordered vacant oxygen sites along (001) planes [34]. When illuminated, the charge carrier density is increased by almost two orders of magnitude. The charge carrier densities of the samples under the dark and illuminated conditions could be directly correlated with the impedance values. The charge carrier density decreased with the number of cycles under the illuminated condition.

Figure 12a, b illustrates the Bode plots of the anodic nanoporous Bi_2O_3 sample annealed at 240 °C for 6 h under dark and illuminated conditions after each 20-min

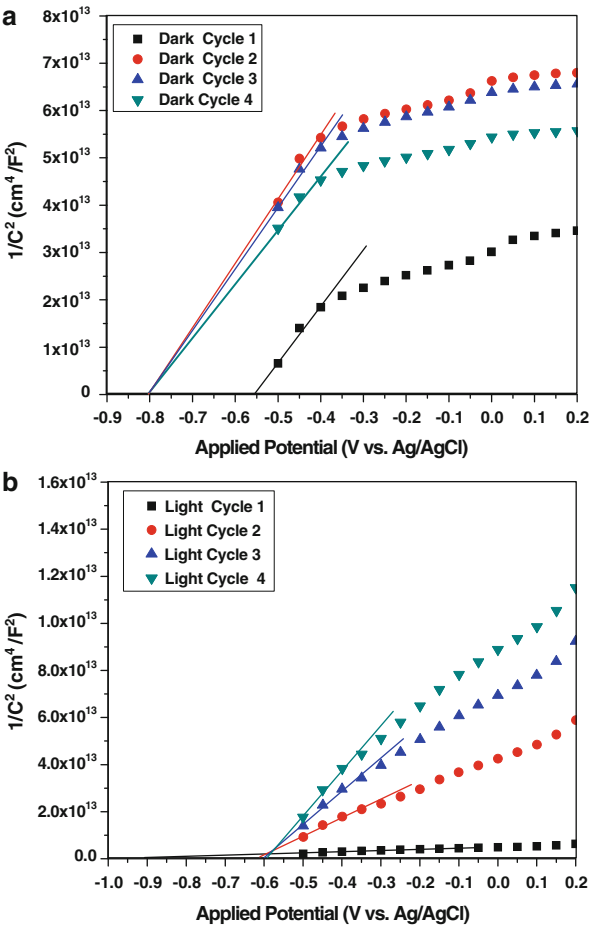

Fig. 13 Mott-Schottky of the anodic nanoporous Bi_2O_3 annealed at 240 °C for 6 h in 1 M KOH without (**a**) and (**b**) with illumination

illumination cycles, respectively. The results are almost similar to those of the samples annealed at 240 °C for 4 h. Figure 13a, b shows the Mott-Schottky results of the sample annealed at 240 °C for 6 h under dark and illuminated conditions. Tables 2 and 3 summarize the Mott-Schottky results of the sample annealed at 240 °C for 6 h and 2 h, respectively. It was observed that the charge carrier density values remained almost similar in spite of different annealing times and variations in the phase contents. Even though the sample annealed for 6 h showed the presence of relatively higher volume fraction of α-Bi_2O_3, the charge carrier density did not vary significantly. Comparing the photocurrent densities of the samples and correlating with the structural and electronic properties, it can be suggested that the charge carrier density influenced the photocurrent more than the phase content of the material. Among the three annealing times, higher photocurrent density was obtained from sample annealed for 2 h. This sample also had the highest charge carrier density and more negative flat band potential. The more negative is the flat

Table 2 Summary of Mott-Schottky results of the anodic nanoporous Bi_2O_3 sample annealed at 240 °C 6 h after different illumination cycles

Cycle	Flat band potential $V_{Ag/AgCl}$	Charge carrier density, cm^{-3}
Dark cycle 1	−0.55	2.58×10^{16}
Dark cycle 2	−0.80	2.24×10^{16}
Dark cycle 3	−0.80	2.44×10^{16}
Dark cycle 4	−0.80	3.01×10^{16}
Light cycle 1	−0.72	3.18×10^{18}
Light cycle 2	−0.61	3.88×10^{17}
Light cycle 3	−0.60	2.24×10^{17}
Light cycle 4	−0.59	1.48×10^{17}

Each cycle represents illumination of the sample using 1-sun intensity simulated solar light for 20 min under an applied potential of 0.2 $V_{Ag/AgCl}$ in 1 M KOH

Table 3 Summary of Mott-Schottky results of the anodic nanoporous Bi_2O_3 sample annealed at 240 °C for 2 h after different illumination cycles

Cycle	Flat band potential $V_{Ag/AgCl}$	Charge carrier density, cm^{-3}
Dark cycle 1	−0.53	1.32×10^{16}
Dark cycle 2	−0.78	2.14×10^{16}
Dark cycle 3	−0.86	2.61×10^{16}
Dark cycle 4	−0.90	3.16×10^{16}
Light cycle 1	−1.26	3.93×10^{18}
Light cycle 2	−0.89	6.40×10^{17}
Light cycle 3	−0.80	3.36×10^{17}
Light cycle 4	−0.75	2.90×10^{17}

Each cycle represents illumination of the sample using 1-sun intensity simulated solar light for 20 min under an applied potential of 0.2 $V_{Ag/AgCl}$ in 1 M KOH

band potential, better will be the PEC activity of the *n*-type electrode. This behavior can be explained using an energy level diagram.

Figure 14 shows the schematic of the potential level diagram illustrating the positions of the Fermi level, and conduction band edge of the anodic nanoporous Bi_2O_3 with reference to the Ag/AgCl electrode. The Fermi level of the material was determined from the flat band potential. The conduction band minimum was observed to be at −3.85 eV with reference to the absolute vacuum scale. The potentials of the hydrogen and OERs pertain to pH:14. It was observed after long-term illumination, the conduction band edge of the sample was below the hydrogen reduction potential indicating requirement of an external bias to split water. Since the valence band was well below the oxygen evolution potential, the holes were energetic for participating in the water oxidation reaction. It should be noted that during the initial period of illumination the flat band potential was negative enough for spontaneous hydrogen reduction reaction. For example, the sample annealed for 2 h (Table 3) showed a flat band potential of −1.2 V during cycle 1. With the continuous illumination, the flat band potential shifted to more

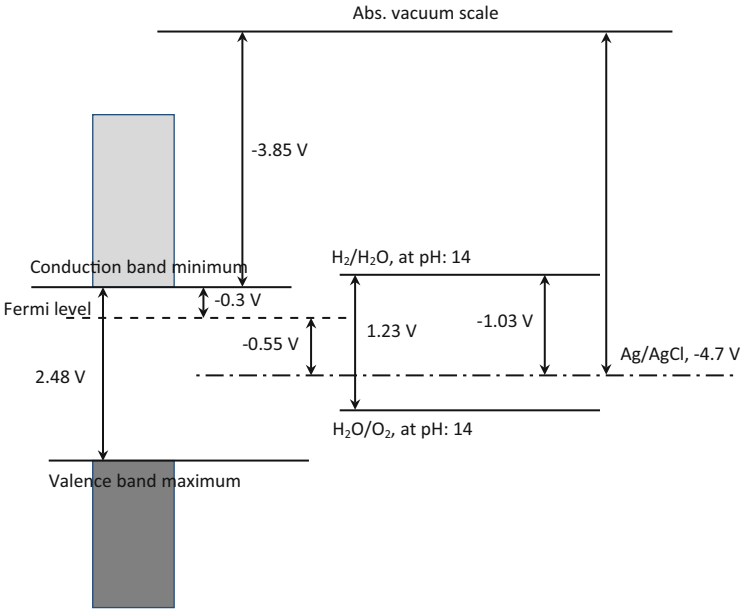

Fig. 14 Schematics of the potential levels of anodic nanoporous Bi_2O_3 in pH:14 solution with reference to absolute vacuum scale and saturated Ag/AgCl electrode. All energy scales were converted to potential scale (1 eV corresponds to 1 V)

positive values. A correlation between the volume fraction of α-Bi_2O_3 and flat band potential could be observed. The flat band potential increased to more positive values with the increase in the α-Bi_2O_3 in the sample.

Photo decomposition: Cathodic decomposition of Bi_2O_3 has been proposed as a mechanism of instability in the photoactivity [35]. The critical cathodic decomposition for Bi_2O_3 in 1 M KOH based on the reaction:

$$Bi_2O_3 + 3H_2O + 6e^- \rightarrow 2Bi(s) + 6OH^- E_O = -0.65\ V_{Ag/AgCl} \quad (14)$$

It is observed that this critical potential is more positive than the observed flat band potentials during initial illumination cycles. Therefore, if the electrode was not anodically polarized, the cathodic decomposition could be a mechanism of instability under illumination at open circuit. In the present investigation, the samples were anodically polarized. Therefore, cathodic decomposition was not thermodynamically possible. The observed decay in the photocurrent density could be attributed to the formation of more stable α-Bi_2O_3 phase that showed *p*-type semiconductivity. In addition, the nanoporous anodic oxide showed possibly low activity for oxygen evolution similar to the behavior reported for $BiVO_4$ [36]. In order to make the anodic nanoporous bismuth oxide layer a practically useful electrode material for water splitting, two modifications could be implemented:

(1) Addition of hole scavengers such as hydrogen peroxide and methanol. The hole scavengers may potentially mitigate accumulation of holes on the nanoporous surface which could increase the photocurrent and hinder photo oxidation of Bi^{3+} to higher valence states. However, the drawback of this approach would be difficult in controlling the electrolyte chemistry in a practical device. Furthermore, addition of hole scavenger would not lead to stoichiometric hydrogen and oxygen evolution by water splitting reaction since the oxygen evolution would still be retarded. (2) The next approach would be provision of a layer of catalyst that promotes OER such as cobalt phosphate, FeOOH, NiOOH, and nickel borate. Deposition of a transparent OER catalyst on the anodic nanoporous bismuth oxide layer would help not only stabilize the photocurrent but also enhance the photoactivity [36].

5 Summary

Thin films of nanoporous bismuth oxide were synthesized by a simple electrochemical anodization of bismuth substrate. Annealing the anodic nanoporous Bi_2O_3 at 240 °C for 2 h resulted in stabilization of the metastable β-Bi_2O_3 phase that showed tetragonal symmetry and *n*-type semiconductivity. Longer annealing times resulted in formation of the more stable α-Bi_2O_3 phase that showed monoclinic lattice structure and *p*-type semiconductivity. The stability of the PEC behavior of the Bi_2O_3 nanoporous structure was observed to be affected by in situ formation of the α-Bi_2O_3 phase during the illumination under an applied bias.

References

1. Fujishima, A.; Honda, K., Electrochemical Photolysis of Water at a Semiconductor Electrode. *Nature* **1972,** *238* (5358), 37-+.
2. Liu, Z.; Pesic, B.; Raja, K. S.; Rangaraju, R. R.; Misra, M., Hydrogen generation under sunlight by self ordered TiO_2 nanotube arrays. *International Journal of Hydrogen Energy* **2009,** *34* (8), 3250-3257.
3. Rangaraju, R.; Panday, A.; Raja, K.; Misra, M., Nanostructured anodic iron oxide film as photoanode for water oxidation. *Journal of Physics D: Applied Physics* **2009,** *42* (13), 135303.
4. Yang, X.; Wolcott, A.; Wang, G.; Sobo, A.; Fitzmorris, R. C.; Qian, F.; Zhang, J. Z.; Li, Y., Nitrogen-Doped ZnO Nanowire Arrays for Photoelectrochemical Water Splitting. *Nano Letters* **2009,** *9* (6), 2331-2336.
5. Kudo, A.; Omori, K.; Kato, H., A Novel Aqueous Process for Preparation of Crystal Form-Controlled and Highly Crystalline $BiVO_4$ Powder from Layered Vanadates at Room Temperature and Its Photocatalytic and Photophysical Properties. *Journal of the American Chemical Society* **1999,** *121* (49), 11459-11467.
6. Tang, J.; Zou, Z.; Ye, J., Efficient Photocatalytic Decomposition of Organic Contaminants over $CaBi_2O_4$ under Visible-Light Irradiation. *Angewandte Chemie International Edition* **2004,** *43* (34), 4463-4466.
7. Rao, P. M.; Cai, L.; Liu, C.; Cho, I. S.; Lee, C. H.; Weisse, J. M.; Yang, P.; Zheng, X., Simultaneously Efficient Light Absorption and Charge Separation in $WO_3/BiVO_4$ Core/Shell

Nanowire Photoanode for Photoelectrochemical Water Oxidation. *Nano Letters* **2014,** *14* (2), 1099-1105.
8. Zhao, Z. B.; Wang, P.; Fan, L. B.; Chen, Z. F.; Yang, D. L., A PbS Film Synthesized by Ultrasonic Wave Assisted Chemical Bath Deposition Method and its Application in Photoelectrochemical Cell. *Advanced Materials Research* **2013,** *820*, 3-6.
9. Mandal, K. C.; Basu, S.; Bose, D. N., Surface-modified CdTe PEC solar cells. *Solar Cells* **1986,** *18* (1), 25-30.
10. Gerischer, H., On the stability of semiconductor electrodes against photodecomposition. *Journal of Electroanalytical Chemistry and Interfacial Electrochemistry* **1977,** *82* (1), 133-143.
11. Cheng, H.; Huang, B.; Lu, J.; Wang, Z.; Xu, B.; Qin, X.; Zhang, X.; Dai, Y., Synergistic effect of crystal and electronic structures on the visible-light-driven photocatalytic performances of Bi_2O_3 polymorphs. *Physical chemistry chemical physics: PCCP* **2010,** *12* (47), 15468-75.
12. Yang, X.; Lian, X.; Liu, S.; Jiang, C.; Tian, J.; Wang, G.; Chen, J.; Wang, R., Visible light photoelectrochemical properties of β-Bi_2O_3 nanoporous films: A study of the dependence on thermal treatment and film thickness. *Applied Surface Science* **2013,** *282*, 538-543.
13. Yang, X.; Lian, X.; Liu, S.; Wang, G.; Jiang, C.; Tian, J.; Chen, J.; Wang, R., Enhanced photocatalytic performance: a β-Bi_2O_3 thin film by nanoporous surface. *Journal of Physics D: Applied Physics* **2013,** *46* (3), 035103.
14. Lv, X.; Zhao, J.; Wang, X.; Xu, X.; Bai, L.; Wang, B., Novel Bi_2O_3 nanoporous film fabricated by anodic oxidation and its photoelectrochemical performance. *Journal of Solid State Electrochemistry* **2013,** *17* (4), 1215-1219.
15. Brezesinski, K.; Ostermann, R.; Hartmann, P.; Perlich, J.; Brezesinski, T., Exceptional Photocatalytic Activity of Ordered Mesoporous β-Bi_2O_3 Thin Films and Electrospun Nanofiber Mats. *Chemistry of Materials* **2010,** *22* (10), 3079-3085.
16. Chunzhi Li, J. Z., Kejia Liu A New Method of Enhancing Photoelectrochemical Characteristics of Bi-Bi_2O_3 Electrode for Hydrogen Generation via Water Splitting. *International Journal of Electrochemical Science* **2012,** *74* (6), 5028-5034.
17. Qin, F.; Li, G.; Wang, R.; Wu, J.; Sun, H.; Chen, R., Template-free fabrication of Bi_2O_3 and $(BiO)_2CO_3$ nanotubes and their application in water treatment. *Chemistry* **2012,** *18* (51), 16491-7.
18. Schlesinger, M.; Schulze, S.; Hietschold, M.; Mehring, M., Metastable beta-Bi_2O_3 nanoparticles with high photocatalytic activity from polynuclear bismuth oxido clusters. *Dalton transactions* **2013,** *42* (4), 1047-56.
19. Yu, Z.; Zhang, J.; Zhang, H.; Shen, Y.; Xie, A.; Huang, F.; Li, S., Facile solvothermal synthesis of porous Bi_2O_3 microsphere and their photocatalytic performance under visible light. *Micro & Nano Letters* **2012,** *7* (8), 814.
20. Dutta, D. P.; Roy, M.; Tyagi, A. K., Dual function of rare earth doped nano Bi_2O_3: white light emission and photocatalytic properties. *Dalton transactions* **2012,** *41* (34), 10238-48.
21. Li, S.; Morasch, J.; Klein, A.; Chirila, C.; Pintilie, L.; Jia, L.; Ellmer, K.; Naderer, M.; Reichmann, K.; Gröting, M.; Albe, K., Influence of orbital contributions to the valence band alignment of Bi_2O_3, Fe_2O_3, $BiFeO_3$, and $Bi_{0.5}Na_{0.5}TiO_3$. *Physical Review B* **2013,** *88* (4).
22. Lei, Y. H.; Chen, Z. X., Density functional study of the stability of various alpha-Bi_2O_3 surfaces. *The Journal of chemical physics* **2013,** *138* (5), 054703.
23. Matsumoto, A.; Koyama, Y.; Togo, A.; Choi, M.; Tanaka, I., Electronic structures of dynamically stable As_2O_3, Sb_2O_3, and Bi_2O_3 crystal polymorphs. *Physical Review B* **2011,** *83* (21), 214110.
24. Matsumoto, A.; Koyama, Y.; Tanaka, I., Structures and energetics of Bi_2O_3 polymorphs in a defective fluorite family derived by systematic first-principles lattice dynamics calculations. *Physical Review B* **2010,** *81* (9).
25. Xu, Z.; Tabata, I.; Hirogaki, K.; Hisada, K.; Wang, T.; Wang, S.; Hori, T., UV-induced formation of activated Bi_2O_3 nanoflake: an enhanced visible light driven photocatalyst by platinum loading. *RSC Advances* **2012,** *2* (1), 103.

26. J. Hou, C. Yang, Z. Wang, W. Zhou, S. Jiao, H. Zhu, In situ synthesis of α-β phase heterojunction on Bi_2O_3 nanowires with exceptional visible-light photocatalytic performance, Appl. Catal. B: Environmental, 2013, 142-143, 504-511
27. M. Vila, C. Diaz-Guerra, J. Piqueras, Laser induced α-δ phase transformation in Bi_2O_3 nanowires, Appl. Phys. Lett., **2012**, 101, 071905.
28. P. M. Sirimanne, K. Takahashi, N. Sonoyama, T. Sakata, Photocurrent enhancement of wide bandgap Bi_2O_3 by Bi_2S_3 over layers, Solar Energy Materials & Solar Cells **2002**, 73, 175-187
29. E. T. Al Waisy, M. S. Al Wazny, Structural, Surface Morphology and Optical Properties of Bi_2O_3 Thin Film Prepared By Reactive Pulse Laser Deposition, J. of university of Anbar for pure science: **201**3, 7(2) 001.
30. F.D. Hardcastle, I.E. Wachs, The molecular structure of bismuth oxide by Raman spectroscopy, J. Solid State Chemistry, 1992, 97, 319-331.
31. L. Kumari, J. H. Lin, Y. R. Ma, Synthesis of Bi oxide nanostructures by PVD, Nanotechnology, **2007**, 18, 295605.
32. Nozik, A.J. and Memming, R. Physical chemistry of semiconductor-liquid interfaces. Journal of Physical Chemistry, **1996**, 100 (31), 13061-13078.
33. Y. Xu, M.A.A. Schoonen, The absolute energy positions of conduction and valence bands of selected semiconducting minerals, American Mineralogist, **2000**, 85, 543-556.
34. Y. Wang, Y. Wen, H. Ding, Y. Shan, Improved structural stability of Ti-doped β-Bi_2O_3 during visible light activated photocatalytic processes, J. Mater. Sci., **2010**, 45, 1385-1392.
35. M. Metikos-Hukoviv, The photoelectrochemical properties of anodic Bi_2O_3 films, Electrochim. Acta, **1981**, 26 (8), 989-1000.
36. T. W. Kim and K.-S. Choi, Nanoporous $BiVO_4$ Photoanodes with Dual-Layer Oxygen Evolution Catalysts for Solar Water Splitting, Science, **2014**, 343, 990-994.

Passivating the Surface of TiO_2 Photoelectrodes with Nb_2O_5 and Al_2O_3 for High-Efficiency Dye-Sensitized Solar Cells

Zhaoyue Liu and Lin Li

1 Introduction

Dye-sensitized solar cells (DSSCs) have been studied extensively in the past two decades [1–8]. An efficiency as high as 12 % has been achieved [9–11]. The photoelectric conversion of the cell is achieved by ultra-fast electron-injection from photoexcited dye into the conduction band of TiO_2, subsequently dye regeneration by I^- and electrons transportation to the counter electrode. Dye-sensitized nanoporous TiO_2 photoelectrode is its heart component. Due to the small size of the TiO_2 particles in the electrode, the space charge layer may not form at the electrode/electrolyte interface [12–15]. So, under illumination, the photo-induced electrons in the conduction band of TiO_2, which are injected from the excited state of the dye, may have two important recombination steps: back-reacting with the oxidized dye and reducing I_3^- to I^-.

Increasing studies into the DSSC are the passivation of the surface of TiO_2 electrode to form man-made energy barriers, which suppress the recombination of the photo-generated electrons and holes and enhance the conversion efficiency of the DSSC. Zaban and co-workers [16, 17] designed energy barriers on the surface of the TiO_2 electrode by using TiO_2/Nb_2O_5 core-shell electrode and found the conversion efficiency was improved by about 35 %. Durrant et al. [18, 19] deposited conformal Al_2O_3 layer on the surface of the TiO_2 electrode and the insulating energy barriers formed. The photo-generated electrons in the excited dye could tunnel the insulating layer and the recombination process was slowed.

Our novel strategy to passivate the surface of TiO_2 photoelectrode was to deposit Nb_2O_5 and Al_2O_3 layer in turn on the surface of the TiO_2 photoelectrode. The

Z. Liu (✉) • L. Li
Key Laboratory of Bio-Inspired Smart Interfacial Science and Technology of Ministry of Education, School of Chemistry and Environment, Beihang University, No. 37 Xueyuan Road, Haidian District, Beijing 100191, China
e-mail: liuzy@buaa.edu.cn

B. Viswanathan et al. (eds.), *Materials and Processes for Solar Fuel Production*, Nanostructure Science and Technology 174, DOI 10.1007/978-1-4939-1628-3_10

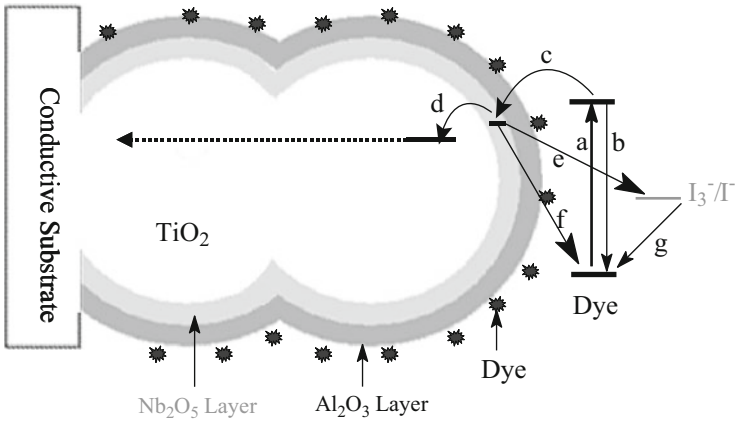

Scheme 1 The structure and the possible electron transfer processes of $TiO_2/Nb_2O_5/Al_2O_3$ electrode sensitized by N3 dye. (**a**) The excitation of the dye. (**b**) The excited dye decay to ground. (**c**) The electrons tunneling the Al_2O_3 layer to the conduction band of the Nb_2O_5. (**d**) The electrons transferring to the conduction band of the TiO_2. (**e**) The recombination of the electrons with electrolyte and (**f**) with excited dye

structure of the electrode and the possible electron transfer process were shown in Scheme 1. We expect our passivation for the TiO_2 electrode could achieve two objectives. (a) The photo-generated electrons tunnel the Al_2O_3 layer from the excited dye to the conduction band of Nb_2O_5 (step c), and the Al_2O_3 layer slows the recombination of the electrons on the conduction band of the Nb_2O_5 with the holes in the excited dye or electrolyte (steps e and f). (b) The photo-generated electrons on the conduction band of Nb_2O_5 transfer rapidly to the conduction of the TiO_2 (step d) and further reduce the recombination of the electrons on the conduction band of the Nb_2O_5 and the holes in the excited dye or electrolyte.

2 Experimental Sections

2.1 Chemicals

All the chemicals are analytic regent grade without specific note and used without further purification. Isopropanol, iodine, calcium oxide, hydrochloric acid, ethanol, sodium sulfate, titanium *n*-butoxide [Ti $(OC_4H_9)_4$] and acetonitrile were purchased from Beijing Chemical Co. Nobium(V) chloride (99.9 + %) and aluminum tri-sec-butoxide [$Al(O^sBu)_3$, 97 %] were purchased from Aldrich. The dye, cis-di (isothiocyanato)-bis(4,4′-dicarboxy-2,2′-bipyridine) ruthenium (II) (N3) was purchased from Solaronix SA. Lithium iodide (anhydrous, 99 %) and 3-methyl-2-oxazolidinone were purchased from Acros. TiO_2 (P25, 20 % rutile and 80 %

anatase) was purchased from Degussa Co. Isopropanol were dried by calcium oxide. Deionized water ($R = 18$ MΩ cm^{-1}) was used in the experiment.

2.2 Preparation of the TiO_2 Electrode

TiO_2 colloid was prepared by the sol–gel method [20]. The mixture of 2 mL of hydrochloric acid, 10 mL of ethanol, and 4 mL of H_2O was added to the solution of 20 mL of Ti $(OC_4H_9)_4$ and 25 mL of ethanol. The as-prepared solution was stirred at 40 °C for 4 h. The concentration of the colloid was about 5.9 wt%.

680 mg of TiO_2 (P25) was added to 3 mL of the TiO_2 colloid and stirred for 12 h, and then a suspension with 17.5 wt% of the TiO_2 content was obtained. A layer of adhesive tape (about 50 μm) was stuck to the four edges of the conducting glass (sheet resistance = 30 Ω/sq, thickness = 3 mm). TiO_2 film thickness was controlled by the tape. The suspension was spread on the conducting glass by glass rod. After dried in air for 30 min, the electrodes were sintered at 450 °C for 30 min.

2.3 Passivating the Surface of the TiO_2 Photoelectrode with Nb_2O_5 and Al_2O_3 Layer, and Assembly of the Solar Cells

The passivation of Nb_2O_5 layer was achieved by dipping the TiO_2 electrode in the 5 mM $NbCl_5$ in the ethanol for 30 s. After sintered at 500 °C for 30 min, the TiO_2/Nb_2O_5 electrode was obtained [16, 17].

Al_2O_3 layer was deposited on the TiO_2/Nb_2O_5 electrode by dipping the electrode in 0.1 M Al $(O^sBu)_3$ in anhydrous isopropanol for 15 min at 60 °C. After rinsing with anhydrous isopropanol thoroughly, the electrode was dried at room temperature and sintered at 450 °C for 30 min [19]. One repetition of the above process, two Al_2O_3 coating layers were prepared. In our experiments, all the electrodes were prepared and sintered in the same batch.

The electrodes were sensitized in 0.5 mM of N3 at room temperature for 14 h and cohered together with a platinized conducting glass [21] by epoxy resin. The electrolyte consisting of 0.5 M LiI/0.05 M I_2 in 1:1 acetonitrile/3-methyl-2-oxazo lidinone (V/V) was admitted by capillary action.

2.4 Instruments

X-ray photoelectron spectroscopy (XPS) was carried on the EscaLab 220-IXL X-ray Photoelectron Spectrum with Al Kα X-ray source (1,486.6 eV).

Scanning electron microscope images (SEM) were taken on a PHILIP XL-30-DS field-emission electron microscope operated at 20 kV voltage.

Electrochemical impedance spectroscopy (EIS) measurements were conducted by a Solartron 1255 frequency response analyzer combined with a Solartron 1286 electrochemical interface (Solartron Farnborough, UK). An IEEE-interface (National Instruments, USA) was employed to couple the two Solartron instruments with a computer. The impedance spectra were recorded using a perturbation signal of 10 mV within the frequency range of 1–10 kHz. The semiconductor electrode acted as the working electrode and the Pt electrode acted as the counter electrode. The reference electrode was the saturated calomel electrode (SCE). The applied bias was at between −0.9 V and 0.7 V. The electrolyte was 0.2 M Na_2SO_4. Zview2 software was used to model the impedance spectra.

Photocurrent–voltage (I–V) curves were recorded by an M273 EG&G Princeton Applied Research Scanning Potentiostat/Galvanostat (EG&G Princeton Applied Research, USA). The effective area of the cell was 0.1 cm^2. A 400 W Xe lamp was used as light source. Its intensity was about 1,000 W/m^2 measured with a radiometer (Photo-electronic Instrument Co. attached to Beijing Normal University, China).

3 Results and Discussion

The SEM image of TiO_2 electrode was shown in Fig. 1. The mean diameter of TiO_2 nanoparticles was about 40 nm, which formed an interconnected network. The electrode experienced high porosity, and the internal surface area of the film was much higher than its geometric surface. This morphology ensured good conductivity and penetration of electrolyte among TiO_2 electrode [22].

Figure 2 shows the XPS of the Nb 3d, Ti 2p, and Al 2p orbits in the $TiO_2/Nb_2O_5/Al_2O_3$ electrodes. The Ti $2p_{3/2}$ and $2p_{1/2}$ band appeared at 458.5 and 464.2 eV, respectively, and existed as Ti^{4+}. The Nb $3d_{5/2}$ band appeared at 206.5 eV and existed as Nb^{5+}. The Al 2p band appeared around 74 eV and existed as Al^{3+}. Because the deposition of the Nb_2O_5 and Al_2O_3 layer on the surface of the TiO_2 electrode were achieved by sintering the electrode at 500 and 450 °C, respectively, for 30 min, the nobium hydroxide and aluminum hydroxide were impossible to exist. The results of XPS confirmed the existence of the TiO_2, Nb_2O_5, and Al_2O_3 contents in this electrode [23].

Figure 3 shows the photocurrent-voltage curves of the TiO_2, TiO_2/Nb_2O_5, and $TiO_2/Nb_2O_5/Al_2O_3$ cell. The short-circuit photocurrent (J_{sc}), open-circuit photovoltage (V_{oc}), filled factor (FF), and photoelectric conversion efficiency (η) of these cells are listed in Table 1. The TiO_2 cell generated a J_{sc} of 14.3 mA/cm^2, a V_{oc} of 0.54 V, an FF of 46 %, and a η of 3.6 %. After passivating with Nb_2O_5 layer, the J_{sc} of TiO_2/Nb_2O_5 cell increased to 15.4 mA/cm^2 and V_{oc} increased to 0.61 V. But the FF decreased to 42 %. As a result, the cell's conversion efficiency increased to 4.0 %. The decrease of the FF may result from the partial blocking of the pores of the nanoporous TiO_2 electrode by the Nb_2O_5 layer, which effected the transport of

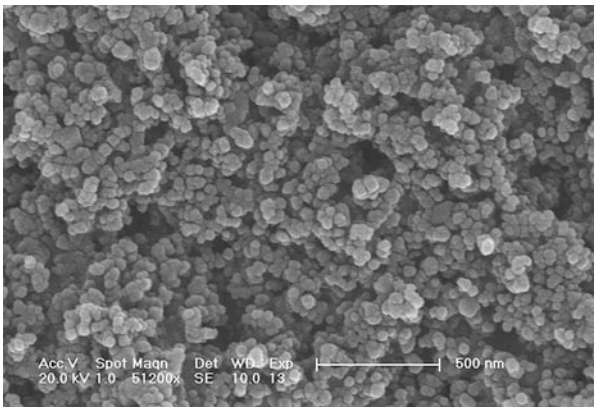

Fig. 1 The SEM image of TiO_2 electrode. The average size of the TiO_2 was about 40 nm

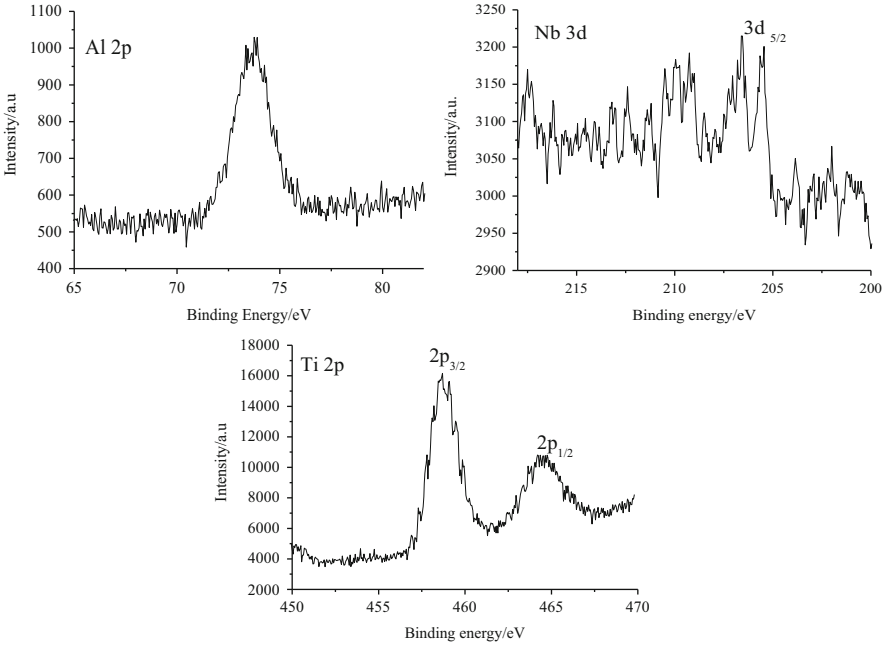

Fig. 2 The XPS spectra of the Ti 2*p*, Nb 3*d*, and Al 2*p* in the $TiO_2/Nb_2O_5/Al_2O_3$ electrode

the ions (I_3^- and I^-) in the electrolyte. After the TiO_2/Nb_2O_5 electrode was coated with Al_2O_3 layer, the J_{sc}, V_{oc}, and η were all improved and increased to 18.3 mA/cm^2, 0.63 V, and 5.0 %, respectively. The FF remained unchanged, which indicated the ultrathin Al_2O_3 layer may not effect the transport of I_3^- and I^- in the electrolyte. The efficiency of the $TiO_2/Nb_2O_5/Al_2O_3$ cell was improved by 25 % comparing with that of the TiO_2/Nb_2O_5 cell. Further increasing the thickness of the Al_2O_3 layer

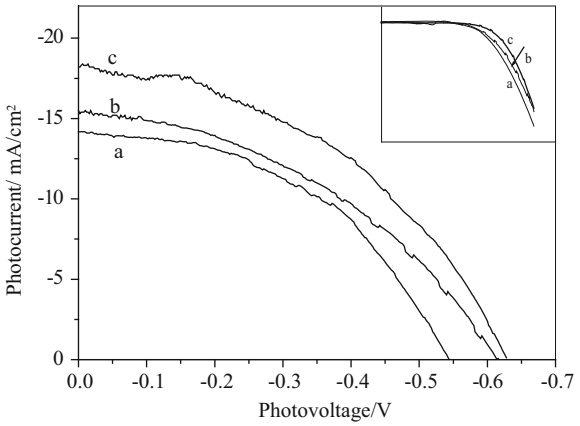

Fig. 3 The photocurrent-voltage curves and the dark current curves (inset) of TiO_2 (**a**), TiO_2/Nb_2O_5 (**b**), and $TiO_2/Nb_2O_5/Al_2O_3$ (**c**) solar cell. The effective area of the cell was 0.1 cm^2. A 400 W Xe lamp was used as a light source. Its intensity was about 1,000 W/m^2

Table 1 The short-circuit photocurrent (J_{sc}), open-circuit photovoltage (V_{oc}), fill factor (FF), and photoelectric conversion efficiency (η) of TiO_2, TiO_2/Nb_2O_5 and $TiO_2/Nb_2O_5/Al_2O_3$ electrode

Solar cell	J_{sc}/mA/cm^2	V_{oc}/V	FF/%	η/%
TiO_2	14.3	0.54	46	3.6
TiO_2/Nb_2O_5	15.4	0.61	42	4.0
$TiO_2/Nb_2O_5/Al_2O_3$	18.3	0.63	43	5.0

by two coating layers, the J_{sc}, V_{oc}, and FF all decreased. As a result, the η decreased. The thicker Al_2O_3 layer suppressed the injection of the photo-generated electrons in the excited dye to the conduction band of the Nb_2O_5.

The dark currents of the TiO_2, TiO_2/Nb_2O_5, and $TiO_2/Nb_2O_5/Al_2O_3$ cell as a function of the applied potentials are shown in the inset of Fig. 3. When the I_3^- ions in the electrolyte penetrate into the porous semiconductor electrode, at specific potential, the electrons in the conduction band of the semiconductor reduce the I_3^- and the dark current generates [24, 25]. Although the measurements of the dark current are not a direct method to detect the recombination process, the comparison of the dark currents of different cells could provide the evidence for the formation of the energy barrier on the surface of the electrode [17]. After the TiO_2 electrode was passivated with Nb_2O_5 layer, the dark current of the TiO_2/Nb_2O_5 cell decreased greatly in the potential ranged from −300 mV to −700 mV. This indicated that the energy barrier formed between TiO_2 and Nb_2O_5, which suppressed the electrons on the TiO_2 conduction band transferring to the electrolyte. When the TiO_2/Nb_2O_5 electrode was coated with Al_2O_3 layer, the dark current of the cell further decreased comparing with that of the TiO_2/Nb_2O_5 electrode. It has been reported that the dark currents were all suppressed in the TiO_2/Nb_2O_5 [16], TiO_2/SnO_2 [13], and TiO_2/Al_2O_3 [18] cell. The suppression of the dark current resulted in the improvement of the photocurrent and the photovoltage of the TiO_2/Nb_2O_5 and $TiO_2/Nb_2O_5/Al_2O_3$ cell.

In order to investigate the influence of the Nb_2O_5 and Al_2O_3 layer on the Helmholtz layer capacitance of the TiO_2 electrode, we measured the impedance

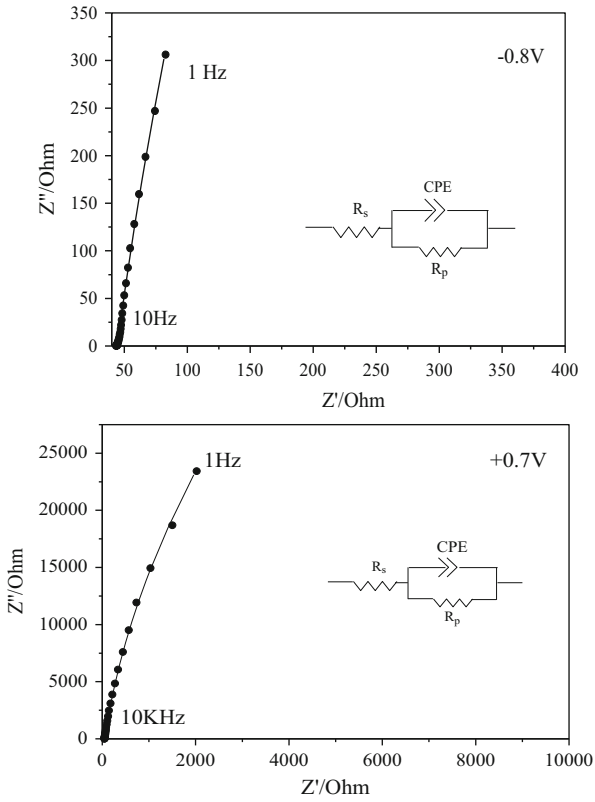

Fig. 4 Nyquist plot of EIS of TiO_2 electrode at −0.8 and +0.7 V (vs. SCE). Experimental data are represented by symbols and the solid lines correspond to the fit. Inset was the equivalent circuit of the TiO_2 electrode. The spectra were measured between 10 kHz and 1 kHz in 0.2 M Na_2SO_4 solutions in the dark

spectra of the TiO_2, TiO_2/Nb_2O_5, and $TiO_2/Nb_2O_5/Al_2O_3$ electrode under different applied biases. Figure 4 shows the two typical impedance spectra (10 kHz to 1 Hz) of the TiO_2 electrode at +0.7 V and −0.8 V potential. The measured spectra resembled the beginning of a larger, slightly depressed semicircle. An equivalent circuit represented in Fig. 4 was used to fit the impedance spectra. Excellent fits were obtained for the TiO_2, TiO_2/Nb_2O_5, and $TiO_2/Nb_2O_5/Al_2O_3$ electrodes at all applied potential. R_s represented the solution resistor and R_p represented the resistance of TiO_2 layer. The constant phase element (CPE) was used to model a parallel circuit of a charge transfer resistor (R) and a Helmholtz layer capacitor (C_{HL}) that have some distribution of time constant (α). The impedance of CPE (Z_{CPE}) was defined as [26]:

$$Z_{CPE} = \frac{R}{[1 + (i\omega C_{HL})^{\alpha}]}$$

Figure 5 represented the calculated Helmholtz layer capacitance of the TiO_2, TiO_2/Nb_2O_5, and $TiO_2/Nb_2O_5/Al_2O_3$ electrode as a function of the applied

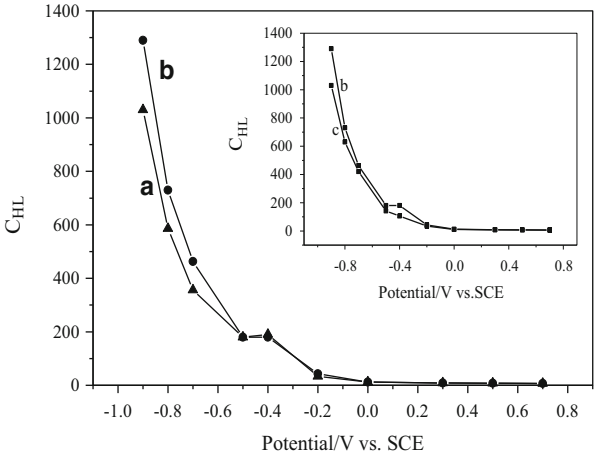

Fig. 5 The calculated Helmholtz layer capacitance (C_{HL}) of the TiO_2 (**a**), TiO_2/Nb_2O_5 (**b**), and $TiO_2/Nb_2O_5/Al_2O_3$ electrode (**c**) as a function of the applied potentials on the electrode. The capacitance was extracted from the impedance spectra using the electrical equivalent circuit

potential. For TiO_2 electrode, when the applied potential scanned from 0.7 V (vs. SCE), the C_{HL} remained a constant at first, followed by a sharp increase at −0.2 V. When the applied potential was positive than −0.2 V, the electrons could not inject into the conduction band of the TiO_2. The surface of the TiO_2 was electrochemically inserted, i.e., the amount of the charge on the surface of the TiO_2 electrode was negligible, so the Helmholtz layer capacitance was very little based on the definition of the capacitance ($C = Q/U$). The measured little capacitance was due to the C_{HL} of the exposed substrate. When the applied potential was negative than −0.2 V, the electrons could inject into the conduction band of the TiO_2. The TiO_2 was changed to be conductive and electrochemically active. It is known that the capacitance is linearly dependent on the surface areas of TiO_2 electrode with electrochemically active. So the Helmholtz layer capacitance increased sharply.

Comparing with TiO_2 electrode, we found that the Helmholtz layer capacitance of the TiO_2/Nb_2O_5 electrode increased at potential negative of −0.5 V and remained unchanged at potential positive of −0.5 V. Because the size of the deposited Nb_2O_5 particles was very small, the Nb_2O_5 layer increased the effective electrochemical active areas of the electrode, which increased the Helmholtz layer capacitance. The difference between the conductions of the TiO_2 and Nb_2O_5 was only 0.1 V [17], so it was difficult to detect the influence of the energy barriers between TiO_2 and Nb_2O_5 on the capacitance of the TiO_2/Nb_2O_5 electrode. After the TiO_2/Nb_2O_5 electrode was coated by Al_2O_3 layer, from Fig. 5, the Helmholtz layer capacitance of $TiO_2/Nb_2O_5/Al_2O_3$ electrode decreased at potential negative of −0.2 V. The Al_2O_3 is a kind of insulator, which reduces effective electrochemical active areas of the electrode. This was a new evidence for the existence of the insulating energy barriers formed by the Al_2O_3.

4 Conclusions

Passivating the surface of TiO_2 electrode was very necessary to optimize the performance of the DSSC. After the TiO_2 electrode was passivated by Nb_2O_5 layer, the efficiency of the TiO_2/Nb_2O_5 cell increased from 3.6 to 4.0 %. The Al_2O_3 layer on the TiO_2/Nb_2O_5 composite electrode further suppressed the generation of the dark current, resulting in 25 % improvement in device performance comparing with that of the TiO_2/Nb_2O_5 cell. The EIS provided the evidences for the formation of the insulating energy barriers by Al_2O_3 on the surface of the TiO_2/Nb_2O_5 electrode.

Acknowledgements This work was supported by the National Key Basic Research Program of China (2011CB935704, 2014CB931803), National Natural Science Foundation of China (21003008), Beijing Natural Science Foundation (2133066), "Young Talents Plan" for the Universities in Beijing City, Fundamental Research Funds for the Central Universities (YWF-14-HHXY-004), and Scientific Research Foundation for the Returned Overseas Chinese Scholars, State Education Ministry of China.

References

1. B. O'Regan, M. Grätzel, A low-cost, high-efficiency solar cell based on dye- sensitized colloidal TiO_2 films, Nature, 353 (1991) 737.
2. M. Grätzel, Photoelectrochemical cells, Nature, 414 (2001) 338.
3. J. Burschka, N. Pellet, S. Moon, R. Humphry-Baker, P. Gao, M. K. Nazeeruddin, M. Grätzel, Sequential deposition as a route to high-performance perovskite-sensitized solar cells, Nature, 499 (2013) 316.
4. A. Yella, H. Lee, H. Tsao, C. Yi, A. K. Chandiran, M. Nazeeruddin, E. Diau, C. Yeh, S. M. Zakeeruddin, M. Grätzel, Porphyrin-sensitized solar cells with cobalt (II/III)-based redox electrolyte exceed 12 percent efficiency, Science, 334 (2011) 629.
5. M. K. Nazeeruddin, A. Kay, I. Rodicicio, R. Humphry-Baker, E. Muller, P. Liska, N. Vlachopoulos, M. Grätzel, Conversion of light to electricity by *cis*-X_2 bis (2, 2-′-bipyridyl-4, 4′-dicarboxylate) ruthenium (II) charge-transfer sensitizers ($X = Cl^-$, Br^-, I^-, CN^-, and SCN^-) on nanocrystalline titanium dioxide electrodes, J. Am. Chem. Soc., 115 (1993) 6382.
6. A. Hagfeldt, M. Grätzel, Light-induced redox reactions in nanocrystalline systems, Chem. Rev., 95 (1995) 49.
7. Z. Y. Liu, K. Pan, Q. L. Zhang, M. Liu, R. K Jia, Q. Lü, D. J. Wang, Y. B. Bai, T. J. Li, The performances of the mercurochrome-sensitized composite semiconductor photoelectrochemical cells based on TiO_2/SnO_2 and ZnO/SnO_2 composites, Thin Solid Film, 468 (2004) 291.
8. Z. Y. Liu, K. Pan, M. J. Wang, M. Liu, Q. Lü, Y. B. Bai, T. J. Li, Influence of the mixed ratio on the photocurrent of the TiO_2/SnO_2 composite photoelectrodes sensitized by mercurochrome, J. Photochem. Photobiol. A: Chem., 157 (2003) 39.
9. Y. Chiba, A. Islam, Y. Watanabe, R. Komiya, N. Koide, L. Han, Dye-sensitized solar cells with conversion efficiency of 11.1 %, Jpn. J. Appl. Phys., Part 2, 45 (2006) L638.
10. F. Gao, Y. Wang, D. Shi, J. Zhang, M. Wang, X. Jing, R. Humphry-Baker, P. Wang, S. M. Zakeeruddin, M. Grätzel, Enhance the optical absorptivity of nanocrystalline TiO_2 film with

high molar extinction coefficient ruthenium sensitizers for high performance dye-sensitized solar cells, J. Am. Chem. Soc., 130 (2008) 10720.
11. M. Grätzel, Dye-sensitized solar cells, J. Photochem. Photobiol. C: Photochem. Rev., 4 (2003) 145.
12. Y. Diamant, S. G. Chen, O. Melamed, A. Zaban, Core-shell nanoporous electrode for dye sensitized solar cells: the effect of the $SrTiO_3$ shell on the electronic properties of the TiO_2 core, J. Phys. Chem. B, 107 (2003)1977.
13. S. Chappel, S.G. Chen, A. Zaban, TiO_2-coated nanoporous SnO_2 electrodes for dye-sensitized solar cells, Langmuir, 18 (2002) 3336.
14. D. Cahen, G. Hodes, M. Grätzel, J. F. Guillemoles, I. Riess, Nature of photovoltaic action in dye-sensitized solar cells, J. Phys. Chem. B, 104 (2000) 2053.
15. L. Kavan, M. Grätzel, S. E. Gilbert, C. Klemenz, H. J. Scheel, Electrochemical and photoelectrochemical investigation of single-crystal anatase, J. Am. Chem. Soc. 118 (1996) 6716.
16. A. Zaban, S. G. Chen, S. Chappel, B. A. Gregg, Bilayer nanoporous electrodes for dye sensitized solar cells, Chem. Commun., 2000, 2231.
17. S. G. Chen, S. Chappel, Y. Diamant, A. Zaban, Preparation of Nb_2O_5 coated TiO_2 nanoporous electrodes and their application in dye-sensitized solar cells, Chem. Mater., 13 (2001) 4629.
18. E. Palomare, J. N. Clifford, S.A. Haque, T. Lutz, J. R. Durrant, Slow charge recombination in dye-sensitised solar cells (DSSC) using Al_2O_3 coated nanoporous TiO_2 films, Chem. Commun., 2002, 1464.
19. E. Palomare, J. N. Clifford, S.A. Haque, T. Lutz, J. R. Durrant, Control of charge recombination dynamics in dye sensitized solar cells by the use of conformally deposited metal oxide blocking layers, J. Am. Chem. Soc., 125 (2003) 475.
20. Z. Liu, K. Pan, M. Liu, M. Wang, Q. Lü, J. Li, Y. Bai, T. Li, Electrochim. Acta, 50 (2005) 2583.
21. N. Papageorgiou, W. F. Maier, M. Grätzel, An iodine/triiodide reduction electrocatalyst for aqueous and organic media, J. Electrochem. Soc., 144 (1997) 876.
22. X. T. Zhang, I. Sutanto, T. Taguchi, K. Tokuhiro, Q. B. Meng, T. N. Rao, A. Fujishima, H. Watanabe, T. Nakamori, M. Uragami, Al_2O_3-coated nanoporous TiO_2 electrode for solid-state dye-sensitized solar cell, Sol. Energy Mater. Sol. Cells, 80 (2003) 315.
23. The reference value of the binding energy: Ti^{4+} (TiO_2) $2p_{1/2}$ 464.2 eV, $2p_{3/2}$ 458.5 eV. Nb^{5+} (Nb_2O_5) $3d_{5/2}$ 207.3 eV. Al^{3+}(Al_2O_3) 2p 74.7 eV. Handbook of the X-ray Photoelectron Spectroscopy, Perkin Elmer Corporation, Published by Physical Electronics.
24. M. L. Rosenblut, N. S. Lewis, " Ideal" behavior of the open circuit voltage of semiconductor/liquid junctions, J. Phys. Chem., 93 (1989) 3735.
25. A. Kumer, P. G. Santangelo, N. S. Lewis, Electrolysis of water at strontium titanate ($SrTiO_3$) photoelectrodes: distinguishing between the statistical and stochastic formalisms for electron-transfer processes in fuel-forming photoelectrochemical systems, J. Phys. Chem., 96 (1992) 835.
26. A. Zaban, A. Meier, B. A. Gregg, Electric potential distribution and short-range screening in nanoporous TiO_2 electrodes, J. Phys. Chem. B., 101(1997) 7985.

Reduction of Carbon Dioxide: Photo-Catalytic Route to Solar Fuels

B. Viswanathan

1 Introduction

It is known that earth receives nearly around 4.3×10^{20} J/h of energy while the requirement of energy for the earth is around 4.7×10^{16} J/h and thus showing that if one can harness 1 h energy from sun, it will be sufficient for nearly 9,200 h of energy needs of the earth or nearly the energy need for more than 1 year. These figures on the so-called freely available energy source, namely solar energy are always tempting for the greedy human beings. However, there is always a catch in anything that is available for free so also solar energy. Scientific methodologies have been devised for harnessing solar energy in a variety of ways; one of them is using solar energy for the conversion of waste products like carbon dioxide into value-added chemicals and fuels. It must be remembered that the reduction of carbon dioxide with water to give typical fuel like methanol and oxygen is an uphill process involving free energy change of +689 kJ/mol while for the reaction of water to produce fuel hydrogen and oxygen involves a free energy change of +457.2 kJ/mol, thus implying that the effort of converting waste product experiences greater barrier as compared to conversion of water to fuel. In spite of this limitation, one will have to recognize that the efforts for conversion of carbon dioxide to chemicals and fuels employing solar energy have received considerable attention in recent times. It should be recognized that carbon dioxide conversion to chemicals and fuels can also be achieved by means of other routes like chemical, electro-catalytic and biochemical ways [1–6]. These methodologies have specific advantages and disadvantages over the photo-catalytic route but these are not our immediate concern. The photo-catalytic route has received considerable attention due to its possible similarity to artificial photosynthesis [7–20].

B. Viswanathan (✉)
National Centre for Catalysis Research, Indian Institute of Technology, Madras, Chennai 600 036, Tamil Nadu, India
e-mail: bvnathan@iitm.ac.in

B. Viswanathan et al. (eds.), *Materials and Processes for Solar Fuel Production*, Nanostructure Science and Technology 174, DOI 10.1007/978-1-4939-1628-3_11

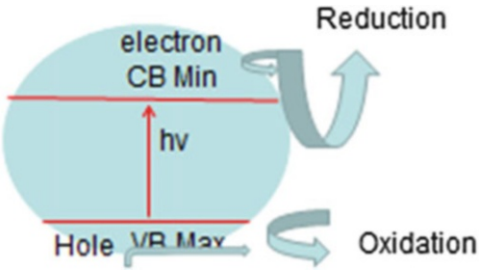

Fig. 1 Schematic representation of both oxidation and reduction reactions on a typical photo-catalytic system

In spite of adequate knowledge of photosynthesis and its similarity to carbon dioxide conversion process, it has to be remarked that the observed photo-catalytic conversion rates have been too low so far. This low rate of conversion has not shown any drastic improvement ever since this process was demonstrated on semiconductors like TiO_2, ZnO, CdS, GaP, SiC and WO_3 by Inoue et al., in 1979 [21]. One of the reasons that has been recognized in literature is the fact the carbon dioxide in the ground state is a linear molecule and most stable and as such activation of linear molecules for chemical conversion is a difficult process [2, 3].

The fundamentals of photo-catalytic and photo-electrochemical processes have some aspects in common. In a typical photo-catalytic reaction, photons are absorbed by a semiconductor so that the reducing power of the semiconductor is altered by the excitation of the electron from the valence band to the conduction band and the bottom of the conduction band of the semiconductor reflects in electrochemical sense the reducing power of the semiconductor under illumination conditions. Under the same conditions, the oxidizing power of the semiconductor is denoted by the valence band maximum of the semiconductor. Schematic diagram of this situation is given in Fig. 1. One has to recognize that both oxidation and reduction of the substrate is simultaneously possible and for example in the case of water decomposition both hydrogen and oxygen can be evolved by the reduction and oxidation of water molecules. The simultaneous possibility of carrying out both the opposing reactions on the same surface provides a number of possibilities for the production of value-added chemicals and also for promoting reactions for environmental protection [22–24] and pollution abatement. This added advantage of the processes has been exploited in a number of studies for decontamination of water, generation and use of self-cleaning tiles, and also hydrophobic wind shields and many other practical applications thus opening a new avenue for scientific research.

Photo-catalytic and photo-electrochemical routes have been advocated as viable alternative methodologies for future production of chemicals. Even though this concept appears to be appealing, its implementation appears to have met with limited success. The conversion levels so far reported even in the case of photo-catalytic reduction (PCR) of carbon dioxide is only at a few micromoles per gram per hour which is far from the levels required for development of economically viable processes. This situation has been addressed in the literature and has been accounted for in terms of the multi-step nature of the photo-catalytic processes,

namely photon absorption, charge separation, charge transport, surface reaction and desorption of the substrates and each of these steps has to sequentially take place in the case of formation of multi-electron reduction products like formaldehyde, methanol and methane from CO_2.

Another hurdle faced is that the semiconductor materials that have been tried (~over 400 in number) are having limitations with respect to the response wavelength of the radiation or undergo simultaneous photo-corrosion. This aspect has been addressed in literature in terms of sensitization of the semiconductor materials or by the so-called bandgap engineering but both these possibilites have not yielded the desired results; the quantum efficiencies have always remained low at less than 10 % in any meaningful device though higher efficiencies are claimed in laboratory performed experiments. This is another question that has to be addressed as soon as possible.

Major limitation in realizing these processes as viable alternatives is with respect to measures used to indicate the reactivity of the system for comparison and selection of materials [4]. These measures are based on either the catalyst systems used (in terms of the quantity, surface area or possibly the number of active centres) or on the illumination employed (in terms of either total number of photons or in terms of photons absorbed). In a multi-step photo-catalytic process, the total number of photons is not directly reflecting the ultimate activity of the catalyst system employed. It appears that one has to evolve a totally new scale of measure for representing the photo-catalytic activity. This new scale can be combining the existing scales based on catalyst and illumination but can also be entirely independent of these two parameters. The new scale that will be evolved must be based on the number of successful photons absorbed and this quantity if not easily available since the striking photons undergo multiple events like scattering at various points of the incidence and the count of the successful photons will truly gives the quantum efficiency and also shows how far the system is not promoting the recombination of generated charge carriers.

The photo-catalytic activity of various systems is usually compared with what is observed with P25 Degussa TiO_2. The issues of relevance in this context are:

1. P25 TiO_2 is a 80:20 mixture of Anatase and Rutile forms of TiO_2. The consequence of these two phase boundaries in the observed reactivity has to be distinctly delineated.
2. The two phases can give rise to specific configurations like core-shell and the relevance of this for the observed reactivity has to be established.
3. Nearly 40 % of the materials that have been tried for photo-catalytic studies are based on titania and this preference has to be accounted for.
4. Comparison and reference standards are necessary but the chosen one has to be carefully established that the system meets the criteria that have to be used for such a selection.

The purpose of this presentation is to examine the current status of PCR of carbon dioxide to chemicals and fuels. In spite of intense research in the past over four decades, the progress made appears to be marginal in terms of the activity of

Table 1 The reduction potential (E_0) of CO_2 for various products, potential values are versus NHE

Reduction reaction	E_0 (V) vs. NHE
$CO_2 + e \rightarrow CO_2^{-\cdot}$	−1.90
$CO_2^{-\cdot} + 2H^+ + 2e \rightarrow HCOOH$	−0.61
$CO_2 + 2H^+ + 2e \rightarrow CO + H_2O$	−0.53
$CO_2 + 4H^+ + 4e \rightarrow C + 2H_2O^{\bullet}$	−0.20
$CO_2 + 2H^+ + 2e \rightarrow HCHO + H_2O$	−0.48
$CO_2 + 6H^+ + 6e \rightarrow CH_3OH + H_2O$	−0.38
$CO_2 + 8H^+ + 8e \rightarrow CH_4 + 2H_2O$	−0.24
$2CO_2 + 12H^+ + 12e \rightarrow C_2H_5OH + 3H_2O$	−0.16

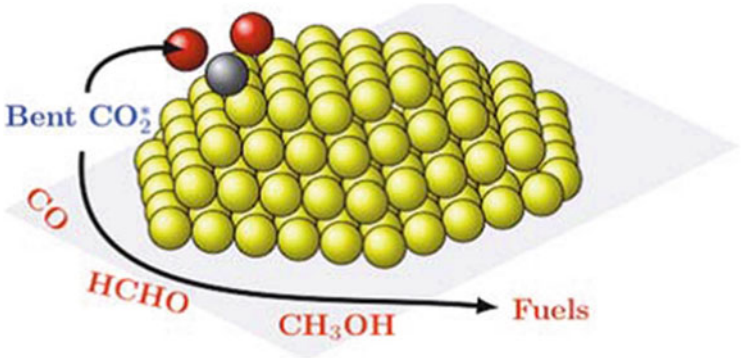

Fig. 2 A model for the initial activation of CO_2 (Reproduced from Refs. [2, 3])

the systems considered. It is always necessary that in frontier areas of research like the carbon dioxide reduction to chemicals and fuels, one has to periodically assess the progress so that the diversions can be avoided and the goal can be achieved [25–28]. The activation of carbon dioxide (a linear molecule) is difficult and the initial step of adding an electron to form CO_2 anion radical is a high energy barrier step requiring an over-potential of 1.9 V. The subsequent steps to form products like CO, HCHO, HCOOH, CH_3OH, CH_4 and other coupled products do not experience similar kind of barrier, even though the mechanistic details of these subsequent steps are still not fully revealed. However, the initial activation of carbon dioxide appears to hold the key for these conversion reactions. The reduction potentials for various products from CO_2 vs. NHE are assembled in Table 1 for reference. In recent publications, it has been shown that similar-sized copper particles prepared by different methods did not show similar catalytic activity, but multidimensional "defects" could be the reason for the observed significant enhancements observed in selectivity of electro-catalytic reduction of CO_2 [29, 30]. All these reports indicate that the key to efficient CO_2 reduction hangs on the activation of CO_2 at the appropriate sites with appropriate centres in the molecule. This aspect has been addressed earlier wherein it has been deduced that the bond angle of CO_2 should be reduced from 180° towards the tetrahedral angle. The pictorial representation of this postulate is shown in Fig. 2.

In this presentation the main objective is to consider on the issues which stand in the way of realizing the desired levels of activity for the PCR of carbon dioxide.

The specific aspects that will be addressed in this presentation include:

1. The discrimination required in the analysis of products obtained from the residual carbonaceous impurities present while preparation of the reaction system or from the species introduced in the reaction system as sacrificial agents and solvents [14].
2. The most appropriate analysis protocol for studying the progress of PCR of carbon dioxide.
3. The considerations required for evolving a reasonable measure of activity of photo-catalytic system embracing both the catalyst and illumination.
4. Evolving governing principles for selection of semiconductor materials for possibly efficient PCR of carbon dioxide. Up to now the choice of semiconductor materials is based on the bandgap values (on energetics) while it may be necessary that one has to also take into account the type of surface active sites that the semiconductors can offer for the reduction reaction of CO_2.

2 Activation of Carbon Dioxide

For any catalytic reaction to proceed in the desired direction, the activation of the substrate in the appropriate manner is a necessary condition. In the case of PCR of carbon dioxide, one has to consider simultaneously the evolution of hydrogen from hydrogen source (water or other solvents) and its incorporation in the carbon moiety after stripping oxygen from CO_2 to the extent required. It has been already established that specific crystal faces of rutile TiO_2 (100) is active for PCR of CO_2 while (110) crystal face is not that active for this reaction [31]. The characteristic centres and their functionalities in the CO_2 molecule are shown in Scheme 1.

Carbon dioxide is a linear molecule with a short C−O bond distance of 1.16 Å. Overall the molecule is non-polar, CO_2 possesses polar bonds due to the difference in electronegativity between C and O. The molecule is susceptible for both nucleophilic attack at the carbon centre and electrophilic attack at oxygen centres. With an ionization potential of 13.78 eV, CO_2 is nonbasic and interacts only weakly with Bronsted and Lewis acids. With a carbon centred-localized LUMO, CO_2 is susceptible to attack by nucleophiles and to reduction. The first step in the reduction of CO_2 involves in a decrease of the C−O bond order. Activation is envisaged mostly in the bending of the molecule. Bent CO_2 interacts with electrophiles and nucleophiles through the frontier orbitals. The lowest unoccupied molecular orbital (LUMO) exhibits strongly localized wave function characteristics, enhancing the interaction with nucleophiles by facilitating the transfer of electron density from the nucleophile into the LUMO. The highest occupied molecular orbital (HOMO) with its localized electron density can interact with electrophiles. The difficulty in the activation of CO_2 is realized in the highly negative potential (nearly −1.9 V) for the

O
||

C ← Lewis base → M→C → M is electron rich

|| ← π Complex → Donor acceptor bond → appropriate orbitals

O ← Lewis Acid → M ← O → M is electron deficient

Scheme 1 Reactive positions in CO_2 molecule and the typical reactive sites required for bonding with CO_2

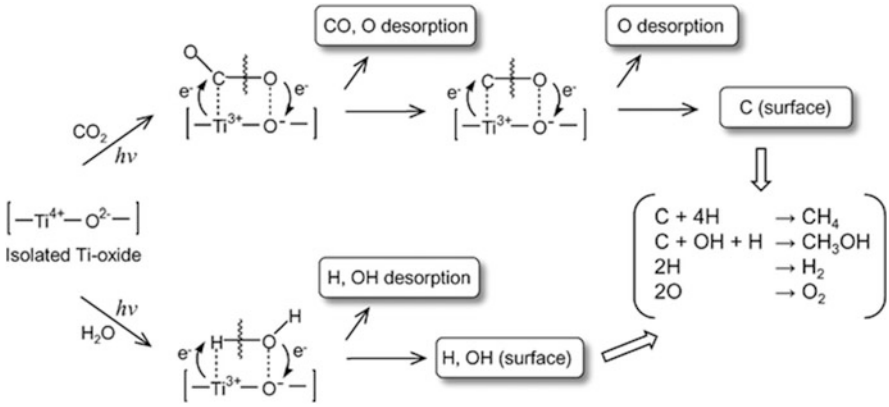

Fig. 3 Possible route photo-catalytic reduction of carbon dioxide with water (Figure reproduced from Ref. [32], Kohsuke Mori, Hiromi Yamashita and Masakazu Anpo, RSC Adv., 2, 3165–3172 (2012))

first electron reduction. The necessity for activation at both the centres of CO_2 gives rise to various modes of activation for CO_2.

Multiple bonding characteristics in CO_2 are responsible for the activation of the molecule in more than one mode. The bonding can involve one or multiple metal/active centres with both electron donor and acceptor characteristics. This possibility of a variety of surface activation may be one of the prime reasons why a variety of reduced products are observed in the PCR of CO_2. One such model has been used by Anpo et al. [32] for explaining the variety of products obtained in the PCR of CO_2. Their model is reproduced in Fig. 3. It can be seen from Fig. 3, the carbon dioxide activation is envisaged through the activation of both Lewis acid and base centres of the molecule. Similarly one can visualize a variety of modes of activation of carbon dioxide molecule if the photo-catalyst exhibits multiple activation centres. It should be realized that many of the photo-catalysts may possess multiple activation centres due to sensitization of the semiconductors in a variety of ways including doping and metallization.

3 Catalytic Systems Examined

The PCR of carbon dioxide has been examined on number of semiconductors, especially oxides, nitrides, sulphides and phosphides in addition to a few elemental semiconductors. Among them, the majority of studies have been on titania and titania-based semiconductors. The reasons for examining extensively [7–20] titania-based systems are:

(a) The conduction band minimum is at −0.16 V vs. NHE (Normal Hydrogen Electrode) and this value is favourable for hydrogen evolution from water.
(b) The life time of the excitons created by photon absorption is probably sufficient for the reduction reaction.
(c) The recombination rate especially for anatase is lower as compared to other semiconductors.
(d) The valence band maximum is at a positive potential so that the desired oxidation reactions like oxygen evolution and also pollutant abatement are favourable in this system.

However, the valence band maximum is highly positive to that of oxygen evolution reaction and hence it is amenable for alteration and thus facilitates generation of active semiconductor systems for photo-catalytic pollutant removal. This can be achieved if one can alter the valence band maximum to less positive potential with respect to that in titania system without affecting the conduction band minimum. This appears to be feasible if suitable cations can be introduced so that they contribute to the valence band while still the conduction band is arising from d states of the principal cation. This situation is exemplified in the case of tantalates and niobates where the conduction band is contributed by the 5d and 4d states of the tantalum and niobium cations, respectively, while in the silver tantalates and silver niobates, the valence band is contributed by the 2p state of oxygen and silver 4d state thus the valence band in these systems is less positive with respect to the corresponding sodium compounds as seen from Fig. 4.

In Table 2, the reported data on the PCR of CO_2 are assembled. For more comprehensive data base, the readers are requested to refer to the references cited [7–20].

While majority of the PCR studies are concerned with titania and its modified versions [14] as catalysts, several mixed oxide semiconductors, like $SrTiO_3$ [49], $ZnGa_2O_4$ [50] and Zn_2GeO_4 [51], with valence and conduction band energy positions suitable for oxidation of water and reduction of CO_2, respectively, and structural features that favour facile transport of charge carriers and promote the adsorption of the substrates in the modes required for the desired selectivity are being explored.

Notable among them are the mixed metal oxides that belong to the family of perovskites, ABO_3, especially those with layered structure like $ALa_4Ti_4O_{15}$ (A = Ca,Sr,Ba) with Ag as co-catalyst [48] and $SrTiO_3$ with different co-catalysts [52], which are reported to display good activity for PCR. It has been reported that

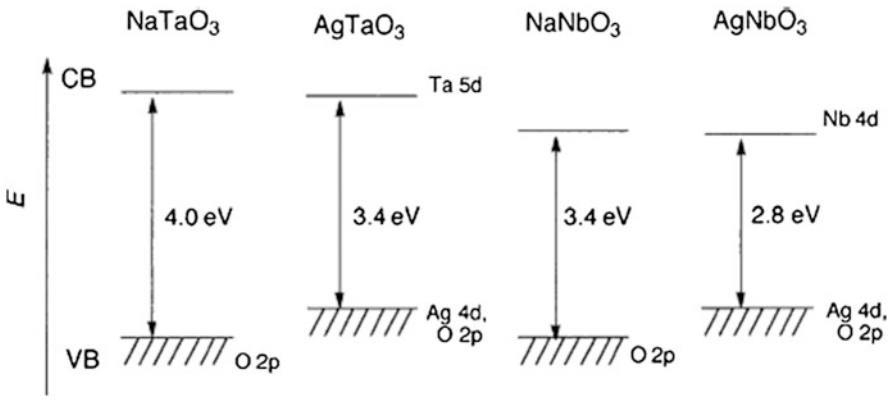

Fig. 4 The VB and CB positions in sodium and silver tantalates and niobates to demonstrate how silver substitution alters only the valence band maximum

Table 2 Data on the typical catalysts for the photo-catalytic reduction of carbon dioxide

	Reactants			
Photo-catalyst	CO_2	H_2	Major product	Ref.
TiO_2 (P25)	Saturated	Liquid	CO	[33]
Anatase	Gas	Gas	Methane	[31]
TiO_2 (MWCT)	Gas	Gas	C_2H_5OH, HCCOH, CH_4	[34]
TiO_2-Y Zeolite	Gas	Gas	CH_4, CH_3OH	[35]
Pt-Ti-Y zeolite	Gas	Gas	Methane	[35]
Ti-SBA15	Gas	Gas	Ethane, methane	[36]
CdSe-Pt/TiO_2	Gas	Gas	Methane methanol	[37]
PbS-Cu-TiO_2	Gas	Saturated	Co, methane	[38]
Cu/TiO_2	Saturated	0.2 M NaOH	Methanol	[39, 40]
Cu-N-TiO_2	Gas	Saturated	Methane	[41]
ZnO	Saturated	Liquid	HCHO, CH_3OH	[21]
CdS	Saturated	Liquid	HCHO, CH_3OH	[21]
GaP	Saturated	Liquid	HCHO, CH_3OH	[21]
SiC	Saturated	Liquid	HCHO, CH_3OH	[21]
CdS-Monmorillonite	Saturated	0.2 M NaOH	Methane	[42]
NiO	Saturated	0.2 N $KHCO_3$	Methane	[43]
$BiWO_6$	Saturated	Liquid	Methane	[44]
$BiVO_3$	Saturated	Liquid	Ethanol	[45]
HSb_3O_8	Gas	Gas	Methane	[46]
RuO_2-Zn_2GeO_4	Gas	Gas	Methane	[47]
Ag/$BaLa_4Ti_4O_{15}$	Saturated	Liquid	CO, formic acid	[48]

significant and stable activity is displayed by perovskite type $NaTaO_3$ catalysts [53] with various co-catalysts, Pt, Ag, Au, Rh, CuO, NiO and RuO_2. Another layered perovskite, $Sr_3Ti_2O_7$, on doping with S, N and Fe_2O_3, displays high activity for PCR of carbon dioxide in the visible region.

The results of this study on the PCR of carbon dioxide [54] are given in Table 3 and the extent of overall conversion of carbon dioxide is shown in the form of bar chart in Fig. 5. These results indicate that there is scope for improvement and the realization of a commercial possibility appears to be in the near future.

The PCR of CO_2 on La-doped $NaTaO_3$ with a variety of co-catalysts has been studied by Jeyalakshmi et al. [55]. The changes in the positions of conduction band minimum and valence band maximum brought out by loading lanthanum in $NaTaO_3$ is shown in Fig. 6, together with the redox potentials for various products in the photo-catalytic reduction of carbon dioxide. Methane, ethane and acetaldehyde were formed in very small quantities (~1–10 μmol/g) and hence not considered. Cumulative products formed on all the catalysts studied after 20 h of irradiation, along with total CO_2 consumed are given in Fig 7 and Table 4. It is observed from Table 4 that lanthanum and various co-catalysts incorporated in $NaTaO_3$ significantly influence the overall CO_2 conversion as well as selectivity to various products like methanol/ethanol. Addition of lanthanum and NiO separately to $NaTaO_3$ results in marginal increase in conversion. In the presence of both La and NiO, CO_2 conversion increases by four times with respect to neat $NaTaO_3$. Among the co-catalysts employed, NiO and CuO display maximum increase in activity and relatively higher selectivity towards ethanol. Other co-catalysts like Pt, Ag, Au and RuO_2 do promote CO_2 photo-reduction but are not as effective as NiO and CuO. Initially methanol is formed at a higher rate and later, the rate tapers off, once ethanol formation by coupling of surface C_1 species picks up.

Lanthanum-doped $NaTaO_3$ was studied in view of its promoting effect on splitting of water under UV radiation. According to Kudo and Miseki [56], doping of lanthanum facilitates the formation of crystalline phase and induces nano level step sites on the surface, which help to retard charge carrier recombination and facilitates CO_2 activation. With an increase in the bandgap value (3.9–4.1 eV) on lanthanum doping, the conduction band energy level becomes more negative thus favouring increase in activity (refer to Fig. 6). Finely dispersed NiO crystallites act as efficient centres for hydrogen generation. Such changes lead to increase in activity for water splitting as well as CO_2 photo-reduction. The location of the conduction band of NiO (at −0.96 eV) with respect to that of $NaTaO_3$ (at −1.06 eV) facilitates easy transfer of photo-generated electrons from $Na_{(1-x)}La_xTaO_{(3+x)}$ to the conduction band of NiO [53]. Increase in the availability of photo-generated electrons in the conduction band of NiO facilitates deeper reduction of CO_2 to alcohols.

Other co-catalysts, Pt, Ag, Au and RuO_2, act as effective electron traps and help in hydrogen generation and CO_2 reduction. However, these are not as effective as NiO and CuO. Pt in $Pt/Na_{(1-x)}La_xTaO_{(3+x)}$ promotes backward reaction of hydrogen and oxygen to form water and hence the activity does not match with that obtained in the presence of NiO/CuO. Surface plasmon resonance band due to nano

Table 3 Typical results on the photo-catalytic reduction of neat and doped $Sr_3Ti_2O_7$

Catalyst	Extent of products formed after 6 h of irradiation in (μmol/g)									Conv. (%)
	CH_4	C_2H_4	C_2H_6	CH_3OH	C_2H_4O	C_2H_6O	C_3H_6O	C_3H_6	CO_2	
$Sr_3Ti_2O_7$	0.5	0.2	0.2	249	8	53	0	0.2	373	0.5
$N/Sr_3Ti_2O_7$	0.5	0.2	5	58	6	24	0	0.2	419	0.59
$N,S/Sr_3Ti_2O_7$	0.7	1	0.7	440	15	62	25	0.3	676	0.95
$Fe/Sr_3Ti_2O_7$	0.6	2.4	0.4	459	27	86	27	0.2	774	1.1
$Fe,N/Sr_3Ti_2O_7$	0.7	1.1	0.4	482	5	161	15	0.2	863	1.2
$Fe,N,S/Sr_3Ti_2O_7$	0.1	5.4	0.2	561	2	284	25	0.9	1,222	1.7

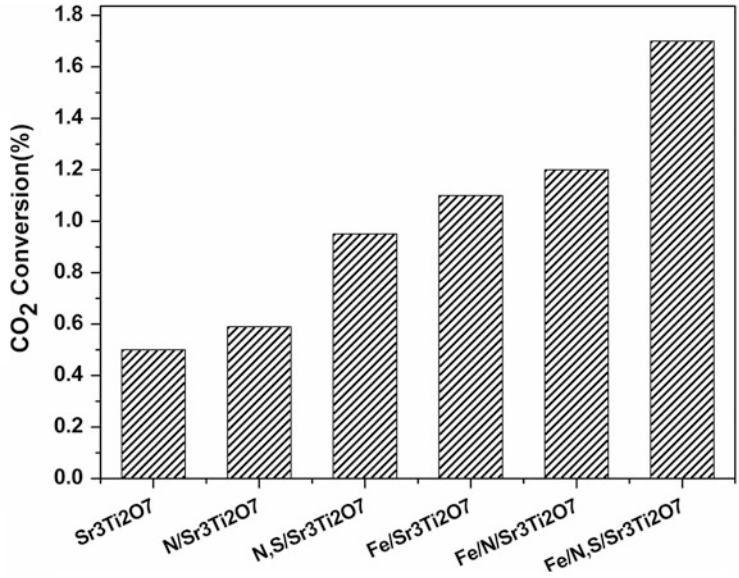

Fig. 5 Photo-catalytic reduction of carbon dioxide on $Sr_3Ti_2O_7$ and N-, S- and Fe-doped systems. The energy level diagrams of these systems are normally generated from that of $Sr_3Ti_3O_7$ in the usual manner

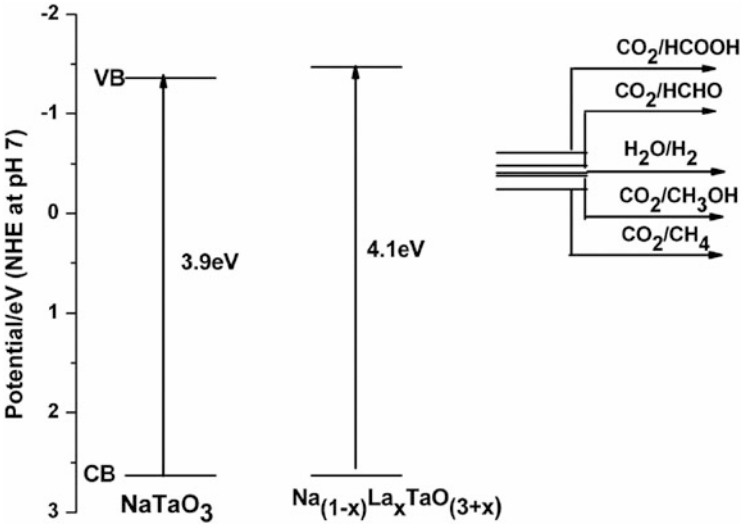

Fig. 6 Effect of La loading on conduction band energy level for $NaTaO_3$- vis-à-vis reduction potentials to various products from CO_2

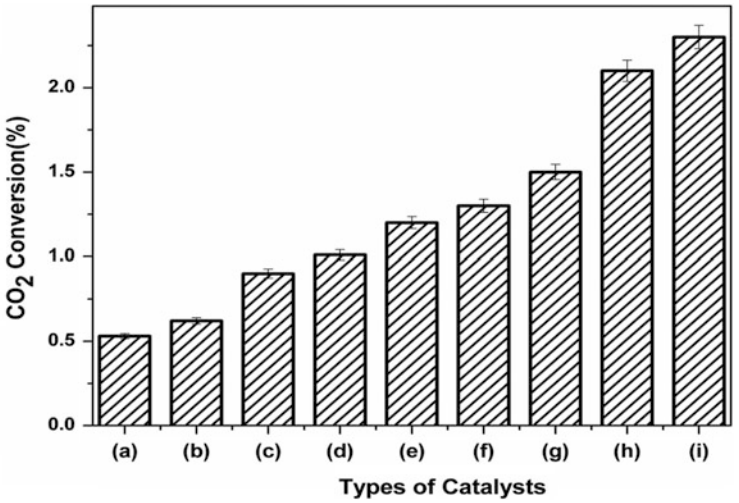

Fig. 7 Comparison of activity of neat and modified $NaTaO_3$ catalysts: (**a**) $NaTaO_3$, (**b**) $NiO/NaTaO_3$, (**c**) $Na_{(1-x)}La_xTaO_{(3+x)}$, (**d**) 1 wt%$Au/Na_{(1-x)}La_xTaO_{(3+x)}$, (**e**) 1 wt%$Ag/Na_{(1-x)}La_xTaO_{(3+x)}$, (**f**) 1 wt%$RuO_2/Na_{(1-x)}La_xTaO_{(3+x)}$, (**g**) 0.15 wt%$Pt/Na_{(1-x)}La_xTaO_{(3+x)}$, (**h**) 1 wt%$CuO/Na_{(1-x)}La_xTaO_{(3+x)}$, (**i**) 0.2 wt%$NiO/Na_{(1-x)}La_xTaO_{(3+x)}$

Table 4 Cumulative product patterns for CO_2 photo-reduction on neat and modified $NaTaO_3$ catalysts

Catalyst	Products formed after 20 h of irradiation (μ mol/g)						Con. (%)
	CH_4	C_2H_6	CH_3OH	CH_3CHO	C_2H_5OH	Total CO_2 consumed	
$NaTaO_3$	0.3	0.10	245.6	12.9	52.2	376.4	0.53
$NiO/NaTaO_3$	0.4	0.20	334.9	2.5	48.9	438.5	0.62
$Na_{(1-x)}La_xTaO_{3+x}$	1.3	0.10	544.9	0.5	47.5	642.4	0.9
1 wt%$Au/Na_{(1-x)}La_xTaO_{3+x}$	0.5	0.20	604.4	1.5	57.7	723.8	1.0
1 wt%$Ag/Na_{(1-x)}La_xTaO_{3+x}$	0.5	0.3	608.5	8	128.1	881.8	1.2
1 wt%$RuO_2/Na_{(1-x)}La_xTaO_{3+x}$	0.4	0.2	536.2	1.1	197.9	935.1	1.3
0.15 wt%$Pt/Na_{(1-x)}La_xTaO_{3+x}$	7.3	0.5	1,007.7	3.1	21.3	1,064.1	1.5
1 wt%$CuO/Na_{(1-x)}La_xTaO_{3+x}$	0.2	0.3	940.1	7.1	270.5	1,496.1	2.1
0.2 wt%$NiO/Na_{(1-x)}La_xTaO_{3+x}$	0.4	0.2	1,030.6	7.7	280.7	1,608.2	2.3

The catalysts appear to be photostable even after 20 h irradiation

size Au observed at 560 nm in Au/$Na_{(1-x)}La_xTaO_{(3+x)}$ induces additional light absorption in visible region resulting in perceptible improvement in activity compared to neat $NaTaO_3$, but less than that achieved with NiO/CuO as co-catalysts. Unique matching of electronic levels in the conduction band of $NaTaO_3$ is not observed with other tantalates (Li and K) or with co-catalysts other than NiO and CuO. Thus two distinct mechanisms, coupling of semiconductors and trapping of photo electrons, both leading to effective charge carrier separation are operative in the promoting action of co-catalysts with $Na_{(1-x)}La_xTaO_{(3+x)}$.

4 Some Issues

The major aim of the studies on the PCR of CO_2 is to be able to recycle CO_2 into fuel. If this could be achieved, then there are many obvious and not so obvious benefits to the energy-starved society. However, achieving this goal appears to be eluding the scientific community at present. It is as stated above necessary that one periodically assesses the situation and try to bring in remedies for the difficult jobs on hand. In this section, we shall consider seemingly main issues at present in the PCR of CO_2.

It is often doubted that the reduction products obtained in the PCR of CO_2 could have arisen from the conventional carbon impurities invariably present in the starting stage. Blank experiments without the added CO_2 have shown the probability of such a possibility. However it has been repeatedly argued that [4, 15] (a) the residual carbon impurities cannot give rise to sustained generation of reduction products. (b) The inherent carbon impurities could give rise to spurt of activity in the early stages of the photo-catalytic reaction and a gradient change will be observed in the product yield as a function of time and hence a suitable correction can be effected for reporting the activity data and (c) the product slate obtainable from carbon impurities can be different from that of the PCR of CO_2.

Essentially, the results reported in literature, though not rule out the possibility of impurities as the source for the reduction products formed, the realization of PCR of CO_2 appears to be a realistic process.

It has been already pointed out that the results reported in literature are based on analysis of products by a single (mostly gas chromatographic analysis) technique [15]. The points of relevance in this connection are:

1. It is necessary that one is clear about the detection limit of these analytical techniques that are employed since sometimes the products formed can be below the detection levels of these analytical techniques employed.
2. Many of the products are capable of interacting among themselves in the analysis column and this interference can also cause some uncertainty in the analysis results. In the literature, there is no clear mention of this factor in the analysis.

3. There may be advantages if the analysis results are substantiated by two or more independent techniques so that the confidence level is increased.
4. Though GC analysis appears best suited from the point of view of simplicity and adoptability, will this be sufficient is not established.
5. It may be possible that alternate analysis methodologies have to be adopted since the solid catalyst is simultaneously present in the reaction medium with the products and one has to establish suitable and standard procedure for this analysis.
6. Instead of a combination of techniques for analysis like GC-MS, GC-IR, it may be necessary to evolve a preferred analysis protocol for the reaction products for this reaction.

Another issue demanding some immediate attention is the measure to express the reactivity of the photo-catalytic system. This has been done so far in terms of the catalyst characteristics (like per gram, per m^2) or in terms of extent of illumination (photon flux or total illumination power). Both these measures assess activity grossly from a single direction whereas the real activity must have been a combination of both of them. In addition, it should be realized that not all the exposed illumination can be utilized for the photo-catalytic reaction since there can be scattering and also other recombination factors and hence expressing activity in terms of total photon flux is grossly inadequate to assess the reactivity of the photo-catalytic system chosen. As the illumination is on a dispersed system in the photo-catalytic studies, it is possible not all the photons are utilized in the charge separation act and hence the measure of the photo-catalytic activity in terms of illumination has to be examined more carefully and the apparent (Formal) Quantum Efficiency (FQE) that is normally reported does not directly reflect on the efficiency of the photo-catalyst employed either in terms of the active sites of the photo-catalyst employed or on the number of effective photons absorbed. The use of gross parameters may affect the development of efficient photo-catalyst. Even if one were to measure per photon striking the surface, the measure is not reflecting the activity of the catalyst system employed. It appears at this stage that one has to evolve a new independent measure comprising both the catalyst and the effective illumination and the bench mark system has to be evolved instead of the Degussa P25 as this is not a pure single component system. In Fig. 8 the situation with respect to the illumination of a surface is shown. It is seen that majority of the photon flux are not directly available for the photo-catalytic reaction.

The governing principles for the selection of semiconductors have been based on the energy of the bandgap and possibly photon absorbing characteristics of the semiconductors chosen. However in the case of CO_2 reduction which is a multiple electron process, there is a need to suitably improve the redox potential of the electron so that it can effectively create the carbon dioxide anion radical in the first step. This step being the important step of the whole process, it appears that one has to consider modulating the conduction band minimum with respect to the first reduction potential of CO_2 (namely -1.9 V) and this aspect has to be given possibly due attention in future.

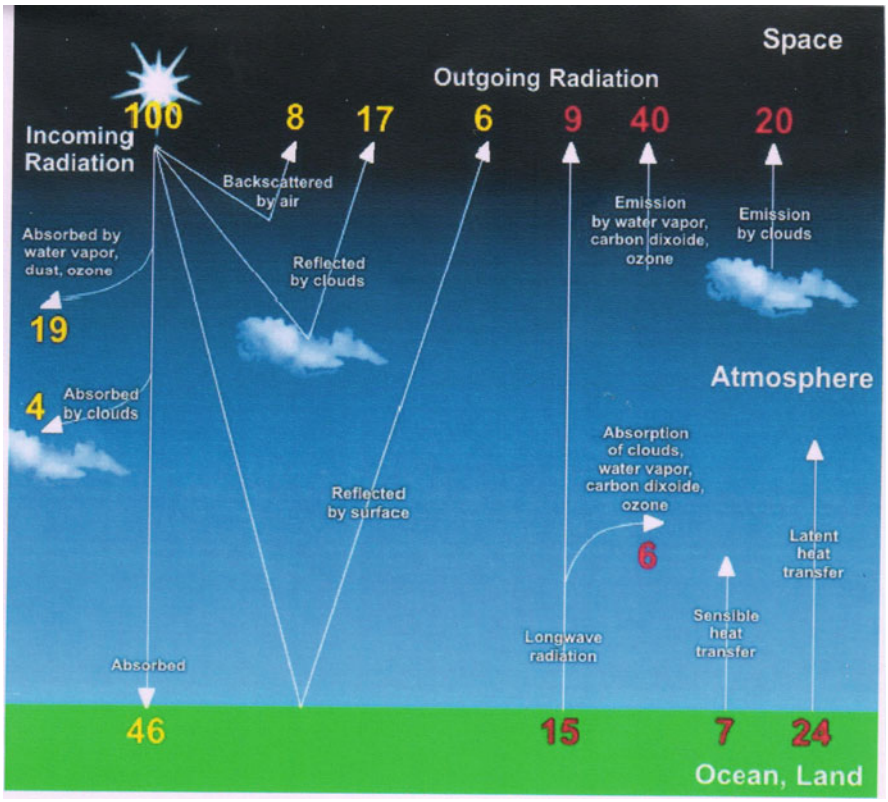

Fig. 8 An approximate photon count striking the earth from sun and the distribution of them in various events (Reprinted from Ref. [57])

5 Photo-Catalysis and Photosynthesis

It appears that one has to learn a lot more from the photosynthesis routes since this is one of the possibly efficient ways of harnessing carbon dioxide. Biochemical reduction of CO_2 in the form of photosynthesis has been studied in detail and the literature has been reviewed recently [5]. Six biochemical pathways have been identified for fixing inorganic carbon in organic carbon in photosynthesis. These have been identified as the reductive acetyl-CoA or phospho-glyceraldehyde pathway or reductive citric acid pathway. A simplified schematic of photosynthesis is shown in Fig. 9. The point of interest and connection between these two processes is the fact that the net electron transfer pathway in biochemical route is highly energy modulated with a number of appropriate transfer agents and possibly this is what is being attempted by the so-called process of sensitization of the semiconductor in the PCR of CO_2. Since in most of the semiconductors employed in the PCR of CO_2 the conduction band minimum (i.e., reducing power) is not conducive for the first

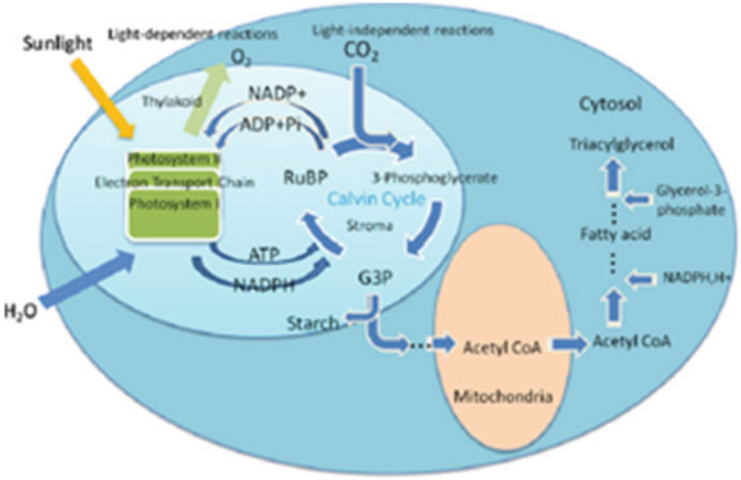

Fig. 9 A simplified photosynthesis pathway (Figure reproduced from Ref. [19])

Table 5 Comparison of photo-catalytic decomposition of water and the reduction of carbon dioxide

Photo-catalytic decomposition of water	Photo-catalytic reduction of CO_2
1. The products of the reaction are simple—hydrogen and oxygen only	1. Multiple products are formed like CO, HCHO, CH_3OH and CH_4
2. The number of electrons transferred are limited (Maximum 4)	2. The total number of electrons involved can be a variable number (>8)
3. The mechanistic pathway of the decomposition is simple	3. The mechanistic pathway has yet to be completely elucidated
4. The products being gases diffuse out of the reaction centres	4. The products formed may be adsorbed on the catalyst
5. Thermodynamically uphill reaction with the free energy of formation of water being—228.4 kJ/mol	5. Thermodynamically less favourable with free energy of formation of CO_2 is—394 kJ/mol
6. Electrons reduce the protons to molecular hydrogen	6. Initial electron transfer to CO_2 requires high (−1.9 V) over-potential
7. Water photo-catalytic decomposition is an independent reaction	7. Water decomposition can be a prerequisite for CO_2 reduction

electron transfer, the over-potential required for this step is of the order of −1.9 V; there is need for suitable transfer agents for initiating this reduction process.

It is necessary that one considers the situation with respect to the photo-catalytic decomposition of water and the reduction of CO_2. This will be possible only if we can compare these two challenging photo-catalytic processes. A simple comparison of these two processes is given in Table 5.

In Fig. 10, a simplified flow diagram is given to show how the CO_2 cycle could be effected to generate back the fuel which on combustion gives rise to CO_2. This

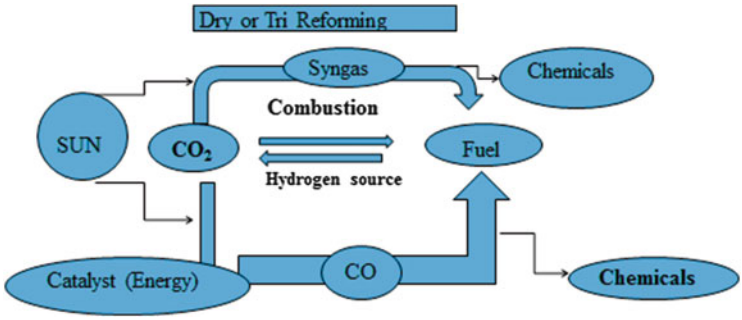

Fig. 10 A simplified flow diagram for the conversion of CO_2 to fuels and back to CO_2—Natural photosynthesis involves solar energy to recycle CO_2 (and H_2O) into (biomass) and fuels. Typical reforming of CO_2 yields syngas, synthetic fuels and commodity chemicals

diagram may possibly provide some clues for the effect utilization of CO_2 in man-made processes.

Even though this may show the similarity of PCR of CO_2 to that of photosynthesis, it must be realized that natural photosynthesis appears to be a facile process with a number of intermediate species which are appropriately placed with respect to the value of the reduction potential and a smooth electron transfer pathway has been ensured. Even though the sensitization of the semiconductors is one of the ways of achieving this, it is not an appropriate substitute for natural photosynthesis since the redox potentials of the intermediate species are self-adjustable in the case of photosynthesis while these are not alterable at present in the man-made substitutes.

6 Perspectives

It has to be realized that the formation rates of products from the conversion of carbon dioxide has not exceeded few tens of micromoles/h g of the catalyst and this is nowhere near a possible process. These low levels of activity have been improving at a slow pace in the past few decades and it can gallop up soon.

Even though the electrochemical reduction of carbon dioxide is a well-known process, from economic point of view the photo-catalytic reduction of CO_2 may be desirable.

Even though some guidelines for the choice of photo-catalytic systems have been formulated in terms of the electronic configuration of the cations as d^0 or d^{10} (oxides, oxynitrides, sulphides and phosphides), this principle has not led to the formulation of new photo-catalytic systems which can give product yields of commercial viability.

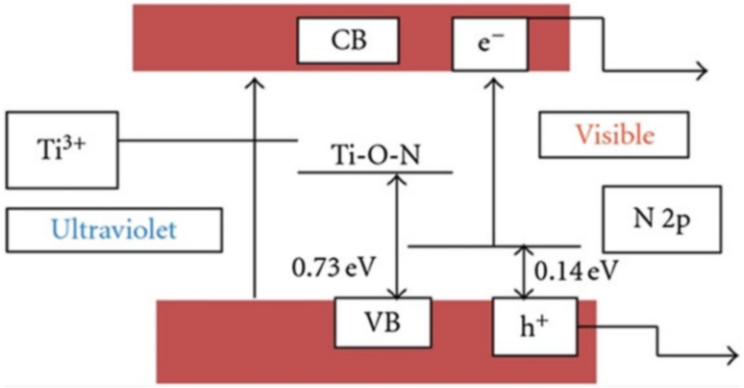

Fig. 11 Schematic energy level diagram for nitrogen substituted TiO_2 (Bare semiconductor absorbs UV radiation while the localized energy levels of nitrogen above valence band facilitate the visible light absorption) (Reproduced from Ref. [58])

From the point of view of the mechanism of the reduction reaction, even though the complete reaction sequence and sequential electron transfer steps are not yet clear, it is recognized that the first step of activation of CO_2 is the most difficult step from the point of reduction. Though this has been realized, the ways and means of increasing the reducing power of the semiconductor (i.e., the appropriate position of the conduction band minimum) has not yet been achieved to the desired levels though the alteration of the position of the valence band maximum has been achieved in a number of ways including the substitution by heteroatoms in the lattice (refer to Fig. 11).

Even though the modulation of the charge carrier dynamics has been achieved in a variety of ways like the addition of co-catalyst, the state of photo-catalytic system (the so-called nano-state), addition of sacrificial agents, the consequences realized are not up to the desired levels.

It is known that majority of photo-catalytic studies on CO_2 reduction has been on titania-based systems and Degussa (presently Evonik) titania P25 is considered to be the bench mark system, the studies have not yet reached a stage for the real-life solar fuel applications. This situation warrants a complete overhaul of our concepts in this field.

As has been pointed out earlier, the charge separation and effective utilization of the charges are necessary and essential steps for this process to become a viable one. In the case of anatase, the recombination rate is 10 times lower compared to that in Rutile. Both anatase and rutile crystallize in tetragonal form while Brookite crystallizes in orthorhombic form and yet another monoclinic TiO_2 is also available. In anatase ($E_g = 3.2$ eV) and rutile ($E_g = 3.0$ eV) which are considered to be photo-active materials, the charge recombination time is of the order of 10 ns and thus 90 % of the charge separation results in recombination. From this point of view, one has to look to other options like photo-electrochemical cells or hybrid systems where the charge separation can be a natural phenomenon.

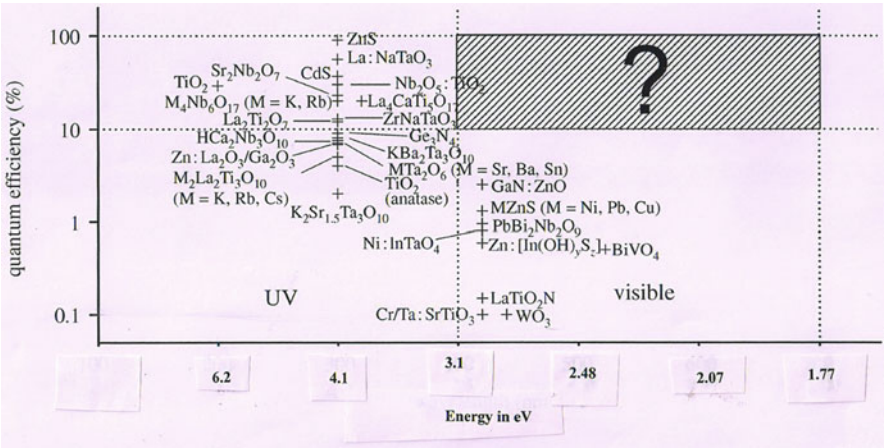

Fig. 12 The current status of materials in the photo-catalytic splitting of water. The figure indicates what type of materials is desirable for this reaction (Reproduced from Ref. [28])

It appears that the heterogeneous PCR of CO_2 on semiconductor catalysts is not yet ready to be implemented in real-life solar fuel applications. The silver line in this gloomy situation is the fact that the research and development activity in this field is enormous and the pace of activity may facilitate the understanding of the basic steps of the reduction process and thus facilitate formulation of new materials, stripping away the conventional outlook which may facilitate the realization of this process in the near future.

It is appropriate to comment on the possible methodology to be adopted for the search of new materials for PCR of carbon dioxide. In Fig. 12 the quantum efficiency for photo-catalytic water splitting is plotted against the bandgap energy of the semiconductors employed for this reaction. This plot is an adaptation of the figure in Ref. [28]. Even though this plot has been originally proposed by Osterloh [59] for water splitting, it may have some message for the combination reaction of carbon dioxide reduction in the presence of water. As shown in the figure, at present no material has yet been identified whose quantum efficiency is above 10 % and also active in the visible region. However, this projection has led to examining oxynitrides, tantalates, vanadates and other exotic combination materials.

It has been repeatedly pointed out that the charge separation is the most important step for PCR. In this connection, it has been realized that the charges move fast in structures with corner shared polyhedra. Typical structures of the systems employed for photo-catalytic water splitting are given in Fig. 13. It can be seen that the structures not only consist of corner shared polyhedra but also form some kind of layered systems. It is necessary that the relevance of lattice structures for the observed photo-catalytic activity has to be realized and established soon to enable further search for suitable materials.

In conclusion, it can be stated that though the current level of knowledge does not permit formulation of an economically viable processes for the conversion of

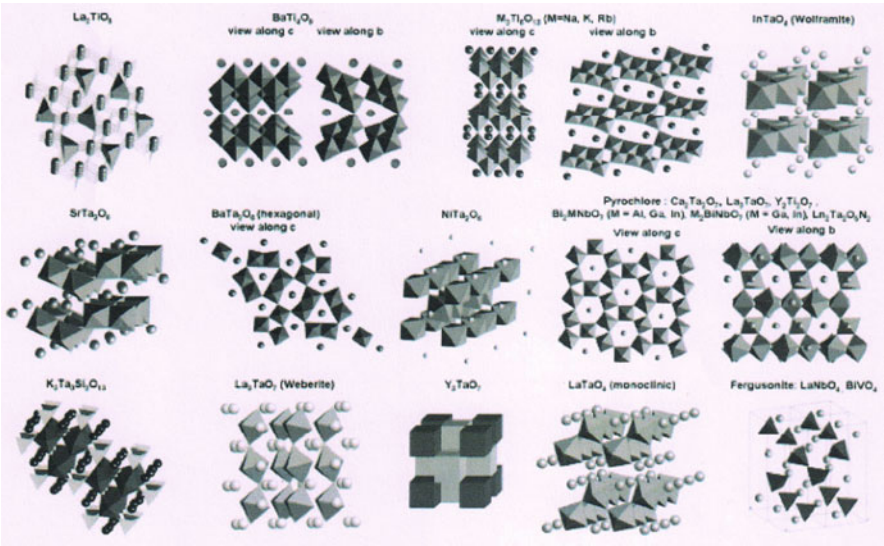

Fig. 13 Structures of typical materials used for photochemical splitting of water (Reproduced from Ref. [59])

carbon dioxide to fuels, but the indications are strong that sooner this will become a reality. The direction to achieve this goal is to formulate governing principles appropriately backed up with scientific reasoning for formulation of photo-catalysts and also identifying suitable reaction medium which will not give rise to any ambiguity with respect to the source for the products obtained.

Acknowledgements The author wishes to thank the Department of Science and Technology, Government of India for supporting the National Centre for Catalysis Research. Colleagues in the Centre and Hindustan Petroleum Corporation Limited contributed, respectively, to the knowledge and financial domains.

References

1. B. Viswanathan, Electro-Catalytic Reduction of Carbon Dioxide, chapter 10 in New and Future developments in catalysis, (Ed. S.L. Suib), Elsevier 2013.
2. B. Viswanathan, Reflections on the electrochemical reduction of carbon dioxide on metallic surfaces, Indian Journal of Chemistry, 51A, 166-173 (2012).
3. York R Smith, Vaidyanathan Ravi Subramanian, B Viswanathan, Photo-Electrochemistry & Photo-Biology for the Sustainability, Bentham Science (2010).
4. Severin N. Habisreutinger, Lukas Schmidt-Mende, and Jacek K. Stolarczyk, Photo-catalytic Reduction of CO_2 on TiO_2 and Other Semiconductors, AngewanteChemie, 52, 7372-7408 (2013).

5. Aaron M. Appel, John E. Bercaw, Andrew B. Bocarsly, Holger Dobbek, Daniel L. DuBois, Michel Dupuis, James G. Ferry, Etsuko Fujita, Russ Hille, Paul J. A. Kenis, Cheryl A. Kerfeld, Robert H. Morris, Charles H. F. Peden, Archie R. Portis, Stephen W. Ragsdale, Thomas B. Rauchfuss, Joost N. H. Reek, Lance C. Seefeldt, Rudolf K. Thauer, Grover L. Waldrop, Frontiers, Opportunities and challenges in biochemical and chemical catalysis of CO_2 fixation, Chemical Reviews, 113, 6621-6658 (2013).
6. B. Viswanathan, CO_2 to Chemicals and Fuels (25 presentations in youtube), https://www.youtube.com/channel/UCwFaAcfBs9K7zFYv4upgt0A
7. Masakazu Anpo, Photo-catalytic reduction of CO with H_2O on highly dispersed Ti-Oxide catalysts as a model of artificial photosynthesis, Journal of CO_2 Utilisation 1, 8-17 (2013).
8. Rakshit Ameta, Shikha Panchaol, Noopur Ameta and Suresh C. Ameta, Photo-catalytic reduction of carbon dioxide, Materials Science Forum Vol. 5, 83-96 (2013).
9. Yucheng Lan, Yalin Lu, and Zhifeng Ren, Mini Review on Photo-catalysis of titanium dioxide nanoparticles and their solar applications, Nano Energy, 2,1031-1045 (2013).
10. Jeffrey C.S. Wu and Hung-Ming Lin, Photo-reduction of CO_2 to methanol via TiO_2 photo-catalyst, International Journal of Photoenergy, Vol. 7, 115-119 (2005).
11. Richard Reithmeier, Christian Bruckmeier and Bernhard Rieger, Conversion of CO_2 via visible light promoted Homogeneous redox catalysis, Catalysts, 2, 544-571 2012.
12. Kihsuke Mori, Hiromi Yamashita and Masakazu Anpo, Photo-catalytic reduction of CO_2 with water on various titanium oxide photo-catalysts, RSC Advances, 2, 31165-3172 (2012).
13. Shifwru Kohtani, Eito Yoshioka and Hideto Miyabe, Photo-catalytic hydrogenation on semi-conductor particles, Intech, Chapter 12, 291-307 (2012).
14. Yasuo Izumi, Recent advances in the photo-catalytic conversion of carbon dioxide to fuels with water and/or hydrogen using solar energy and beyond, Coordination Chemistry Reviews, 257, 171-186 (2013).
15. Jindui Hong, Wei Zhang, Jia Ren and Rong Zu, Photo-catalytic reduction of CO_2: a brief review on product analysis and systematic methods, Analytical methods, 5, 1086-1097 (2013).
16. Masakazu Anpo, Photocatalytic reduction of CO with H_2O on highly dispersed Ti-Oxide catalysts as a model of artificial photosynthesis, Journal of CO_2 Utilisation 1, 8-17 (2013).
17. Kamila Koci, Lucie Obalova and Zdenek Lacny, Photocatalytic reduction of CO_2 over TiO_2 based Catalysts, Chemical Papers, 62, 1-9 (2008).
18. Stefan Neatu, Juan Antonio Marcia-Augullo, Hermenegildo Garica, Solar light Photo-catalytic CO_2 reduction: General considerations and selected Bench Mark Photo-catalysts, International J. Molecular Sci., 15, 5246-5262 (2014).
19. Wei-Ning Wang, Johnathon Soulis, Y. Jeffrey Yang and Pratim Biswas, Comparions of CO_2 photoreduction systems: A review, Aerosol and Air Quality Research, 14, 533-549 (2014).
20. Gael Gobaille-Shaw, A review of the reduction of carbon dioxide into useful products using transition metal catalysts, http://www.tutorhunt/resource/3111/ (2012).
21. T. Inoue, A. Fujishima, S. Konishi and K. Honda, Photo-electro-catalytic reduction of carbon dioxide in aqueous suspensions of semiconductor powders, Nature, 277,637 (1979).
22. B. Viswanathan and M.A. Scibioh, Photo-electrochemistry—principles and practices, Narosa Publishing House New Delhi, (2013) pp.
23. Muhammad Umar and Hamidi Abdul Aziz, Photo-catalytic degradation of organic pollutants in water, http://www.intechopen.com/books/organic-pollutant-monitoring-risk-and treatment (2013).
24. R. Ameta, S. Benjamin, A. Ameta and S.C. Ameta, Photocatalytic degradation of organic Pollutants: A Review, Materials Science Forum Volume 734, Ed. Rajesh J. Tayade, pp. 247-272 (2012).
25. V. Jeyalakshmi, K. Rajalakshmi, R. Mahalakshmy, K. R. Krishnamurthy, B. Viswanathan, Application of photo catalysis for mitigation of carbon Dioxide, Res. Chem. Intermed. 39, 2565-2602 (2013).
26. V. Jeyalakshmi, R. Mahalakshmy, K. R. Krishnamurthy, B. Viswanathan, Photocatalytic Reduction of Carbon Dioxide by Water: A Step towards Sustainable Fuels and Chemicals,

Materials Science Forum (Volume 734), Photocatalytic Materials & Surfaces for Environmental Cleanup-II, Editor: Rajesh J. Tayade pp. 1-62 (2013).
27. V. Jeyalakshmi, R. Mahalakshmy, K.R. Krishnamurthy, and B. Viswanathan, Titania based catalysts for photoreduction of carbon dioxide: Role of modifiers, Indian J. Chem., 51A, 1263-1283 (2012).
28. Z. Jiang, T. Xiao, V.L. Kuznetsov and P.P. Edwards, Turning carbon dioxide into fuel, Phil. Trans. R. Soc., 368, 3343-3364 (2010).
29. Aaron M. Appel, Electrochemistry: Catalysis at the boundaries, Nature, 508, 460-461 (2014).
30. Li, C. W., Ciston, J. & Kanan, M. W. Electroreduction of carbon monoxide to liquid fuel on oxide-derived nanocrystalline copper, *Nature* 508, 504-507 (2014).
31. M. Anpo, H. Yamashita, Y. Ichihashi, S. Ehara, Photocatalytic reduction of CO_2 with H_2O on various titanium oxide catalysts, J. Electroanal. Chem., 396, 21-26 (1995).
32. Kohsuke Mori, Hiromi Yamashita and Masakazu Anpo, Photocatalytic reduction of CO_2 with H_2O on various titanium oxide photocatalysts, RSC Adv., 2, 3165-3172 (2012).
33. T. Yui, A. Kan, C. Saitoh, K. Koike, T. Ibusuki, and O. Ishitani, Photochemical reduction of CO_2 using TiO_2: effects of organic adsorbates on TiO_2 and deposition of Pd onto TiO_2, Appl. Mater. Interfaces, 3, 2594–2600 (2011).
34. X.H. Xia, Z.J. Jia, Y. Yu, Y. Liang, Z. Wang and L.L. Ma, Preparation of multi-walled carbon nanotube supported TiO_2 and its photo-catalytic activity in the reduction of CO_2 with H_2O, Carbon 45 717–721(2007).
35. M. Anpo, H. Yamashita, Y. Ichihashi, Y. Fujii and M. Honda, Photo-catalytic Reduction of CO_2 with H_2O on Titanium Oxides Anchored within Micropores of Zeolites: Effects of the Structure of the Active Sites and the Addition of Pt, J. Phys. Chem. B 101, 2632–2636 (1997).
36. C.C. Yang, J. Vernimmen, V. Meynen, P. Cool, and G. Mul, Mechanistic study of hydrocarbon formation in photo-catalytic CO_2 reduction over Ti-SBA-15, J. Catal. 284 1–8 (2011).
37. C. Wang, R.L. Thompson, J. Baltrus and C. Matranga, Visible Light Photo-reduction of CO_2 Using CdSe/Pt/TiO_2 Heterostructured Catalysts, J. Phys. Chem. Lett. 1, 48–53 (2010).
38. C. Wang, R.L. Thompson, P. Ohodnicki, J. Baltrus and C. Matranga, Size-dependent photocatalytic reduction of CO_2 with PbS quantum dot sensitized TiO_2 heterostructured photocatalysts. J. Mater. Chem. 21, 13452–13457 (2011).
39. I.H. Tseng, W.C. Chang, and J.C.S. Wu, Photo-reduction of CO_2 using sol–gel derived titania and titania-supported copper catalysts, Appl. Catal. B 37, 37–48 (2002).
40. I.H. Tseng, J.C.S. Wu, and H.Y. Chou, Effects of sol–gel procedures on the photo-catalysis of Cu/TiO_2 in CO_2 photoreduction, J. Catal. 221,432–440 (2004).
41. O.K. Varghese, M. Paulose, T.J. LaTempa and C.A. Grimes, High-Rate Solar Photo-catalytic Conversion of CO_2 and Water Vapor to Hydrocarbon Fuels, Nano Lett. 9, 731–737 (2009).
42. P. Praus, O. Kozák, K. Kocí, A. Panácek, and R. Dvorsky, CdS nanoparticles deposited on montmorillonite: Preparation, characterization and application for photo-reduction of carbon dioxide, J. Colloid Interface Sci. 360, 574–579 (2011).
43. P.W. Pan and Y.W. Chen, Photocatalytic reduction of carbon dioxide on NiO/InTaO 4 under visible light irradiation, Catal. Commun. 8, 1546–1549 (2007).
44. Y. Zhou, Z. Tian, Z. Zhao, Q. Liu, J. Kou, X. Chen, J. Gao, S. Yan and Z. Zou, High-Yield Synthesis of Ultrathin and Uniform Bi_2WO_6 Square Nanoplates Benefitting from Photocatalytic Reduction of CO_2 into Renewable Hydrocarbon Fuel under Visible Light, Appl. Mater. Interfaces 3, 3594–3601 (2011).
45. Y. Liu, B. Huang, Y. Dai, X. Zhang, X. Qin, M. Jiang, M.H. Whangbo, Y. Liu, B. Huang, Y. Dai, X. Zhang, X. Qin, M. Jiang, and M.H. Whangbo, Catal. Commun. 11, 210–213 (2009).
46. X. Li, H. Pan, W. Li and Z. Zhuang, Photo-catalytic reduction of CO_2 to methane over HNb3O8 nanobelts Appl. Catal. A 413/414, 103–108 (2012).
47. Q. Liu, Y. Zhou, J. Kou, X. Chen, Z. Tian, J. Gao, S. Yan and Z. Zou, High-Yield Synthesis of Ultralong and Ultrathin Zn_2GeO_4 Nanoribbons toward Improved Photo-catalytic Reduction of CO_2 into Renewable Hydrocarbon Fuel, J. Am. Chem. Soc. 132, 14385–14387 (2010).

48. K. Iizuka, T. Wato, Y. Miseki, K. Saito and A. Kudo, Photo-catalytic Reduction of Carbon Dioxide over Ag Cocatalyst-Loaded $ALa_4Ti_4O_{15}$ (A = Ca, Sr, and Ba) Using Water as a Reducing Reagent, J. Am. Chem. Soc. 133, 20863–20868 (2011).
49. M. Halmann, M. Ulaman,B.A. Blajeni, Photochemical solar collector for the photoassisted reduction of aqueous carbon dioxide, Solar Energy, 31, 429–431 (1983).
50. S.C. Yan, S.X. Ouyang, J. Gao, M. Yang, J.Y. Feng, X.X. Fan, L.J. Wan, Z.S. Li, J.H. Ye, Y. Zhou, and Z.G.Zou, A Room-Temperature Reactive-Template Route to Mesoporous $ZnGa_2O_4$ with Improved Photocatalytic Activity in Reduction of CO_2, Angew. Chem. Int. Ed. 49, 6400.(2010).
51. N. Zhang, S.X. Ouyang, P. Li, Y.J. Zhang, G. C. Xi, T. Kako, and J.H. Ye, Ion-exchange synthesis of a micro/mesoporous Zn2GeO4 photocatalyst at room temperature for photoreduction of CO_2 Chem. Commun. 2011,47, 2041–2043 (2011).
52. Han Zhou, JianjunGuo, Peng Li, Tongxiang Fan, Di Zhang and Jinhua Ye, Leaf-architectured 3D Hierarchical Artificial Photosynthetic System of Perovskite Titanates Towards CO_2 Photoreduction Into Hydrocarbon Fuels, Scientific Reports, 3: 1667. DOI: 10.1038/srep01667 (2013).
53. V. Jeyalakshmi,, R. Mahalakshmy, K.R. Krishnamurthy, B. Viswanathan, 6th Asia Pacific Congress on Catalysis-APCAT-6, Oct 13–17, **2013**, Taipei, Taiwan.
54. V. Jeyalakshmi, Mahalakshmy R, Ramesh Kanaparthi, Peddy, V.C. Rao, Nettam V. Choudary Gandham Sri Ganesh, K.R. Krishnamurthy and B. Viswanathan, Visible light driven reduction of CO_2 **by water on modified** Sr_3 Ti_2O_7, Abstract accepted for presentation in 248th ACS meeting in San Fransisco August (2014).
55. V. Jeyalakshmi, R. Mahalakshmy, K. R. Krishnamurthy and B Viswanathan, Photo catalytic reduction of carbon dioxide by alkaline water on La modified sodium tantalate with different co-catalysts under UV-Visible radiation (manuscript under preparation).
56. Kudo and Y. Miseki, Heterogeneous photo-catalyst materials for water splitting, Chem. Soc. Rev., 38, 253–278 (2008).
57. Nathan I. Hammer, *Photo-catalytic Reduction of CO_2 and Water Splitting, I,* http://home.olemiss.edu/~cmchengs/Global%20Warming/Session%2019%20Photocatalytic%20Reduction%20of%20CO2%20and%20Water%20Spliting%20I/Photocatalytic_Splitting_I.pdf
58. B. Viswanathan and K.R .Krishnamurthy, Nitrogen Incorporation in TiO_2: Does It Make a Visible Light Photo-Active Material? International Journal of Photoenergy, Vol. 2012 (2012) Article ID 269654, 10 pages, http://dx.doi.org/10.1155/2012/269654
59. F.E. Osterloh, Inorganic Materials as catalysts for photo-chemical splitting of water, Chemistry of Materials, 20, 35–54 (2008).

Index

A
Ab-initio calculations, 114, 177
Acrylic, 33
$AgBiW_2O_8$, 129–130
Al_2O_3, 32, 33, 98, 201–209

B
Bandgap, 2, 4–6, 14, 24, 43, 44, 46–51, 58, 75, 76, 78–80, 82–84, 87–88, 97–101, 103, 104, 106, 107, 110, 113–121, 123, 124, 126, 129, 130, 136, 140, 145, 146, 150, 173–178, 183, 187, 189, 213, 215, 219, 224, 229
Band structure, 49, 50, 75–92, 99, 101, 103, 104, 106, 114, 116–119, 122–124, 126, 129, 130, 178, 180
Barrier properties, 28–36
Bi_2O_3, 124, 174–179, 181–197
$Bi_2Ti_2O_7$, 124

C
Capacitance, 28, 81, 180, 206–208
Carbon-based materials, 5, 12–14
CdS, 1–15, 49, 52, 54, 55, 57–59, 87, 92, 140, 142, 145, 146, 149, 153–167, 173, 212, 218
CdS-ZnS, 142, 149
Cells, 23–36, 42, 47, 84, 85, 92, 97, 98, 104, 105, 109, 118–120, 127, 135–150, 177, 183, 201–209, 228
Cell performance, 146
Chalcogenides, 4, 87, 97, 109, 154, 155, 161, 167
Chemiluminescence, 88–92
CO_2, 1, 41, 54, 64, 98, 137, 140, 213–219, 221–227, 229
  activation, 219, 228
  reduction, 219, 224–228
Co-catalyst effects, 44, 47–50, 54, 55, 64, 217, 219, 223, 228
Composite photocatalyst, 166
Conduction edge, 4, 47, 49, 76, 81–88, 103, 121, 129, 131, 174, 192, 195, 203
Crystal structures, 98, 100–108, 110, 122, 124, 126, 130, 158, 177
$CuNbO_3$, 99–103, 107, 109, 110
$CuNb_3O_8$, 102–105, 107, 109, 110
$Cu_3Ta_7O_{19}$, 105–108, 110
$Cu_5Ta_{11}O_{30}$, 107–108, 110
$CuWO_4$, 114, 121–124

D
Delafossites, 98, 99, 108, 114, 115, 126–129
Density functional theory (DFT), 100, 103, 106, 115–117, 121–123, 130, 177
Dye-sensitized solar cells (DSSCs), 136, 145, 201–209

E
Electrochemical characterization, 157–160
Electrochemical impedance, 105, 179, 190, 193, 204
Electron microscopy, 204
Electron transfer, 4, 10, 11, 59, 91, 92, 123, 124, 202, 225–228

B. Viswanathan et al. (eds.), *Materials and Processes for Solar Fuel Production*, Nanostructure Science and Technology 174, DOI 10.1007/978-1-4939-1628-3

Encapsulation, 23–36
Energy levels, 48, 49, 57, 174

F
Forbidden gaps, 76, 83–85

G
Gold, 29, 77

H
Heterojunction, 1–15, 26, 98, 99
Hydrogen, 1–15, 34, 41–66, 75, 97, 113, 138, 153–167, 173, 211
Hydrogen sulfide (H_2S), 2–4, 6, 7, 52, 59–60

I
Impedance, 63, 81, 105, 179, 180, 189, 190, 193, 204, 206–208
Incident photon to current conversion efficiency (IPCE), 148–150, 175
Indirect transition, 79, 101
Inorganic sacrificial agent, 57–59, 66

L
Large scale hydrogen, 43, 46
Lifetime, 2, 14, 23, 25–27, 32–35

M
Metal substitution, 120–124
Methyl orange, 4, 157, 160, 163–165
Mixed metal oxides, 217
Modeling, 113–131
Mott–Schottky, 76, 81–82, 156, 160, 179, 180, 190–195

N
Nano-/bulk-junctions, 6–8, 26
Nanocrystalline, 136, 139, 142, 149
Nanoporous, 173–197, 201, 204
Nanostructures, 136, 142, 144, 174, 175
Nanowires, 6–8, 176
Nb_2O_5, 102, 201–209
Non-oxide, 76, 140, 227
n-type, 76, 81–83, 97, 109, 115, 116, 121, 126, 173, 174, 177, 187, 192, 193, 195, 197
Nyquist plot, 105, 207

O
Optical characterization, 75–92, 183
Organic PV (OPV), 23–27, 32, 33
Organic sacrificial agent, 51–57

P
P25, 62, 64, 142, 154–162, 202, 203, 213, 218, 224, 228
Partial DOS, 118–120, 122–124
PEDOT:PSS, 26
Performance improvement, 209
PGM, 154, 159, 161, 167
Phase, 7, 8, 11, 14, 49, 63, 99, 101, 102, 107, 109, 115, 122, 129, 141, 154, 156, 158, 174–176, 179, 182–185, 187, 188, 194, 196, 197, 213, 219
pH effect, 87, 137, 138
Photoanodes, 47, 102, 113, 135, 137, 141–146, 149, 150, 173–197
Photocatalysis, 3, 9–14, 43, 51, 124, 154, 157, 160–162, 167
Photodegradation, 136, 138, 153–167
Photoelectrochemical response, 167
Photo-fuelcell, 136, 137
Photon, 2, 3, 43–47, 49, 56, 62, 75, 76, 78–80, 83, 126, 135, 137, 146, 148, 157, 175, 212, 213, 217, 224, 225
Photosynthesis, 211, 212, 225–227
Photovoltaics, 23, 24, 26, 36, 41, 42, 129, 135
Platinum, 179
Pollutant treatment, 136, 163
Polymorphs, 174–178
Polysulfide, 59, 60, 146, 161, 162, 166, 167
Poly vinyl alcohol (PVA), 33, 34
p-type photocatalysts, 76
PVA. *See* Poly vinyl alcohol (PVA)

R
Raman, 183, 184
Redox reactions, 4, 140, 153, 166

S
Sacrificial agent, 7, 41, 51–62, 64–66, 146, 153–167, 215, 228
Semiconductor, 2, 23, 41, 75, 97, 114, 136, 165, 173, 204, 212
Solar cell, 23–36, 98, 136, 139, 145, 148, 201–209
Solar conversion efficiency, 48
Solar fuel, 75, 77, 149, 150, 211–230

Spectral irradiance profile, 45
Stability, 7, 13, 15, 24, 26, 27, 33, 36, 49, 65, 89, 91, 97–99, 102, 105, 109, 114–116, 129, 130, 136, 146, 150, 153, 154, 160, 163, 166, 167, 173–197
Surface passivation, 88, 201–209

T
Tauc plots, 180, 187, 189
TiO_2, 4, 36, 41, 86, 98, 113, 136, 153–167, 173, 201–209, 212
TiO_2 nanosheets, 6–8
Titania, 136–142, 144–146, 149, 213, 217, 228
Total densities-of-states (DOS), 101, 119, 120, 124, 125, 128
Tungsten carbide (WC), 5, 11–12

V
Valence edge, 81–88
Visible light activity, 124

W
Waste water, 176
Water reduction, 2, 49, 50, 65, 107
Water splitting principle, 2, 43–45
WC. *See* Tungsten carbide (WC)
WO_3, 4, 49, 55, 99, 117–121, 129–131, 173, 174, 185, 212

Z
ZnO, 4, 33, 49, 50, 55, 97, 98, 116, 117, 128, 129, 144, 173, 174, 212, 218